ON THE RESPONSE OF THE SPECIAL SENSOR MICROWAVE/IMAGER TO THE MARINE ENVIRONMENT - IMPLICATIONS FOR ATMOSPHERIC PARAMETER RETRIEVALS

A DISSERTATION SUBMITTED IN PARTIAL FULFILLMENT
OF THE REQUIREMENTS FOR THE DEGREE OF
DOCTOR OF PHILOSOPHY

Grant W. Petty
Department of Atmospheric Sciences AK-40
UNIVERSITY OF WASHINGTON
Seattle, WA 98195

December 1, 1990

TECHNICAL REPORT
NASA GRANT NAG5-943

ON THE RESPONSE OF THE SPECIAL SENSOR MICROWAVE/IMAGER TO THE MARINE ENVIRONMENT - IMPLICATIONS FOR ATMOSPHERIC PARAMETER RETRIEVALS

A DISSERTATION SUBMITTED IN PARTIAL FULFILLMENT
OF THE REQUIREMENTS FOR THE DEGREE OF
DOCTOR OF PHILOSOPHY

Grant W. Petty
Department of Atmospheric Sciences AK-40
UNIVERSITY OF WASHINGTON
Seattle, WA 98195

December 1, 1990

TECHNICAL REPORT
NASA GRANT NAG5-943

ON THE RESPONSE OF THE SPECIAL SENSOR MICROWAVE/IMAGER TO THE MARINE ENVIRONMENT - IMPLICATIONS FOR ATMOSPHERIC PARAMETER RETRIEVALS

FOREWORD

This report is the doctoral thesis of Grant W. Petty. It represents the major achievement of a series of projects carried out under two consecutive NASA Grants, NAG5-943, and its forerunner NAG5-354, administered respectively by Dr. Ramesh Kakar and Dr. Robert Curran at NASA headquarters. It follows our early studies with microwave radiometer data from the Seasat and Nimbus 7 SMMRs. Its goal is comprehensive and internally consistent development of optimal algorithms for interpretation of signals from the Special Sensor Microwave/Imager (SSM/I) on Defense Meteorological Satellites over the oceans in terms of columnar atmospheric content of water as vapor, cloud water, rain and precipitation-size ice particles while accounting for variations in the background radiation.

Grant Petty has looked in detail at the basic principles underlying the emission, absorption, attenuation and scattering of microwave radiation by smooth and rough sea surfaces and by gases, cloud droplets, rain drops and precipitation size ice in the overlying atmosphere. Both analytic and numerical solutions to the radiative transfer equations are found and interactions between different retrieved parameters, and minimum uncertainties in the derived quantities are evaluated. Sensitivities to several non-derived but implied quantities are also calculated. Finally, a set of practical semi-empirical, self-consistent algorithms for atmospheric water as vapor, cloud water, rain and precipitation size ice particles and sea surface wind speed are presented. An example of an occluded midlatitude cyclone "seen" with SSM/I is provided.

Several other projects were undertaken with support from these grants and from NASA grant NAGW-1688 administered by Dr. James Dodge at NASA Headquarters. A collection of other recent publications from our group at the University of Washington, some in collaboration with French and Scandinavian colleagues, will soon be available as a Technical Report in two volumes entitled *"Microwave Radiometer Studies of Atmospheric Water Over the Oceans"* (Katsaros et al., 1991).

December 1, 1990

Kristina B. Katsaros
Principal Investigator

University of Washington

Abstract

On the Response of the Special Sensor Microwave/Imager to the Marine Environment — Implications for Atmospheric Parameter Retrievals

by Grant William Petty

Chairperson of the Supervisory Committee: Professor Kristina B. Katsaros
Department of Atmospheric Sciences

The objective of this dissertation is to provide a reasonably rigorous basis for understanding and extracting the physical information content of Special Sensor Microwave/Imager (SSM/I) satellite images of the marine environment. To this end, a comprehensive algebraic parameterization is developed for the response of the SSM/I to a set of nine atmospheric and ocean surface parameters. The brightness temperature model includes a closed-form approximation to microwave radiative transfer in a non-scattering atmosphere and fitted models for surface emission and scattering based on geometric optics calculations for the roughened sea surface. The combined model is empirically tuned using suitable sets of SSM/I data and coincident surface observations.

The brightness temperature model is then used to examine the sensitivity of the SSM/I to realistic variations in the scene being observed and to evaluate the theoretical maximum precision of global SSM/I retrievals of integrated water vapor, integrated cloud liquid water, and surface wind speed. A general minimum-variance method for optimally retrieving geophysical parameters from multichannel brightness temperature measurements is outlined, and several global statistical constraints of the type required by this method are computed.

Finally, a unified set of efficient statistical and semi-physical algorithms is presented for obtaining fields of surface wind speed, integrated water vapor, cloud liquid water, and precipitation from SSM/I brightness temperature data. Unique features include: (i) a semi-physical method for retrieving integrated cloud liquid

water at 15 km resolution and with rms errors as small as $\sim$0.02 kg m^{-2}; (ii) a 3-channel statistical algorithm for integrated water vapor which was constructed so as to have improved linear response to water vapor and reduced sensitivity to precipitation; and (iii) two complementary indices of precipitation activity (based on 37 GHz attenuation and 85 GHz scattering, respectively), each of which are relatively insensitive to variations in other environmental parameters.

Table of Contents

List of Figures

List of Tables

List of Abbreviations

AFGWC	Air Force Global Weather Center
DMSP	Defense Meteorological Satellite Program
DOD	Department of Defense
ECMWF	European Centre for Medium-Range Weather Forecasting
EMEX	Equatorial Mesoscale Experiment
ESMR	Electrically Scanned Microwave Radiometer
FGGE	First GARP Global Experiment
FNOC	Fleet Numerical Oceanography Center
FIRE	First ISCCP Regional Experimental
FOV	field of view
GARP	Global Atmospheric Research Programme
GLA	Goddard Laboratory for Atmospheres
GOASEX	Gulf of Alaska – Seasat Experiment
ISCCP	International Satellite Cloud Climatology Project
ITCZ	intertropical convergence zone
JASIN	Joint Air-Sea Interaction experiment
LST	Local Standard Time
MPM	Millimeter-wave Propagation Model
MSU	Microwave Sounding Unit
NASA	National Aeronautics and Space Administration
NEMS	Nimbus-E Microwave Sounder
NET	Nimbus Experiment Team
NOAA	National Oceanographic and Atmospheric Administration
NRL	Naval Research Laboratory
OLS	Operational Linescan System
PCT	polarization corrected temperature
RMS	root-mean-squared
RSS	Remote Sensing Systems, Inc.
RTE	radiative transfer equation
SMMR	Scanning Multichannel Microwave Radiometer
SOP	Special Observing Period
SSH	Special Sensor Humidity
SSM/I	Special Sensor Microwave/Imager
SSM/T	Special Sensor Microwave/Temperature
TAMEX	Taiwan Area Mesoscale Experiment
TDR	Temperature Data Record
THIR	Temperature and Humidity Infrared Radiometer
TIROS	Television and Infrared Observations Satellite
TRMM	Tropical Rainfall Measuring Mission
WMONEX	Winter Monsoon Experiment

Acknowledgments

I would like to express my appreciation to Drs. Kristina Katsaros, Conway Leovy, Richard Reed, and Stephen Warren, not only for serving on my Supervisory Committee, but also for helping to define the standards of excellence against which I will always measure my own work. I am especially indebted to my advisor, Dr. Kristina Katsaros, for her support and encouragement, her scientific and professional counsel and her personal friendship.

Many students and staff members in the Department of Atmospheric Sciences at the University of Washington provided useful discussions and/or invaluable technical assistance. Of these, I particularly wish to thank Drs. Dean Churchill and Harry Edmon, Mark Michelson, and my office mates Serhad Atakturk and Douglas Miller. Above all, I am grateful to my wife Antje, who has been an unfailing source of love and moral support throughout my graduate studies.

This work was performed under NASA grant NAG5-943. SSM/I Antenna Temperature Tapes were generously made available by Frank Wentz of Remote Sensing Systems, Inc. Dr. John Alishouse of NOAA/NESDIS was particularly kind in allowing me to use the radiosonde-SSM/I comparison data sets which he and his colleagues painstakingly compiled.

1. INTRODUCTION

Microwave radiometry from space, using passive sensors operating at frequencies for which the atmosphere is relatively transparent, is gaining recognition as a valuable diagnostic tool in a variety of meteorological and oceanographic applications. Satellite microwave data are unique in being able to provide large-scale maps of integrated atmospheric water vapor, integrated cloud liquid water, and physically direct observations of precipitation over the world's oceans. Ocean surface roughness, sea ice coverage, and several land surface parameters (e.g., soil moisture, snow coverage) may also be estimated under most weather conditions.

A wide range of experimental and operational applications for these data have been proposed or demonstrated during the past decade or so, and new possibilities continue to be recognized. For example, several studies have demonstrated the use of satellite microwave estimates of integrated atmospheric water vapor and surface wind speed to estimate surface latent heat fluxes over the global oceans. Numerous recent conference papers have also explored applications of microwave data to the diagnosis of tropical cyclone structure and intensity, and the potential use of microwave observations for obtaining physically direct estimates of tropical precipitation has become a major research focus. Microwave images have been found to be a valuable tool in the analysis of midlatitude oceanic cyclones and their associated surface fronts, and quantitative satellite estimates of the water content in marine stratus clouds can potentially complement surface and aircraft measurements of cloud dynamical and radiative properties in experiments like the First ISCCP (International Satellite Cloud Climatology Project) Regional Experiment (FIRE).

On June 20, 1987, the first Special Sensor Microwave/Imager (SSM/I) was successfully launched on board the F-8 satellite in the Defense Meteorological Satellite Program (DMSP). In several respects, the deployment of this sensor marked the beginning of a new era in passive microwave remote sensing. First

of all, the SSM/I is the first imaging microwave radiometer to see routine, *real-time* use in meteorological analysis and forecasting. Secondly, both the sensor calibration and sampling characteristics represent a marked improvement over the SSM/I's predecessor, the Scanning Multichannel Microwave Radiometer (SMMR). Thirdly, new high-frequency channels (85 GHz) were incorporated for the first time, yielding microwave imagery of unprecedented spatial resolution and high sensitivity to precipitation. Perhaps most importantly, the SSM/I on board the F-8 satellite is only the first of a series of identical sensors planned for deployment by the Defense Department. Together, these should provide a long and relatively continuous set of high quality satellite microwave observations of several geophysical parameters which are not readily obtained via conventional methods.

One may gain some sense of the interest generated by the new SSM/I by considering the 99 papers presented at the American Meteorological Society Fourth Conference on Satellite Meteorology and Oceanography (San Diego, May 16-19, 1989); of these, 26 focus entirely or in part on the SSM/I and its applications. A similar number (20) were presented at the more recent Fifth Conference in London (September 3–7, 1990; held jointly with the Royal Meteorological Society), and papers describing research applications of SSM/I data have gradually begun to appear in refereed journals as well.

All of the attention notwithstanding, published theoretical and empirical guidance for understanding and fully exploiting the information content of the SSM/I data remains scanty. Despite being the beneficiary of nearly two decades of experience with passive microwave radiometry from space, including one decade with the SMMR (which has several channels similar to those of the SSM/I), the SSM/I is a distinctly new instrument, whose capacity to fulfill specific tasks cannot necessarily be directly extrapolated from that of the earlier instruments.

One example of the persisting gap between theory and reality can be found in the theoretically-derived geophysical algorithms developed for the SSM/I prior to

launch, under contract from Hughes Aircraft Company, the sensor's designer and manufacturer. These algorithms, which for some time were the only operational algorithms available for the U.S. Fleet, have generally failed to meet Government accuracy specifications (Hollinger 1988). A year after launch, it was possible in some cases to replace the old algorithms with new ones based simply on linear statistical regression of SSM/I against actual *in situ* measurements of the desired parameters. However, this approach adds little to our understanding of the physics involved and is, in any case, of doubtful value for those parameters (e.g., integrated cloud water) for which coincident *in situ* measurements simply cannot be obtained over the ocean under a sufficiently wide range of conditions.

The objective of this dissertation is therefore to document and expand the theoretical and practical basis for the inversion and meteorological interpretation of SSM/I multichannel imagery obtained over the world's ice-free oceans. To this end, I shall examine in some detail the quantitative relationship between the state of the ocean-atmosphere system and observed SSM/I brightness temperatures, relying in part on a theoretical, closed-form brightness temperature model which is empirically calibrated against SSM/I data. Various factors bearing on the feasibility and accuracy of geophysical parameter retrievals are discussed, and the foundation is provided for the eventual development of optimal physical retrieval algorithms. In addition, a unified package of simplified algorithms is presented for estimating several parameters of interest, including what seems to be the first documented SSM/I algorithm for retrieving integrated cloud liquid water content at 15 km resolution.

To help lay the groundwork for the more detailed work to be presented in later chapters, Chapter 2 first offers a qualitative overview of the basic principles and motivation behind passive microwave remote sensing techniques. This is followed by a review of the history of passive microwave remote sensing as it relates to

the SSM/I (Chapter 3) and a description of the SSM/I sensor itself and of the characteristics of the DMSP satellite platform (Chapter 4).

Following this background material, Chapters 5–7 focus on the development of comprehensive parameterizations of the interaction of microwave radiation with the atmosphere and ocean surface at SSM/I frequencies. Chapter 8 then uses SSM/I data to empirically calibrate the theoretical brightness temperature model developed in the previous chapters. Chapter 9 summarizes the brightness temperature sensitivities of the SSM/I to the relevant environmental parameters, with quantitative examples for selected conditions. It is beyond the scope of this thesis to consider in detail the radiative characteristics of precipitation or the problem of retrieving quantitative rain rates; however, a qualitative discussion of these issues is offered in Chapter 10 in order to provide the background necessary for developing simple techniques for identifying precipitation and for understanding the potential impact of precipitation on the accuracy of other geophysical retrievals.

Having considered the effect of the ocean-atmosphere system on SSM/I brightness temperatures in Chapters 5–10 (i.e., the forward problem), Chapter 11 reviews existing approaches to microwave atmospheric parameter retrievals and explores a topic which appears to have been neglected in the past; namely, the applicability of optimal estimation theory to the inversion of SSM/I observations. This in turn lays the groundwork for examining the theoretical maximum retrieval precision achievable for selected parameters, based on the analytic brightness temperature model, combined with the global statistics of model input parameters. A unified set of statistical and semi-statistical algorithms is presented for retrieving integrated water vapor, integrated cloud liquid water, surface wind speed, and qualitative indices of precipitation intensity. These algorithms, while not optimal in the strict sense of the word, are believed to offer certain improvements over other SSM/I algorithms currently in use.

2. PHYSICAL PRINCIPLES: AN OVERVIEW

Like the more familiar satellite technique of infrared radiometry, which for years has routinely provided forecasters and researchers with an invaluable birds-eye view of the evolution of storms and other weather systems, microwave radiometry relies on the detection of thermally emitted electromagnetic radiation. The difference between the two methods lies in the wavelength of the radiation measured — whereas infrared imagers typically sense radiation in the neighborhood of $\sim 10^{-5}$ m ($\sim$10 μm), microwave radiometers operate at wavelengths $\sim 10^{-2}$ m ($\sim$1 cm).

The very long electromagnetic wavelengths which define the microwave portion of the spectrum interact very differently with the atmosphere than infrared or visible radiation. Unlike visible light, microwave radiation undergoes negligible scattering in the atmosphere, except in the presence of precipitation. Unlike infrared radiation, microwave radiation is virtually unaffected by cirrus clouds of any thickness, and even moderately thick non-precipitating liquid water clouds do not completely obscure the surface. As for thermal infrared radiation, however, gaseous absorption and emission — mainly by water vapor and oxygen — is always of some importance, especially at higher frequencies or in the vicinity of any of the resonant absorption bands.

For the purposes of this thesis, the important gaseous absorption features in the microwave spectrum include a single, weak resonant line due to water vapor at 22.235 GHz, one relatively strong oxygen band between 50 and 70 GHz and another oxygen band at 118.75 GHz (Fig. 2.1).

In addition, there are non-resonant absorption contributions ('continuum absorption'), arising from both dry air and water vapor, which increase monotonically with increasing frequency. The spectral regions between the stronger absorption bands are described as spectral 'windows.' Within these windows, gaseous absorption alone is not sufficient to obscure the surface from the satellite.

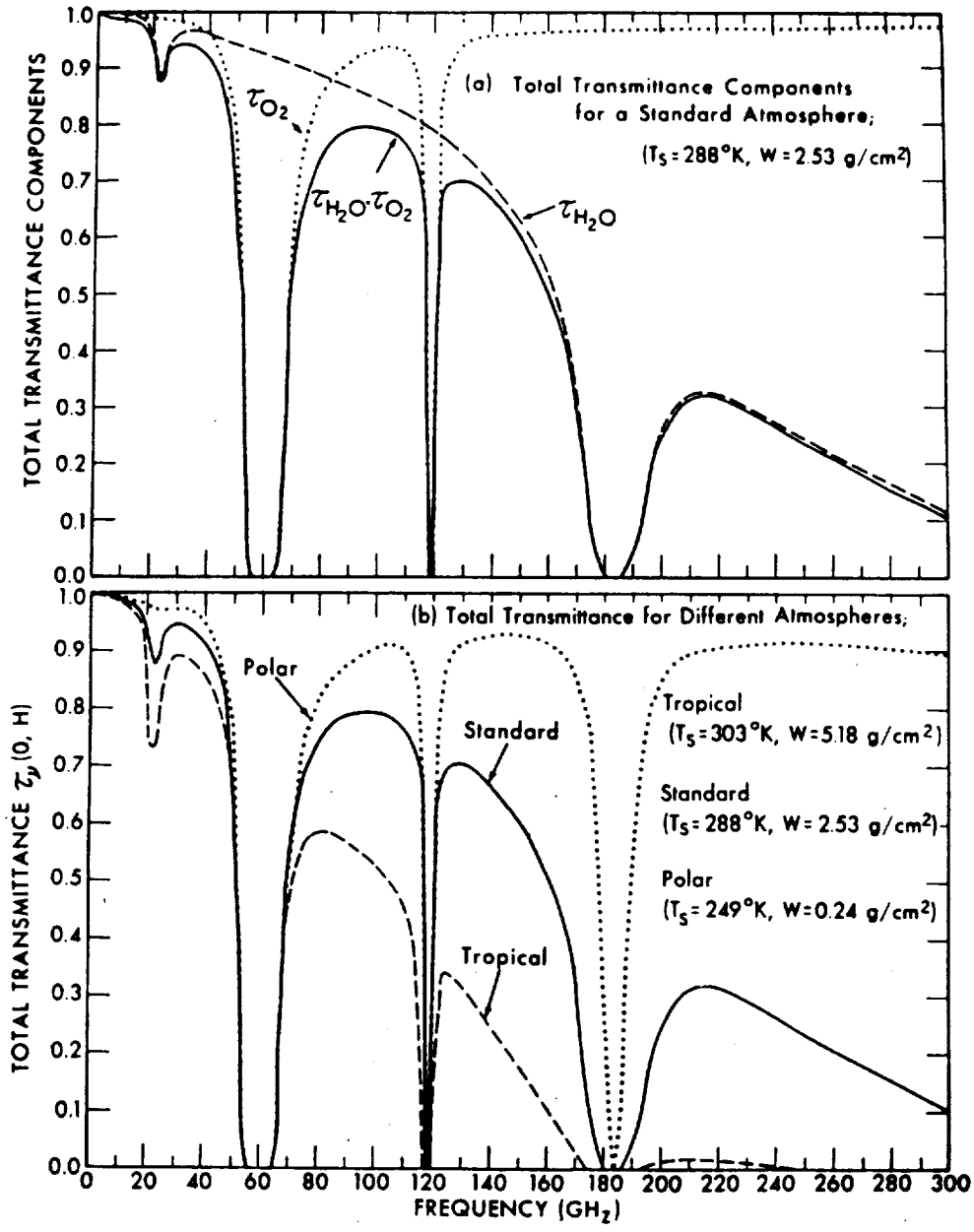

Fig. 2.1 Vertical atmospheric transmittance as function of frequency. (a) Separate oxygen and water vapor constituents for standard atmosphere. (b) Combined constituents for different atmospheres. (from Grody 1976)

Absorption by cloud water is qualitatively very similar to non-resonant gaseous absorption — i.e., there is no appreciable scattering of microwave energy by cloud-size droplets, the mass absorption coefficient is independent of drop size distribution and it increases approximately in proportion to the square of the frequency. However, within the spectral windows, the mass absorption coefficient of liquid water is considerably higher than that of oxygen or water vapor, so that clouds may often be the largest contributor to the total atmospheric emission and absorption, despite containing only a small fraction of the total water mass (liquid plus vapor) in the column.

Passive microwave imagers like the SSM/I and its predecessors have channels located exclusively at window frequencies. This characteristic distinguishes this class of instruments from microwave sounders, such as the TIROS-N (Television and InfraRed Observations Satellite) Microwave Sounding Unit (MSU), which view the atmosphere at frequencies within the wings of a strong absorption band in order to obtain vertical distributions of temperature and/or humidity. As a result, the radiant energy observed by each channel of the SSM/I normally consists of some combination of surface emission/reflection and the integrated emission and attenuation occurring in the atmosphere. The SSM/I has seven channels, representing four frequencies and two orthogonal polarizations (one frequency, 22.235 GHz, is observed in only vertical polarization); as a consequence, the differing spectral and polarization characteristics of surface and atmospheric emissions may be exploited in order to estimate the contributions due to each geophysical parameter.

Because of the relative transparency of the atmosphere in the microwave windows, the surface contribution to the signal observed from space is never negligible and always plays a crucial role in determining which atmospheric parameters can be retrieved and with how much accuracy. At issue is not only the strength and the spectral characteristics of the surface emission relative to those of the atmosphere, but also their spatial and temporal variability and, ultimately, the accuracy

with which the surface contribution can be directly or indirectly estimated and subtracted from the satellite observed signal.

Over land, surface emissivity typically is between 0.9 and 1.0, so that the upwelling radiance at the surface may correspond to that of a hypothetical black body which is only ~10–30 K cooler than the true surface temperature. Because atmospheric emission is concentrated in the lowest few kilometers, where air is the densest and the water vapor and cloud liquid water content is the highest, the effective emitting temperature of the atmosphere is also normally ~10 K colder than the surface. Consequently, even large variations in atmospheric opacity may give rise to very small or even negligible variations in the total radiance observed from space. Furthermore, thermal emission from a land surface is itself highly variable in space and time, depending as it does on temperature, soil composition, soil moisture, and snow or vegetation cover. In other words, the absolute sensitivity of a satellite microwave radiometer to atmospheric variations is intrinsically quite small over land, and the situation is worsened still by a comparatively large background 'noise' level. Similar considerations apply to ice-covered ocean surfaces, where the surface emissivity may depend on fractional ice coverage, thickness, brine content, air content, snow cover, etc. Of course, if surface parameters, rather than atmospheric parameters, are the principal objects of interest, then the roles of 'noise' and 'signal' are reversed. It may therefore be concluded that *passive microwave radiometers operating at window frequencies are ill-suited to observing atmospheric emission over land or sea ice, but may be well-suited to retrieving land surface and sea ice parameters under a wide range of weather conditions.*

Over the open ocean, the situation is quite different. Water surfaces have microwave emissivities which are both relatively low ($\varepsilon \sim 0.5$) and highly polarized. Atmospheric emissions (which are unpolarized) are therefore readily apparent against the 'cold', polarized radiometric background of the ocean. The ocean's

emissivity and temperature are also more uniform and predictable, so that, overall, the signal-to-noise ratio is substantially improved in comparison to that over land.

To summarize, *satellite passive microwave sensing of the atmosphere (using window frequencies) is generally a practical proposition only when the ice-free ocean serves as the background* *. Of course, which atmospheric and surface parameters can be retrieved from a given set of radiometer channels, and how accurate the estimates will be, depends on the strength and uniqueness of each parameter's microwave signature compared with the total 'noise' contribution from the sensor itself and from all other sources of radiometric variability. These are the issues which are examined in detail in this dissertation for the specific case of the SSM/I.

* The one significant exception to this rule occurs in the case of precipitating clouds bearing significant concentrations of large ice particles above the freezing level. This exception is touched on briefly in Chapter 10.

3. A HISTORY OF SATELLITE PASSIVE MICROWAVE SENSING AT WINDOW FREQUENCIES

3.1 Pioneering Work

By the time the first operational radars appeared on the scene in the years just prior to World War II, one of the more interesting properties of microwave radiation, namely the ability to penetrate even thick clouds with only modest attenuation, was already well known. During these same years, microwave radiometric techniques were also under development, primarily for the purpose of measuring extraterrestrial electromagnetic radiation (Ulaby et al. 1981). In the course of that work, Dicke et al. (1946) became the first investigators to report another interesting property of microwaves: a relationship between microwave thermal emission and atmospheric moisture, both in vapor and liquid forms. This discovery initiated a period of basic experimentation with surface microwave radiometric observations of the atmosphere that lasted through the 1950s.

More sophisticated and ambitious applications of surface-based passive microwave observations began to appear in the 1960s. For example, Barrett and Chung (1962) noted that the atmospheric water vapor profile could be estimated from surface observations of the 22.235 GHz water vapor resonance. Such observations were subsequently performed by Staelin (1966), who further noted that the water vapor and liquid water abundances in the atmosphere could be determined separately by virtue of their different spectral characteristics.

Interestingly, the first spacecraft-borne passive microwave device was used not for observing the earth and its atmosphere but rather for observing Venus during the Mariner 2 flyby in 1962 (Barrett and Lilley 1963). By analyzing data from the two-channel radiometer (15.8 and 22.2 GHz), scientists were able to place an upper limit on water vapor in the Venusian atmosphere and to infer that the temperature of the planetary surface was near 600 K.

At around the same time, the potential value of satellite microwave observations of the terrestrial atmosphere and ocean was also becoming apparent. For example, Buettner (1963) showed, using results of simple radiative transfer calculations, that microwave radiometric observations from space near 1.6 cm (19 GHz) could be used to map precipitation, especially over the ocean. A short time later, a limited number of experimental observations of the microwave brightness temperature of a water surface, followed by theoretical calculations of Stogryn (1967), revealed the dependence of sea surface microwave emissivity on the degree of roughening of the surface by wind. Williams (1969) discussed microwave radiometry of the ocean with special attention to the possibility of marine wind velocity determination from satellite observations.

Kreiss (1969) used a simple radiative transfer model of effects of liquid water clouds on upwelling microwave brightness temperatures over the ocean to show that "most water clouds should produce a nonnegligible if not a measurable increase in brightness temperature" for nadir viewing in the 1–2 cm wavelength range. These computational results were confirmed with NASA aircraft observations of water clouds over the Pacific, using the 19.35 GHz Electrically Scanned Microwave Radiometer (ESMR) which was subsequently launched on board the Nimbus-5 satellite.

Staelin (1969) presented probably the first comprehensive theoretical analysis of ground-based and space-based microwave radiometric remote sensing techniques, including a detailed discussion of the relevant physics, the problem of inverting measurements, and proposing a number of meteorological, oceanographic, and geological applications. Potential applications discussed include atmospheric temperature profile measurements, atmospheric constituents (especially water vapor, clouds, precipitation), and surface properties (sea state, sea surface temperature, etc.). Among his more interesting conclusions:

- "Microwave sensors provide the only remote sensing technique capable of measuring atmospheric temperature profiles in the presence of clouds."
- "Microwave sensors appear to be unique in their ability to measure the temperature profile above 50 km."
- "Microwaves are unique in their ability to yield measurements of tropospheric water vapor in the presence of clouds."
- "Microwaves provide a powerful tool for measuring the total liquid water content of clouds, and even though there may be some ambiguity in the presence of large particles or precipitation, the data are still quite unique."
- "Microwaves offer promise of yielding such surface characteristics as sea state, snow cover, ice cover, ground water, etc."

In the meantime, Soviet scientists had been conducting their own microwave sensing research, the details of which remained largely unavailable in the English-language scientific literature. These culminated in the very first space-based microwave observations of the earth's surface and atmosphere, aboard the Cosmos 243 satellite. This nadir-looking instrument, launched on 23 September 1968, measured brightness temperatures at 8.5, 3.4, 1.35, and 0.8 cm wavelengths (3.5, 8.8, 22.235, and 37 GHz) for about two weeks. Among other things, integrated water vapor and integrated liquid water were inferred from the measurements, using unspecified algorithms. Variations in these parameters were observed to correspond generally to large-scale meteorological features, such as cyclones, anticyclones, and the intertropical convergence zone (Basharinov et al. 1971). A subsequent instrument, the Cosmos 384, was launched in 1970 but functioned for only two days.

The first U.S. satellite-based microwave instruments, the 19.35 GHz ESMR and the Nimbus-E Microwave Spectrometer (NEMS, an atmospheric profiler), went into space in 1972 on board Nimbus-5. A 37 GHz version of the ESMR

was launched three years later on board the Nimbus-6 satellite. The deployment of the ESMR marked the beginning, for the West at least, of the present era of rapid progress in the development, validation, and application of passive microwave techniques for observing the surface and atmosphere.

An excellent overview of the work accomplished in this field prior to 1980 may be found in an article by Njoku (1982). In the following section, we highlight some key results from those satellite microwave sensors which preceded the appearance of the SSM/I in 1987, restricting ourselves to those developments which proved more or less directly relevant to the SSM/I and its meteorological applications over the ocean.

3.2 Early Satellite Microwave Sensing Results

Rosenkranz et al. (1972) field-tested the ability of the NEMS instrument to measure atmospheric layer thicknesses (i.e., mean temperatures) in frontal systems, viewing downward from an aircraft. Integrated water vapor and liquid water estimates were also made using this sensor, and these were compared with direct measurements by the aircraft. Retrieved water vapor values were found to fall within the large experimental uncertainty of the direct measurements; absolute liquid water values were "not as accurate as expected," due to calibration difficulties with one of the NEMS channels. However, "the relative accuracy enabled the pattern of liquid water in the frontal systems to be discerned clearly."

Staelin et al. (1975), while studying the effects of clouds on atmospheric temperature profiles obtained from NEMS, observed that heavy clouds and precipitation were identifiable as "cold spots" in 53.65 GHz brightness temperatures. They concluded that "such minima can be used to detect the presence and significance of major storm systems over both land and sea. The use of slightly longer wavelengths should enhance this capability." Although the practical significance of these observations appears to have gone largely unrecognized for some time,

the phenomenon described now lies at the heart of some promising recent rain rate retrieval techniques using 37 GHz or 85.5 GHz radiometric observations (e.g., Spencer 1986, Spencer et al. 1989).

Grody (1976) derived integrated water vapor and integrated liquid water algorithms for the 22.235 and 31.4 GHz channels of the nadir-viewing Nimbus-5 NEMS, using linear statistical regression applied to a set of brightness temperatures computed theoretically from 60 radiosonde soundings. He claimed standard errors of 3.2 kg m^{-2} and 0.12 kg m^{-2} for water vapor and liquid water, respectively, based on the theoretical analysis. He also compared actual NEMS water vapor retrievals, using his algorithm, with 6 nearby radiosonde soundings. The results agreed to within about 10%, but a systematic positive bias was noted in the NEMS results. Liquid water retrievals were found to be in qualitative agreement with THIR (Temperature and Humidity Infrared Radiometer) 11.5 μm images. He concluded that microwave radiometers demonstrate the capability to measure atmospheric water content on a global basis, for the purpose of "studying changes in the earth radiation budget and forecasting the development of storm activities."

Staelin et al. (1976) also looked at integrated water vapor and liquid water derived from the NEMS using two-channel (22.235 and 31.4 GHz) regression algorithms. They qualitatively compared nadir-looking NEMS estimates with THIR and ESMR images for several swaths over the ITCZ and for a number of tropical and midlatitude storms, and also produced NEMS-derived global water vapor and liquid water distributions for three 5-day periods in 1973. They pointed out that normal variations in vertical distribution of water vapor and other variables could lead to errors of order 0.1 kg m^{-2} for liquid water and 2 kg m^{-2} for water vapor and concluded that "additional frequencies near 1 cm wavelength would reduce the errors introduced by variable water vapor scale height, and frequencies ranging from 0.3 to 20 cm and observed with dual polarization at an oblique angle would reduce errors introduced by uncertainties in sea temperature and sea state."

Chang and Wilheit (1979) discussed techniques for measuring water vapor, surface wind speed, and liquid water from space with the NEMS and ESMR on Nimbus-5. They developed a quasi-statistical algorithm which was then applied to observations of a Pacific typhoon. Integrated water vapor estimates were found to agree well with the few *in situ* measurements near the typhoon. Liquid water estimates were in qualitative agreement with infrared images. Wind observations in the 7–15 m s^{-1} range, away from the storm center, were consistent with the microwave estimates.

Grody et al. (1980) concluded that the Nimbus-6 SCAMS 22 and 31 GHz brightness temperatures could produce estimates of integrated water vapor approaching the accuracy of radiosondes (~10%), using a non-linear algorithm. They showed that it was possible to display the large variability in integrated water vapor distributions over the tropical Pacific "which previously could only be surmised from the limited number of island radiosonde reports and by subjective analysis of satellite-cloud observations."

3.3 The Scanning Multichannel Microwave Radiometer

In 1978, two copies of a new sensor, the Scanning Multichannel Microwave Radiometer (SMMR) were launched, one on board the Seasat-A oceanographic satellite and the second on board the Nimbus-7 meteorological satellite (Gloersen and Barath 1977). This instrument was the most advanced of the microwave radiometers launched up to that time, with vertically and horizontally polarized channels at 6.6, 10.7, 18.0, 21.0, and 37.0 GHz. The purpose of the SMMR was to provide estimates of sea-surface temperature, surface wind speed, sea ice coverage and age, atmospheric water vapor and liquid water distributions, rain rate, and other geophysical parameters of potential interest in weather prediction, oceanographic research, and commercial operations. The large number of channels of the SMMR allowed better discrimination between the various geophysical parameters

observed, and validation and calibration of SMMR retrievals was undertaken in a much more systematic way than had been possible with its predecessors. One somewhat unexpected result of this thorough 'shakedown' of the SMMR was the uncovering of significant shortcomings in both the microwave sensing hardware itself and the existing theoretical basis for retrieving geophysical parameters from the observed microwave brightness temperatures.

Several competing atmospheric and oceanic parameter retrieval algorithms were developed for the two SMMRs. The most prominent of these were the regression-based Wilheit and Chang (1980) algorithm and its subsequent refinements and a non-linear, iterative physical retrieval algorithm (Bierman et al. 1978) based on the analytic brightness temperature model of Wentz (1983). Each provided retrievals of sea surface temperature, sea surface wind speed, integrated water vapor, integrated liquid water, and rain rate. Both the so-called Wilheit algorithm and the Wentz algorithm were initially derived based on theoretical radiative transfer calculations and were then tuned empirically at various stages using *in situ* meteorological observations from the Gulf of Alaska-Seasat Experiment (GOASEX), the Joint Air-Sea Interaction Experiment (JASIN), and a number of radiosonde sites in the tropics.

Several studies examined the performance of these two algorithms in comparison both with *in situ* data and with each other, mostly using SMMR data from the Seasat satellite. For example, Katsaros et al. (1981) concluded that "integrated water vapor values retrieved with Seasat SMMR algorithms are as accurate in midlatitudes as integrations of radiosonde data and more representative. When care is taken in selecting data pairs for intercomparisons in the tropics, the Wentz algorithm agrees within 10% with a limited number of radiosondes." In lieu of *in situ* comparison data, liquid water and rain rate estimates from the Wentz algorithm and Wilheit algorithm were simply compared with each other and found to give rather disparate results, implying that more work was needed in

order to generate confidence in SMMR estimates of these two parameters. Lipes (1982), summarizing the validation work accomplished up to that point, reported estimates of the maximum accuracy for SMMR retrievals to be $\sim$2.5 m s^{-1} for surface wind speed and $\sim$4 kg m^{-2} for integrated water vapor.

Alishouse (1983), using later versions of the Wentz and the Wilheit algorithms, found good agreement (rms difference $\sim$3 kg m^{-2}) between radiosonde estimates of water vapor amounts and Seasat SMMR estimates using both methods. Evaluations of the performance of rain rate retrieval algorithms were inconclusive, owing to the absence of comparable surface truth over the ocean, but it appeared that both algorithms underestimated rain in the midlatitudes and had particular trouble with tropical convective precipitation which did not fill the satellite field-of-view. Despite the quantitative uncertainty, "the precipitation results ... indicate the SMMR to be a reliable detector of precipitation in the tropics and larger-scale precipitation events in the mid-latitudes."

The above conclusions about the accuracy of SMMR retrievals were based mainly on experience with the Seasat instrument. The Nimbus-7 instrument, which functioned for a much longer period of time ($\sim$9 yr rather than only $\sim$100 days) was found to be plagued with calibration and stability problems which greatly hampered the development of quantitatively reliable retrieval algorithms for certain parameters. Particularly the 21 GHz channels exhibited long term drifts which introduced serious biases in water vapor retrievals. Nevertheless, correction schemes (e.g., Francis 1987) were developed which permitted water vapor and certain other parameters to be estimated with some confidence for at least the first four years of the Nimbus-7 SMMR dataset.*

* The 'production algorithm' for integrated water vapor adopted by the Nimbus Experiment Team (NET) was neither the Wentz algorithm nor the Wilheit algorithm but rather a distinct regression-type water vapor algorithm described by Chang et al. (1984).

Reasonably accurate, unbiased estimates of integrated cloud liquid water were never conclusively demonstrated for either of the SMMR instruments, partly because of the extreme difficulty of obtaining comparable *in situ* observations of this parameter over the ocean and partly because of the aforementioned calibration problems with the Nimbus-7 SMMR, both of which impeded the empirical refinement of retrieval algorithms. Production retrievals of SMMR integrated liquid water were even found to be *negative* over large portions of the ocean, sometimes as low as -0.1 kg m^{-2} ; nevertheless, qualitative patterns were found to be consistent with visible and infrared cloud imagery (Katsaros and Lewis 1986).

Despite considerable effort expended on quantitative rain rate retrieval algorithms for the SMMR (e.g., Spencer et al. 1983; Spencer 1986; Olson 1989; Alishouse et al. 1990b; Petty and Katsaros 1990a; Petty and Katsaros 1990b), reproducible successes in this area have also been limited, presumably because of the complex nature of the interaction between precipitation and microwave radiation, the coarse spatial resolution of the SMMR, and not least, the difficulty of obtaining independent verification of rain rate estimates. Nevertheless, it is generally agreed that certain of the SMMR channels provide an excellent *qualitative* indication of the location and relative intensity of precipitation.

3.4 Applications to Meteorological and Oceanographic Problems

The studies highlighted above, with few exceptions, belong to a large class of papers devoted almost exclusively to *evaluating* or *demonstrating* the capability of microwave sensors to estimate specific meteorological parameters. Despite the availability of passive microwave instruments in space for over two decades, disappointingly few studies have gone beyond the demonstration phase and actually *used* satellite microwave data within the larger context of an investigation of specific meteorological questions or in the operational analysis and forecasting of oceanic weather systems.

Several possible reasons may be offered to explain this failure. First of all, due to the experimental nature of the instruments, no data from any sensor prior to the SSM/I were available in near-real time; consequently, operational use of microwave data in nowcasting and forecasting was ruled out. Secondly, the sampling characteristics of the SMMRs were far from optimal for studying synoptic scale weather features: data swaths were very narrow (600–800 km) so that overlapping spatial coverage between successive swaths occurred only at very high latitudes; moreover, repeat passes over a given geographic point could occur at most once every twelve hours and were, on average, much less frequent than that. Sampling was especially problematic for the Nimbus-7 SMMR, which operated only on alternate days owing to power constraints. Finally, investigators specifically interested in meteorological applications of microwave data were probably deterred in part by continuing questions about the quantitative reliability of the geophysical retrievals: both the retrieval algorithms and the sensor calibration for the most promising and versatile instrument, the SMMR, continued to be 'tuned' behind the scenes for several years after launch. A final, comprehensive documentation of SMMR 'production' algorithms and their performance remained conspicuously absent from the open literature.

Nevertheless, since the launch of the first ESMR in 1972, a few workers have in fact crossed the threshold from demonstration to practical application of satellite microwave data. For example, Rao et al. (1976) applied the rain rate algorithm of Wilheit et al. (1977) to ESMR 19 GHz observations in order to produce a rainfall climatology over the world's oceans. Qualitative patterns in rainfall appeared reasonable and reflected the expected differences between El Nino and non-El Nino years. It became apparent, however, that the simple algorithm produced rain rates of unreasonable magnitude in higher latitudes, possibly as a result of uncertainties concerning the mean climatological depth of the rain layer.

In one of the first meteorological applications of the Seasat SMMR, Taylor et al. (1981) showed that SMMR-derived patterns of integrated water vapor provided a means to identify and track atmospheric fronts over the open ocean, even in the absence of a frontal cloud band detectable by visible or infrared satellite imagery. In particular, they found that the passage of a cold front was marked by a rapid decrease in integrated water vapor, as determined from fast-sampling radiosonde soundings, and that this decrease was also evident in SMMR water vapor imagery as a sharp gradient just behind the front. The authors noted that the ability of the SMMR to detect synoptic fronts had proven of some practical value in the analysis of meteorological data from JASIN.

The hypothesis that microwave observations of atmospheric water — in vapor, liquid, and frozen forms — could aid in the diagnosis of midlatitude oceanic cyclone location, structure, and intensity provided the impetus for a series of studies conducted at the University of Washington using SMMR data. For example, McMurdie and Katsaros (1985) provided further verification of the utility of SMMR water vapor and precipitation fields to locate fronts over the ocean, and Katsaros and Lewis (1986) described further mesoscale and synoptic scale features of these parameters in selected North Pacific cyclones. McMurdie et al. (1987) found consistency between SMMR-derived water vapor and precipitation fields and scatterometer-derived surface wind convergence fields in three midlatitude cyclones. They also found that details of the storms, such as frontal waves, were identifiable using this data set and that surface analyses were improved as a result. They concluded that microwave data, both active and passive, would be of particular value in the synoptic analysis of Southern Hemisphere weather systems, owing to the sparsity of conventional data there. McMurdie (1989) examined the relationship between SMMR-derived water vapor maxima in frontal zones and the corresponding air mass trajectories and concluded that higher maximum water vapor amounts were generally associated with air parcel trajectories originating in

lower latitudes. Katsaros et al. (1989) developed and successfully demonstrated an objective technique for flagging the location of surface fronts based on the magnitude of horizontal gradients in the integrated water vapor field. Finally, in a slightly different type of application, Katsaros et al. (1988) used Nimbus-7 SMMR data to evaluate water vapor and precipitation fields generated by a limited-area numerical forecast model for selected midlatitude cyclones over the North Atlantic.

Other investigators have compared satellite microwave data with numerical model fields on a more global scale. Eymard et al. (1989) compared Nimbus-7 SMMR sea surface temperature, surface wind, and integrated water vapor data with European Centre for Medium Range Weather Forecasting (ECMWF) model daily analyses for the first Special Observing Period (SOP) of the First GARP (Global Atmospheric Research Programme) Global Experiment (FGGE), partly in order to assess the suitability of the SMMR data for direct model assimilation. Among other things, they concluded that the SMMR integrated water vapor estimates, while providing no vertical structural information, could potentially serve to constrain water vapor fields in the numerical model, which otherwise tended to show a global mean bias of 3 kg m^{-2} and even larger local biases. On the other hand, they found the SMMR wind estimates of limited value for supplementing model-derived wind information, partly because of unresolved instrument problems and because of the absence of directional information. Monthly mean latent heat fluxes derived from SMMR data using the method of Liu (1984; see below) were found to be rather accurate and it was suggested that they could be used for *a posteriori* validation of forecast model fluxes.

In another study, Pedigo and Vincent (1990) used Nimbus-7 SMMR estimates of water vapor as a cross-check for the NASA Goddard Laboratory for Atmospheres (GLA) data fields during FGGE SOP-1. These fields served as the basis for the estimation of tropical precipitation rates from heat and moisture budget considerations. The authors found that patterns of integrated water vapor

from the SMMR agreed well with those from GLA, and concluded that greater emphasis could be placed on the exploitation of SMMR water vapor data in the future.

A rather popular application of satellite microwave data has been the production of maps of temporally averaged atmospheric water parameters and/or surface wind speed, with a particular emphasis in certain cases on the deviations associated with El Nino episodes (Prabhakara et al. 1982; Njoku and Swanson 1983; Chang et al. 1984; Prabhakara et al. 1985; Prabhakara et al. 1986; Liu 1988). In addition to studying the raw water vapor and wind fields themselves, Liu (1984, 1986, 1988) showed that it is possible to use these fields to obtain estimates of monthly average surface latent heat flux over the ocean, based in part on a surprisingly good statistical relationship between integrated water vapor and surface specific humidity.

Undoubtedly, many of the applications pioneered with SMMR data will be developed further with the SSM/I. The improved characteristics of the SSM/I create numerous new possibilities as well, and reports of creative and imaginative uses for passive microwave data have multiplied rapidly in conference proceedings since the SSM/I was launched. Essential to the success of the more quantitative applications, of course, is a solid understanding of the response of the SSM/I to the environment and of the capabilities and limitations of the available algorithms for retrieving specific environmental parameters. The remainder of this dissertation is dedicated to helping fulfill that prerequisite.

4. THE SPECIAL SENSOR MICROWAVE / IMAGER

The first Special Sensor Microwave Imager (SSM/I) was launched on 19 June 1987 on board the F-8 satellite (Block 5D-2 model) in the Defense Meteorological Satellite Program (DMSP). DMSP is funded and operated by the Department of Defense (DOD) and provides the Navy and Air Force with operational imagery of weather systems and remote sensing data on critical surface and atmospheric parameters. Block 5D-2 satellites are commanded and controlled from sites located at Offutt Air Force Base (AFB), Nebraska, and Fairchild AFB, Washington, which also receive stored data from tape recorders aboard the spacecraft. Stored sensor data are physically received by ground tracking stations in Hawaii, in Thule, Greenland, and at Fairchild AFB. These data are then transmitted over commercial satellite links to the Air Force Global Weather Central (AFGWC) at Offutt, and to the Navy's Fleet Numerical Oceanography Center (FNOC) in Monterey, California. In addition, direct real-time data may be received by Air Force, Navy, and Marine ground terminals at various sites around the world.

4.1 Sensor and Platform Characteristics

The F-8 satellite was placed in a near polar (98.8°) circular (±7 m) sun-synchronous orbit, at a mean altitude of 833 km and with a period of 6118 s (102 minutes). This orbital period corresponds to 14.12 complete orbits per 24 hr period. The ascending leg of the F-8 satellite orbit crosses the equator near 0613 Local Standard Time (LST); the descending leg occurs near 1900 LST on the opposite side of the globe. Other meteorological sensors normally included on Block 5D satellites in addition to the SSM/I include the Operational Linescan System (OLS — a fine resolution visual and infrared imager) the Special Sensor H (SSH — an infrared humidity, temperature, and ozone sounder) and the Special Sensor M/T (SSM/T — a microwave temperature sounder).

The SSM/I has seven channels; these sense atmospheric and surface thermal emission at 19.35, 22.235, 37.0 and 85.5 GHz (1.55, 1.35, 0.81, and 0.35 cm). Each frequency is observed in both vertical and horizontal polarization, except for 22 GHz, which is observed in vertical polarization only. For convenience, the seven individual channels are often referred to in shorthand form as 19V, 19H, 22V, 37V, 37H, 85V, and 85H.

The antenna of the SSM/I consists of an offset parabolic dish of diameter 61 by 66 cm. The angular resolution of the antenna is limited primarily by diffraction and is thus proportional to the wavelength. Hence, the 19 GHz channels have the poorest angular resolution (1.9° beamwidth), while the 85 GHz channels have the best resolution (0.43°).

The entire SSM/I antenna/receiver assembly rotates about the spacecraft vertical axis, reflecting radiation from a spacecraft-relative boresight angle of 44.8° into a feedhorn which is upward directed and centered on this axis (Fig. 4.1).

For the SSM/I's altitude of 859 km, this scanning configuration has the effect of maintaining a near-constant nadir viewing angle of approximately 53.1° at the earth's surface. Altitude variations due to the earth's oblateness give rise to incidence angle variations of approximately ±0.5°.

Although the SSM/I rotates continuously through 360° with a period of 1.9 s, only an arc segment of 102.4° aft of the spacecraft and centered on the subtrack is actually used to observe the earth. This corresponds to a surface data swath which is 1394 km wide. During other portions of the scan, cold and hot references are sampled in order to provide calibration updates. Geographic coverage by the SSM/I during a typical 24 hr period is indicated in Fig. 4.2.

During each scan, the 85 GHz channels are sampled 128 times with an integration period of 3.89 ms for each sample. For lower frequencies, only 64 samples are taken over the 102.4° arc, and the integration period is 7.95 ms. Only alternate scans are sampled at the lower frequencies. Scans associated with measurements

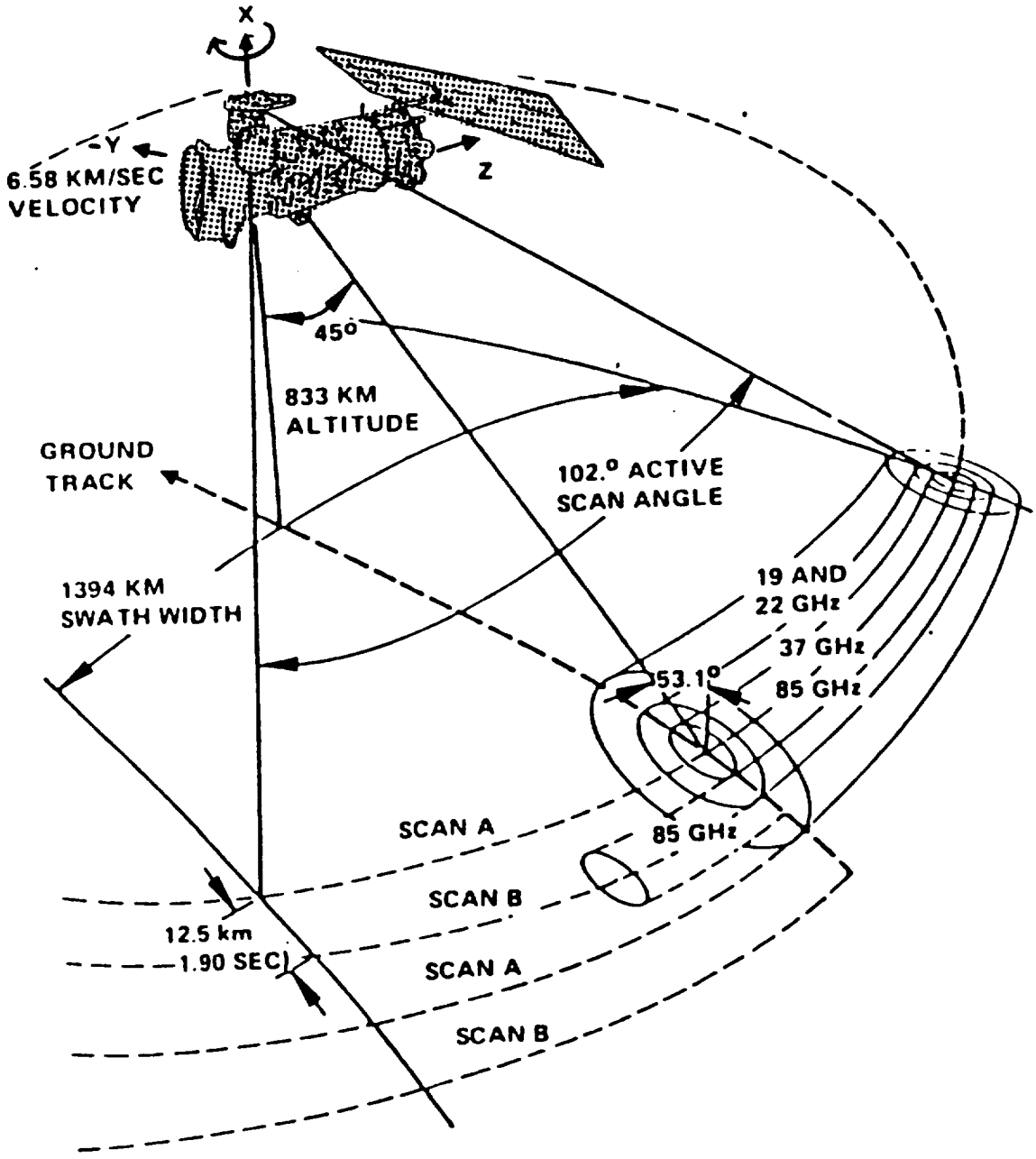

Fig. 4.1 Scan geometry of the Special Sensor Microwave/Imager.

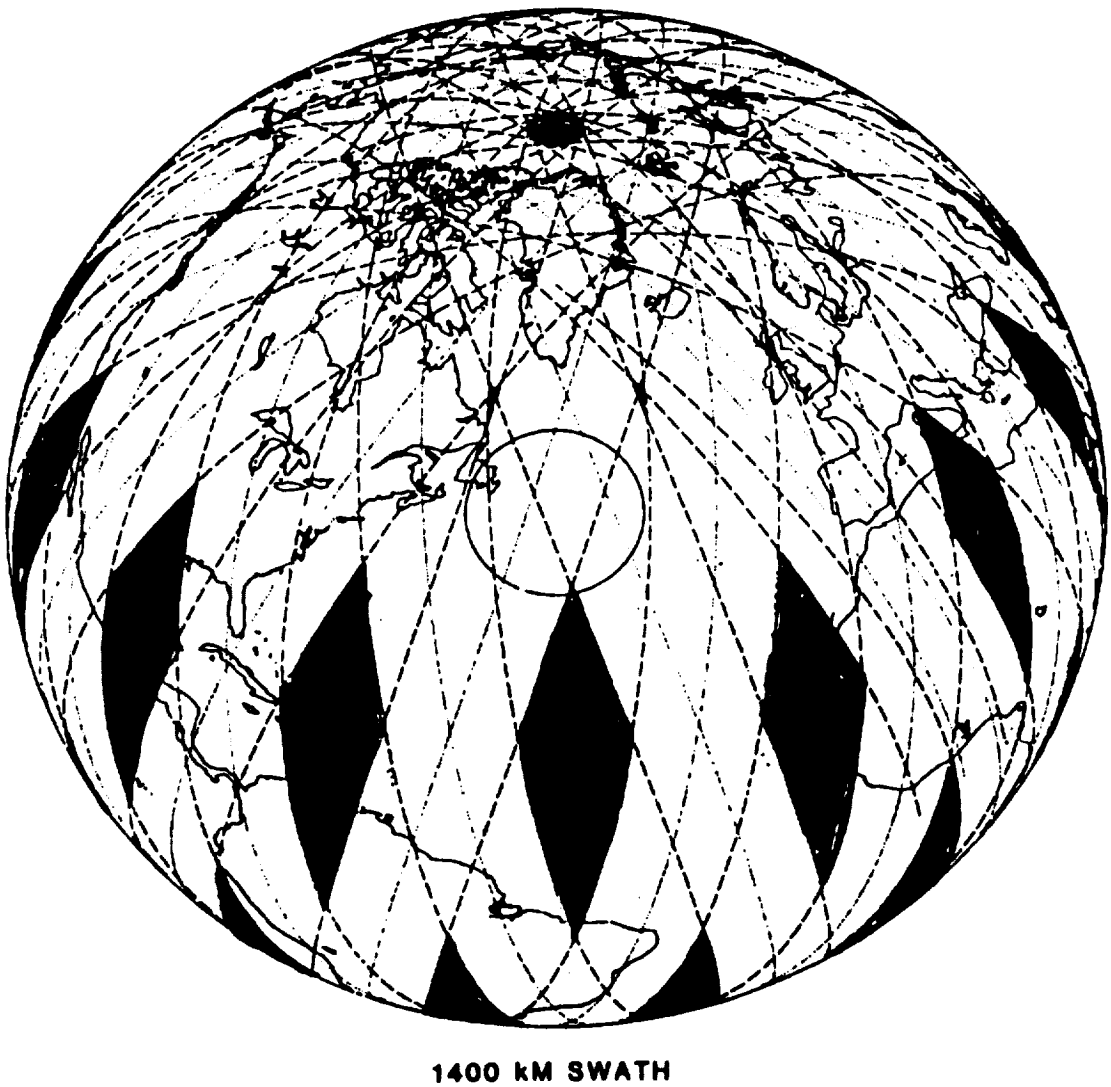

Fig. 4.2 Global coverage of the SSM/I in a 24-hour period.

by all seven channels are called A-scans; scans with only 85 GHz information are called B-scans (Figs. 4.1, 4.3). The sampling strategy described, combined with the forward motion of the satellite, leads to the 85 GHz channels being sampled at 12.5 km intervals both along the scan and along the satellite track; at lower frequencies the sampling interval is 25 km in both directions.

The actual effective surface resolution of each channel is generally poorer than suggested by these sampling densities, owing to both the limitations in antenna angular resolution and the along-scan "smearing" effect of the sample integration time. Effective 3-dB surface resolutions for each channel are given in Table 4.1.

Altogether, seven SSM/Is are scheduled for launch on Block 5D-2 satellites over the coming years. As of this writing, the second of these is tentatively scheduled for late 1990. In addition, there are plans to develop and eventually launch a modified SSM/I, the SSMIS (passive microwave imager/sounder), which will combine the capabilities of the present SSM/I and the SSM/T in a single package. The SSMIS will be carried on board the slightly larger Block 5D-3 satellite series which will follow the Block 5D-2 series. For further details of the present status of the Defense Meteorological Satellite Program, the reader is referred to Goyette et al. (1990).

4.2 Sensor Performance and Calibration

A detailed account of SSM/I antenna temperature calibration procedures, as well as predicted and measured instrument performance parameters, may be found in the Calibration/Validation ("Cal/Val") report released by the Naval Research Laboratory (Hollinger 1988). For the purposes of this thesis, the observed sensitivity, stability and absolute calibration of each SSM/I channel are the parameters of principal interest and these are summarized here.

For the period from launch (June 1987) through October 1988, individual channel sensitivities (i.e., noise equivalent temperature differential $NE\Delta T$) were

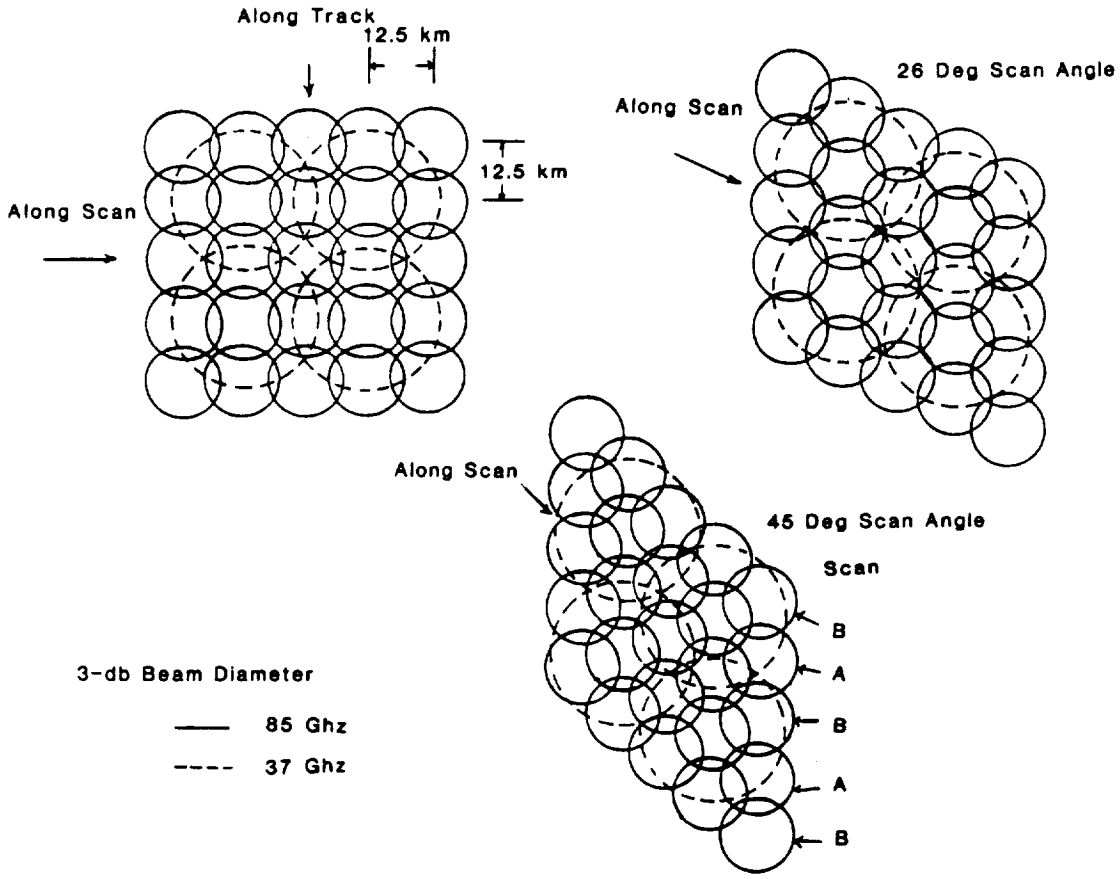

Fig. 4.3 Spatial sampling characteristics of the SSM/I, as exemplified by the 37 and 85.5 GHz channels.

Table 4.1: Effective 3-dB Spatial Resolution of SSM/I Channels

Freq. (GHz)	Polarization	Along-track	Cross-track
19.35	Vertical	69 km	43 km
19.35	Horizontal	69 km	43 km
22.235	Vertical	50 km	40 km
37.0	Vertical	37 km	28 km
37.0	Horizontal	37 km	29 km
85.5	Vertical	15 km	13 km
85.5	Horizontal	15 km	13 km

observed to be stable at values ranging from ~0.3 to ~0.7 K, except for 85V, whose $NE\Delta T$ began near 0.8 K and became significantly worse following a six-week shutoff (2 December 1987 to 13 January 1988) of the SSM/I which had been prescribed to counteract an overheating problem which developed. Because of increasing noise, the 85V channel became progressively less usable after late 1988. Channel gain stability, as well as antenna temperature repeatability for targets like the Amazon and Congo basins, the Sargasso Sea, and certain deserts, were found to be very good for all channels, again except for the 85V channel.

Absolute sensor calibration is difficult to establish with confidence, owing to a shortage of suitable reference targets. Based on comparisons of SSM/I brightness temperatures with aircraft radiometric underflights undertaken by the Naval

Research Laboratory (NRL) and with theoretically modeled brightness temperatures for certain surface types and meteorological conditions, the Cal/Val team concluded that "although there is an apparent trend for the absolute calibration of the SSM/I to be low, especially at 37 GHz, both the aircraft simulator and model differences are consistent with little or no errors in the SSM/I absolute brightness temperatures. The present assessment of the standard error of determination of the absolute calibration of the SSM/I is that it is ±3 K" (Hollinger 1988). In Chapter 8 of this dissertation, some additional independent checks on the absolute calibration are discussed.

4.3 Antenna Temperature to Brightness Temperature Conversion

The electromagnetic signal detected by a radiometer like the SSM/I is not entirely confined to that arriving from the nominal "footprint" of the satellite at the earth's surface. Rather, the detected signal is better expressed as a weighted integral (including cross-polarization terms) over solid angle of *all* microwave radiation impinging on the SSM/I's antenna subsystem from all directions, including that bypassing the parabolic reflector and impinging directly on the feedhorn. Fortunately, the relatively narrow "main beam" of the antenna is responsible for a very large fraction of the total power received by the radiometer, so that the *antenna temperature* T_A is close to the desired *brightness temperature* T_B of the scene being observed. Nevertheless, the difference is large enough to require attention.

In principle, this conversion of T_A to T_B entails a deconvolution operation, which in turn implies the solution of a Fredholm integral equation of the first kind, entirely analogous to the inversion of satellite temperature profile observations. There are several obstacles to this approach. First, knowledge of the entire radiance field affecting the antenna is required; in practice, this field can only be reliably estimated for the region directly sampled by the SSM/I, namely, the

~1400 km data swath. Second, a rigorous inversion of the observed (i.e., convolved) radiance field is excessively computation-intensive for most routine purposes and, unless the algorithm is designed with care, can lead to serious noise amplification.

Fortunately, the problem is considerably simpler if the goal is not to completely deconvolve the radiance field, but rather simply to mitigate the effects of feedhorn spillover and antenna sidelobe contributions on the estimated scene brightness temperature averaged over the main beam. Some possible approaches to this less ambitious task are described in the NRL Cal/Val Report (Hollinger 1988) and by Wentz (1988).

4.4 Geolocation

Surface latitudes and longitudes for each SSM/I footprint are computed based on assumptions concerning the SSM/I scan geometry together with satellite ephemeris data. Among the assumptions included in the Hughes Aircraft Company (HAC) geolocation algorithm are "that (1) the spacecraft nadir vector is always pointed in a direction normal to the geoid, (2) the surface of the earth is adequately modeled by an oblate spheroid, and (3) no corrections are necessary for possible spacecraft attitude variations or for possible misalignment of the SSM/I to the spacecraft" (Hollinger 1988).

Pre-launch analysis suggested that maximum geolocation errors resulting from the HAC geolocation algorithm should be no more than ~2–4 km. In fact, observed errors of 20–30 km, as determined from SSM/I imagery of coastlines, have been routine. The Calibration/Validation Team undertook a comprehensive analysis of the various possible sources of the observed geolocation error and concluded, among other things, that apparent errors could be reduced to below 3–5 km by assuming fixed corrections to the pitch, yaw, and roll values utilized by the geolocation algorithm. As a consequence of the inferred pitch and roll errors, it appears

that pixel earth incidence angles vary considerably ($\sim$0.9°) across a scan, rather than remaining essentially constant as was intended.

Geolocation correction algorithms have since been developed by several parties, including F.J. Wentz of Remote Sensing Systems, Inc., and C. Swift at the University of Massachussetts. None of these algorithms has been applied to the SSM/I data employed in this thesis.

In addition to the above-described geolocation problem, an additional problem has arisen from an apparent "bug" in the processing software at FNOC. As a result of this bug, sizable sections of data from occasional SSM/I orbits are time-tagged incorrectly. Incorrect time tags lead to incorrect geolocation; corresponding SSM/I images may appear displaced 1000s of km from from their true location. A comprehensive list of affected data blocks has been compiled by RSS, and this list may be used to screen and discard bad blocks.

4.5 Data

Data from DMSP satellites are transmitted to ground in both tactical (direct readout) and strategic (stored data) modes. Real time direct readout sites include U.S. Navy aircraft carriers and several island and shore based air stations (Navy and Air Force). As of 1972, DMSP data have been declassified and are made available to the civilian scientific community through archives at the National Environmental Satellite Data and Information Service (NOAA/NESDIS). Although real-time SSM/I data had been available only to Defense Department sites as recently as August 1990, the data are now released in real time to the U.S. National Weather Service as well.

SSM/I antenna temperature data employed in this study were obtained in Compact Tape format from Remote Sensing Systems (RSS), Inc. These tapes contain reformatted data from the Temperature Data Records (TDRs) produced by the Fleet Numerical Oceanographic Center (FNOC). In contrast to the TDR

tapes, only eight Compact format tapes (6250 BPI) are required to archive one month's worth of global SSM/I data. A typical single orbit consists of approximately 1600 low-resolution scans and requires a total of approximately 3 MB of digital storage.

Each scan record includes pixel antenna temperatures for each SSM/I channel (85 GHz at 12.5 km sampling density; all remaining channels at 25 km), pixel latitudes and longitudes, pixel surface type flags (e.g., open ocean, coast, land, possible sea ice, etc.), time and nominal incidence angle for the scan, and certain engineering and calibration parameters as well.

Input and decoding of Compact format tape data and conversion of SSM/I antenna temperatures to brightness temperatures is accomplished using FORTRAN subroutines provided by RSS. The derivation of the algorithm for T_A to T_B conversion is described by Wentz (1988).

Interactive graphic display and analysis of SSM/I data in the University of Washington Department of Atmospheric Sciences is accomplished using a custom software package written by the author for use on a Masscomp 5520 Graphics Workstation. The program is written in C and runs under the Unix operating system. Work is currently in progress to modify this program for use in an industry standard X-Windows environment so that it can eventually be run on a wide variety of computer workstations.

5. FORMAL RADIATIVE TRANSFER THEORY, TERMINOLOGY, AND NOTATION

For passive microwave remote sensing purposes, the most important fundamental radiative quantity is the *monochromatic radiance* $L(\theta, \phi)$ (units J s^{-1} m^{-2} sr^{-1} Hz^{-1}), which represents the radiant flux density (at a specified frequency ν) per unit of frequency and solid angle, propagating in the direction specified by the spherical coordinates θ and ϕ.

It is often necessary to also consider the polarization of the radiation; i.e., the orientation of the electric field vector relative to the horizontal plane. In such cases, it is conventional to decompose the signal into mutually orthogonal horizontally (H) and vertically (V) polarized components and to treat these individually. For variables which depend on polarization, the subscript p will be used to indicate this dependence and may be replaced throughout an equation by V or H, as appropriate.

According to Beer's Law, the depletion (or *extinction*) of radiation along an increment of path ds is proportional to the the mass density ρ along that path, with the constant of proportionality, i.e., the *mass extinction coefficient* κ_e, being dependent on the chemical composition of the mass, as well as other physical variables. That is,

$$dL = -\kappa_e \rho L \, ds. \tag{5.1}$$

Radiative extinction corresponds to a combination of *absorption*, by which radiative energy is converted to heat, chemical, or some other form of energy, and *scattering*, which is simply the redirection of radiative energy out of the path in question. Thus

$$\kappa_e = \kappa_a + \kappa_s, \tag{5.2}$$

where κ_a is the *mass absorption coefficient* and κ_s is the *mass scattering coefficient.* Equivalently, we may choose to use the *volume* extinction, absorption, and scattering coefficients, defined by $k_e = \rho\kappa_e$, $k_a = \rho\kappa_a$, and $k_s = \rho\kappa_s$, respectively.

Acting in opposition to the extinction of radiation are the thermal *emission* of radiation and the scattering of radiation into the path from other directions. By Kirchhoff's Law, thermal emission of radiation by matter is proportional to κ_a and to Planck's function $B(T)$, which is given by

$$B(T) = \frac{2h\nu^3}{c^2(e^{h\nu/KT} - 1)}, \tag{5.3}$$

where T is the thermodynamic temperature, c is the speed of light, h is Planck's constant, and K is Boltzmann's constant.

The enhancement of radiation by scattering into the path may be expressed as the product of the *single scatter albedo* $\varpi \equiv k_s/k_e$ and an average over solid angle of the radiance L incident from all directions, the latter weighted by the *phase function* $P(\theta, \phi; \theta', \phi')$.

With all of the above definitions, the full *Radiative Transfer Equation* (RTE) may be written

$$\begin{aligned} dL(\theta,\phi) = k_e \Bigg[& (1-\varpi)B(T) - L(\theta,\phi) \\ & + \frac{\varpi}{4\pi} \int\int P(\theta,\phi;\theta',\phi') L(\theta',\phi') \sin\theta \; d\theta' d\phi' \Bigg] ds. \end{aligned} \tag{5.4}$$

For microwave radiation, an important simplification may be introduced by noting that for $h\nu/KT \ll 1$ the Planck Function (5.3) reduces to $(2\nu^2 K/c^2)T$; in other words, the radiance is proportional to the thermodynamic temperature T of a blackbody of equivalent brightness . This approximation, known as the Rayleigh-Jeans approximation, allows one to factor the Planck function B out of the RTE and express L in terms of a *brightness temperature* T_B, which has units of degrees Kelvin. The accuracy of the Rayleigh-Jeans approximation is satisfactory

for all SSM/I frequencies; for T ranging from 240 K to 300 K, the maximum error arising from assuming a proportionality between L and T is $\sim$0.5 K at 85.5 GHz, comparable to the intrinsic sensitivity of the SSM/I.

Outside of precipitation, the atmosphere does not significantly scatter microwave radiation, hence $\varpi = 0$ and $k_e = k_a$. Under this assumption, the differential form of the RTE incorporating the Rayleigh-Jeans approximation reduces to

$$dT_B(\theta, \phi) = k\,[T - T_B(\theta, \phi)]\,ds. \tag{5.5}$$

(Here and elsewhere, both k_e and k_a are represented by k whenever the two are equivalent.)

Under most conditions (the most notable exception again being precipitation) it is also sufficient to consider microwave radiative transfer only for a plane-parallel atmosphere; i.e., one in which k and T are functions of height z only and for which curvature of the earth's surface may be ignored. One may then replace ds in (5.5) with dz/μ, where $\mu \equiv \cos\theta$, and integrate over the depth of the atmosphere to find the downward directed radiance $T_B{}^{\downarrow}$ seen from the surface:

$$T_B{}^{\downarrow}(\mu) = \tau(0, \infty) T_B^C + \frac{1}{\mu} \int_0^{\infty} T(z) k(z) \tau(0, z)\, dz, \tag{5.6}$$

where τ is the transmittance between two levels in the atmosphere, i.e.

$$\tau(z_1, z_2) = \exp\left[\frac{-1}{\mu} \int_{z_1}^{z_2} k(z)\, dz\right]; \qquad z_2 > z_1, \tag{5.7}$$

and $T_B^C \approx 2.7$ K is the cosmic background brightness temperature.

Similarly, the upward-directed *atmospheric* component of the brightness temperature $T_B{}^{\uparrow}$ seen from the top of the atmosphere is given by

$$T_B{}^{\uparrow}(\mu) = \frac{1}{\mu} \int_0^{\infty} T(z) k(z) \tau(z, \infty)\, dz. \tag{5.8}$$

The brightness temperature T_B observed from space includes contributions from both (5.6) and (5.8) — the former due to reflection from the lower boundary — as well as surface emission. The simplest case is that of specular surface reflection, for which

$$T_B(\mu) = T_B{}^{\uparrow}(\mu) + \tau(0,\infty)\left[\varepsilon_p T_S + (1-\varepsilon_p)T_B{}^{\downarrow}(\mu)\right] \tag{5.9}$$

where ε_p is the surface emissivity for the polarization p of the observed radiation and T_S is the surface thermodynamic temperature.

In most situations, however, surface reflection is not strictly specular; hence, a more realistic expression for T_B must include diffuse reflection by the lower boundary, i.e.,

$$\begin{aligned} T_B(\mu,\phi) = T_B{}^{\uparrow}(\mu) + \tau(0,\infty)\Bigg[&\varepsilon_p(\mu,\phi)T_S \\ &+ \frac{1}{\pi}\int_0^{2\pi}\int_0^1 r_p(\mu,\phi;\mu',\phi')\mu' T_B{}^{\downarrow}(\mu')\, d\mu'\, d\phi'\Bigg], \end{aligned} \tag{5.10}$$

where the bidirectional reflectance $r_p(\mu,\phi;\mu',\phi')$ expresses the angular weighting of the downward atmospheric radiances scattered upward in the direction of the satellite sensor (depending on the context and the normalization used, this weighting function may be referred to in the literature as the *bistatic radar cross-section*, the *bistatic scattering coefficient*, the *differential scattering coefficient* or any of a variety of other names). Note that if the atmospheric emission $T_B{}^{\downarrow}$ were polarization dependent (which it generally is not) it would be necessary to separately specify like-polarized and cross-polarized bidirectional reflectances.

The emissivity ε_p of the diffusely reflecting surface is directly related to r_p via an integral over the upper hemisphere:

$$\varepsilon_p(\mu,\phi) = 1 - \frac{1}{\pi}\int_0^{2\pi}\int_0^1 r_p(\mu,\phi;\mu',\phi')\mu\, d\mu'\, d\phi'. \tag{5.11}$$

To summarize, the microwave brightness temperature observed from space depends only on the thermodynamic temperature profile $T(z)$, the absorption profile $k(z)$, the surface temperature T_S, and the bidirectional reflectance $r_p(\mu, \phi; \mu', \phi')$. Of these, $k(z)$ and r_p depend on the frequency of the radiation observed, and r_p depends further on polarization. To an excellent approximation, both are ultimately determined by only a handful of meteorological variables. The following two chapters are devoted to reducing the RTE (5.10) to closed form expressions for SSM/I brightness temperatures in terms of meteorological variables alone.

6. THE ATMOSPHERIC COMPONENT OF SSM/I BRIGHTNESS TEMPERATURES

In the atmosphere, absorption and emission at frequencies below 120 GHz is determined almost entirely by three constituents: molecular oxygen, water vapor, and liquid water. The first two, the gaseous constituents, are discussed together in the following subsection; cloud water (excluding precipitation) is treated in section 6.2. In section 6.3, a closed-form mathematical model is developed which computes the atmospheric contribution to SSM/I brightness temperatures as functions of integrated water vapor, vapor scale height, integrated cloud water, mean cloud height, effective surface temperature and atmospheric lapse rate, and surface pressure. This model is intended to aid in understanding the information content of each SSM/I channel, in developing and testing retrieval algorithms, and in correcting for atmospheric effects in the observation of surface parameters.

6.1 Gaseous Absorption in the Atmosphere

Two gaseous constituents are of primary importance in determining the radiative properties of the atmosphere at SSM/I frequencies: oxygen and water vapor. Other constituents also have weak absorption lines in the vicinity of the SSM/I channels, but these are present in only trace amounts so that their impact on SSM/I brightness temperatures is negligible.

The oxygen spectrum in the frequency range of interest is dominated by two complexes of strong resonant lines, one centered near 60 GHz and another near 118 GHz. In the spectral "windows" between these absorption bands, atmospheric attenuation due to dry air is rather weak, resulting mainly from contributions by the far wings of the oxygen lines and from a non-resonant dry air "continuum" absorption which increases monotonically with frequency.

The water vapor spectrum exhibits a weak resonant absorption line at 22.235 GHz; otherwise, the principal contribution by water vapor within the windows between the oxygen bands is due to a moderately strong continuum absorption which increases approximately as the square of the frequency. The physical basis for the continuum absorption is not well understood, though it is speculated by some that short-lived clusters of H_2O molecules may play an important role. This theory is supported in part by the relatively strong observed increase of the mass absorption coefficient with water vapor density.

The total atmospheric transmission spectrum due to water vapor and oxygen, for the SSM/I viewing angle of 53°, is depicted in Fig. 6.1. Five model atmospheres were used, ranging from wintertime polar to tropical. The large range of total water vapor associated with these different models (from ~5 to ~60 kg m^{-2}) is responsible for most of the obvious variation in transmittance.

For radiative transfer calculations, the shape of the resonant absorption lines in this band is usually assumed to be well approximated by the Van Vleck-Weisskopf model (Ulaby et al. 1981, pp. 266–269) with possible minor modifications to describe line overlap effects (e.g., Rosenkranz 1975). The width and strength of each line are generally non-linear functions of pressure, temperature, and absorber concentration. In particular, absorption lines are naturally very sharp at low ambient pressures but broader and blunter with increasing pressure owing to collisions between the absorbing molecules. Consequently, the monochromatic mass absorption coefficient near the center of a line generally *increases* markedly with increasing altitude in the troposphere, while it decreases with altitude on the wings of the line.

Models for the behavior of water vapor continuum absorption are not as certain, owing to the lack of a well-established physical mechanism. However, experimental data indicate that the mass absorption coefficient decreases with decreasing ambient pressure and with decreasing water vapor pressure.

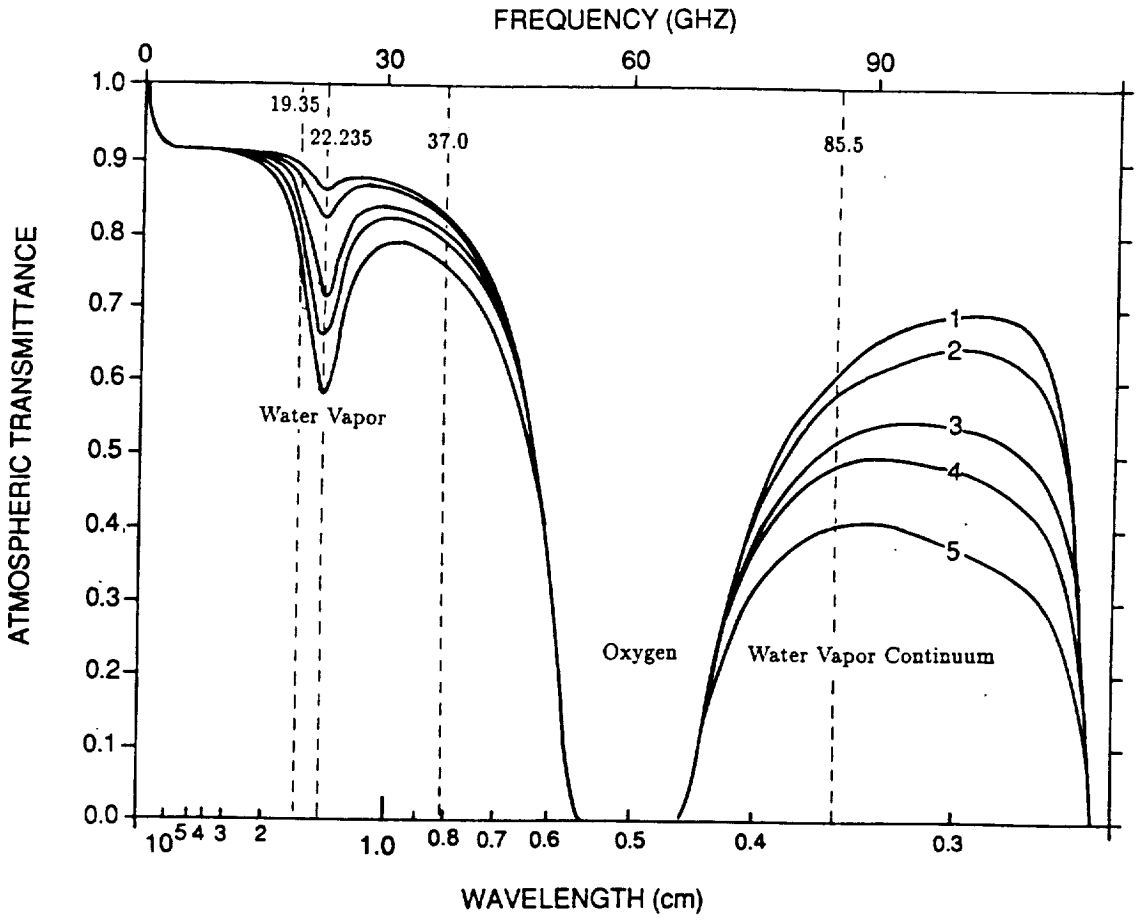

Fig. 6.1 Total atmospheric microwave transmission for a zenith angle of 53°. Model atmospheres used are (1) wintertime polar, (2) summertime polar, (3) wintertime midlatitude, (4) summertime midlatitude, and (5) tropical. Plots were generated using the FASCOD3 line-by-line code package (Clough et al. 1989).

The four frequencies used by the SSM/I are distributed within the two spectral windows bounded by the 60 GHz and 118 GHz oxygen complexes. Dry air absorption is therefore rather low for all SSM/I channels, and variations are relatively small and predictable owing to the nearly invariant vertical mass distribution of oxygen in the atmosphere. By comparison, water vapor absorption exceeds dry air absorption in importance for all four frequencies in all but a dry polar atmosphere and is highly variable in space and time. Especially the 22.235 GHz and 85.5 GHz channels are sensitive to such variations; the former because of its position at the center of a water vapor line, the latter because of the relatively strong continuum absorption at higher frequencies.

Earlier microwave radiative transfer calculations for remote sensing purposes have usually relied on absorption data published by Barrett and Chung (1962) or Waters (1976) for water vapor, and Meeks and Lilly (1963) or Rosenkranz (1975) for oxygen. Recently, Liebe (1985) has collected the latest empirical and theoretical data on water vapor and dry air absorption into a unified Millimeter-wave Propagation Model (MPM), which calculates microwave attenuation as a function of temperature, humidity, pressure, and hydrosol content, over a wide range of atmospheric conditions. Notable improvements over earlier models include new empirically-derived formulations for both water vapor and dry air continuum absorption, as well as improved line parameters obtained from recent measurements.

Comparisons between water vapor attenuation values calculated using an updated version of the MPM model (Liebe, personal communication, 1988) and those obtained from earlier formulations revealed differences of order $\sim$10% at some frequencies, primarily in spectral regions where continuum absorption dominates. Particularly for the 85.5 GHz channels of the SSM/I, the uncertainties in the water vapor absorption models appear to be significant, and these in turn imply uncertainty in the accuracy of theoretical brightness temperature calculations.

As the new MPM model benefits from a more extensive base of empirical measurements than was available at the time the earlier models were developed, we chose to use an adaptation of the gaseous absorption routines in MPM for the radiative transfer calculations of the present study. In Chapter 8, we discuss the need for empirical corrections to theoretically derived water vapor optical depths, as determined from comparisons of the theoretical brightness temperatures with observed SSM/I brightness temperatures.

6.2 Cloud Absorption Properties

a. Cloud Liquid Water

Cloud liquid water is defined as that portion of the atmospheric liquid water content consisting of droplets which are too small to precipitate. The conventional radius threshold used for distinguishing between cloud water droplets and precipitating droplets is 100 μm (Rogers and Yau, 1989). Fortunately, and fortuitously, most such droplets are also small enough relative to SSM/I wavelengths to permit a particularly simple treatment of their radiative properties. In particular, the mass extinction (or absorption) coefficient of cloud droplets is independent of drop size, so that the attenuation and emission of microwave radiation by a cloud layer depend only on the total cloud water mass and on the temperature of the cloud. An overview of the more difficult radiative properties of precipitation will be provided in a later chapter.

The general theory behind the absorption properties of cloud water have been discussed in some detail by many other authors; here we highlight only those results needed to derive computationally efficient expressions for cloud water absorption at each of the four SSM/I frequencies, together with a quantitative assessment of the range of validity of the small-droplet assumption for these frequencies.

Following standard notation, we introduce a non-dimensional size parameter x which expresses the ratio of the circumference $2\pi a$ of a spherical particle to the wavelength λ of the incident radiation:

$$x = \frac{2\pi a}{\lambda}. \tag{6.1}$$

For sufficiently small x, the extinction and absorption efficiencies of a spherical particle with complex index of refraction m are essentially identical (i.e., scattering is negligible) and may be expressed (Bohren and Huffman, 1983) by

$$Q_{abs} \approx Q_{ext} = 4x\Im\left[\frac{m^2-1}{m^2+2}\right], \tag{6.2}$$

where $\Im$ implies the imaginary part of the complex expression in brackets. This approximation is valid for $|m|x \ll 1$. Since at microwave wavelengths the index of refraction of water $|m| \sim 5$, the above condition is generally fulfilled when $x \ll 0.2$.

Q_{ext} multiplied by the physical cross-sectional area ($A = \pi a^2$) of the particle yields its extinction cross-section C_{ext} (units m^2/particle). For fixed m, C_{ext} is thus proportional to a^3 and hence to droplet volume. By dividing C_{ext} by the droplet mass ($\frac{4}{3}\pi a^3 \rho_w$) one obtains a dropsize-independent mass absorption coefficient κ_c:

$$\kappa_c = \frac{6\pi}{\lambda \rho_w}\Im\left[\frac{m^2-1}{m^2+2}\right]. \tag{6.3}$$

where ρ_w is the density of liquid water.

For our calculations, the index of refraction m for water was obtained from the modified Debye formula of Ray (1972).

For any given microwave frequency, m, and consequently κ_c, is found to be a smoothly varying function of temperature. For convenience in SSM/I applications we may therefore approximate (6.3) using a separate polynomial fit of κ_c to temperature for each SSM/I frequency. Table 6.1 gives coefficients a_i for a cubic fit of κ_c to temperature T_C in degrees Celsius ($\equiv T - 273.15$), *i.e.*,

$$\kappa_c \approx a_0 + a_1 T_C + a_2 {T_C}^2 + a_3 {T_C}^3. \tag{6.4}$$

Table 6.1: Coefficients of a cubic fit of κ_c to temperature (°C) for each SSM/I frequency.

Freq. (GHz)	a_0	a_1	a_2	a_3	Max. error (%)
19.35	0.786−1	−0.230−2	0.448−4	−0.464−6	1.0
22.235	0.103+0	−0.296−2	0.557−4	−0.558−6	1.0
37.0	0.267+0	−0.673−2	0.975−4	−0.724−6	0.3
85.5	0.988+0	−0.107−1	−0.535−4	0.115−5	0.3

The maximum fractional error of the fit is given for the interval −20°C to 35°C, which reflects the approximate temperature range over which cloud water may normally be found in liquid form in the marine atmosphere.

Microwave absorption due to cloud liquid water is found to increase approximately in proportion to $\nu^{1.7}$ (Fig. 6.2). The impact of clouds on 85 GHz brightness temperatures is thus an order of magnitude greater than at 19 GHz. For example, a fairly heavy non-precipitating cloud might contain as much as 0.5 kg m^{-2} of liquid water. Assuming a mean temperature of 0° C and the SSM/I viewing angle of 53°, the microwave transmittance of such a cloud ranges from 94% at 19 GHz to only 44% at 85 GHz.

The change in opacity with changes in cloud temperature may be quite substantial. A decrease of cloud temperature from 20° C to 0° C represents only a 7% decrease in absolute temperature but gives rise to a 70% increase in cloud optical depth at 19 GHz. The increase in optical depth is smaller (30%), but still

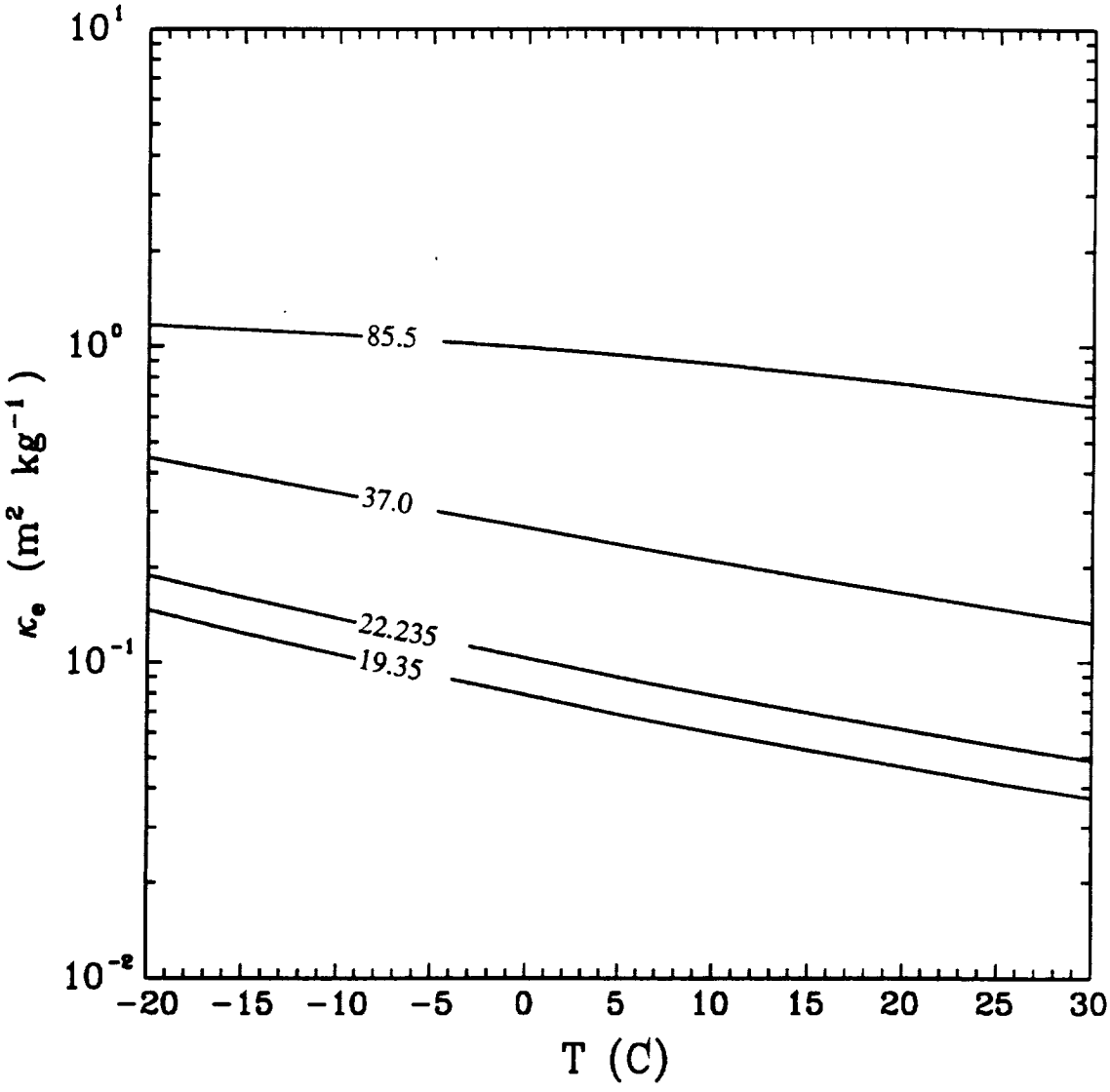

Fig. 6.2 Temperature dependence of the mass extinction coefficient κ_e of cloud liquid water at SSM/I frequencies.

Table 6.2: Maximum cloud droplet radii (μm) for which Eqn. (6.3) is valid to 1% and 5% accuracy, plus maximum radii for which ϖ does not exceed 0.01 and 0.05.

	$\delta\kappa_a$		ϖ	
Freq. (GHz)	1%	5%	.01	.05
19.35	48	110	253	529
22.235	47	104	224	460
37	42	89	158	297
85.5	29	64	85	153

significant, at 85 GHz. As a consequence, we have the seemingly paradoxical result that, in the microwave spectrum, *an optically thin cloud of fixed liquid water content radiates more brightly as its thermodynamic temperature decreases.*

If larger drops are present, microwave absorption by liquid water may no longer be well approximated by (6.3). Table 6.2 lists the maximum droplet radii at each SSM/I frequency for which the small-sphere approximation for absorption is valid to within 1% and 5%, based on comparisons with the more exact Mie theory. Also listed are the radii for which scattering begins to become significant, as indicated by single scattering albedos ϖ in excess of 0.01 and 0.05.

In a survey article, Pruppacher (1981) showed representative drop size spectra for a variety of non-precipitating clouds, both continental and maritime. With few exceptions, the number concentration $N(a)$ of droplets with radii $a > 30$ μm is quite small. By replotting the data as *mass concentration* ($\propto a^3 N(a)$) vs radius, we verified that the fractional contribution to the total cloud liquid water mass by these larger droplets is also small. Referring to Table 6.2, we conclude that,

for most non-precipitating clouds, the small-droplet assumption, and hence the polynomial approximation (6.4), holds to ~1% accuracy or better for all SSM/I frequencies.

b. Cloud ice

For cloud ice particles which are small compared with SSM/I wavelengths, as might be expected in the majority of non-precipitating cirriform clouds, the same approximation can be used as for cloud liquid water. The complex index of refraction m of ice is much different than that for liquid water, however, and we should therefore expect dramatically different optical properties of ice clouds. Substituting values of m obtained from Warren (1984) into (6.2), we find that the mass absorption coefficient κ_a for cloud ice ranges from only $\sim 1.5 \times 10^{-3}$ m^2 kg^{-1} at 19 GHz to $\sim 1.3 \times 10^{-3}$ m^2 kg^{-1} at 85 GHz (these are maximum values, corresponding to ice at a temperature of $-1°$ C; for colder ice, absorption is even lower). Because the total mass of ice in most cirrus clouds is normally much less than even 0.1 kg m^{-2} , it may be concluded that cirrus is likely to have little or no measurable impact on SSM/I brightness temperatures.

This result highlights one of the most important and well-known strengths of satellite microwave sensors like the SSM/I — *the SSM/I is able to consistently provide information on the middle and lower level structure of weather systems, irrespective of the presence of even thick and/or widespread cirriform cloudiness.*

It must be emphasized that the above conclusion is only valid for equivalent particle radii of $\lesssim 100$ μm. As ice particle size increases beyond this, as might be expected in precipitating cloud systems, the extinction coefficient increases quite dramatically, primarily as a result of increased scattering. It is now well established that precipitation size ice particles may have a dramatic effect on the 85 GHz channels and, to a lesser extent, on the 37 GHz channels of the SSM/I. Discussion of such effects are deferred to the chapter on precipitation.

6.3 A Closed-Form Model for Atmospheric Emission and Transmission

The feasibility and utility of a closed-form model for satellite observed microwave brightness temperatures was first made apparent by the work of Wentz (1983), who published a model which predicted SMMR-observed brightness temperatures (6.6, 10.7, 18, 21, and 37 GHz) as functions of atmospheric and oceanic parameters. This model function has been used successfully in non-linear, physical retrieval algorithms.

Motivated by similar considerations, we devote this subsection to (a) demonstrating that atmospheric contributions to SSM/I brightness temperatures are well-determined by a small set of meteorologically meaningful variables, and (b) quantifying the dependence on those variables. The variables include integrated water vapor, vapor scale height, integrated cloud water, effective cloud height, effective surface temperature and lapse rate for the lower troposphere, and surface pressure. Despite a general conceptual similarity between our model and that of Wentz (1983), we find that a considerably more detailed physical and mathematical analysis is warranted for the SSM/I than proved necessary for the SMMR. This is in part because of the higher water vapor opacities encountered at 22.235 and 85.5 GHz and because of the absence of low frequency channels for sensing the surface with minimal atmospheric interference. Furthermore, we wish to be able to examine in detail the potential impact of uncertainties in certain non-retrievable parameters on the retrievals of the remaining parameters and, where possible, design algorithms which minimize that impact.

In the next subsection, an analytic mathematical model is derived which approximates the integral form of the microwave radiative transfer equation for a plane-parallel, non-scattering atmosphere. This is followed by the development of specific models of transmittance and absorption profiles of water vapor and oxygen at 19.35, 22.235, 37.0, and 85.5 GHz. The chapter is then concluded by describing the global statistical characteristics of the model's input parameters.

a. Mathematical Development

In Chapter 5, the atmospheric contributions to the microwave brightness temperature at the top and the bottom of the atmosphere were shown to be given formally by

$$T_B{}^{\downarrow}(\mu) = \frac{1}{\mu}\int_0^{\infty} T(z)k(z)\tau(0,z)\,dz \tag{6.5}$$

$$T_B{}^{\uparrow}(\mu) = \frac{1}{\mu}\int_0^{\infty} T(z)k(z)\tau(z,\infty)\,dz. \tag{6.6}$$

where τ is the transmittance between two levels in the atmosphere, i.e.

$$\tau(z_1,z_2) = \exp\left[\frac{-1}{\mu}\int_{z_1}^{z_2} k(z)\,dz\right]; \qquad z_2 > z_1, \tag{6.7}$$

and

$$\mu \equiv \cos\theta. \tag{6.8}$$

As discussed earlier, these equations are valid for a plane-parallel, non-scattering atmosphere; i.e., one in which there are no precipitation size hydrometeors and for which the volume absorption coefficient k and the temperature T are functions of height z only.

It is always possible, of course, to numerically integrate (6.5) and (6.6) for appropriate absorption and temperature profiles $k(z)$ and $T(z)$. However this approach is neither computationally efficient nor does it contribute much to understanding or quantifying the essential relationship between the state of the atmosphere and its corresponding microwave signature. Indeed, it is only because the number of *radiatively important* degrees of freedom in the atmosphere-ocean system is small — vastly smaller, in fact, than implied by the arbitrary z-dependence of T and k in (6.5) and (6.6) — that there is any possibility at all of making useful estimates of geophysical parameters from only the seven channels of the SSM/I.

We begin by considering a horizontally homogeneous atmosphere in which only gaseous absorption and emission are important. Moreover, we restrict our

attention for the time being to the layer of the atmosphere bounded by the surface and an arbitrary geometric altitude z_c above the surface. The optical depth of this layer is given by $\sigma_1(z_c)$, where

$$\sigma_1(z) = \int_0^z k(z')\, dz'. \tag{6.9}$$

Correspondingly, the path transmittance is given by $\tau_1(z_c)$, where

$$\tau_1(z) = \exp\left[\frac{-\sigma_1(z)}{\mu}\right]. \tag{6.10}$$

For an observer on the surface viewing upward, the brightness temperature contribution from the layer below z_c can be written

$$T_B{}^{\downarrow}{}_1 = \frac{1}{\mu}\int_0^{z_c} T(z)k(z)\tau_1(z)\, dz. \tag{6.11}$$

Similarly, for an observer at altitude z_c viewing downward, the analogous quantity is

$$T_B{}^{\uparrow}{}_1 = \frac{\tau_1(z_c)}{\mu}\int_0^{z_c} T(z)k(z)\tau_1^{-1}(z)\, dz. \tag{6.12}$$

$T_B{}^{\downarrow}{}_1$ may be rewritten as the product of a bulk layer emissivity (equal to one minus the transmittance) and an effective emitting temperature $T^{\downarrow}{}_1$, which is just a weighted average of the thermometric temperature throughout the layer:

$$T_B{}^{\downarrow}{}_1 = [1 - \tau_1(z_c)]\, T^{\downarrow}{}_1, \tag{6.13}$$

where

$$T^{\downarrow}{}_1 = \int_0^{z_c} T(z)w(z)\, dz, \tag{6.14}$$

$$w(z) = \frac{k(z)\tau_1(z)}{1 - \tau_1(z_c)}. \tag{6.15}$$

The denominator in (6.15) is simply the integral of the numerator over the depth of the layer; in other words, $w(z)$ satisfies

$$\int_0^{z_c} w(z)\, dz = 1. \tag{6.16}$$

Results analogous to (6.11)–(6.15) are obtained for the effective emitting temperature $T^{\uparrow}{}_1$ seen from the top of the layer; the only difference is that the slightly different weighting function

$$y(z) = \frac{\tau_1(z_c)k(z)}{\tau_1(z)[1-\tau_1(z_c)]} \tag{6.17}$$

must be substituted for $w(z)$.

Up to this point, no assumptions have been made regarding the atmospheric temperature or radiative absorption profile. Henceforth, we assume that the temperature profile in the lower atmosphere may be approximated by an effective surface temperature T_A and lapse rate Γ, i.e.,

$$T(z) = T_A - \Gamma z, \tag{6.18}$$

allowing us to rewrite $T^{\downarrow}{}_1$ and $T^{\uparrow}{}_1$ as

$$T^{\downarrow}{}_1 = T_A - \Gamma \int_0^{z_c} z w(z)\, dz, \tag{6.19}$$

$$T^{\uparrow}{}_1 = T_A - \Gamma \int_0^{z_c} z y(z)\, dz. \tag{6.20}$$

It is apparent that the integrals in these expressions may be interpreted as *effective emitting heights* corresponding to the brightness temperatures seen from the bottom and top of the layer.

In order to evaluate these integrals, we require a model for the profile of absorption in the atmosphere. Here, we assume that the total absorption is equal to the sum of two exponentially decaying absorption profiles corresponding to dry air and water vapor, with total optical depths σ_o and σ_v and scale heights H_o and H_v, respectively:

$$k(z) = \frac{\sigma_o}{H_o} \exp\left(\frac{-z}{H_o}\right) + \frac{\sigma_v}{H_v} \exp\left(\frac{-z}{H_v}\right). \tag{6.21}$$

From (6.21), we also have

$$\sigma_1(z) = \sigma_o \left[1 - \exp\left(\frac{-z}{H_o}\right)\right] + \sigma_v \left[1 - \exp\left(\frac{-z}{H_v}\right)\right]. \tag{6.22}$$

It is not possible to analytically integrate (6.19) and (6.20) for the $k(z)$ given by (6.21). Consequently, we seek functions $f(z)$ and $g(z)$ which are good approximations to $w(z)$ and $y(z)$, respectively, and for which reasonably simple closed-form solutions may be found for

$$h^{\downarrow} = \frac{\int_0^{z_c} z f(z)\, dz}{\int_0^{z_c} f(z)\, dz}, \tag{6.23}$$

$$h^{\uparrow} = \frac{\int_0^{z_c} z g(z)\, dz}{\int_0^{z_c} g(z)\, dz}. \tag{6.24}$$

Since $[\sigma_1(z)/\mu] \lesssim 0.5$ for the frequencies and viewing angle of the SSM/I, we set $f(z)$ and $g(z)$ equal to second-order Taylor expansions of $w(z)$ and $y(z)$, respectively:

$$w(z) \approx f(z) \equiv \frac{k(z)\left[1 - \frac{\sigma_1(z)}{\mu} + \frac{\sigma_1^2(z)}{2\mu^2}\right]}{1 - \tau_1(z_c)}, \tag{6.25}$$

$$y(z) \approx g(z) \equiv \frac{\tau_1(z_c)k(z)\left[1 + \frac{\sigma_1(z)}{\mu} + \frac{\sigma_1^2(z)}{2\mu^2}\right]}{1 - \tau_1(z_c)}. \tag{6.26}$$

Integrating (6.25) and (6.26) then yields

$$h^{\downarrow} = \frac{d^-(p_1 - q_1) + \frac{1}{4\mu}c^-(p_2 - q_2) + \frac{1}{18\mu^2}(p_3 - q_3)}{d^-(\alpha - \beta) + \frac{1}{2\mu}c^-(\alpha^2 - \beta^2) + \frac{1}{6\mu^2}(\alpha^3 - \beta^3)}, \tag{6.27}$$

$$h^{\uparrow} = \frac{-d^+(p_1 - q_1) + \frac{1}{4\mu}c^+(p_2 - q_2) - \frac{1}{18\mu^2}(p_3 - q_3)}{-d^+(\alpha - \beta) + \frac{1}{2\mu}c^+(\alpha^2 - \beta^2) - \frac{1}{6\mu^2}(\alpha^3 - \beta^3)}, \tag{6.28}$$

where

$$\alpha = \sigma_o + \sigma_v, \tag{6.29}$$

$$\beta = \sigma_o \exp\left(\frac{-z_c}{H_o}\right) + \sigma_v \exp\left(\frac{-z_c}{H_v}\right), \tag{6.30}$$

$$p_n = \sum_{i=0}^{n} \binom{n}{i} \sigma_v^{n-i} \sigma_o^i \bar{H}_{n-i,i}, \tag{6.31}$$

$$\begin{aligned} q_n = \sum_{i=0}^{n} & \left[\sigma_v \exp\left(\frac{-z_c}{H_v}\right)\right]^{n-i} \left[\sigma_o \exp\left(\frac{-z_c}{H_o}\right)\right]^{i} \\ & \times \bar{H}_{n-i,i} \left[1 + z_c \left(\frac{n-i}{H_v} + \frac{i}{H_o}\right)\right], \end{aligned} \tag{6.32}$$

$$\bar{H}_{mn} = \frac{m+n}{m/H_v + n/H_o}, \tag{6.33}$$

$$c^{\pm} = 1 \pm \frac{\alpha}{\mu}, \tag{6.34}$$

$$d^{\pm} = 1 \pm \frac{\alpha}{\mu} + \frac{\alpha^2}{2\mu^2}. \tag{6.35}$$

Note that when $z_c \to \infty$, q_n and β vanish, so that

$$h_\infty^{\downarrow} \equiv \lim_{z_c \to \infty} h^{\downarrow} = \frac{d^- p_1 + \frac{1}{4\mu} c^- p_2 + \frac{1}{18\mu^2} p_3}{d^- \alpha + \frac{1}{2\mu} c^- \alpha^2 + \frac{1}{6\mu^2} \alpha^3}, \tag{6.36}$$

$$h_\infty^{\uparrow} \equiv \lim_{z_c \to \infty} h^{\uparrow} = \frac{-d^+ p_1 + \frac{1}{4\mu} c^+ p_2 - \frac{1}{18\mu^2} p_3}{-d^+ \alpha + \frac{1}{2\mu} c^+ \alpha^2 - \frac{1}{6\mu^2} \alpha^3}. \tag{6.37}$$

We now have closed-form, approximate expressions for the upwelling and downwelling brightness temperature contributions from the atmosphere below z_c:

$$T_B{}^{\uparrow}{}_1 \approx [1 - \tau_1(z_c)]\,(T_A - \Gamma h^{\uparrow}), \tag{6.38}$$

$$T_B{}^{\downarrow}{}_1 \approx [1 - \tau_1(z_c)]\,(T_A - \Gamma h^{\downarrow}). \tag{6.39}$$

By simply allowing $z_c \to \infty$, we also have expressions for the *total* atmospheric emission:

$$T_B{}^{\uparrow}{}_\infty \approx (1 - \tau_\infty)(T_A - \Gamma h_\infty^{\uparrow}), \tag{6.40}$$

$$T_B{}^{\downarrow}{}_\infty \approx (1 - \tau_\infty)(T_A - \Gamma h_\infty^{\downarrow}), \tag{6.41}$$

where

$$\tau_\infty = \exp\left[\frac{-1}{\mu}(\sigma_v + \sigma_o)\right]. \tag{6.42}$$

It may then be easily shown that the corresponding upward and downward brightness temperature contributions from the atmospheric layer extending *above* z_c are given by

$$T_B{}^{\uparrow}{}_2 = T_B{}^{\uparrow}{}_{\infty} - \tau_1(z_c) T_B{}^{\uparrow}{}_1, \tag{6.43}$$

$$T_B{}^{\downarrow}{}_2 = \tau_1^{-1}(z_c) \left[T_B{}^{\downarrow}{}_{\infty} - T_B{}^{\downarrow}{}_1 \right]. \tag{6.44}$$

The transmittance $\tau_2(z_c)$ of the upper layer is obtained from the identity

$$\tau_{\infty} \equiv \tau_1(z_c)\tau_2(z_c). \tag{6.45}$$

Up to this point, we have treated only gaseous absorption and emission by the atmosphere, under the assumptions of low total opacity and exponentially decaying absorptivity profiles. It is a simple matter, however, to generalize the above results to include a liquid cloud layer of arbitrary opacity at a height z_c above the surface. If the cloud layer has an optical depth of σ_c and effective radiating temperatures $T_c^{\downarrow}$ and $T_c^{\uparrow}$, then the cloud transmittance is

$$\tau_c = \exp\left(\frac{-\sigma_c}{\mu}\right), \tag{6.46}$$

and the net brightness temperatures seen at the bottom and top of the atmosphere are

$$T_B{}^{\downarrow} = T_B{}^{\downarrow}{}_1 + \tau_1(z_c) \left[(1-\tau_c) T_c^{\downarrow} + \tau_c T_B{}^{\downarrow}{}_2 \right], \tag{6.47}$$

$$T_B{}^{\uparrow} = T_B{}^{\uparrow}{}_2 + \tau_2(z_c) \left[(1-\tau_c) T_c^{\uparrow} + \tau_c T_B{}^{\uparrow}{}_1 \right]. \tag{6.48}$$

This model for the contribution of the clouds is of course approximate in that it ignores the geometric depth of the cloud layer. We have found, however, that this simplification usually has a negligible effect on $T_B{}^{\downarrow}$ and $T_B{}^{\uparrow}$ when the cloud opacity and its effective radiating temperatures $T_c^{\downarrow}$ and $T_c^{\uparrow}$ are correctly specified. Moreover, it can be easily verified that $T_c^{\downarrow} \approx T_c^{\uparrow}$ except when both $\sigma_c \gtrsim 1$ *and* the

cloud layer spans a relatively large temperature range. Thus, for many purposes, it is sufficiently accurate to assume

$$T_c^{\downarrow} \approx T_c^{\uparrow} \quad \approx \quad T_c \equiv T_A - \Gamma z_c. \tag{6.49}$$

Fig. 6.3 schematically illustrates the complete atmospheric model on which (6.47) and (6.48) and the various terms contained therein are based.

The model does not directly allow for multiple cloud layers. In the microwave spectrum, the radiative characteristics of multiple cloud layers should be virtually indistinguishable from those of a single cloud layer with large geometric depth. Since non-precipitating clouds are rarely optically thick at SSM/I frequencies, it is expected that the single-layer approximation will still be adequate, provided that z_c in (6.49) is interpreted as an effective cloud height which is near the optical center of the combined set of cloud layers present. In practice, it seems likely that the bulk of the total cloud liquid water will in most cases be contributed by a single dominant cloud layer.

There is one further situation occurring in nature which might not easily be reconciled with the geometric model used here; namely, the case of optically thick convective towers whose horizontal dimensions are comparable to or smaller than their vertical dimension. Often, such clouds contain precipitation, in which case they fall beyond the scope of the model presented in this chapter. When the clouds are not large enough or deep enough to contain precipitation, then the spatial averaging of the upwelling brightness temperature field which follows from the relatively coarse resolution of the SSM/I might intuitively be expected to reduce the radiative impact of non-plane-parallel geometry, but this question has not yet been investigated in detail.

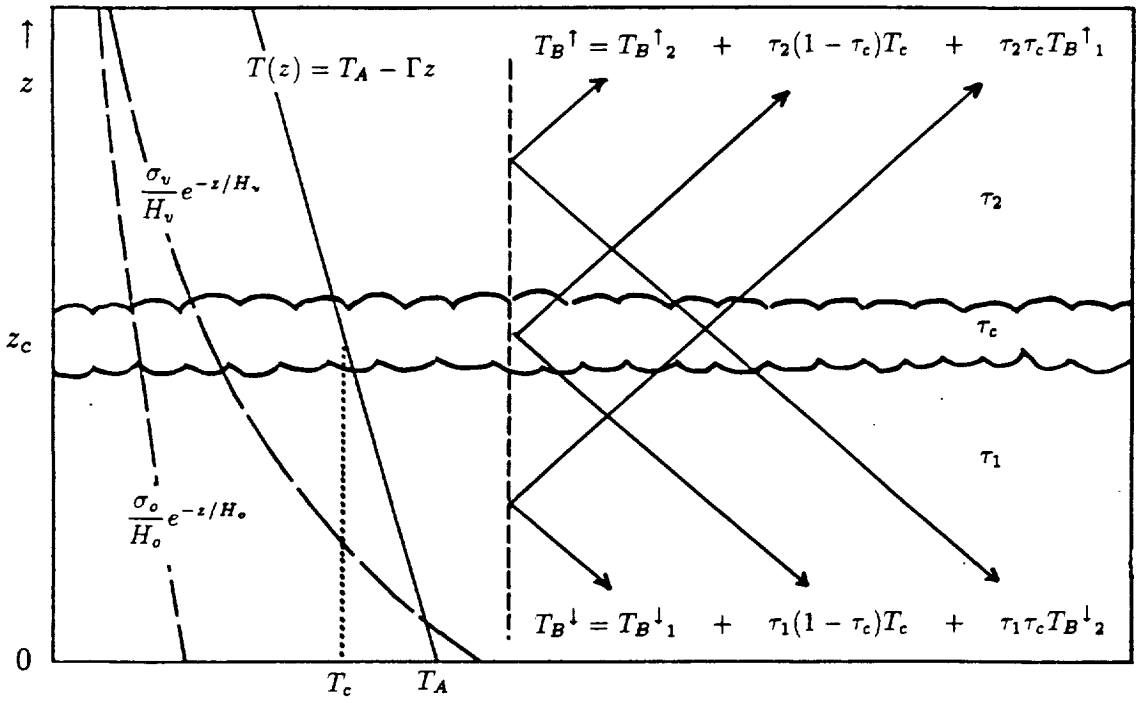

Fig. 6.3 Schematic depiction of the simplified atmospheric model used in deriving closed-form expressions for upwelling and downwelling atmospheric radiances.

b. Large-Angle Correction

At viewing angles approaching the horizon (i.e., $\theta \rightarrow 90°$, implying $\mu \rightarrow 0$), the ratio σ/μ may be of order unity or greater. This is especially true when σ itself is not much less than unity, as might be the case at 85 GHz in a tropical atmosphere. Under these circumstances, the polynomial expansions in (6.25) and (6.26) cease to adequately approximate $w(z)$ and $y(z)$, and the brightness temperature model loses accuracy.

For SSM/I applications (where $\theta \approx 53°$ for the upward and specularly reflected downward component of atmospheric emission), the failure of the model at large angles is only a problem when calculating the contribution due to diffuse reflection at the surface, i.e., when downward sky radiances from directions near the horizon may contribute significantly to the integral term in (5.10) and consequently to the satellite-observed T_B.

For near grazing angles, one expects $T_B{}^{\downarrow}(\mu)$ to approach T_A. In fact, the model described above significantly underestimates $T^{\downarrow}$ at large angles. The solution employed here is an *ad hoc* correction term which forces $T_B{}^{\downarrow} \rightarrow T_A$ as $[\sigma/\mu] \rightarrow \infty$:

$$T_B{}^{\downarrow'} = (1-\gamma)T_B{}^{\downarrow} + (1-\tau_\infty)\gamma T_A \tag{6.50}$$

where

$$\gamma = \left\{ .637 \tan^{-1}\left[\frac{1}{\mu}(\sigma_o + \sigma_v)\right]\right\}^2 . \tag{6.51}$$

The angular dependence of $T_B{}^{\downarrow}$ obtained from the model, both with and without correction, is compared with the correct (i.e., numerically integrated) results in Fig. 6.4 for typical atmospheric conditions.

This completes the mathematical framework of the model for atmospheric emission and absorption at microwave window frequencies. To summarize, (6.27)–(6.49) provide analytic expressions for the upwelling microwave brightness temperature at the top of the atmosphere and the downwelling brightness temperature

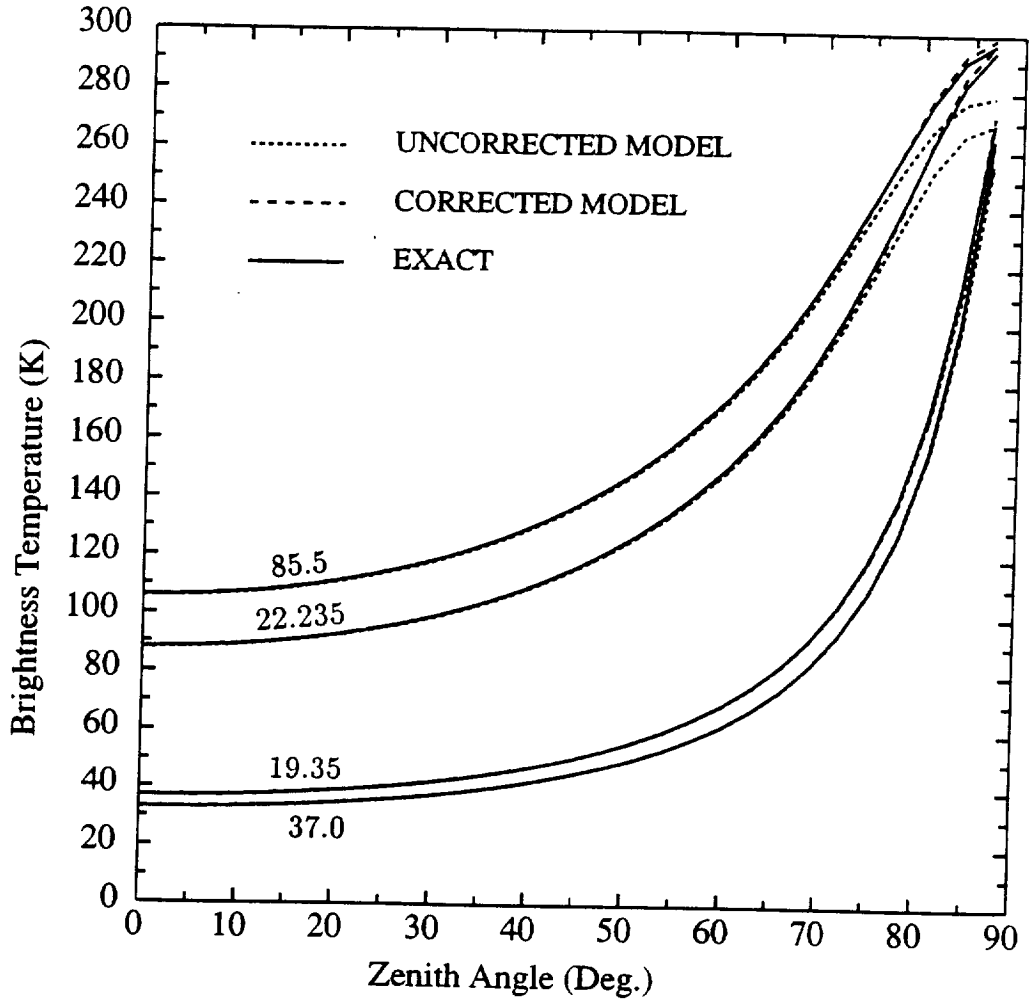

Fig. 6.4 Angular dependence of downwelling atmospheric brightness temperatures computed via the uncorrected and corrected analytic brightness temperature model and compared with numerical results for typical atmospheric conditions.

at the surface, in terms of μ, σ_o, σ_v, H_o, H_v, T_A, Γ, z_c, and σ_c. In addition, when downwelling brightness temperature at large angles are required for computing diffuse reflection from the surface, then the brightness temperature correction given by (6.50) and (6.51) should also be included.

In the following two subsections, we examine the dependence of σ_o, σ_v, H_o, H_v, and σ_c on the relevant meteorological variables for the four SSM/I microwave frequencies.

c. Absorption Profile Parameters for Water Vapor and Dry Air

The aim of this subsection is to accurately parameterize the dry air and water vapor absorption profile parameters (σ_o, H_o, σ_v, H_v) for each SSM/I frequency (19.35, 22.235, 37.0, and 85.5 GHz) in terms of the relevant meteorological variables and to demonstrate that the model successfully reproduces atmospheric brightness temperatures obtained by explicit numerical integration of the radiative transfer equations (6.5) and (6.6) for a wide range of atmospheric temperature and humidity profiles.

For this purpose, a calendar year's worth of radiosonde-derived profiles of atmospheric temperature and humidity were obtained for each of 29 island, coastal, and ship weather stations. These stations were chosen to be as representative as possible of maritime conditions in all latitude belts and at all times of the year. We considered it especially important to include data from stations in the southernmost latitudes, since conventional data over the southern oceans is scarce, so those regions stand to benefit most from accurate satellite observations. Stations located in continental interiors were not included in this analysis, mainly because of the general unsuitability of the SSM/I for sensing atmospheric parameters against a land background.

At midlatitude and polar stations, soundings are usually made at least twice daily, yielding up to 730 soundings per station per year. In the tropics, soundings

are often taken only once daily for part or all of each year, because variability on short time scales tends to be weak.

Each sounding was subjected to quality checks before further processing. Soundings in which the final temperature level occurred below the 200 hPa level were rejected. Those with final valid humidity levels occurring below the 500 hPa level were likewise rejected, except when the temperature at the final level was colder than -30 C. Other obvious inconsistencies in the data which could be detected automatically, such as unrealistic lapse rates, supersaturation, etc., also led to rejection of the sounding. The final data set consisted of a total of 16,893 profiles. Table 6.3 summarizes the atmospheric sounding set used in deriving the relationships which follow, and the geographic locations are indicated in Fig. 6.5.

Computation of radiative quantities was based on atmospheric profiles extending from the surface to the 1 hPa level. Since most operational soundings terminate well below that level (typically between 100 and 10 hPa), each sounding was first extended to the highest mandatory reporting level recorded for that station during the entire year, using the mean temperature and dewpoint depression for each mandatory level for which sounding data was available. A final level having a temperature of 260 K and no moisture was supplied at 1 hPa.

Although this procedure does not account for seasonal and other variability at the highest levels, it at least provides "reasonable" values at high levels for each station, so that the strong latitudinal dependence of tropopause height and stratospheric temperature, for example, is approximately accounted for. In any case, the contribution of the atmosphere above the 200 hPa level to the opacity and brightness temperature at SSM/I frequencies is rather small owing to the effect of low pressure on the width of nearby absorption lines and because of the absence of appreciable moisture. A more rigorous treatment of upper level variations was therefore deemed unnecessary.

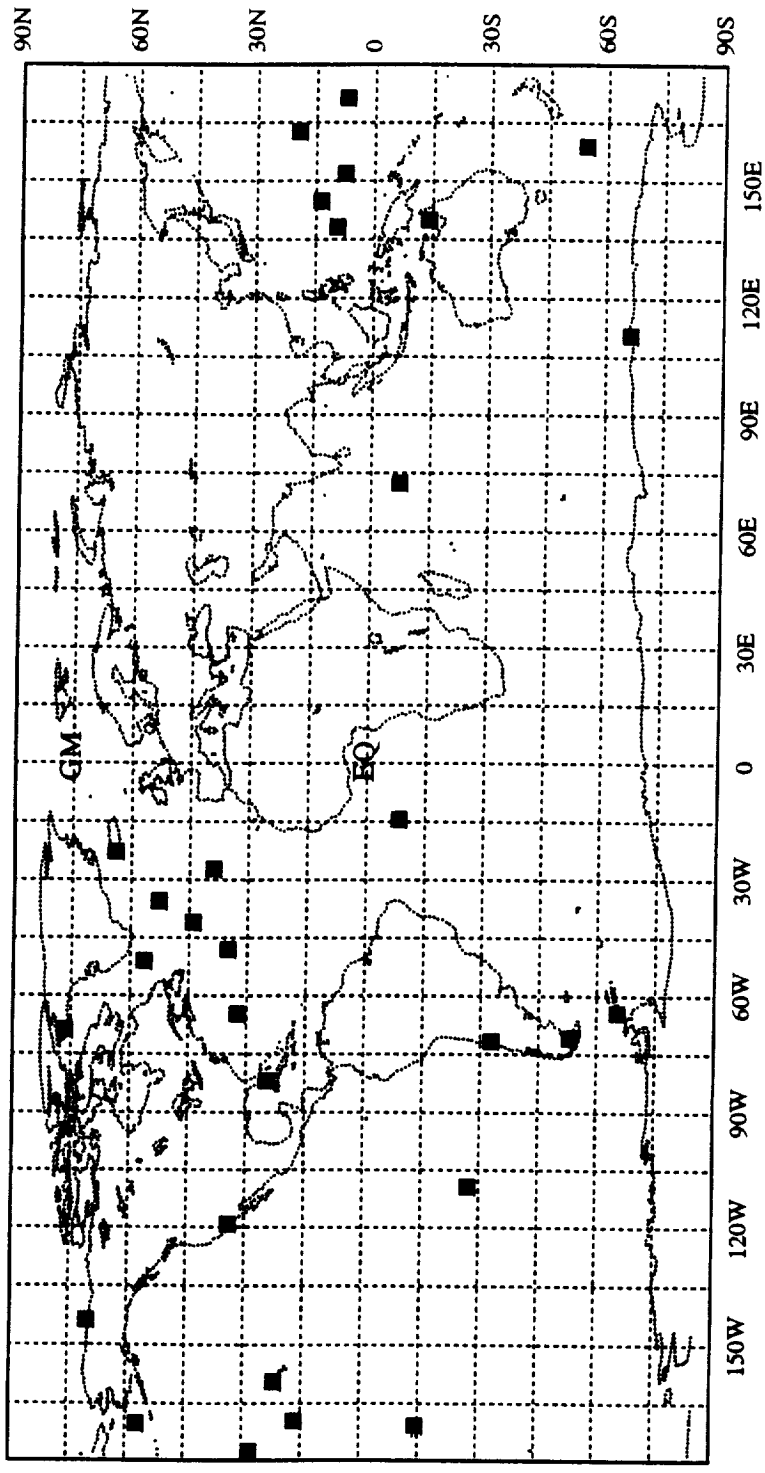

Fig. 6.5 Locations of radiosonde stations employed in model coefficient fits and for generating global atmospheric parameter statistics.

Table 6.3: Radiosonde data set used in model coefficient fits

Station	Year	N	Lat.	Lon.
Thule	1969	632	76.5N	68.8W
Barter	1978	669	70.1N	143.6W
Keflavik	1980	714	64.0N	22.6W
Ship B	1971	690	56.5N	51.0W
Ship C	1971	643	52.8N	35.5W
St. Paul	1979	719	57.2N	170.2W
Ship D	1971	670	44.0N	41.0W
Azores	1970	721	38.8N	27.1W
Ship E	1971	655	35.0N	48.0W
Pt. Mugu	1978	715	34.1N	119.1W
St. George	1970	539	32.4N	64.7W
Midway	1979	569	28.2N	177.4W
Key West	1978	725	24.6N	81.8W
Lihue	1979	725	22.0N	159.4W
Wake	1979	701	19.3N	162.7E
Johnston	1979	724	16.7N	169.5W
Guam	1979	741	13.6N	144.8E
Yap	1979	494	9.5N	138.1E
Truk	1979	487	7.5N	151.9E
Majuro	1979	483	7.1N	171.4E
Diego Garcia	1978	312	7.3S	72.4E
Ascension	1969	509	8.4S	14.4W
EMEX Ship	1987	130	14.0S	140.0E
Pago Pago	1979	716	14.3S	170.7W
Easter	1979	207	27.2S	109.4W
Quintero	1980	443	32.8S	71.6W
Punta Arenas	1980	298	53.0S	70.9W
Macquarie	1975	522	54.5S	159.0E
Argentine	1955	349	65.3S	64.3W
Casey	1975	391	66.3S	110.6E
Total		16,893		

Each profile was numerically integrated to yield total water vapor content V and water vapor scale height H. Upwelling and downwelling brightness temperatures $T_B{}^{\uparrow}$ and *tbdn* were calculated directly from the soundings via (6.5) and (6.6) plus the Liebe MPM model. Values of $T_B{}^{\downarrow}$ computed for each frequency are shown as functions of V in Fig. 6.6. Although V is seen to explain most of the variability of $T_B{}^{\downarrow}$, there is nevertheless significant variability in $T_B{}^{\downarrow}$ which must be due to other factors, especially at 37.0 and 85.5 GHz.

Optical depths σ_o and σ_v and absorption scale heights H_o and H_v were also calculated for each frequency using the MPM model. Scale heights H, H_o, H_v are defined by the following relation, in which the variable x may represent water vapor density or volume absorption coefficient for dry air or water vapor, as appropriate:

$$H_x = \frac{\int_0^\infty zx\ dz}{\int_0^\infty x\ dz}. \tag{6.52}$$

The only remaining input parameters for the radiative transfer model are the effective surface temperature T_A and lapse rate Γ. Real atmospheric profiles, of course, rarely exhibit even near-constant lapse rates throughout the lower troposphere. Thus, the assumption that, for radiative transfer purposes, the variability of the thermal structure of the lower atmosphere can be adequately captured by these two scalar quantities represents one of the more optimistic idealizations implicit in our mathematical formulation.

Furthermore, it is not necessarily obvious that, for given temperature and moisture profiles, there should be a *frequency-independent* Γ and T_A which would adequately predict brightness temperatures simultaneously at all four SSM/I frequencies. For depending on the relative contributions of oxygen and water vapor to the emission at a given frequency, different portions of the atmospheric temperature profile have the greatest influence on the brightness temperatures seen. For example, given a shallow, cold, moist, marine boundary layer capped by a warm,

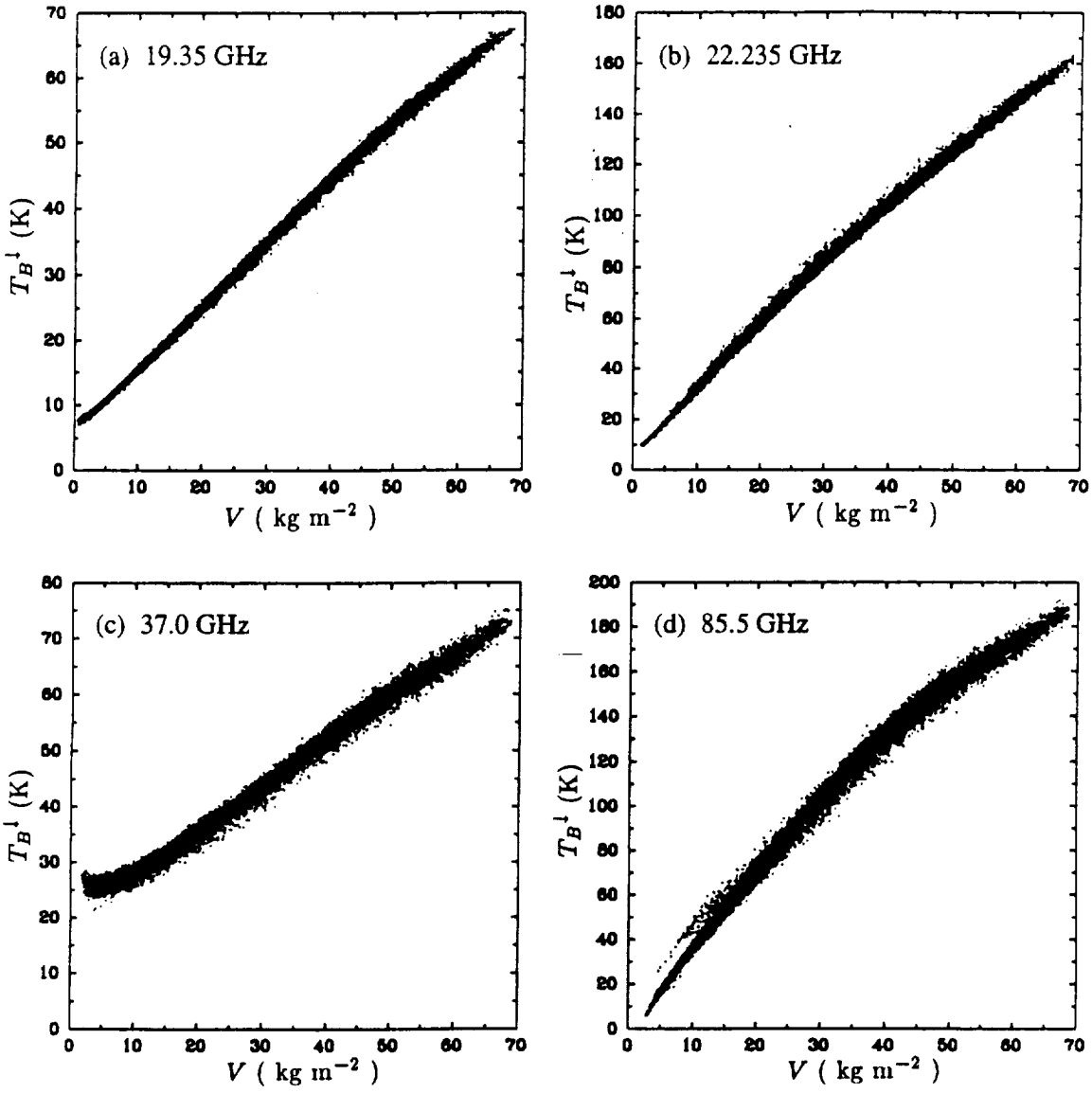

Fig. 6.6 Numerically computed downwelling atmospheric brightness temperatures $T_B{}^{\downarrow}$ vs integrated water vapor V for a viewing angle of 53°.

dry atmosphere, the channels most sensitive to water vapor will "see" the temperature of the boundary layer, whereas the channels proportionally more sensitive to oxygen absorption will "see" more of the warmer air above the boundary layer. Fortunately, the assumption of a single representative, linear temperature profile nevertheless is found to give satisfactory results.

Two different approaches were tested for determining T_A and Γ pairs for each profile. In the first method, the mean and first moment (with respect to z) of the temperature profile below 500 hPa were computed:

$$\bar{T} \equiv \frac{1}{Z_{500}} \int_0^{Z_{500}} T(z)\, dz, \tag{6.53}$$

$$T_\sigma \equiv \frac{1}{Z_{500}^2} \int_0^{Z_{500}} zT(z)\, dz. \tag{6.54}$$

These can then be related to an effective surface temperature and lapse rate as follows:

$$T_{A,0} \equiv 4\bar{T} - 6T_\sigma, \tag{6.55}$$

$$\Gamma_0 \equiv \frac{6}{Z_{500}}[\bar{T} - 2T_\sigma]. \tag{6.56}$$

In the second method, a T_A-Γ pair was iteratively sought (using $T_{A,0}$ and Γ_0 as a first guess) which minimized the mean-square difference between the brightness temperatures at all four frequencies, as calculated directly from the profiles using (6.5) and (6.6), and those predicted by the analytic model using the computed values of σ_o, σ_v, H_o and H_v.

Obtaining T_A and Γ in the latter way proved to be advantageous for two reasons. Not only does the procedure itself provide an immediate test of the validity of our model, by uncovering the limits of its ability to simultaneously reproduce the "exact" T_B at each frequency, as determined by numerical integration, but these values of T_A and Γ, combined with V and H, proved to be better predictor variables for σ_o, σ_v, H_o and H_v than were $T_{A,0}$ and Γ_0.

It must be borne in mind that the temperature parameters T_A and Γ do not necessarily represent the actual surface temperature and mean lapse rate respectively, but rather represent an *effective* surface temperature and lapse rate for that layer of the lower troposphere which most strongly governs the computed microwave brightness temperatures. To illustrate the distinction, Fig. 6.7 depicts T_A plotted vs actual surface air temperature T_0. Although the two are seen to be highly correlated, rms differences are ~5 K. Particularly for $T_0 < 270$ K, the relationship is quite weak, apparently because of the presence of strong surface inversions in many of the corresponding soundings. Thus, while T_A is an important input parameter to the brightness temperature model, its connection to conventional observations of surface temperature may be regarded as somewhat tenuous.

For a given frequency, the mass absorption coefficient of water vapor or dry air depends primarily on local pressure and temperature. Since σ_o, σ_v, H_o and H_v represent *vertical integrations* of absorption coefficient, we expect these variables to possibly depend on T_A, Γ, surface pressure p_0, and in the case of σ_v and H_v, the vapor scale height H. As noted in section 6.1, water vapor absorption coefficients are also dependent on water vapor *density*, so that terms like V/H must be considered.

After some experimentation, we found that the following models provided satisfactory fits to the numerically calculated values from the radiosonde data set:

$$\sigma_o = a_0 + a_1 p_0 + a_2 \left(\frac{1}{\bar{T}_o}\right), \tag{6.57}$$

$$H_o = b_0 + b_1 T_A + b_2 \Gamma, \tag{6.58}$$

$$\begin{aligned}\frac{\sigma_v}{V} = {} & c_0 + c_1 \bar{p} + c_2 \left(\frac{V}{H}\right) + c_3 \left(\frac{1}{\bar{T}_v}\right) + c_4 \bar{p}^2 + c_5 \bar{p} \left(\frac{V}{H}\right) \\ & + c_6 \bar{p} \left(\frac{1}{\bar{T}_v}\right) + c_7 \left(\frac{V}{H}\right) \left(\frac{1}{\bar{T}_v}\right)^2 + c_8 \left(\frac{1}{\bar{T}_v}\right)^2,\end{aligned} \tag{6.59}$$

$$H_v = \gamma H, \tag{6.60}$$

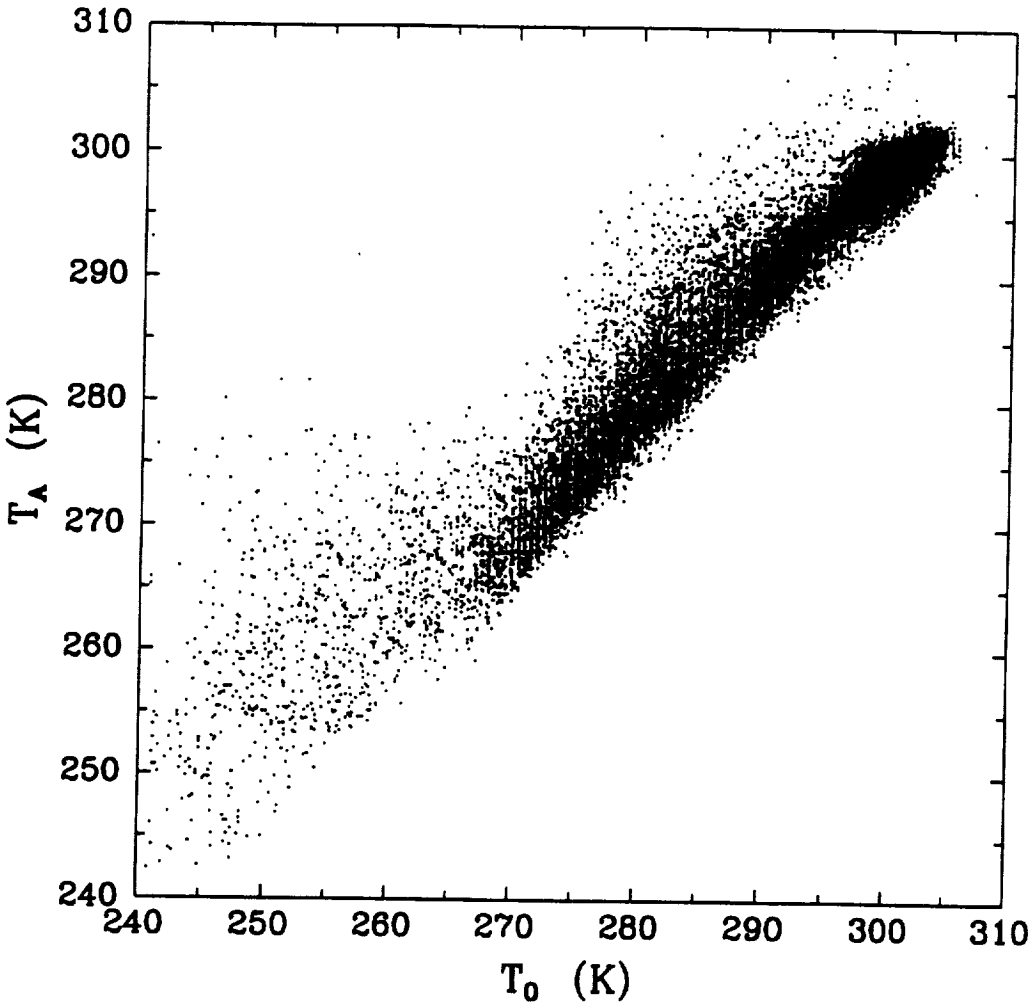

Fig. 6.7 Actual surface air temperature T_0 obtained directly from radiosonde soundings vs effective surface air temperature T_A obtained by minimizing least-squared difference between numerically computed and analytic-model computed brightness temperatures.

where

$$\bar{T}_o = T_A - \Gamma\xi, \tag{6.61}$$

$$\bar{T}_v = T_A - \Gamma H\eta, \tag{6.62}$$

$$\bar{p} = \frac{p_0}{1 + H/H'}. \tag{6.63}$$

$\bar{T}_o$ and $\bar{T}_v$ may be regarded as column absorber-weighted temperatures for dry air and water vapor, respectively. Likewise, $\bar{p}$ is an effective mean pressure acting on the water vapor in the column. Values of a_n, b_n, c_n, γ, ξ, η, and H' are tabulated for each SSM/I frequency in Table 6.4.

Using the radiosonde derived values of V, H, T_A, Γ, and p_0 as inputs, upward and downward brightness temperatures were computed from the analytic model for a viewing angle of 53°. These model-predicted $T_B{}^{\downarrow}$ are compared with the numerically integrated $T_B{}^{\downarrow}$ [using (6.5)] in Fig. 6.8 for each SSM/I frequency. RMS differences for the entire set of 16,893 soundings were 0.07, 0.46, 0.27, and 0.93 K for 19, 22, 37, and 85 GHz, respectively. Nearly identical results are found for model vs numerical $T_B{}^{\uparrow}$. For comparison, recall that the instrument noise level of the SSM/I is estimated to be ~0.5 K.

The excellent agreement between model-predicted and explicitly integrated $T_B{}^{\downarrow}$ and $T_B{}^{\uparrow}$ validates both the mathematical form of the model (including the underlying assumptions) and the regression relations between the absorption/emission profiles and meteorologically meaningful parameters (to the accuracy of the Liebe MPM formulation of oxygen and water vapor absorption).

It must be emphasized that the regression models obtained here can be considered reliable only within the multi-dimensional domain defined by the sounding data used. Since a large number of soundings were employed, representing all seasons and latitude belts, it is likely that most, if not all, *statistically realizable* combinations of H, T_A, Γ, V, and p_0 fall within the domain where the regression

Table 6.4: Model coefficients

Freq. (GHz)	19.35	22.235	37.0	85.5
a_0	−.469−1	−.578−1	−.189+0	.110+0
a_1	.266−4	.317−4	.983−4	.605−4
a_2	.876+1	.110+2	.367+2	−.376+2
b_0	−.359+1	−.389+1	−.431+1	−.170+0
b_1	.298−1	.311−1	.328−1	.136−1
b_2	−.232−1	−.235−1	−.241−1	−.158+0
c_0	−.138−2	.222−1	−.106−2	−.608−2
c_1	0	−.324−4	0	0
c_2	−.431−4	−.108−4	−.129−3	−.709−3
c_3	.146+1	−.636−1	.570+0	.287+1
c_4	0	.170−7	.108−8	.426−8
c_5	0	0	−.176−7	−.829−7
c_6	.251−3	0	0	0
c_7	.146−1	0	.486−1	.262+0
c_8	−.186+3	−.298+2	0	0
γ	.921	1.21	.825	.820
ξ	4.2	4.2	4.2	2.9
η	0.6	2.8	0.2	0.2
H'	5.0	4.9	6.8	6.4

equations are valid. However, it is easy to construct combinations of input parameter values which, taken individually, are "reasonable" but which collectively are improbable or even physically impossible. For such combinations, model computed brightness temperatures may not be meaningful.

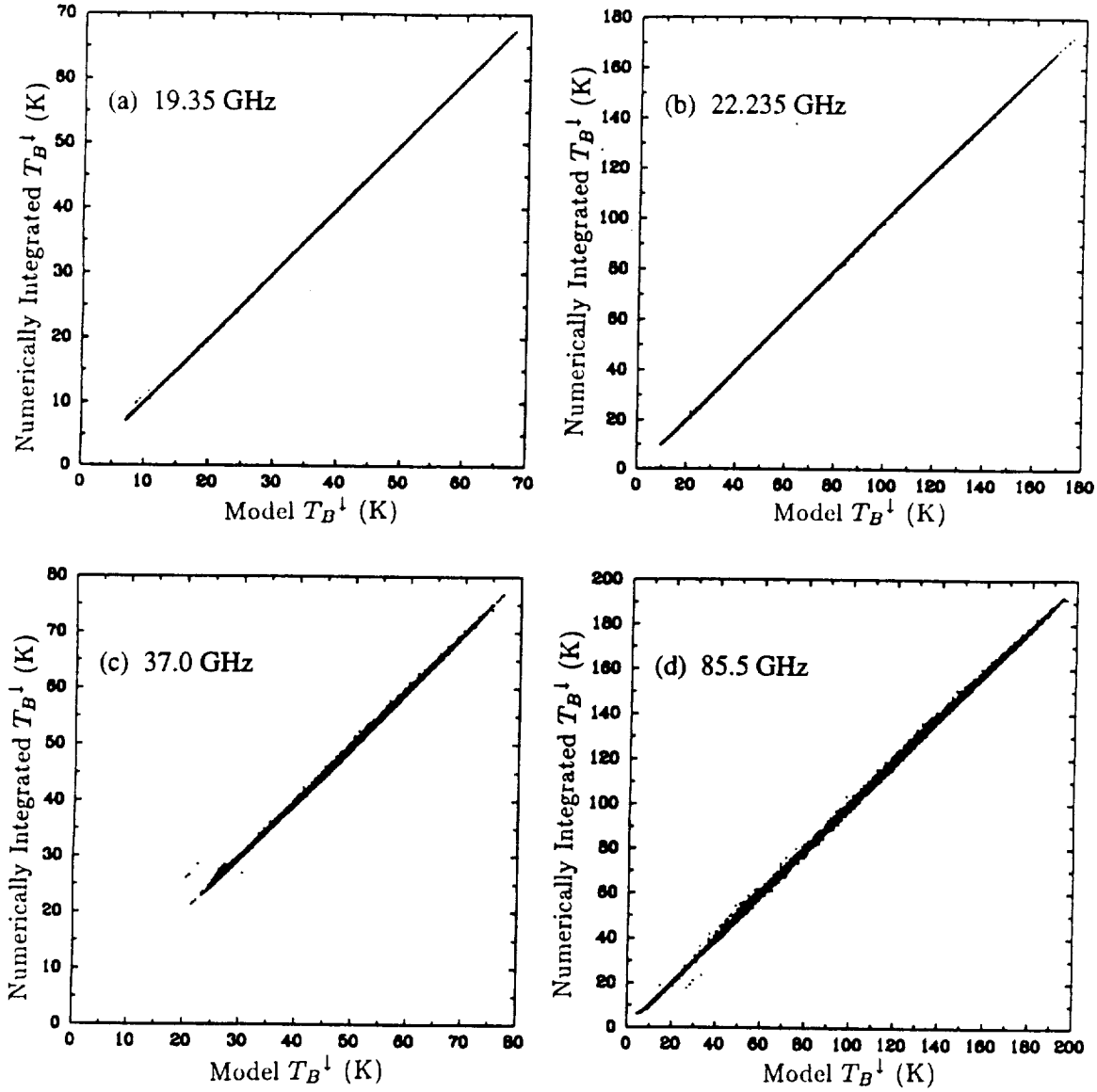

Fig. 6.8 Numerically integrated $T_B^{\downarrow}$ vs analytic model $T_B^{\downarrow}$ for 16,893 radiosonde-derived atmospheric temperature and water vapor profiles. (a) 19.35 GHz (b) 22.235 GHz (c) 37.0 GHz (d) 85.5 GHz.

We now complete the atmospheric brightness temperature model by taking the cloud optical depth σ_c to be approximately the product of the integrated liquid water content L and the mass absorption coefficient κ_c for an effective mean cloud temperature which, in turn, we take to be the same as the effective radiating temperature. That is,

$$\sigma_c = \kappa_c(T_c - 273.15)L, \tag{6.64}$$

where κ_c is given by (6.4) and T_c is given by (6.49).

d. Statistics of Model Input Parameters

There are a number of significant physical and statistical constraints on the combinations of V, H, T_A, Γ, and p_0 that may actually appear in nature. That is to say, the permissible range of values which one variable may take on depends on the values of the remaining four variables. In addition, the exact statistical relationship between variables may itself depend on other variables which are not model input parameters; for example, season or geographical location.

When using the physical model developed in this thesis as a basis for retrieval algorithms for the SSM/I, at least partial knowledge of these relationships is valuable. This is because (a) realistic *a priori* constraints on the retrieved variables can usually be exploited to improve the error statistics of the retrievals, and (b) knowledge of the variability of non-retrievable parameters which may contribute to the retrieval errors can lead to reasonable estimates of those errors and/or to improvements in algorithm design (see Chapter 11).

Not surprisingly, the most clear case of parameter interdependence is that between atmospheric temperature and water vapor content. Fig. 6.9a shows integrated water vapor V plotted vs T_A. As expected, large water vapor content is invariably associated with warm temperatures, and cold temperatures are associated with very low water vapor content. What is somewhat less expected is the rather narrow range of T_A at high water vapor values; the vast majority of data

points with $V > 35$ kg m^{-2} are associated with T_A in the narrow temperature range 297 K and 302 K, despite the fact that a significant number of these points were contributed by subtropical and midlatitude as well as tropical stations.

It is also reasonable to anticipate some interdependence between the integrated water vapor V and vapor scale height H. Fig. 6.9b indicates that, for $V > 40$ kg m^{-2}, there is indeed a marked positive correlation between the two variables. For smaller values of V, there is no obvious correlation; rather, the mean value of H hovers around 1.8 km, but with increasing scatter about this value as V becomes small. The explanation for the latter behavior is that small V can be due either to a very shallow moist boundary layer capped by dry air (corresponding to small H) or to a moderately dry atmosphere at all levels except perhaps for a moister layer at some altitude above the surface (i.e., large H). Larger V, on the other hand, can only be achieved by an atmosphere which has high relative humidity at all levels, so that H is restricted to a rather narrow range.

For $T_A > 270$ K (Fig. 6.9c), Γ is more or less uniformly distributed between 4.5 and 6.5 K km^{-1}. Below this temperature, however, there is a systematic decrease of Γ with T_A, presumably owing to the increasing likelihood of strong near-surface inversions in these subarctic soundings.

Surface pressure p_0 varies widely at midlatitude and polar stations, these normally having T_A below 290 K (Fig. 6.9d). At higher temperatures (corresponding to tropical stations) variations in p_0 are much less pronounced and are as much due to differences in station elevation as anything else. Other than this observation, little useful statistical information on p_0 appears to be offered by knowledge of T_A or any other model input parameter.

In order to put the above observations on a more quantitative footing, means and standard deviations of radiosonde derived quantities were computed for intervals in V of 10 kg m^{-2} . Results for the model input parameters p_0, H, T_A, and Γ, as well as the observed surface temperature T_0 and specific humidity q_0

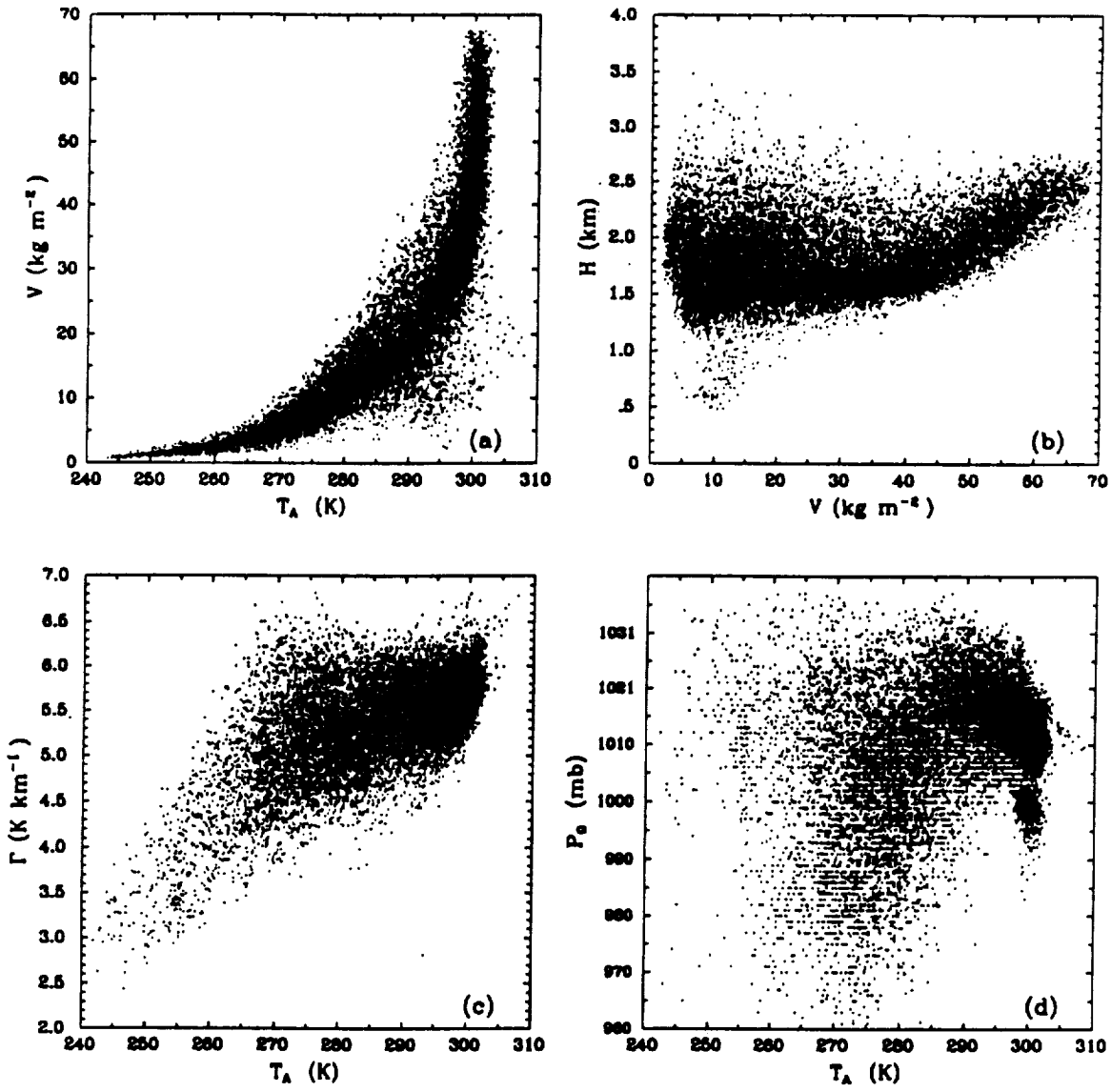

Fig. 6.9 Global associations of selected input parameters for the analytic brightness temperature model, as obtained from 16,893 radiosonde profiles. (a) Integrated water vapor V vs effective surface air temperature T_A, (b) V vs water vapor scale height H, (c) T_A vs effective lapse rate Γ, (d) T_A vs surface pressure p_0.

Table 6.5: Means and standard deviations of atmospheric model parameters.

V(kg m^{-2})	N	p_0(mb)		T_0(K)		q_0(g kg^{-1})		H (km)		T_A(K)		Γ(K km^{-1})	
0–10	3624	1000	(15.3)	270	(10.3)	2.7	(1.8)	1.8	(0.4)	271	(8.5)	5.0	(0.7)
10–20	3930	1010	(12.0)	284	(5.7)	6.6	(2.1)	1.8	(0.3)	285	(5.8)	5.4	(0.4)
20–30	2790	1010	(7.7)	293	(5.7)	11.4	(2.9)	1.8	(0.3)	293	(4.1)	5.5	(0.3)
30–40	2801	1010	(6.3)	298	(3.5)	15.6	(2.3)	1.7	(0.2)	297	(2.4)	5.7	(0.3)
40–50	1951	1010	(5.4)	300	(2.4)	17.9	(1.7)	1.9	(0.2)	299	(1.5)	5.8	(0.2)
50–60	1378	1010	(5.2)	301	(1.9)	19.0	(1.2)	2.2	(0.2)	300	(1.1)	5.7	(0.2)
60–70	428	1010	(5.3)	300	(1.5)	19.4	(0.9)	2.4	(0.2)	300	(1.0)	5.5	(0.2)

are given in Table 6.5. Knowledge of the 10 kg m^{-2} interval in which V falls for a given sounding in is roughly equivalent to knowing the value of V (the center of the interval in this case) with a standard error of 2.9 kg m^{-2} . The latter value is very close to what is generally reported as the accuracy for satellite microwave estimates of V. It is therefore immediately apparent from Table 6.5 that routine remote retrievals of V could provide surprisingly good proxy estimates of both surface temperature T_0 and humidity q_0 under certain conditions.

Correlations were also computed between the above variables (plus V) for each 10 kg m^{-2} interval of V (Table 6.6). By multiplying each element by the appropriate standard deviations from Table 6.5, these correlation matrices are easily converted into covariance matrices of the type which are central to the minimum variance retrieval method described in Chapter 11. It is apparent, however, that in most cases correlations are actually relatively weak within each interval, except among the closely related variables T_0, q_0, and T_A. Little useful information would be lost, therefore, by ignoring parameter covariances and specifying means and standard deviations of the model input variables p_0, H, T_A, and Γ as simple functions of V alone.

Because profiles of cloud liquid water content cannot be reliably inferred from conventional radiosonde soundings alone, no attempt is made here to describe statistical relationships of the model liquid water parameters L and z_c to the other model variables. In general, it is probably only safe to assume that large L will not normally occur in conjunction with very small V. It has also conventionally been assumed — without the benefit of very many direct observations, unfortunately — that $\sim$0.5 kg m^{-2} of integrated cloud liquid water, averaged over a 25–50 km diameter satellite footprint, represents a reasonable upper limit to the amount of liquid water the atmosphere can contain without precipitation occurring.

The permissible range of z_c is probably rather large under most circumstances, being physically limited only by the maximum height at which significant amounts

Table 6.6: Environmental parameter correlations

p_0	T_0	q_0	V	H	T_A	Γ	
1.00	−0.04	0.00	0.00	0.23	0.09	−0.27	p_0
	1.00	0.82	0.76	−0.45	0.84	0.50	T_0
		1.00	0.71	−0.55	0.79	0.39	q_0
			1.00	−0.22	0.79	0.46	V
				1.00	−0.28	−0.40	H
					1.00	0.56	T_A
V = 0–10 kg m^{-2}						1.00	Γ

p_0	T_0	q_0	V	H	T_A	Γ	
1.00	0.42	0.30	0.19	0.01	0.50	−0.10	p_0
	1.00	0.81	0.42	−0.32	0.82	0.30	T_0
		1.00	0.50	−0.43	0.76	0.22	q_0
			1.00	0.05	0.45	0.11	V
				1.00	−0.17	−0.28	H
					1.00	0.32	T_A
V = 10–20 kg m^{-2}						1.00	Γ

p_0	T_0	q_0	V	H	T_A	Γ	
1.00	0.13	0.09	0.00	−0.08	0.13	0.01	p_0
	1.00	0.86	0.39	−0.54	0.86	0.22	T_0
		1.00	0.50	−0.57	0.81	0.25	q_0
			1.00	−0.09	0.42	0.08	V
				1.00	−0.45	−0.29	H
					1.00	0.23	T_A
V = 20–30 kg m^{-2}						1.00	Γ

Table 6.6 (Continued)

p_0	T_0	q_0	V	H	T_A	Γ	
1.00	−0.06	−0.12	−0.05	0.07	−0.18	0.14	p_0
	1.00	0.81	0.23	−0.46	0.85	0.21	T_0
		1.00	0.39	−0.50	0.81	0.24	q_0
			1.00	0.11	0.32	0.14	V
				1.00	−0.42	−0.18	H
					1.00	0.26	T_A
V = 30–40 kg m^{-2}						1.00	Γ

p_0	T_0	q_0	V	H	T_A	Γ	
1.00	0.02	−0.12	−0.05	0.04	−0.09	0.30	p_0
	1.00	0.68	0.11	−0.23	0.79	0.25	T_0
		1.00	0.25	−0.36	0.72	0.20	q_0
			1.00	0.34	0.25	0.09	V
				1.00	−0.23	−0.15	H
					1.00	0.38	T_A
V = 40–50 kg m^{-2}						1.00	Γ

p_0	T_0	q_0	V	H	T_A	Γ	
1.00	0.10	−0.21	−0.17	−0.08	0.00	0.29	p_0
	1.00	0.55	0.01	−0.20	0.70	0.25	T_0
		1.00	0.20	−0.19	0.48	0.06	q_0
			1.00	0.48	0.07	−0.31	V
				1.00	−0.30	−0.47	H
					1.00	0.46	T_A
V = 50–60 kg m^{-2}						1.00	Γ

Table 6.6 (Continued)

p_0	T_0	q_0	V	H	T_A	Γ	
1.00	0.25	−0.13	0.00	−0.11	0.26	0.27	p_0
	1.00	0.44	−0.07	−0.29	0.67	0.42	T_0
		1.00	0.16	−0.20	0.30	0.19	q_0
			1.00	0.34	−0.03	−0.23	V
				1.00	−0.51	−0.63	H
					1.00	0.70	T_A
V = 60–70 kg m^{-2}						1.00	Γ

of liquid water can exist in the atmosphere. This probably implies a maximum z_c somewhere near the height of the -10° C isotherm, i.e., near 5 km in the tropics and near the surface at high latitudes during the winter. One case for which rather strict constraints may be applied with confidence is that of marine stratocumulus, such as is often found off the California coast. These clouds are normally confined to the lowest 1 km of the atmosphere.

7. THE SEA SURFACE COMPONENT OF SSM/I BRIGHTNESS TEMPERATURES

Because the atmosphere is relatively transparent at SSM/I frequencies, thermal emission and scattering from the surface are always important components of the brightness temperatures observed from space. This circumstance has two important consequences: (i) it is possible to observe variations in the surface emission under most conditions, in principle permitting the observations to be interpreted in terms of surface characteristics; and (ii) it is almost always necessary to accurately account for variations in the surface contribution when attempting quantitative retrievals of atmospheric parameters.

The aim of this chapter is to examine the sea surface contribution to observed SSM/I brightness temperatures and to present useful quantitative parameterizations of the most important surface effects. The general theory and qualitative behavior of sea surface emissivity and reflection have been discussed in numerous earlier papers; here we concentrate on deriving closed-form models specifically for use in SSM/I applications. As part of this effort, we also present what we hope is a more realistic approach, relative to earlier studies, to parameterizing the diffusely reflected component of radiation at the sea surface.

The accurate modeling of sea surface microwave emissivity and bidirectional reflectance from first principles is a problem which is probably worthy of an entire dissertation in its own right. It must therefore be emphasized that the following is not a 'state-of-the-art' theoretical treatment of the problem but rather focuses only on obtaining useful relationships which are subsequently calibrated to be consistent with observed SSM/I brightness temperatures. This work was necessitated by the apparent non-existence of well-validated, published parameterizations of sea surface effects at SSM/I frequencies.

7.1 Plane-surface Emission and Reflection

To first order, the sea surface may be approximated as a plane interface between two homogeneous dielectric media: air and seawater. It is straightforward to analytically solve the boundary value problem for electromagnetic plane waves impinging on the interface at an arbitrary angle of incidence θ_i from normal and with arbitrary polarization, in order to determine the fraction R of the incident radiation which is reflected from the interface (e.g., Bohren and Huffman, 1983).

The reflectivity R is a function of θ_i, polarization — i.e., the orientation, relative to the interface, of the plane containing both the electric field vector and the incident ray — and the complex dielectric constants ϵ_a and ϵ_s of air and seawater respectively. ϵ_a is sufficiently close to unity that the solution for R reduces to the well-known Fresnel formulae

$$R_V = \left| \frac{\epsilon_s \cos\theta_i - \sqrt{\epsilon_s - 1 + \cos^2\theta_i}}{\epsilon_s \cos\theta_i + \sqrt{\epsilon_s - 1 + \cos^2\theta_i}} \right|^2 \qquad (7.1a)$$

and

$$R_H = \left| \frac{\cos\theta_i - \sqrt{\epsilon_s - 1 + \cos^2\theta_i}}{\cos\theta_i + \sqrt{\epsilon_s - 1 + \cos^2\theta_i}} \right|^2 , \qquad (7.1b)$$

where the subscripts V and H refer to vertical and horizontal polarization, respectively.

The direction of the reflected radiation, of course, is such that it lies in the plane containing both the incident ray and the local normal vector, and its angle θ_r relative to the local normal is equal to θ_i. Reflection exhibiting these properties is termed *specular*, as contrasted with *diffuse* reflection, in which reflected radiant energy is distributed over a range of angles.

All radiation not reflected from the interface must be transmitted or absorbed. The penetration depth of microwaves in salt water is only ~1 mm, i.e., vastly smaller than the depth of the ocean; hence, the transmissivity is zero and the absorptivity A of the plane sea surface is equal to $1 - R$. By Kirchhoff's Law

$A = E$, where E is the thermal emissivity of the plane surface and represents the ratio of the emitted radiance to that expected from a blackbody of the same thermodynamic temperature. In summary, the brightness temperature $T_{B,plane}$ due to thermal emission from the flat sea surface at polarization $p = V, H$ and surface temperature T_S may be written simply as

$$T_{B,plane} = E_p T_S = (1 - R_p) T_S. \tag{7.2}$$

In order to compute R_V and R_H from (7.1), one still requires the dielectric constant ϵ_s for saltwater. For this study, we have adopted the widely used semi-empirical formula of Klein and Swift (1977). At SSM/I frequencies, the salinity dependence is quite weak. Therefore, we assume a constant value of $S = 36.5$ ppt in the Klein and Swift formula and we restrict our attention in the following to the effects of angle and temperature.

Fig. 7.1 shows contour plots of E_V and E_H for each SSM/I frequency as functions of saltwater temperature T_S and viewing angle θ. In all cases, $E_V > E_H$ everywhere, except at $\theta = 0$, for which the distinction between horizontal and vertical polarization disappears, and at $\theta = 90°$, where emissivity is zero for both polarizations. A well-known consequence of this difference is that, *in general, for an obliquely viewed ocean surface, microwave brightness temperatures are higher for vertically polarized radiation than for horizontally polarized radiation.*

Another interesting (and well-known) feature is the strong, moderately non-linear decrease in E with increasing temperature. This implies that SSM/I oceanic brightness temperatures, in general, are *not* directly proportional to sea surface temperature, in contrast to the usual case for infrared brightness temperatures. Indeed, under many conditions increases in sea surface temperature actually lead to *decreases* in surface emission.

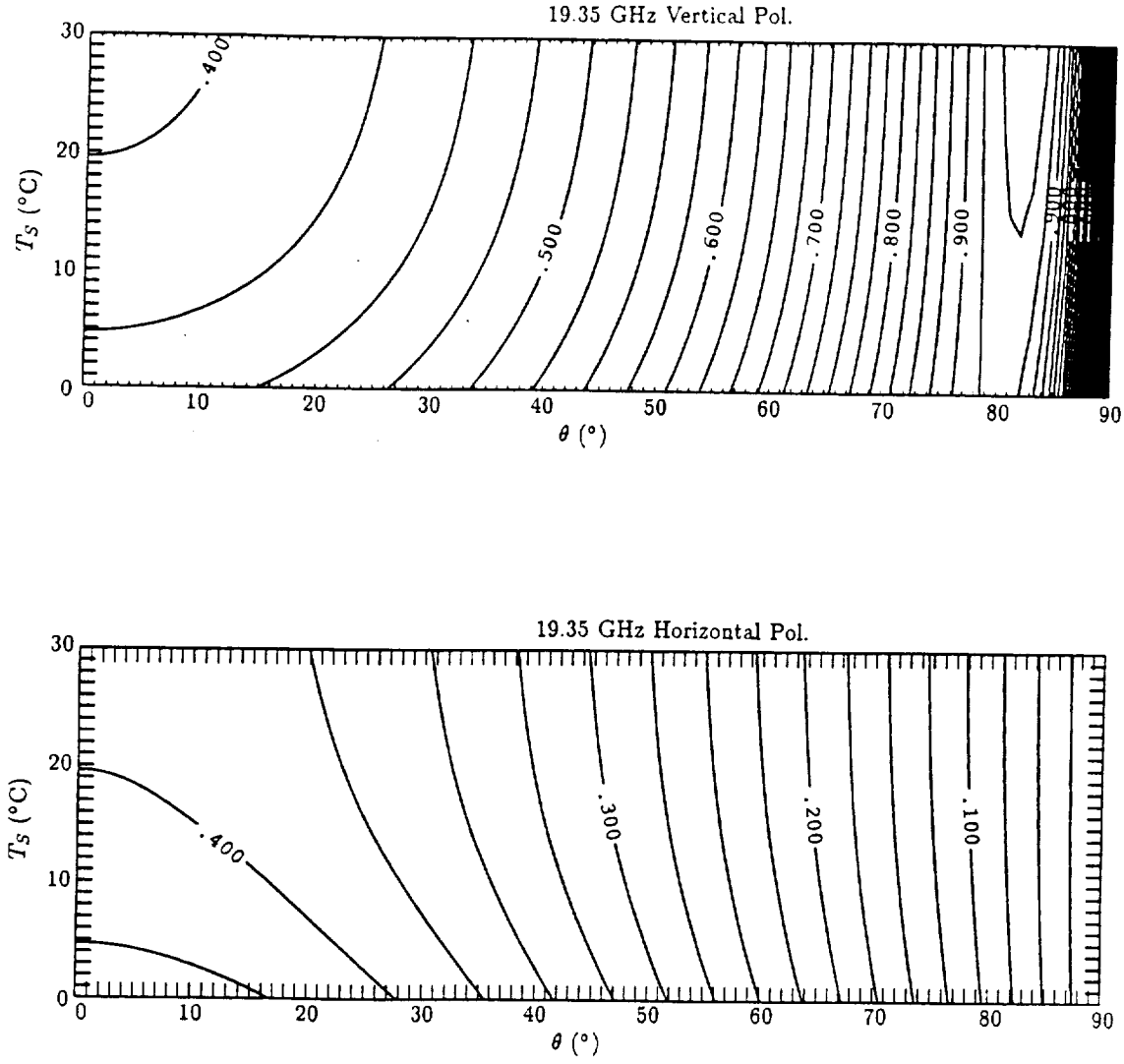

Fig. 7.1 Fresnel emissivity of seawater (salinity 36.6 ppt) as function of viewing angle θ and temperature T_S for vertical polarization (top) and horizontal polarization (bottom). (a) 19.35 GHz

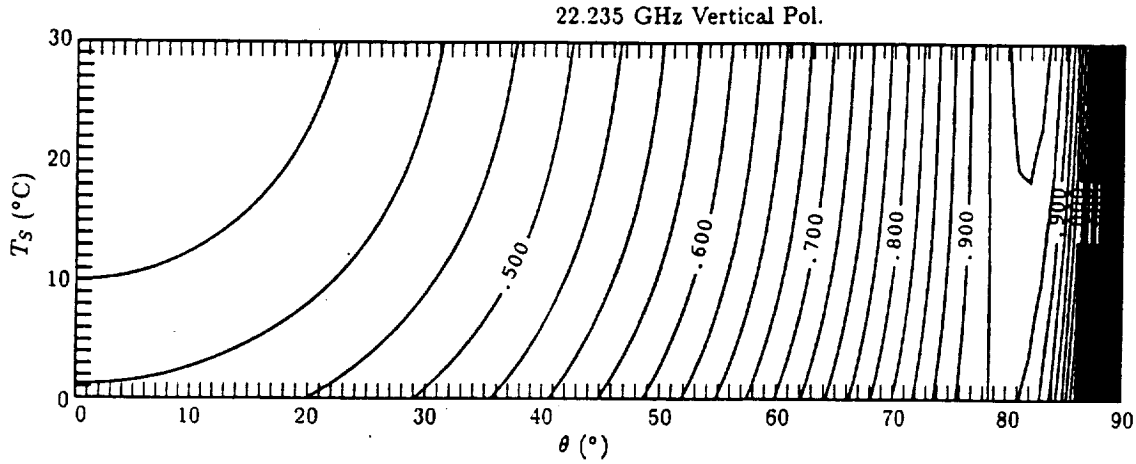

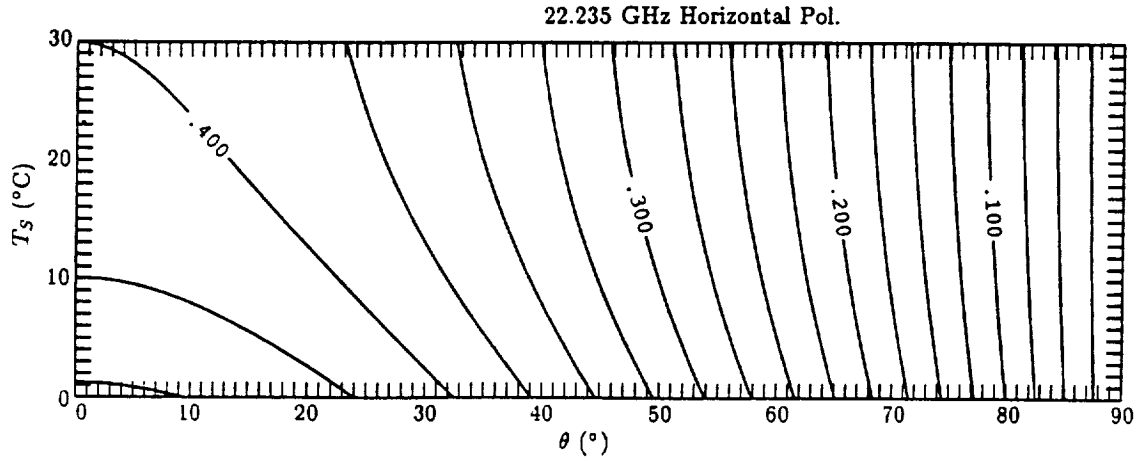

Fig. 7.1 (continued) (b) 22.235 GHz

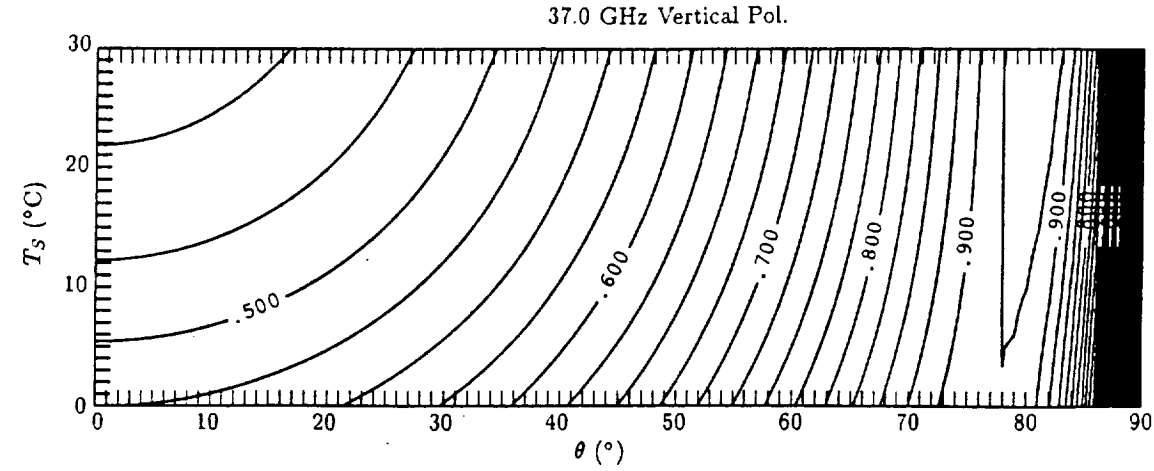

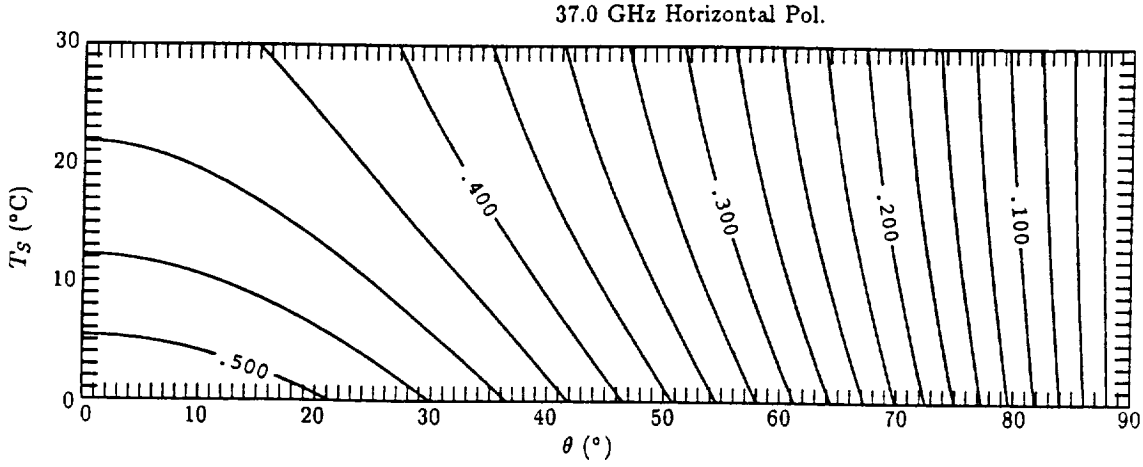

Fig. 7.1 (continued) (c) 37.0 GHz

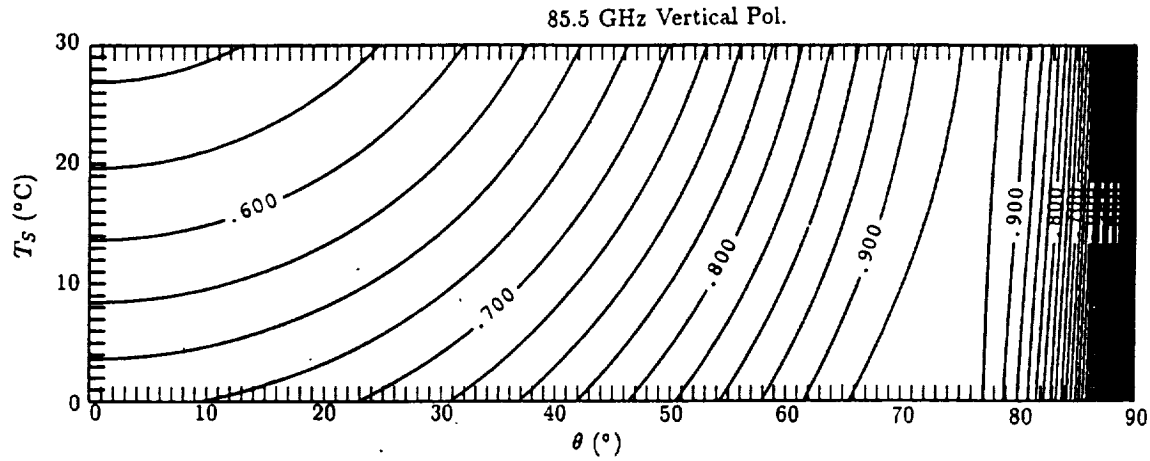

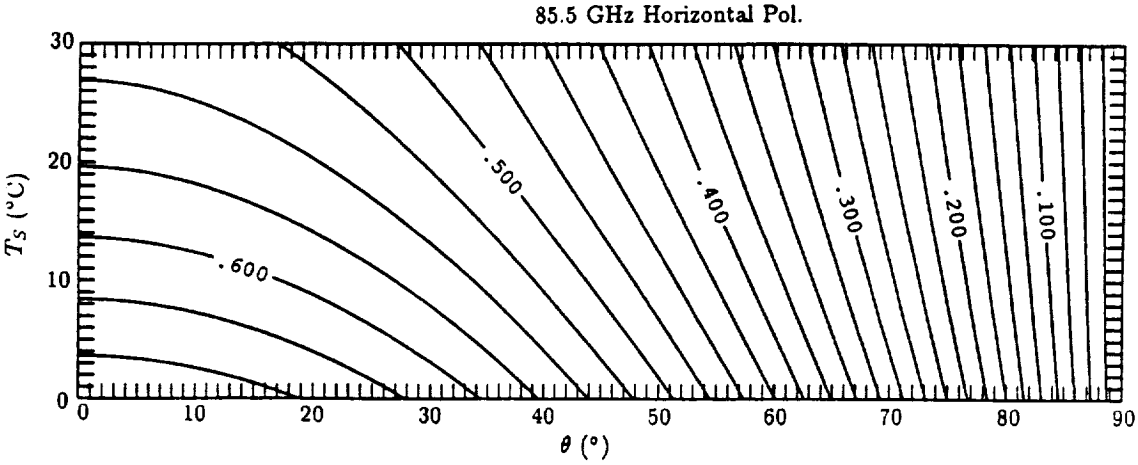

Fig. 7.1 (continued) (d) 85.5 GHz

7.2 Effects of Surface Wind

Numerous investigators have demonstrated, both observationally and theoretically, that the action of wind on the ocean surface can have a substantial effect on microwave brightness temperatures. It is necessary to go beyond the simple plane surface approximation described above in order to account for such effects.

At the wavelengths observed by the SSM/I, the most important contributing factors include the large-scale distribution of surface slopes, which affects both the scene-averaged Fresnel emissivity and the angular weighting of reflected sky emission observed, and the fractional coverage of foam and whitewater, which have much higher emissivity than a smooth water surface. Additional minor emissivity changes may be expected from those small-scale roughness features which are roughly comparable in size to the wavelength of the radiation sensed (0.35 to 1.55 cm for the SSM/I) and for which much more complex radiative interactions must therefore be considered. *The use of microwave radiometers to observe surface wind speed rests on the observation that the above factors affecting the surface brightness temperature vary in a reasonably predictable way with the wind speed U at some standard height above the surface.*

Strictly speaking then, microwave brightness temperatures can only be considered a very indirect indication of wind speed (e.g., Huang et al. 1986). They are more directly indicative of wind stress or friction velocity, which depend not only on U but also on the stability of the surface layer of the atmosphere with respect to mechanical mixing, as well as on the velocity of ocean surface currents. Moreover, the roughness and degree of foam coverage to which a radiometer directly responds are likely to be functions of other variables besides wind stress, including wind fetch, wind duration, swell, seawater viscosity (which depends on temperature), and surface tension (which depends on the presence or absence of

various organic films). Thus, quantitative relationships between microwave observables and ocean surface wind speed U must be understood throughout this thesis as being valid for 'average' conditions over the ocean.

The capability of space-borne microwave radiometers like the SSM/I and its predecessor, the SMMR, to estimate U with reasonable precision is now a well-established fact, as indicated by several successful statistical or empirically-calibrated physical wind speed retrieval algorithms developed for these sensors (e.g., Lipes et al. 1979, Cardone et al. 1983, Wentz et al. 1986, Goodberlet et al. 1989). The precise radiative effects of wind-induced roughening and foam at the SSM/I frequencies and incidence angle, however, have not yet been documented in a form which is suitable for direct incorporation into radiative transfer calculations. This is particularly true of the new 85.5 GHz channels, for which, to our knowledge, no experimental or theoretical data have yet appeared in the published literature. Closed-form emissivity models that were based on physical models calibrated against data from the Seasat SMMR (e.g, Pandey and Kakar 1982, Wentz 1983) did not yield satisfactory results when we attempted to directly adapt them to the SSM/I.

Also, despite the relatively large number of theoretical and empirical studies addressing the relationship between wind speed and surface *emissivity* at various frequencies (e.g., Stogryn 1967, Hollinger 1971, Nordberg et al. 1971, Wu and Fung, 1972, Webster et al. 1976, Wilheit 1979a, Wilheit 1979b, Wentz 1983, Guissard and Sobieski 1987, Sasaki et al. 1987), the majority of these did not attempt to evaluate the sea surface contribution due to *diffusely scattered* downwelling radiation; i.e., that reflected radiation originating from zenith angles deviating greatly from the viewing angle θ. However, the results of those that did explicitly consider this contribution, most notably Stogryn (1967), Hollinger (1971), Wentz

(1983) and Guissard and Sobieski (1987), suggest that the non-specular component of reflected radiation is large enough to be considered an important term in the satellite observed brightness temperature.

Formally, the key to both the surface emissivity and the contribution from scattered sky radiation lies in the bidirectional reflectance function $r(\mu, \phi; \mu', \phi')$ since both may be directly computed for a viewing direction (μ, ϕ) via a weighted integral of r over μ' and ϕ' (see chapter 5). In practice, however, even for a single sea state and viewing direction (μ, ϕ) the accurate determination of r over the important range of μ' and ϕ' may be difficult to achieve either theoretically or experimentally. Furthermore, the required numerical integration of r over the entire hemisphere of solid angle is complicated by the very strong peak in the specular direction — one which increasingly approximates a delta function as surface roughness is reduced.

For passive microwave sensing applications, therefore, it has been typical to bypass the determination of r and the subsequent integration over solid angle and, instead, to estimate the emissivity ε directly from observations and/or simple approximate theories. However, this approach does not solve the problem of estimating the diffusely reflected sky radiation; indeed, it is probably partly for this reason that diffuse reflection has often been neglected in the modeling of microwave brightness temperatures seen from space.

As an interim solution to the problems described, we present a geometric optics model which permits a comparatively simple approximate treatment of the radiative properties of the sea surface, given an arbitrary statistical distribution of surface slopes. The derivation of the present model appears to follow a general line of physical reasoning first outlined in extremely abbreviated form by Wilheit (1979b); because of the lack of computational specifics in that paper, we have as yet been unable to ascertain the degree of correspondence between the Wilheit model and our own. Whereas Wilheit apparently used his model only to calculate

rough-surface emissivity, our model is used here to compute not only emissivity but diffuse reflection as well, and we fit simple mathematical functions to the numerical results obtained for a wide range of surface temperature, slope variance, and atmospheric opacity.

a. Rough Surface Emissivity

One of the earliest and most widely cited theoretical calculations of microwave emission and scattering from a wind-roughened sea surface is that of Stogryn (1967). He employed the "Kirchhoff approximation for scattering from a finitely conducting rough surface" to derive expressions for the bidirectional reflectance of the ocean surface, based on the Gaussian surface slope distribution found by Cox and Munk (1954). Stogryn invoked two assumptions which, together, would appear to be consistent with a geometric optics approximation: namely, that both the mean wave height and the radii of curvature of the sea surface are much greater than the wavelength being observed (Stogryn did not himself use the term geometric optics to characterize his model, though almost all subsequent authors referring to his work do). He then integrated the results over solid angle to derive the thermal emissivity of the roughened sea surface at 19.4 and 35.0 GHz, as well as the contribution of scattered downwelling radiation to the apparent brightness temperature of the sea surface under specific conditions.

The formulation of Stogryn was the theoretical standard against which the empirical results of early workers in this field were evaluated. Some aspects of the model appeared to be confirmed by the data, for example the much stronger wind speed sensitivity of the horizontally polarized brightness temperature compared to the vertically polarized brightness temperature. There were also, however, a number of significant disagreements; for example, the data of Hollinger (1971) indicated greater sensitivity to wind speed at higher frequencies than at lower frequencies, whereas the Stogryn model showed little change of sensitivity with frequency;

also, the observations of Nordberg et al. (1971) showed a much higher than expected brightness temperature sensitivity to wind-induced roughness viewed at near-nadir angles. The first discrepancy appears to relate to the validity of the geometric optics assumption, as the agreement between theory and measurement improves with decreasing wavelength; the second has been attributed to the fact that the Stogryn formulation considered only the effects of large-scale geometry and ignored emissivity increases due to foam and spray.

As the first satellite-borne microwave radiometers went into operation, more accurate sea surface emissivity formulations were needed in order to provide a solid theoretical basis for the remote sensing of sea surface wind speed and temperature under varied conditions, using the available sensor frequencies. Wilheit (1979b), for example, discusses a model intended for use in the frequency range 6.6–37 GHz in support of algorithm development for the Nimbus-7 and Seasat SMMR's. Like Stogryn, Wilheit also resorted to a geometric optics approximation but pointed out that it is unnecessary to derive and integrate over solid angle expressions for the bidirectional reflectance when calculating the sea surface emissivity; instead "one simply averages the Fresnel relations over the distribution of surface slopes, taking care to treat polarization properly and to account for the projection of the facet in the view direction."

Wilheit introduced two refinements intended to improve the agreement between his geometric optics model and existing measurements. The first refinement entailed the explicit inclusion of a foam contribution to the surface emissivity. Secondly, he pointed out that the Cox and Munk (1954) slope variances, which were obtained using visible-light observations of sea surface sun glitter patterns, appeared to overestimate the *effective* slope variance for the lower microwave frequencies. This conclusion is quite plausible, since a significant portion of the true slope distribution is due to short-wavelength, small-amplitude components of the

surface height spectrum which might be expected to have little impact on the radiative characteristics of the surface at the longer microwave wavelengths. Wilheit therefore proposed the use of the Cox and Munk (1954) slope variances for frequencies greater than 35 GHz, and reduced the variance by a factor proportional to frequency below this value.

As noted earlier, Wilheit (1979b) provided neither the computational details of his geometric optics model nor any quantitative results which could be directly utilized by others in radiative transfer calculations. Furthermore, he does not appear to have taken advantage of the opportunity provided by his model to evaluate the surface brightness contribution by diffusely reflected sky radiation. In the following, therefore, we derive a geometric optics model and we use the results of this model to parameterize both roughness-induced emission changes and changes in diffuse reflection in terms of effective slope variance, viewing angle, and sea surface temperature for each SSM/I frequency.

We begin by considering radiation emitted from the ocean surface in the direction described by the unit vector $-\hat{\mathbf{k}}_0$, where $\hat{\mathbf{k}}_0$ is the viewing direction towards the surface from the satellite. That is,

$$\hat{\mathbf{k}}_0 = (\sin\theta\cos\phi, \sin\theta\sin\phi, -\cos\theta), \tag{7.3}$$

where θ is the satellite nadir angle and ϕ is the azimuthal viewing angle relative to the downwind direction $\hat{\mathbf{x}}$ (the crosswind and vertical directions correspond to unit vectors $\hat{\mathbf{y}}$ and $\hat{\mathbf{z}}$, respectively).

The observed radiation consists of horizontally polarized and vertically polarized components, as determined by the projection of the electric field vector on the unit vectors $\hat{\mathbf{h}}$ and $\hat{\mathbf{v}}$, respectively. These are defined here as

$$\hat{\mathbf{h}} = \frac{\hat{\mathbf{z}} \times \hat{\mathbf{k}}_0}{|\hat{\mathbf{z}} \times \hat{\mathbf{k}}_0|} \tag{7.4}$$

and

$$\hat{\mathbf{v}} = \frac{\hat{\mathbf{k}}_0 \times \hat{\mathbf{h}}}{|\hat{\mathbf{k}}_0 \times \hat{\mathbf{h}}|}, \tag{7.5}$$

so that $\hat{\mathbf{h}}$ is both horizontal and normal to $\hat{\mathbf{k}}_0$, and $\hat{\mathbf{v}}$ is normal to both $\hat{\mathbf{k}}_0$ and $\hat{\mathbf{h}}$.

The unit vector $\hat{\mathbf{n}}$ which is locally normal to the sea surface is determined by the x- and y-components of the sea surface slope at that location:

$$\hat{\mathbf{n}} = \frac{(-s_x, -s_y, 1)}{\sqrt{{s_x}^2 + {s_y}^2 + 1}}, \tag{7.6}$$

where

$$s_x = \frac{\partial \eta}{\partial x}, \tag{7.7}$$

$$s_y = \frac{\partial \eta}{\partial y}, \tag{7.8}$$

and η is the local height of the sea surface.

In the geometric optics approximation, the apparent vertical and horizontal emissivities $\varepsilon_V{}'$ and $\varepsilon_H{}'$, as seen by the satellite sensor, are then given by the horizontally and vertically polarized Fresnel emissivities E_V and E_H at the local angle of incidence θ_l, rotated from the local frame of reference into the satellite frame of reference:

$$\varepsilon_H{}' = c_p E_H(\theta_l) + c_s E_V(\theta_l), \tag{7.9}$$

$$\varepsilon_V{}' = c_s E_H(\theta_l) + c_p E_V(\theta_l), \tag{7.10}$$

where

$$\theta_l = \cos^{-1}(-\hat{\mathbf{k}}_0 \cdot \hat{\mathbf{n}}), \tag{7.11}$$

$$c_p = |\hat{\mathbf{h}} \cdot \hat{\mathbf{h}}'|^2, \tag{7.12}$$

$$c_s = 1 - c_p, \tag{7.13}$$

$$\hat{\mathbf{h}}' = \frac{\hat{\mathbf{n}} \times \hat{\mathbf{k}}_0}{|\hat{\mathbf{n}} \times \hat{\mathbf{k}}_0|} \tag{7.14}$$

In the above, $\hat{\mathbf{h}}'$ is analogous to $\hat{\mathbf{h}}$, but is the horizontal unit vector in a frame of reference having $\hat{\mathbf{n}}$ as the local vertical. Both $\hat{\mathbf{h}}'$ and $\hat{\mathbf{h}}$ are perpendicular to $\hat{\mathbf{k}}_0$, so (7.12) gives the cosine-squared of the angle of rotation (viewed along $\hat{\mathbf{k}}_0$) between the satellite and local coordinate systems. Accordingly, (7.13) gives the sine-squared of the same angle.

With the above definitions, it is then straightforward to calculate the effective emissivity ε_r of the roughened surface for each polarization by integrating (7.9) and (7.10) over all slopes s_x and s_y, weighted by the probability density $\rho_s(s_x, s_y)$ of those slopes and by a factor $w(s_x, s_y)$ which is related to the viewing geometry:

$$\varepsilon_{rp} = \frac{\int_{-\infty}^{+\infty}\int_{-\infty}^{+\infty} \varepsilon'_p \rho_s w \; ds_x \; ds_y}{\int_{-\infty}^{+\infty}\int_{-\infty}^{+\infty} \rho_s w \; ds_x \; ds_y}. \tag{7.15}$$

The geometric factor w must account for both the reduction in solid angle subtended by a sea surface element viewed at an oblique angle and the fact that probability density ρ_s gives the distribution of slopes referenced to the horizontal projection of each surface element, rather than giving the desired surface *area* distribution as a function of slope. Additionally, w must be set equal to zero when surface elements are viewed from the wrong side. Accordingly,

$$w = \begin{cases} \dfrac{-\hat{\mathbf{n}} \cdot \hat{\mathbf{k}}_0}{n_z}, & \text{for } \hat{\mathbf{n}} \cdot \hat{\mathbf{k}}_0 < 0 \\ 0, & \text{for } \hat{\mathbf{n}} \cdot \hat{\mathbf{k}}_0 \geq 0 \end{cases}, \tag{7.16}$$

where n_z is the z-component of $\hat{\mathbf{n}}$. Note that in the special case that the ocean surface is viewed vertically from above, $w \equiv 1$. Note also that shadowing (i.e., nearby wave surfaces obscuring more distant surfaces) has been ignored here, as its effect on w is both difficult to compute and is probably inconsequential at the SSM/I viewing angle of 53°.

We must consider one additional complication which arises from the fact that, under certain conditions, the apparent emissivity of a facet is due not only to the

intrinsic emissivity of the surface at that point but also to reflected emission from other facets. This situation is best examined by considering radiation traveling in the reverse direction, that is, downward along the viewing path in direction $\hat{\mathbf{k}}_0$. The unit vector giving the direction of the reflected radiation is

$$\hat{\mathbf{k}}_s = -2(\hat{\mathbf{n}} \cdot \hat{\mathbf{k}}_0)\hat{\mathbf{n}} + \hat{\mathbf{k}}_0. \tag{7.17}$$

When the z-component $k_{s,z}$ of this vector is negative, then the scattered ray is downward directed and will encounter the water surface a second time. The total fraction of the original ray which escapes being absorbed is simply the product of the two reflectivities r_1 and r_2, where $r_i \equiv (1 - \varepsilon_i)$. Thus, the combined effective emittance is

$$\varepsilon' = 1 - (1 - \varepsilon_1)(1 - \varepsilon_2), \tag{7.18}$$

where ε_1 is the emissivity of the first facet encountered and is given by (7.9) or (7.10), and ε_2 is the emittance of the second facet and is obtained here by computing the polarization of the reflected ray after the first reflection and then assuming a simple horizontally oriented plane-surface for the second reflection. Although the latter assumption is crude, it provides qualitatively reasonable conditions for the second reflection and eliminates the necessity of considering higher-order multiple reflection. In any case, numerical experiments using the above scheme confirmed that the contribution by multiple-reflected radiation is exceedingly small for the SSM/I viewing angle of 53°, so that a more rigorous approach to multiple reflection seems unwarranted.

The one factor in (7.15) which remains to be specified before we can proceed with numerical calculations is the slope distribution $\rho_s(s_x, s_y)$. Following Cox and Munk (1954), whose conclusions were based on sun-glitter pattern observations, ρ_s is generally assumed to be well approximated by a bivariate Gaussian distribution, with downwind and crosswind slope variances g_x^2 and g_y^2, each linearly related to surface wind speed U. However, it has become standard in the microwave sensing

literature to ignore the directional dependence of the slope variance and to specify a single slope variance $g^2 = g_x^2 + g_y^2$ so that

$$\rho_s(s_x, s_y) \approx \frac{1}{\pi g^2} \exp\left[-\frac{s_x^2 + s_y^2}{g^2}\right]. \tag{7.19}$$

The introduction of this simplification was first justified by Wu and Fung (1972) on the basis of an observed directional insensitivity of emissions from the sea, as communicated to them privately by J.P. Hollinger. The figures of Stogryn (1967) indicate that the difference between cross-wind and upwind brightness temperature is in fact $\lesssim 2$ K for wind speeds less than 14 m s^{-1} and $\theta = 50°$. Wilheit (1979b) concluded from his own model results that no more than a 2 m s^{-1} error in retrieved wind speed should result from ignoring the effects of anisotropy in the surface emissivity.

Here, we shall conform to precedent and adopt the assumption of a direction-independent, Gaussian slope distribution, as described above. An immediate consequence of this assumption is that the bidirectional reflectance function r depends on μ, μ', and $\phi - \phi'$ only, and the rough surface emissivity ε_r depends only on μ. We also postpone consideration of the relationship between the effective slope variance g^2 and surface wind speed U until a later chapter, leaving g^2 as the independent variable in our model results for the time being.

For each specified surface slope variance g^2, numerical integrations of (7.15) were carried out for a range of values of sea surface temperature T_S (275, 285, 295, and 305 K) and viewing angle θ (50°, 53°, 56°). Specific values of g^2 corresponded to 8 nominal wind speeds (0.2, 2.0, 6.0, 10.0, 14.0, 20.0, 30.0, and 40.0 m s^{-1}) substituted into Wilheit's (1979b) frequency dependent adaptation of the Cox and Munk relationship between g^2 and U. Thus, 96 integrations were performed for each of the four SSM/I frequencies.

The computed rough-surface emissivities were expressed as deviations $\Delta\varepsilon_r$ from the Fresnel emissivity for the same parameter values. Standard multiple

Table 7.1: Coefficients for rough ocean surface emissivity model (Eq. 7.20)

ν(GHz)	Pol.	C_1	C_2	C_3	C_4
19.35	V	−0.556+0	0.357+0	−0.312−1	0.106−1
19.35	H	0.406+0	−0.108+0	0.128−1	0.153−2
22.235	V	−0.670+0	0.455+0	−0.446−1	0.232−1
22.235	H	0.479+0	−0.175+0	0.283−1	−0.131−1
37.0	V	−0.811+0	0.551+0	−0.365−1	0.149−1
37.0	H	0.473+0	−0.160+0	0.312−1	−0.150−1
85.5	V	−0.723+0	0.404+0	−0.735−2	−0.126−1
85.5	H	0.358+0	−0.351−1	0.309−1	−0.121−1

linear regression was then used to fit the following model to the numerical results obtained for each SSM/I channel:

$$\Delta\varepsilon_r \approx g^2 \left[C_1 + C_2 \left(\frac{T_S}{273} \right) + C_3(\theta - 53.0) + C_4(\theta - 53.0) \left(\frac{T_S}{273} \right) \right]. \qquad (7.20)$$

The coefficients C_n for each channel are given in Table 7.1. Maximum absolute errors of the fit occurred for the highest values of g^2 ($\sim$0.2), and ranged from 2×10^{-3} at 19 GHz to 6×10^{-3} at 85 GHz, corresponding to maximum errors in sea surface brightness temperature of $\lesssim 1$ K

Based on these numerical computations, we find that an increase in effective slope variance g^2 leads to a moderate increase in emissivity for horizontally polarized channels and a slightly weaker *decrease* for vertically polarized channels.

b. Rough Surface reflection/scattering

Having considered the effect of roughness on the sea surface emissivity, we now turn to the effects of roughness on the sky emission reflected at the the surface. Again neglecting any azimuthal anisotropy, this contribution may be expressed as

$$T_B^S(\mu) = \frac{1}{\pi} \int_0^{2\pi} \int_0^1 r_p(\mu, 0; \mu', \phi') \mu' T_B{}^{\downarrow}(\mu') \, d\mu' \, d\phi' \tag{7.21}$$

so that the satellite observed brightness temperature (5.10) may be rewritten

$$T_B(\mu) = T_B{}^{\uparrow}(\mu) + \tau(0; \infty) \left[\varepsilon_p(\mu) T_S + T_B^S(\mu) \right], \tag{7.22}$$

Several approaches to dealing with diffusely reflected surface radiation in microwave brightness temperature models have been taken in the past. As already noted, the great majority of the more widely cited passive microwave sensing papers to date appear to have completely ignored diffuse reflection; that is, surface roughness was allowed to modify the sea surface emissivity as described in the previous subsection, but reflected radiation was often assumed to be given by an expression analogous to that for specular reflection; i.e., $T_B^S \approx [1 - \varepsilon_r(\theta)] T_B{}^{\downarrow}(\theta)$.

Certain authors attempted to refine their treatment of diffuse reflection by taking the ocean surface to be a Lambertian rather than a specular reflector, an assumption which in turn was interpreted as requiring that "all of the down-welling radiation is assumed to come from a constant zenith angle of 45°, irrespective of the viewing angle θ" (Milman, 1987, see also Wilheit and Fowler, 1977). Quite apart from the validity of this particular interpretation of Lambertian reflection, it seems doubtful whether Lambertian reflection (implying angle-independent or "perfectly diffuse" scattering from the surface) is likely to offer any better representation of the surface boundary condition than the opposite extreme of perfectly specular reflection.

Finally, Wentz (1983) explicitly parameterized the increase in reflected radiation due to roughening by assuming that the downwelling component of radiation

arrives from the specular direction but using a modified surface reflection coefficient given by $r_p = (1 + \omega_p U)(1 - \varepsilon_p)$. That is, the effective reflectance of the roughened surface was taken to be the specular reflectance plus a term which was proportional to wind speed U (actually, friction velocity u_* was used in Wentz' original formulation). The constant of proportionality ω was determined for each channel of the SMMR by way of a least-squares fit to numerical calculations of surface scattering for a wide range of atmospheric and surface conditions.

Although the Wentz (1983) model was the first to offer a quantitative parameterization of the contribution by non-specular reflection for passive microwave applications, there remained minor problems. Most importantly, Guissard and Sobieski (1987) have pointed out that the Wentz model neglected the dependence of ω on atmospheric transmittance. Atmospheric transmittance, of course, largely determines the angular distribution of atmospheric radiances; the angular distribution, weighted by the bidirectional reflectance function r, in turn determines the net intensity of scattered radiation at the surface.

In the following, we propose an alternative means of parameterizing non-specular reflection from the ocean surface which accounts for changes in atmospheric transmittance. Instead of the modified specular reflectivity employed by Wentz (1983), we assume an effective surface reflectivity equal to one minus the wind roughened emissivity, but allow the *effective zenith angle of the reflected sky emission to deviate from the specular zenith angle* θ. This is accomplished simply by defining an effective zenith angle θ' such that

$$T_B{}^{\downarrow}(\theta') = \frac{T_B^S}{1 - \varepsilon_{r,p}}, \tag{7.23}$$

where $\varepsilon_{r,p}$ is the rough surface emissivity at polarization p as computed in the previous subsection, and T_B^S is the reflected component of the upwelling radiation at the surface, corresponding to (7.21).

Numerical computation of T_B^S using the geometric optics assumption was accomplished in a manner analogous to the rough surface emissivity calculations described above. As already noted in chapter 5, the problem is rendered simpler by the fact that atmospheric emission is unpolarized; therefore, we need only integrate (over the distribution of slopes) the local reflectivities multiplied by the atmospheric brightness temperature in the direction from which the ray corresponding to a given surface element is scattered toward the satellite sensor:

$$T_B^S = \frac{\int_{-\infty}^{+\infty}\int_{-\infty}^{+\infty} T_B(-\hat{\mathbf{k}}_s)(1-\varepsilon_p')\rho_s w \, ds_x \, ds_y}{\int_{-\infty}^{+\infty}\int_{-\infty}^{+\infty} \rho_s w \, ds_x \, ds_y}. \tag{7.24}$$

The indicated integration was performed for the same combinations of values of θ, T_S, and g^2 as for the ε_r calculations. Since reflected radiation from the surface also depends on the intensity and angular distribution of downwelling atmospheric radiation, seven different values of optical depth σ (corresponding to values of V ranging from 0 to 60 kg m^{-2}) and four values of absorption scale height (0.5, 1.0, 2.0, and 3.0 km) were used for each combination of surface variables. The downwelling atmospheric radiance $T_B(-\hat{\mathbf{k}}_s)$ appearing in the integrand of (7.24) was computed using (6.39). Altogether, numerical computations of T_B^S were repeated for a total of 21,504 distinct combinations of surface and atmospheric parameters, frequencies and polarizations, a task which consumed four weeks of CPU time on our Masscomp 5520 computer.

For each combination of parameters, the effective downwelling brightness temperature $T_B{}^{\downarrow}(\theta')$ was determine from T_B^S via (7.23). Fig. 7.2 shows plots of the difference between $T_B{}^{\downarrow}(\theta')$ and $T_B{}^{\downarrow}(\theta)$ as a function of atmospheric optical depth and surface roughness for the two 85.5 GHz channels. Results are qualitatively very similar for all other SSM/I frequencies. (θ' showed only a very weak dependence

on absorption scale height; this dependence is therefore neglected throughout the remainder of this discussion.)

It is apparent that the use of atmospheric radiance from the satellite viewing angle θ as an approximation for the effective atmospheric brightness temperature can lead to errors of order $\sim$10 K for reflected radiation observed in horizontal polarization. For vertical polarization, the potential error is smaller, though not necessarily negligible. Interestingly, for each polarization, there is a value of σ for which the difference is zero, and this value is, unexpectedly, nearly independent of g^2. For vertical polarization this value of σ occurs near 0.4; for horizontal polarization, it is near 1.3 (not visible in Fig. 7.2).

Values of $T_B{}^{\downarrow}(\theta')$ were inverted to obtain θ'. Differences between θ' and the viewing angle of $\theta = 53°$appear in Fig. 7.3. The σ-dependence of the difference vanishes for $g^2 = 0$, as expected for specular reflection, and the g^2-dependence vanishes for a critical value σ_0 of the optical depth, as already pointed out. By trial and error, it was also found that, *for fixed slope variance* g^2, $\log(90° - \theta')$ is nearly linearly dependent on the logarithm of the total atmospheric optical depth. We therefore used multiple linear regression to find coefficients for a model of the form

$$\frac{90° - \theta_0'}{90° - \theta_0} = \exp\left[\sum_{m=1}^{2}\sum_{n=1}^{3} S_{mn}\left[\log_e - c\right]^m \left[g^2\right]^n\right], \tag{7.25}$$

where c was estimated by inspection of the contour plots.

Each point in the regression was weighted by the squared sensitivity of T_B (as seen from space) to errors in θ', in order to ensure that the fit would be best where accurate values are most needed. Plots of this sensitivity appear in Fig. 7.4. For very small atmospheric optical depth σ, the brightness temperature sensitivity is small because of weak total emission from the atmosphere; for large σ, the sensitivity is again small because of the low visibility of the ocean surface. The greatest sensitivity of T_B to errors in θ' is therefore at intermediate opacities, i.e.,

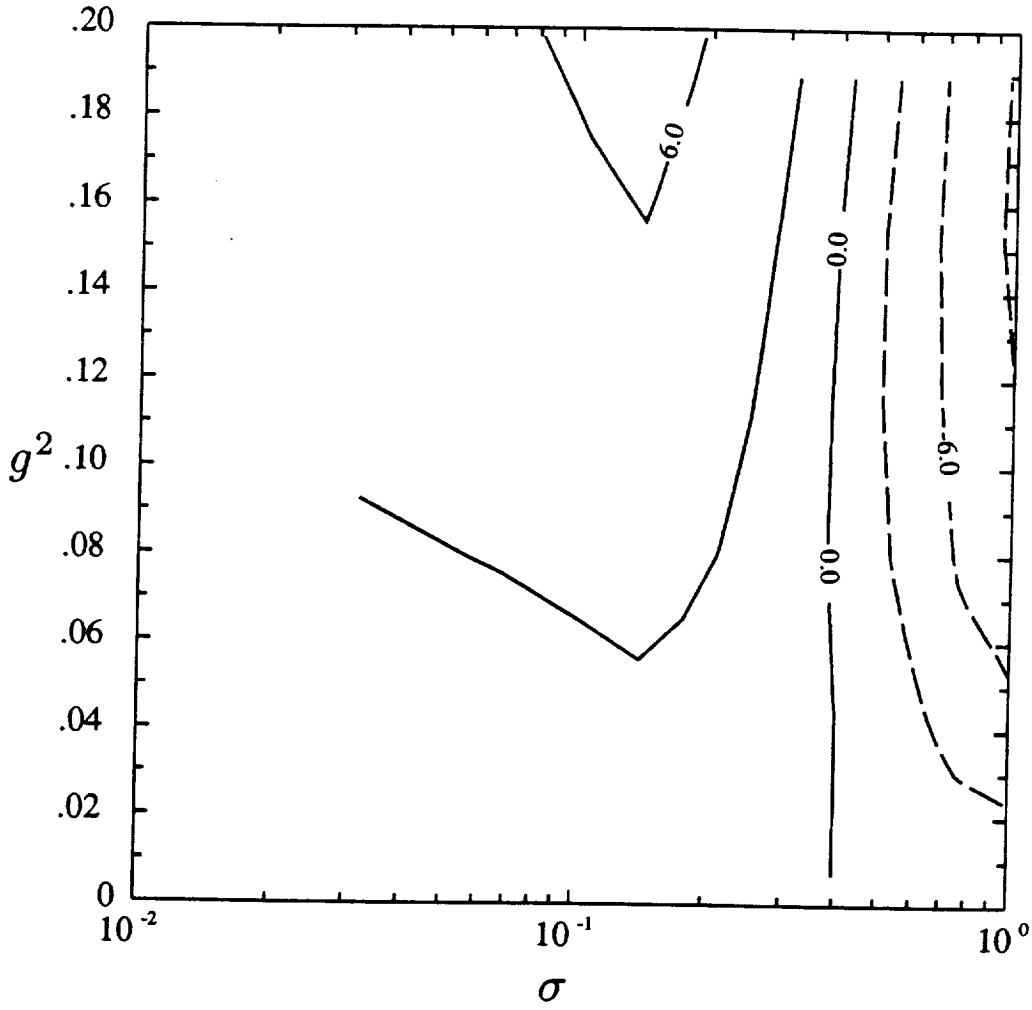

Fig. 7.2 Contour plots of $T_B{}^{\downarrow}(\theta') - T_B{}^{\downarrow}(\theta)$ as functions of atmospheric optical depth σ and surface slope variance g^2. (a) 85.5 GHz, vertical polarization

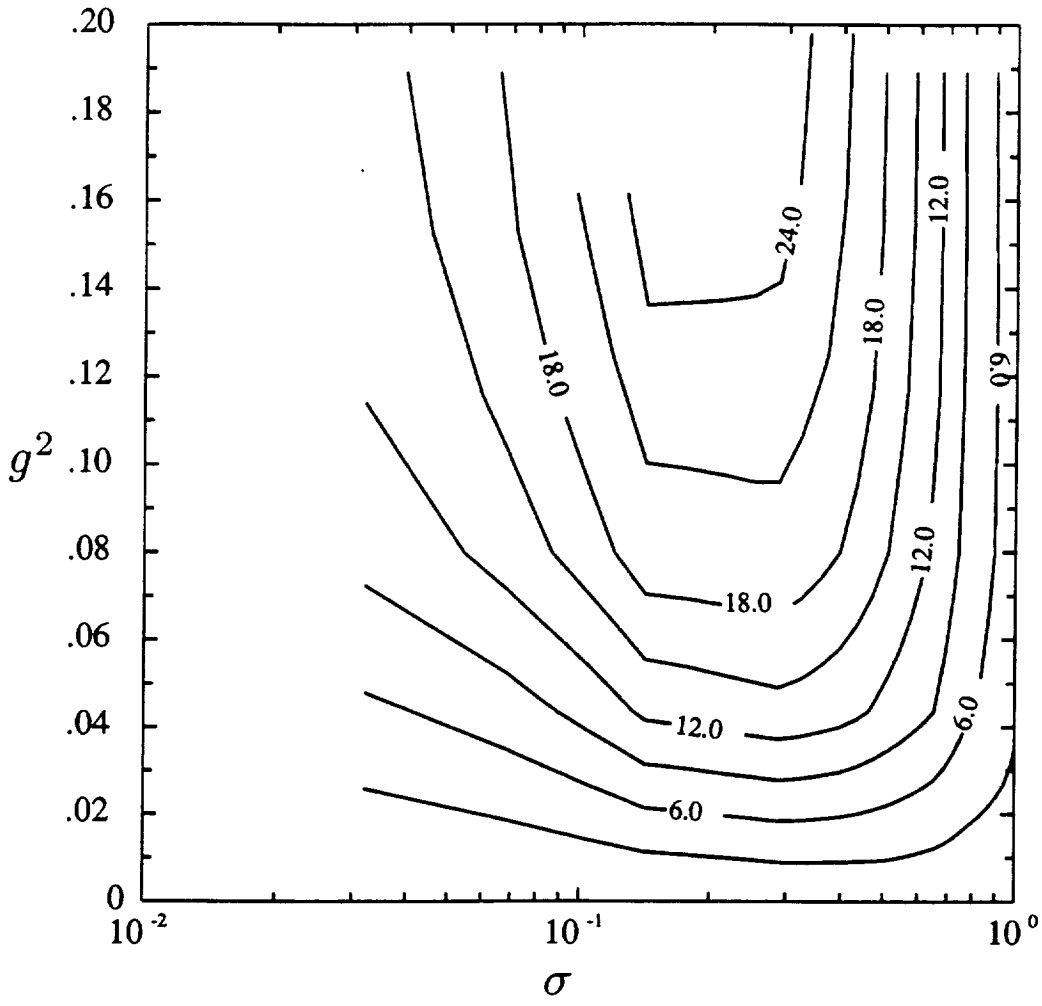

Fig. 7.2 (continued) (b) 85.5 GHz, horizontal polarization

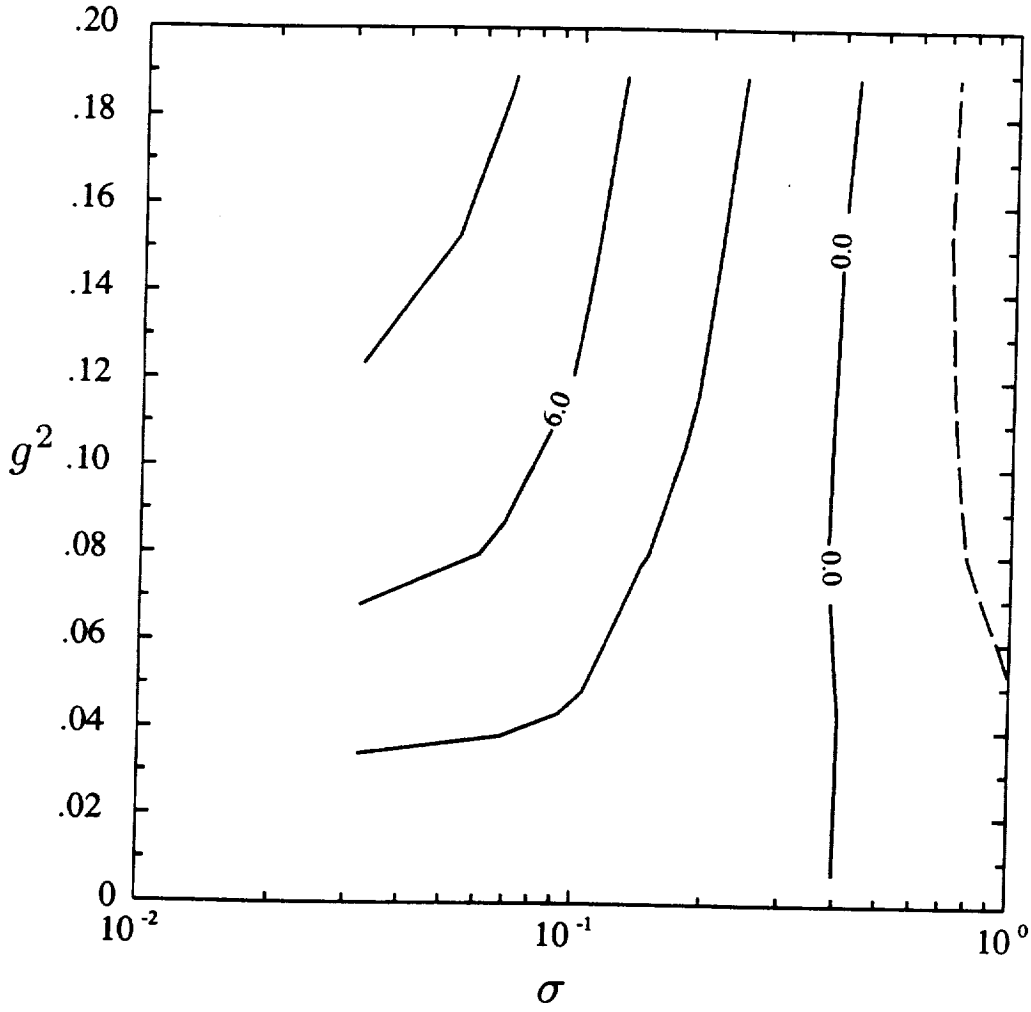

Fig. 7.3 Contour plots of $\theta' - \theta$ as functions of atmospheric optical depth σ and surface slope variance g^2. (a) 85.5 GHz, vertical polarization

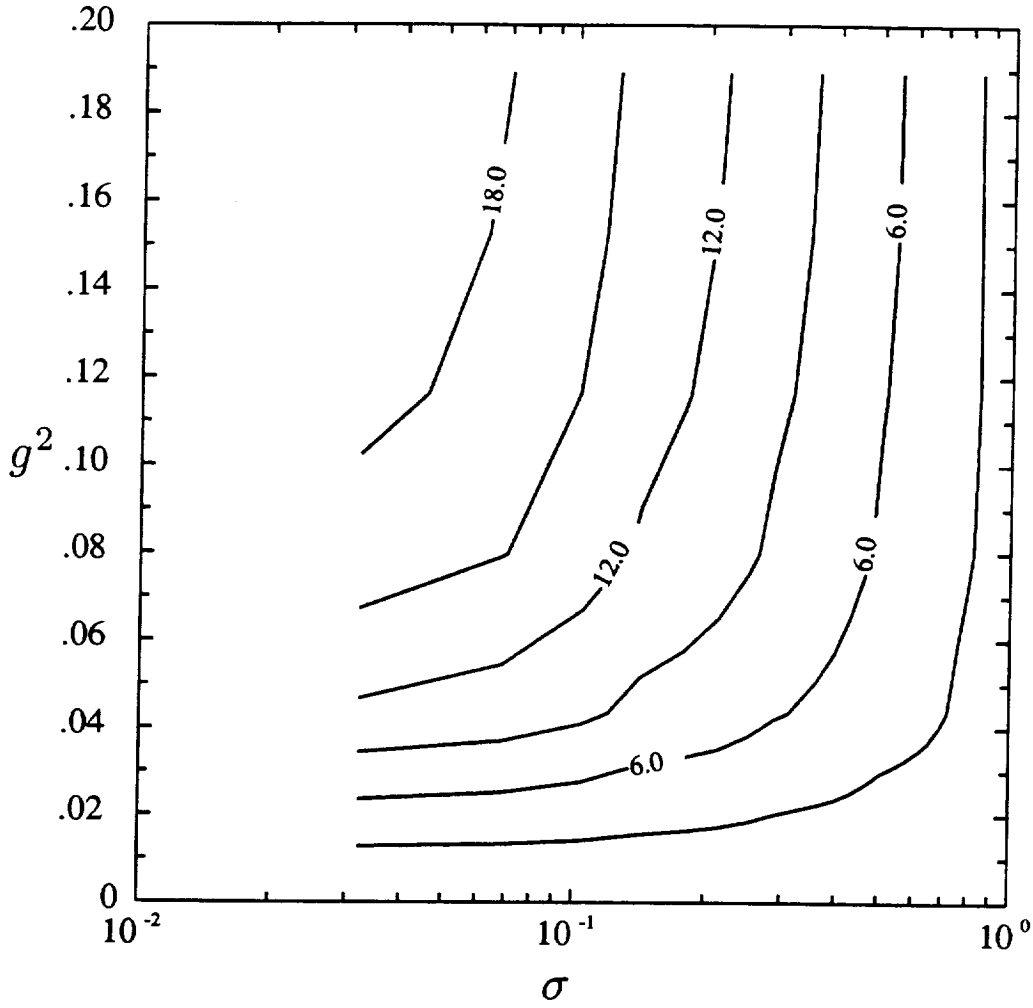

Fig. 7.3 (continued) (b) 85.5 GHz, horizontal polarization

$0.1 \gtrsim \sigma \gtrsim 0.4$, for which it may approach 1.0 K per angular degree for a relatively rough surface viewed in horizontal polarization.

Regression coefficients valid for $\theta = \theta_0 \equiv 53°$ are given in Table 7.2. To test the net accuracy of the complete surface model, which consists of (7.20) and (7.25) combined with the coefficients in Tables 7.1 and 7.2, brightness temperatures observed from space were calculated using both the direct output from the numerical computations for ε_r and θ' and the fitted models (7.20 and 7.25). The differences are plotted for all four SSM/I frequencies and both polarizations in Fig. 7.5. Maximum absolute brightness temperature errors resulting from the use of the fitted models amount to $\lesssim 0.5$ K for all channels.

Lastly, we must consider the effect of minor variations in the viewing angle θ on the effective sky radiation angle θ'. For a calm ocean surface, of course, the two are identical. At larger values of g^2, however, the relationship between the two is found to weaken, consistent with the expectation that quasi-specular reflection will gradually give way to quasi-Lambertian scattering (i.e., θ-independent T_B^S) as the roughness increases indefinitely. Since the viewing angle of the SSM/I is confined to a narrow range, only a small, linear correction to the θ_0' formula obtained for $\theta = 53°$ is necessary to account for other values of θ. This correction is adequately modeled by

$$\Delta\theta' = \begin{cases} (1 - Cg^2)(\theta - 53°), & \text{for } g^2 < 1/C \\ 0, & \text{for } g^2 > 1/C \end{cases} . \tag{7.26}$$

so that

$$\theta' = \theta_0' + \Delta\theta', \tag{7.27}$$

where θ_0' is given by (7.25), and $C \approx 14$ for all frequencies.

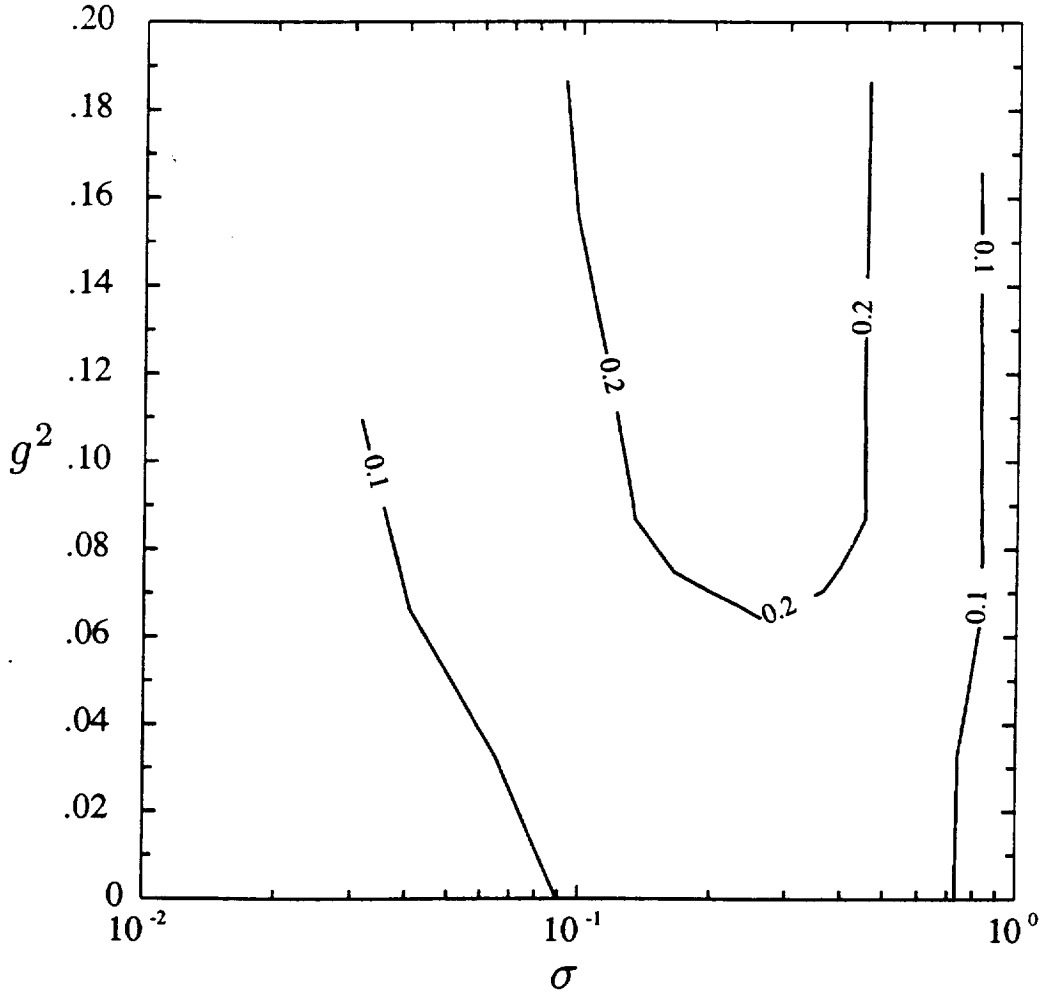

Fig. 7.4 Contour plots of $\partial T_B / \partial \theta'$, i.e., the sensitivity of compute satellite brightness temperatures to errors in θ', as functions of atmospheric optical depth σ and surface slope variance g^2. (a) 85.5 GHz, vertical polarization

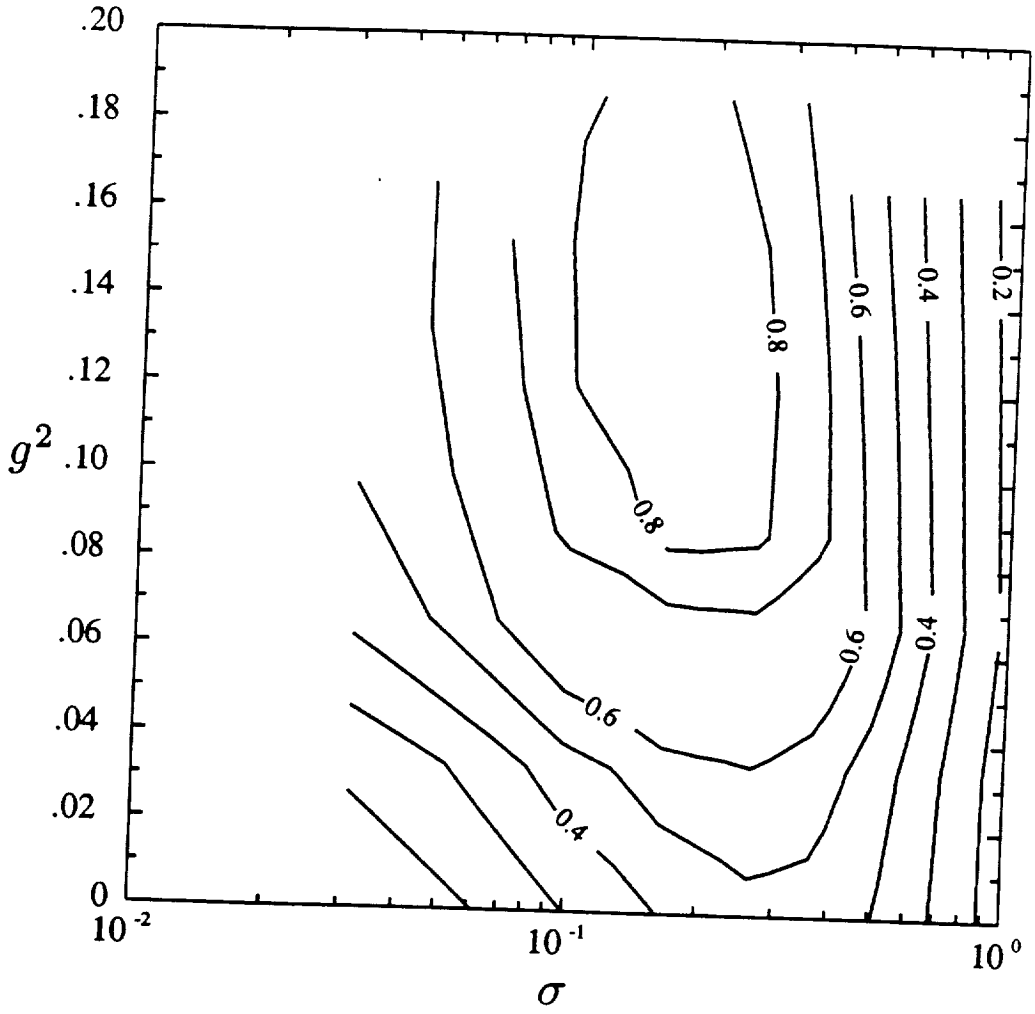

Fig. 7.4 (continued) (b) 85.5 GHz, horizontal polarization

Table 7.2: Coefficients for rough ocean surface scattering model (Eq. 7.25)

ν(GHz)	Pol.	c	S_{11}	S_{21}	S_{12}	S_{22}	S_{13}	S_{23}
19.35	V	−.511	2.62	.402	−23.8	−6.48	69.8	22.5
19.35	H	−.531	2.91	.065	−20.6	−1.91	50.7	7.4
22.235	V	−.511	2.56	.405	−24.0	−7.14	70.1	24.9
22.235	H	−.531	2.77	.008	−19.0	−1.29	44.2	5.0
37.0	V	−.693	2.53	.443	−21.1	−6.70	57.3	21.5
37.0	H	−.182	3.86	.237	−25.7	−3.02	57.1	8.7
85.5	V	−.916	1.75	.270	−10.1	−3.58	26.3	11.6
85.5	H	.300	3.87	.196	−25.4	−2.48	56.8	7.4

c. 'Foam' Effects

In the microwave sensing literature, much attention has been given to parameterizing the effects of the foam patches, breaking waves or whitecaps, spumes, spindrift, and spray etc., all of which are closely linked to wind speed. For the sake of simplicity, the physical distinctions between each of these phenomena have often been ignored, and instead they have come to be collectively referred to in the microwave sensing literature as 'foam', a convention we will follow here as well. A number of studies, both observational and theoretical (e.g., Droppleman 1970, Williams 1971, Rosenkranz and Staelin 1972, Stogryn 1972, Wilheit 1978) have demonstrated that foam has a much higher microwave emissivity than foam-free water surfaces, and the increase of foam coverage (and hence brightness temperature) with wind speed has often assumed a role at least as prominent as that of the

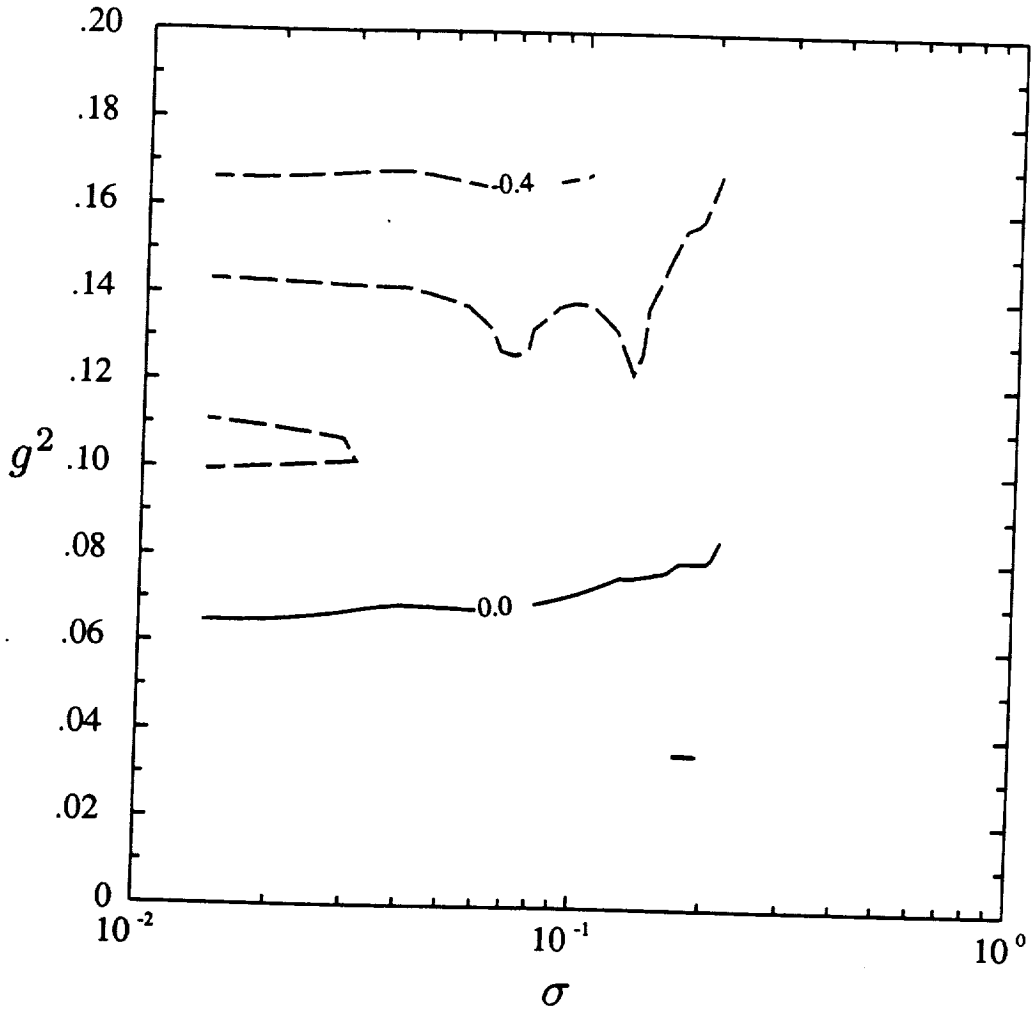

Fig. 7.5 Net satellite brightness temperature error (K) resulting from use of fitted models (7.20) and (7.25) in place of numerical computations of rough surface emissivity/scattering. (a) 19.35 GHz, vertical polarization

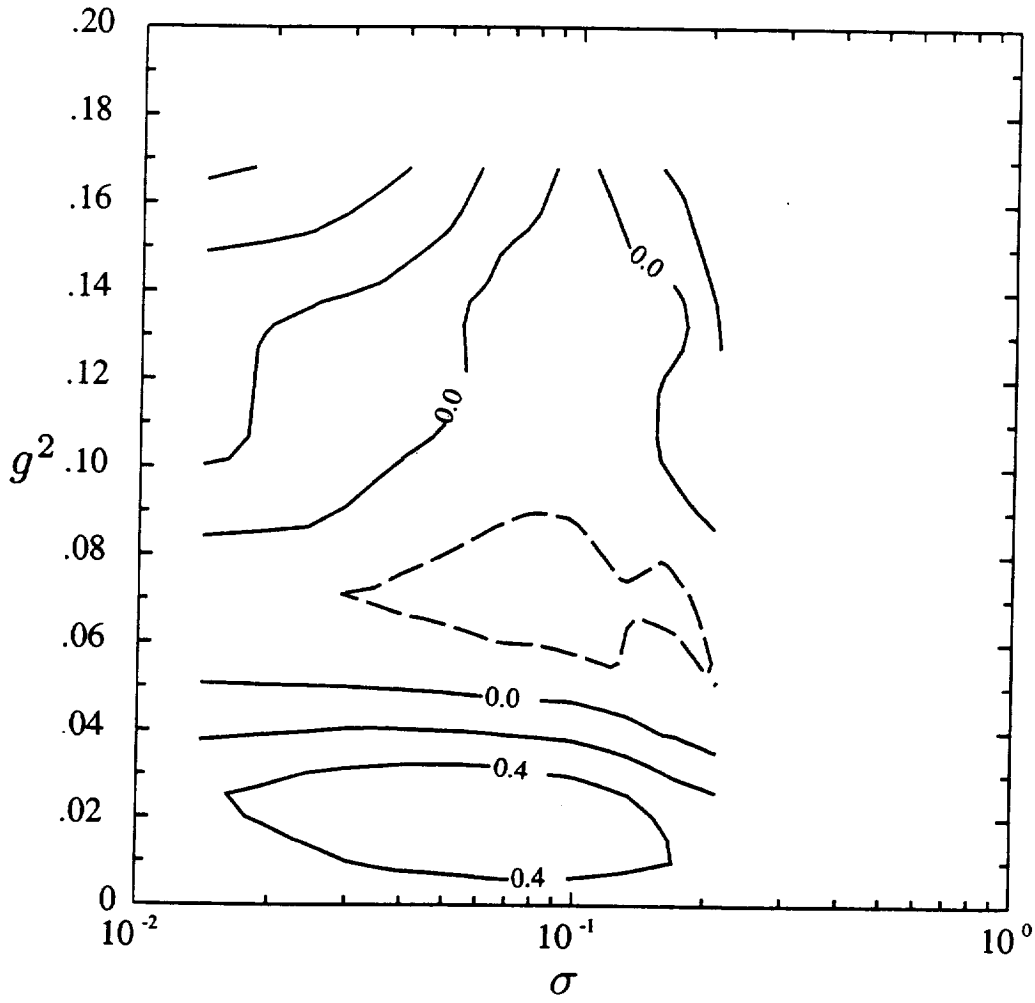

Fig. 7.5 (continued) (b) 19.35 GHz, horizontal polarization

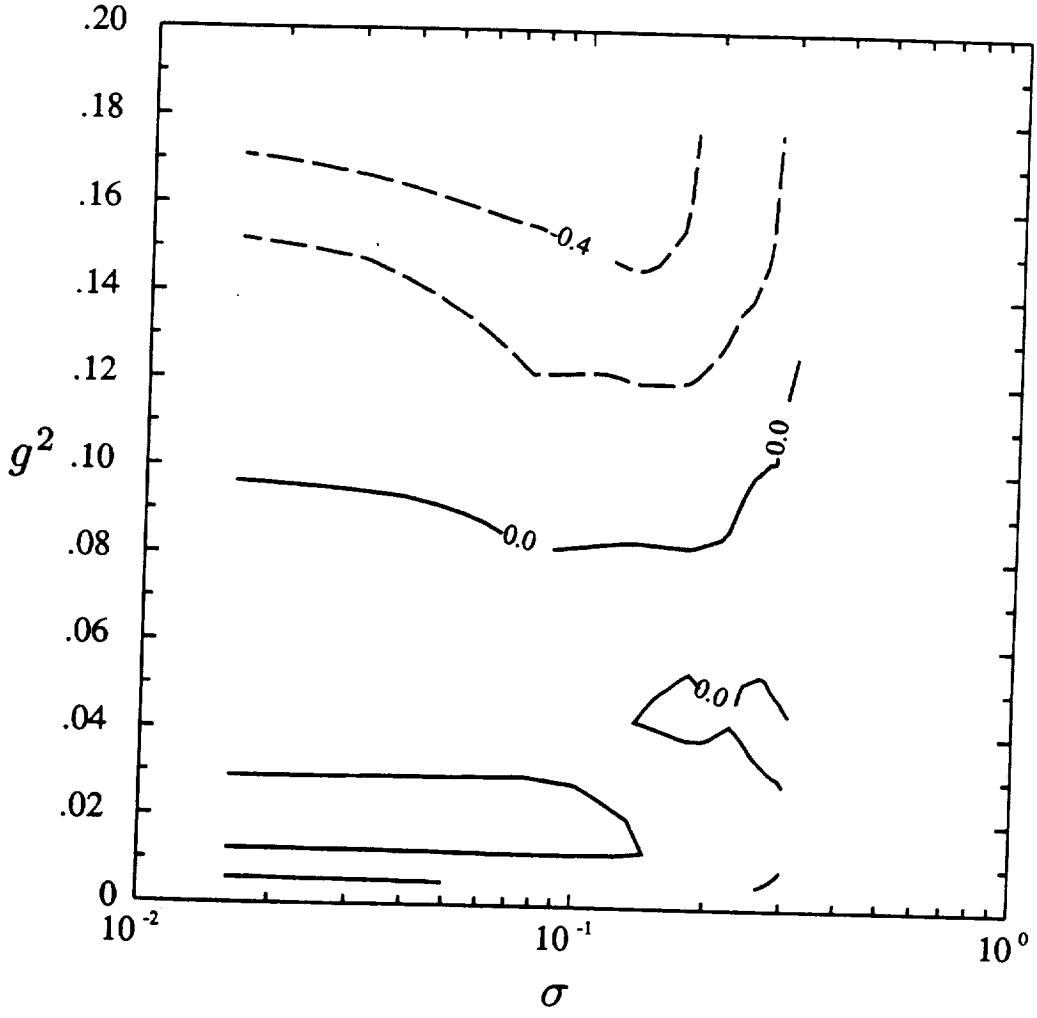

Fig. 7.5 (continued) (c) 22.235 GHz, vertical polarization

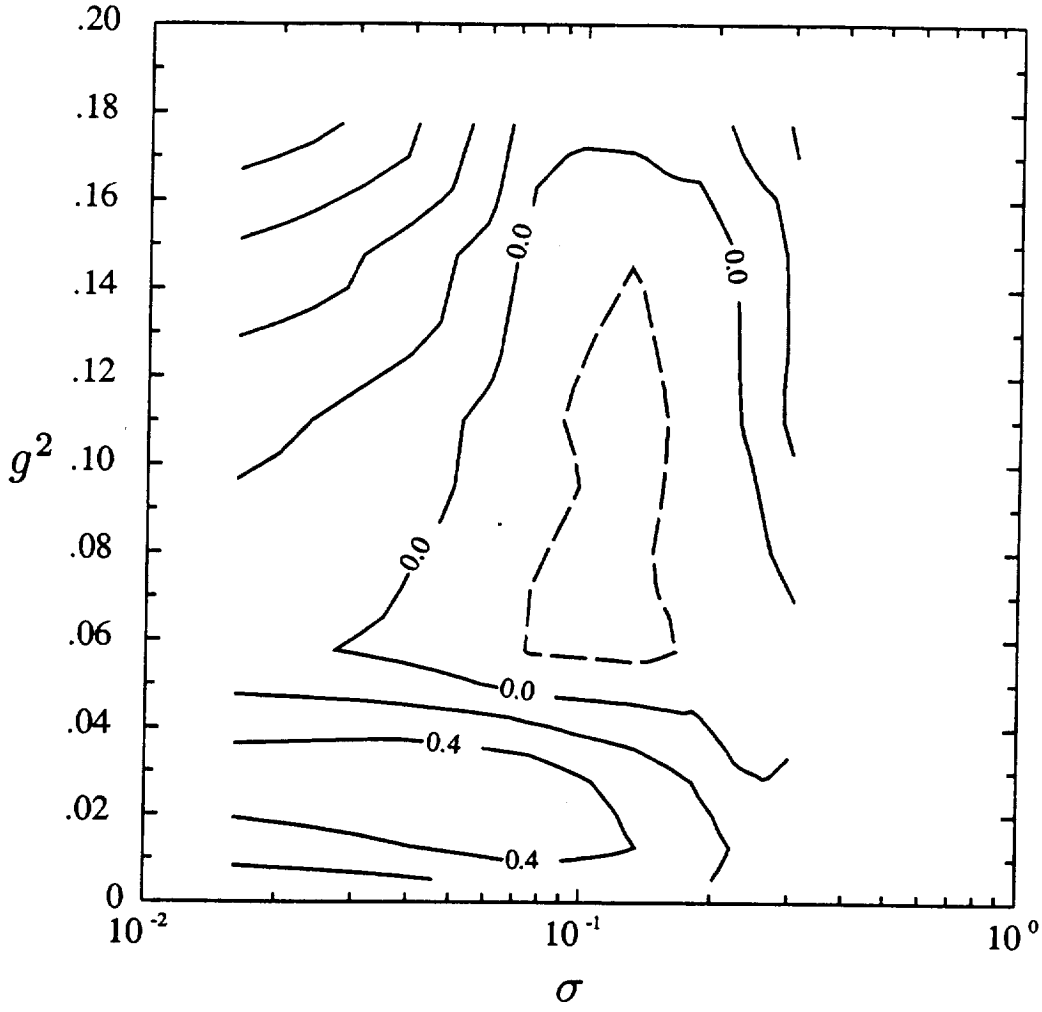

Fig. 7.5 (continued) (d) 22.235 GHz, horizontal polarization

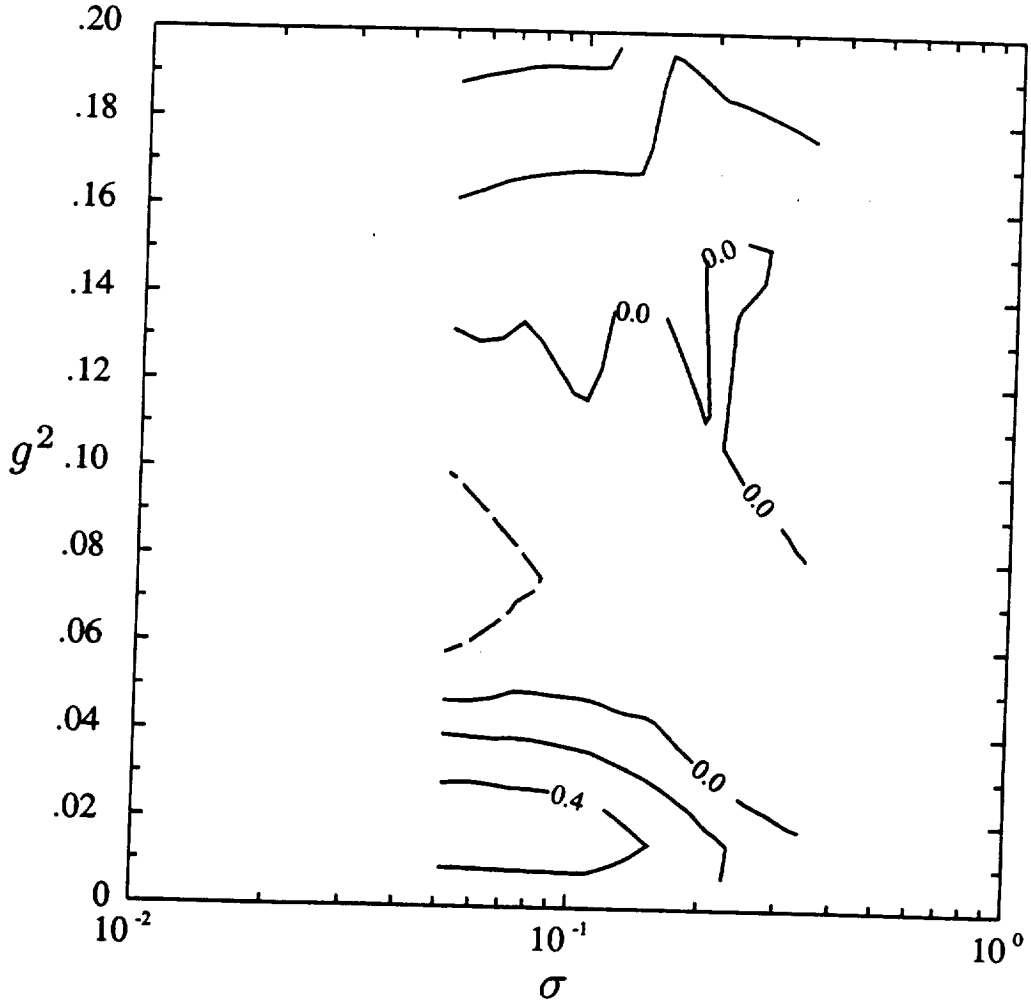

Fig. 7.5 (continued) (e) 37.0 GHz, vertical polarization

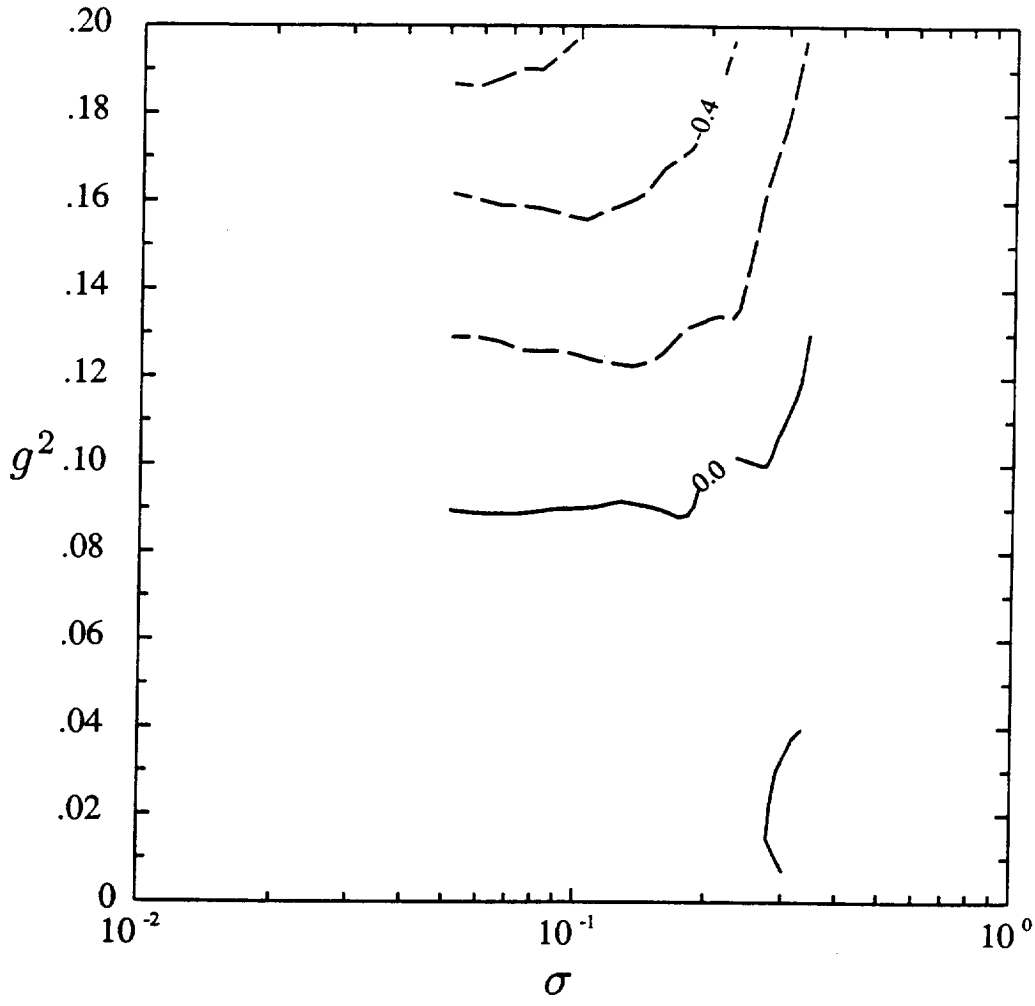

Fig. 7.5 (continued) (f) 37.0 GHz, horizontal polarization

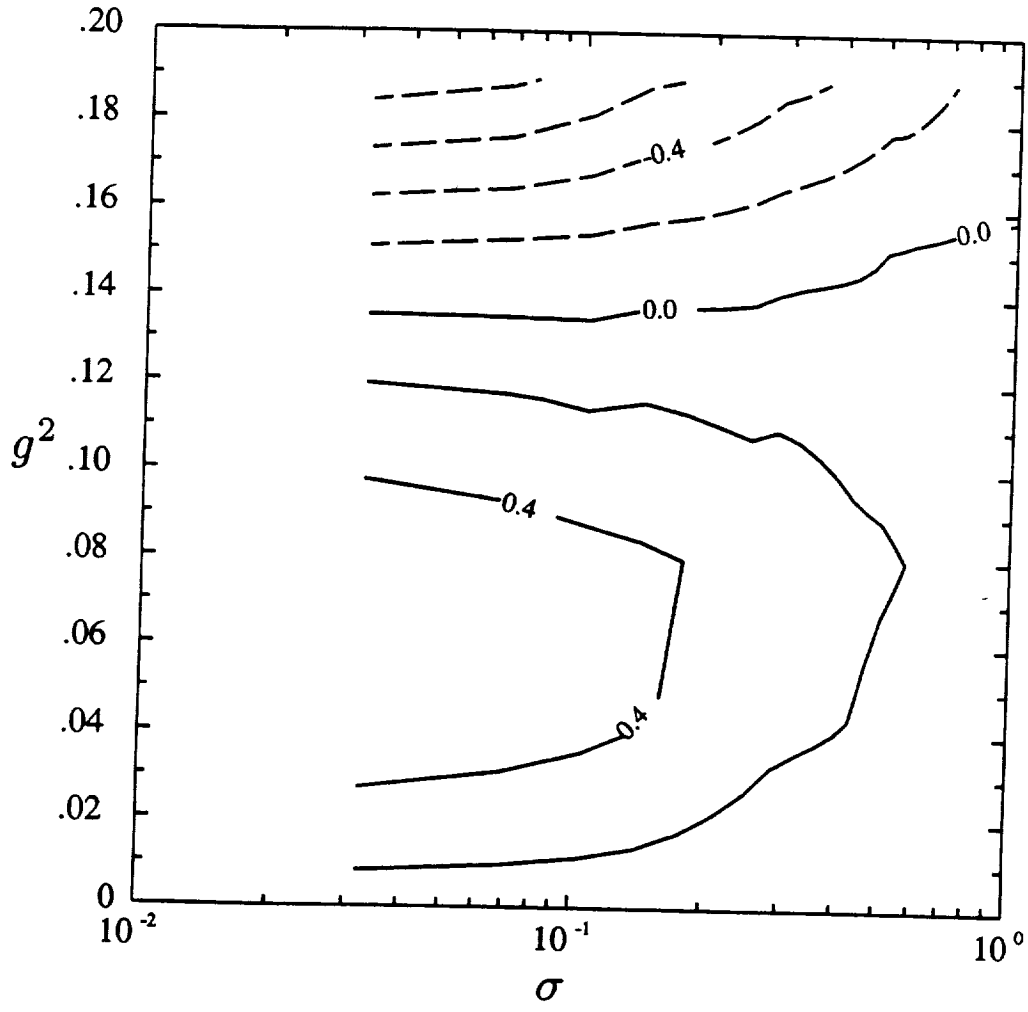

Fig. 7.5 (continued) (g) 85.5 GHz, vertical polarization

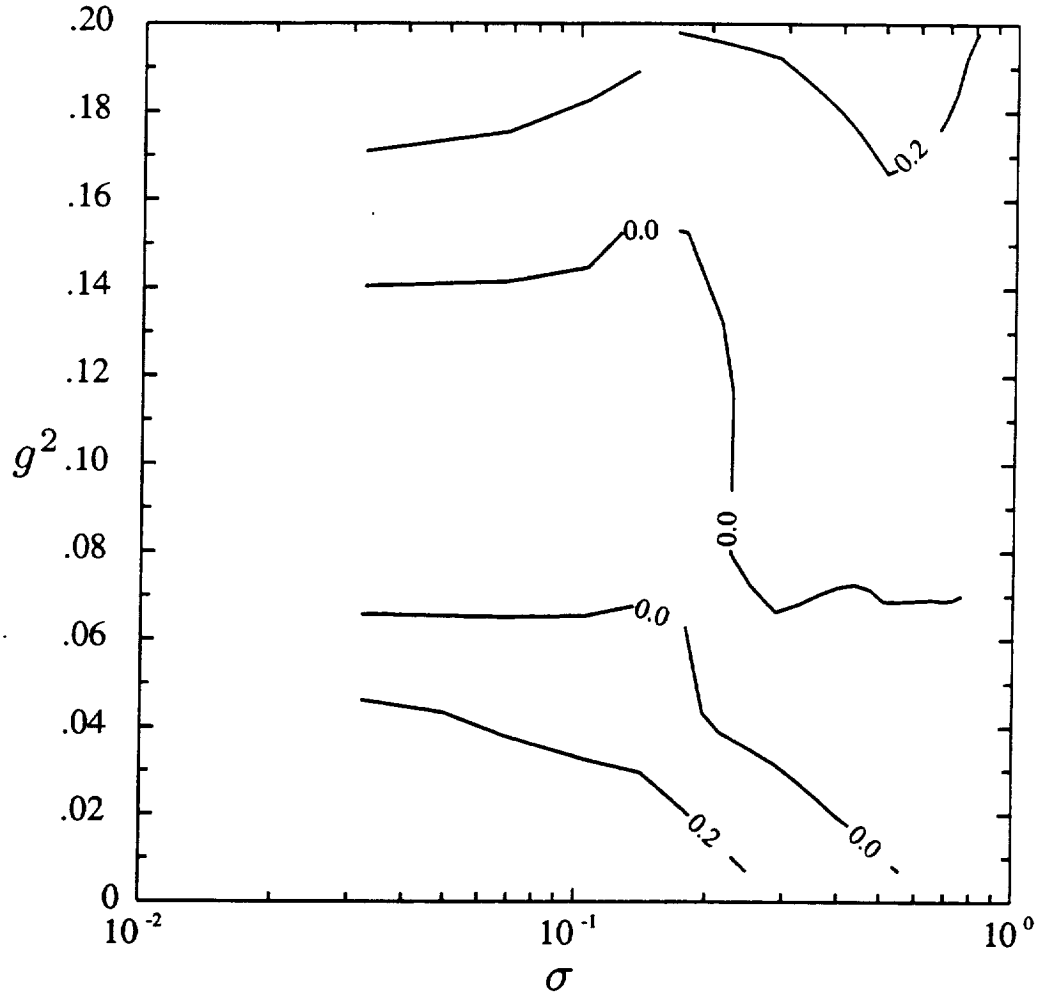

Fig. 7.5 (continued) (h) 85.5 GHz, horizontal polarization

aforementioned rough surface effects in papers proposing microwave radiometric wind speed retrieval techniques.

The simplest model for the brightness temperature effect of foam, and one which we shall adopt as well, is based on the assumption that randomly distributed foam with emissivity ε_f covers a fraction F of the ocean surface (e.g., Wilheit 1979b). Under this assumption, the net sea surface emissivity ε is simply a weighted average of the rough surface emissivity and the foam emissivity:

$$\varepsilon = (1 - F)\varepsilon_r + F\varepsilon_f. \tag{7.27}$$

Given this approach, it is then necessary to establish a reasonable value for ε_f, as well as a functional relationship between F and the near surface wind speed U. Since the definition of fractional coverage by foam is in fact rather arbitrary, it is most convenient to simply specify *a priori* that $\varepsilon_f = 1$ and then concentrate on obtaining a function $F(U)$ (possibly frequency dependent) which correctly predicts observed brightness temperatures.

There has been considerable debate concerning the form of $F(U)$. One approach has been to take F to be zero for $U < 7$ m s^{-1} and to assume a monotonic, or even linear, increase with wind speed for $U > 7$ m s^{-1} (e.g., Wilheit 1979b). This relationship apparently had its roots in the observations of Nordberg et al. (1971), who found that, for nadir viewing, 19 GHz brightness temperatures are approximately independent of wind speed below $\sim$7 m s^{-1} as expected based on Stogryn's (1967) calculations, but increase steadily above this value, a result not predicted by Stogryn. Seeking an explanation for this phenomenon, they cite Monahan (1969) as having found an abrupt increase in whitecap coverage and spray density above 7 m s^{-1} over freshwater lakes.

Since then, a number of more detailed studies have appeared which specifically address the relationship between near surface wind speed and foam coverage (e.g., Ross and Cardone 1974, Wu 1979, Monahan and O'Muircheartaigh 1980) based

on various combinations of theory and observation. Of the studies cited, the latter three support a relationship between whitecap coverage W and wind speed U of the form $W \propto U^{\alpha}$, where the empirically-derived exponent α typically falls between 3.0 and 4.0. It must be pointed out, however, that all of the empirical evidence for such relationships has depended on optical (e.g., photographic) techniques, and it is not at all certain that the foam or whitecap coverage derived in this manner has any direct relevance to apparent fractional foam coverage as measured by a microwave radiometer. Note also that the values of α found in the above studies were determined from data taken at wind speeds generally below 20 m s^{-1} ; at very high wind speeds, the power-law relationships given would seem to predict unrealistically large fractional coverages by whitecaps, exceeding unity in some cases for wind speeds $\gtrsim 40$ m s^{-1} .

In the present study, we take the view that there is, at best, a somewhat tenuous physical correspondence between the actual fraction of the ocean surface which is visibly whitened by "foam" (in the broadest sense defined earlier) and various wind-related surface phenomena which interact with microwave radiation in order to increase the emissivity beyond ε_r. Consequently, we interpret the "foam fraction" F as simply a convenient parameter which describes *all* wind-induced emissivity changes not accounted for by the geometric optics model

As noted earlier, roughness acts to simultaneously depress vertically polarized brightness temperatures and raise horizontally polarized brightness temperatures. "Foam", on the other hand, acts to raise brightness temperatures in both polarizations. Therefore, at a given frequency, a unique combination of F and effective slope variance g^2 can always be found which simultaneously predicts $T_{B,H}$ and $T_{B,V}$. This linear independence of the brightness temperature effects of roughness and foam will be exploited in chapter 8 in order to separately estimate $g^2(U)$ and $F(U)$ from actual SSM/I brightness temperature data.

8. EMPIRICAL CALIBRATION OF THE COMBINED BRIGHTNESS TEMPERATURE MODEL

In Chapter 6, a mathematical model was derived for the atmospheric contributions to microwave brightness temperatures observed from space. An updated version of the theoretical absorption model of Liebe (1985) was used to determine the dependence of model optical parameters on temperature and humidity profiles for each SSM/I frequency. For the sea surface contribution, a geometric optics model was developed in Chapter 7 and used to compute the dependence of emitted and scattered radiation at the surface on the effective surface slope variance, assuming a directionally-independent Gaussian slope distribution and a randomly distributed component of 'foam' with unit emissivity. Both the effective slope variance g^2 and the foam fraction F (both of which may be frequency dependent) are known to be closely related to surface wind speed U, but we have deferred, up to this point, specifying the exact interdependence of these three variables in the present model.

It has already been demonstrated that the atmospheric component of the model performs satisfactorily for predicting *simulated* brightness temperatures obtained via numerical integration of the radiative transfer equation for a wide range of actual atmospheric profiles; moreover, Wilheit (1979b) has demonstrated that a geometric optics approximation of the sea surface appears to provide a reasonable approximation of the effects of wind roughening, especially for higher microwave frequencies. It may therefore be assumed that the model in its present form is already likely to provide an excellent qualitative description of the actual response of the SSM/I to changes in the relevant atmospheric and surface parameters, limited in absolute accuracy mainly by the remaining uncertainties in the values of specific model coefficients.

In order for the model to fulfill its primary intended purpose, that is, the development and validation of multichannel retrieval algorithms, it is essential

that it provide an accurate *quantitative* description of the relationship between input parameters and *observed* brightness temperatures, for the entire range of meteorological conditions which are likely to be encountered.

There are several plausible circumstances under which the model, as described up to this point, might fail to meet this criterion: (i) there could be errors in the calibration of the SSM/I observations or inadequate conversion of SSM/I antenna temperatures to brightness temperatures, so that observed and predicted brightness temperatures do not agree even though the model is correct in all respects; (ii) there could be errors in one or more of the various phenomenological coefficients employed — i.e., gaseous and liquid water absorption coefficients, seawater dielectric constant, etc.; (iii) the geometric optics model for sea surface emission and scattering could be too crude an approximation for the microwave interaction with the sea surface, especially at the longer wavelengths; and finally, (iv) errors might be introduced by certain unmodeled effects — for example, horizontal structure in the cloud liquid water field, surface reflection of solar or galactic radiation, departure of the surface slope distribution from the assumed isotropic Gaussian distribution, etc.

In principle, the more important uncertainties and biases may be removed simply by empirically tuning the model coefficients to maximize agreement between predicted and observed brightness temperatures obtained under varied but well known conditions. In practice, it is impossible to confidently specify the values of more than a couple of the model's input parameters at most locations over the open ocean. Surface wind speed and sea surface temperature are observed routinely by many buoys and ocean-going vessels; water vapor and temperature profiles, on the other hand, are observed much more rarely, and marine observations of integrated cloud water content are practically non-existent. As discussed in Chapter 4, there is even some uncertainty ($\sim 0.5°$) in the viewing angle of the SSM/I, owing to problems with sensor stabilization.

Even if all model input parameters were reasonably well known in a given case, it would still not be a trivial task to determine *which* of the model's many frequency and parameter-dependent coefficients are the best candidates for adjustment. As a result, the calibration and validation of the brightness temperature model against actual SSM/I observations proved to be the most challenging, time consuming and, probably, least conclusive aspect of the work presented in this thesis.

8.1 Verification of SSM/I Calibration

The first step taken was to try to establish some confidence in the absolute calibration of the SSM/I itself. The Calibration/Validation report issued by the Naval Research Laboratory (Hollinger 1988) describes a number of checks that have already been made on SSM/I calibration, including aircraft underflights and comparisons with theoretical brightness temperatures for certain types of targets (e.g, the Amazon rain forest, the Arabian desert, and areas of clear sky and calm ocean). Based on these comparisons, it was concluded that the absolute calibration error of the SSM/I was probably within ± 3 K, though with an "apparent trend for the SSM/I brightness temperatures to be lower than modeled values, especially for the higher frequency channels." Uncertainties in the modeling itself and in the exact state and temperature of the sea surface in most cases prevented a more precise determination from being made.

To independently check the absolute calibration, we examined brightness temperatures over northern Siberia during early Autumn 1987. Our reasoning was that a relatively thick layer of fresh snow at or near the melting point might conceivably behave much like a blackbody, since it would lack a strong discontinuity in dielectric constant at the upper surface (thus excluding Fresnel-type reflection), the penetration depth would be relatively large due to its low density, yet the presence of some liquid water (which absorbs much more strongly than ice) within the layer would drastically reduce the single scatter albedo and hence the degree

of volume scattering. Such a blackbody-like material, if it existed, would thus be characterized by a brightness temperature close to its thermodynamic temperature and be nearly independent of frequency and polarization.

In fact, several regions of the order of 1×10^5 km^2 were found for which all seven channels of the SSM/I gave brightness temperatures within $\sim$1 K each other. For those regions, the mean brightness temperature was also within a degree or two of 273 K, as would be expected of a blackbody at the melting point of water under a relatively transparent atmosphere. On the other hand, some regions were also found for which all channels gave values near 273 K, except for the two 37 GHz channels, which were 2–3 K colder in these cases. Since both the dielectric constant of water and the effect of volume scattering by inhomogeneities (which tends to depress brightness temperatures) change monotonically with frequency in the SSM/I band, it is difficult to conceive of a situation that would give rise to this combination of brightness temperatures naturally. Unfortunately, given the impossibility of knowing what conditions were actually being observed in either of the above cases, no firm conclusions can be drawn from this crude check, except that the two 37 GHz channels are apparently the most likely of the seven to behave in an atypical way.

Although this test did provide some additional confidence in the SSM/I brightness temperature observations near 273 K (barring the possible biases of $\sim$3 K in the 37 GHz T_B), few equivalent opportunities exist to verify the calibration in the 100–200 K range corresponding to the majority of brightness temperature observations over the ocean. For oceanic applications, however, the practical consequences of an instrument gain error affecting the lower brightness temperatures are indistinguishable from those arising from a minor constant bias in the theoretical value of the sea surface emissivity ε. Hence, the empirical corrections obtained below for ε are assumed to account for the sum of such errors.

8.2 Empirical Calibration of the Brightness Temperature Model

The following sources of uncertainties in the model were felt to have the greatest potential for impairing the ability of the model to accurately predict actual SSM/I brightness temperatures: (i) possible absolute biases in the apparent emissivity of the calm ocean surface, owing to errors in the seawater dielectric constant and/or sensor calibration; (ii) possible minor errors in the proportionality between water vapor optical depth at each frequency and column water vapor mass, (iii) ignorance of the ratios of the effective slope variances g^2 for each frequency; and (iv) ignorance of the relationship between the fractional 'foam' coverage F at each frequency and g^2. Finally, to the extent that the SSM/I is to be used to retrieve some meteorologically meaningful measure of the wind speed U at the surface, one must have some knowledge of (v) the relationship between g^2, F, and U.

It is not possible to address any of the above sources of uncertainty in complete isolation from all the others; rather, the calibration of the theoretical brightness temperature model using actual SSM/I data is necessarily an iterative process, since (for example) correctly tuning the sea surface parameterizations requires an accurate estimate of the atmospheric contribution to the observed brightness temperatures and *vice versa*. Furthermore, the confidence with which corrections can be made to the model coefficients in any given case depend heavily on the confidence with which the external variables — i.e., integrated water vapor V, vapor scale height H, effective surface air temperature T_A and lapse rate Γ, sea surface temperature T_S, cloud height z_c, cloud water content L, surface pressure p_0, and viewing angle θ — are known. Needless to say, many of these can rarely be known at all, except insofar as they are assumed to approximately obey the observed statistical relationships described in Chapter 6.

For the purpose of model calibration, the multichannel brightness temperatures observed by the SSM/I are assumed to depend on V, H, T_A, Γ, T_S, U, z_c,

L, p_0, and θ, each of which may vary from one scene to the next, plus 15 calibration constants, which include 7 constant sea surface emissivity bias corrections (one for each channel), 4 multiplicative correction factors for atmospheric water vapor optical depth (one for each frequency) and 4 constants of proportionality relating the effective surface slope variance g^2 at each frequency to a frequency-independent wind speed U. The fractional foam coverages F for each frequency are assumed to be as-yet unknown functions of the same wind speed. If we temporarily restrict our attention to regions of relatively low wind speed, so that F may be neglected, then a total of 25 variables collectively determine the 7 SSM/I brightness temperatures for any single pixel.

Thus, in the modified model, the following replacements are made:

$$\sigma_v \longrightarrow \delta_v \sigma_v, \tag{8.1}$$

$$\varepsilon \longrightarrow \varepsilon + \delta_\varepsilon, \tag{8.2}$$

$$g^2 \longrightarrow C_g U, \tag{8.3}$$

so that δ_v, δ_ε, and C_g are new parameters which must be estimated for each frequency (in the case of δ_v and C_g) or each channel (for δ_ε).

Given initial estimates of the values of all 25 variables in the model for a given pixel, plus associated uncertainties, one may make an 'optimal' revised estimate of one or more of these variables, plus new uncertainties, based on a subset of the 7 co-located SSM/I brightness temperatures in a single pixel. The mathematical basis for doing this is the minimum variance method, described in Chapter 11, applied to a local linearization of the brightness temperature model. The only practical difference here, as compared with the usual problem of estimating geophysical variables, is that the calibration coefficients to be estimated are, by definition, invariant from one scene to the next. Thus the current estimated value and error variance of a coefficient following the processing of a given SSM/I pixel may serve

as the *a priori* constraint on the estimates from subsequent pixels. A large set of SSM/I pixels processed sequentially in this manner will cause the calibration coefficients to converge to constant values which exhibit maximum consistency, in a least squares sense, with the observed SSM/I data combined with the estimates supplied for the model input parameters.

Depending on which coefficients are to be tuned, different characteristics are desirable in an SSM/I comparison data set. For calibrating the sea surface model, for example, it is desirable to have SSM/I observations from regions where the atmospheric component of the signal is small and well-defined, so that brightness temperature variations due to surface roughening can be readily distinguished. For calibrating the atmospheric brightness temperature model, on the other hand, one would like accurate independent estimates of the most important atmospheric parameters, namely V, H, L, and z_c, and variations in the surface contribution should be minimized by choosing scenes for which the surface wind speed is as small as possible. Three different SSM/I datasets were ultimately used to determine the values of the calibration coefficients. Each offered distinct advantages for tuning certain subsets of these coefficients; each had significant shortcomings as well.

The first data set, henceforth referred to as the *Cloud-free Data Set*, consisted solely of SSM/I brightness temperatures obtained from regions subjectively identified as cloud-free at the time of the SSM/I overpass, based on conventional GOES visible imagery for August and September 1987. Most of these regions were located in the Eastern Pacific, north of 15°N latitude, owing to the limitations of the local GOES archive. A few were also found over the Gulf of Mexico and off the Atlantic coast of the U.S. Altogether, the data set consisted of over 12,000 brightness temperatures for each of the seven channels. By excluding SSM/I pixels containing significant cloudiness, two variables in the brightness temperature model — cloud liquid water L and cloud height z_c — could be assumed completely known for this data set. The only other variable for which direct observations were

employed was sea surface temperature T_S, which was estimated to within ± 2 K from the NMC Blended SST Analysis for each region.

The second data set, henceforth referred to as the *Raob Comparison Data Set*, consisted of a large number of radiosonde estimates of integrated water vapor from island and ship stations together with co-located SSM/I brightness temperatures. This extensive data set was made available to the author by Alishouse (personal communication, 1988) and is documented in some detail by Alishouse et al. (1990a). The matchup criteria used by Alishouse et al. were that surface and satellite observations must be coincident within 2° latitude and longitude and within 2 hr time. To minimize land contamination, only weather ships and island stations with areas less than 19% of the area of the 19 GHz field-of-view (FOV) were included. This latter limitation, coupled with the temporal matchup criterion, reduced the number of candidate radiosonde stations to those 19 stations listed in Table 8.1. For a given matchup, only the four nearest SSM/I pixels were saved. The time period for which coincident SSM/I-radiosonde data were collected covered almost a year, from June 1987 through April 1988.

For use in the brightness temperature model calibration, several additional restrictions were imposed. To begin with, we wished to further reduce the potential for serious land contamination, since even a small island could easily increase brightness temperatures by $\sim$10 K or more if it were near the center of the SSM/I pixel in question. Of the four pixels which were provided for each matchup, we therefore discarded all but the one for which 19H T_B was the lowest. We further discarded all matchups for which both the total water vapor $V < 10$ kg m^{-2} and $T19H > 140$ K, since these were clearly affected either by land or by precipitation. Finally, we used an empirical formula to compute a normalized 37 GHz polarization difference P_{37} (Eq. 11.28; see also Petty and Katsaros 1990a, 1990b) indicative of atmospheric opacity due to rain and cloud, and we discarded all matchups for which $P_{37} < 0.925$. This effectively eliminated all cases of probable rain and/or

Table 8.1: Upper air stations used in *Raob Comparison Data Set* (after Alishouse et al. 1990a

Station	ID	Lat.	Lon.	Area (km^2)
Bear Is.	01028	74.5N	19.0E	179
Jan Mayen	01001	70.9N	8.7W	373
Ship M	C7M	66.0N	2.0E	-
St. Paul Is.	70308	57.2N	170.2W	91
Ship L	C7L	57.0N	20.0W	-
Ship C	C7C	52.8N	35.5W	-
Hachija Jima	47678	33.1N	139.8E	70
Kindley Fld.	78016	32.4N	64.7W	53
Minamidaito Jima	47945	25.8N	131.2E	47
Ishigakajima	47918	24.3N	124.2W	215
Roberts Fld.	78384	19.3N	81.4W	183
San Maarten	78866	18.1N	63.1W	85
Barbados	78954	13.1N	59.5W	431
Isla San Andreas	80001	12.6N	81.7W	21
Diego Garcia	61967	7.4S	72.5E	152
Cocos Is.	96996	12.2S	96.8E	14
Easter Is.	85469	27.2S	109.4W	117
I.N. Amsterdam	61996	37.8S	77.5E	62
Macquarie Is.	94998	54.5S	159.0E	109

heavy cloud. The final set consisted of a total of 515 matchups between radiosonde observations of V and SSM/I brightness temperatures.

For this second set of observed SSM/I brightness temperatures, water vapor V and H were known from the radiosondes, though with some residual uncertainty arising from temporal and spatial mismatches of up to 2 hr and/or ~200 km in some cases, together with the intrinsic measurement error of the radiosondes themselves. For both V and H, uncertainties were arbitrarily specified as ±10%.

The effective surface temperature T_A and associated uncertainty were specified as a simple function of the radiosonde surface temperature T_0, reflecting the radiosonde statistics described in Section 6.3.3. The sea surface temperature T_S was assumed equal to $T_0 \pm 5$ K. Most other model variables, with uncertainties, were specified as simple functions of V, based on the data appearing in Table 6.5.

The third and final data set, henceforth referred to as the *Antarctic Airmass Data Set*, was obtained from what appears to have been a surge of extremely dry, and presumably cold, Antarctic air observed by the SSM/I over the South Indian Ocean (roughly 45–55°S, 70–105°E longitude) during the period from ~13 UTC 31 October to ~11 UTC 1 November, 1987. Although no independent meteorological data were obtained for this event, the following characteristics could be inferred from the SSM/I imagery alone: (i) differences between the 22V and 19V brightness temperatures were among the lowest observed over the ocean (i.e., 5–10 K), implying unusually low total water vapor V; (ii) 85H brightness temperatures were very low (160–180 K) and appeared very smooth within the affected region, suggesting very little, if any, cloud water present (85 GHz imagery of cloud cover normally exhibits obvious spatial structure on scales of ~10 km); and (iii) despite the uniformly low atmospheric opacity implied by (i) and (ii), 19H brightness temperatures varied between approximately 95 K to 110 K, suggesting a considerable range of surface roughening due to wind.

Of the above data sets, only the Raob Comparison Data Set included direct observations of integrated water vapor, one of the two most important atmospheric variables affecting SSM/I brightness temperatures. On the other hand, only the Cloud-free Data Set offered quantitative constraints on L (zero, with insignificant uncertainty). *None* of the data sets included direct observations of surface wind speed, the most important single surface variable. Therefore, in order to supply useful constraints on V, L, and U in those data sets for which they were not

measured, it was necessary to exploit *a priori* knowledge of the their relationship to observed SSM/I brightness temperatures.

Surface wind speed U, for example, was estimated from the SSM/I brightness temperatures themselves, using a multiple linear regression algorithm by Goodberlet et al. (1989; 'Global D-Matrix' algorithm, hereafter referred to as the GSW algorithm). This statistical algorithm was obtained from coincident SSM/I data and surface buoy observations of wind speed scaled to reflect a height of 19.5 m above the surface. Estimated precision of the wind speed estimates is ± 2 m s^{-1} outside of precipitation. For water vapor V, we derived our own regression algorithm (19V, 19H, and 22V) from the Raob Comparison Data set (see Chapter 11), so that consistent water vapor estimates could be immediately obtained for the other two data sets without resorting to physical retrievals based on the as-yet uncalibrated model. The uncertainty in V obtained in this way was assumed to be the greater of 2 kg m^{-2} or 13%. Finally, two simple semi-physical algorithms for L were derived, each of which was empirically 'zeroed' using the Cloud-free Data Set; these were used primarily to screen out SSM/I pixels contaminated by obvious heavy cloud or precipitation. All of the above algorithms are described in greater detail in Chapter 11. *

---

* The use of SSM/I-derived estimates of U, V, and L to help calibrate a model for the SSM/I response to U, V, and other parameters, may raise some questions regarding the 'independence' of some of the independent comparison data. In fact, the use of the empirical algorithms to estimate model input parameters in this case simply translates into an implicit assumption that statistical relationships between environmental parameters and brightness temperatures observed in one data set (the one used in the regression) are universal and should be reproduced by a correctly calibrated model applied to other data sets as well. This interpretation, of course, only applies to the calibration of those channels used in the initial determination of U and V; for other channels, SSM/I estimates of V and U may indeed be viewed as independent, if also indirect.

For all model input parameters which were neither directly measured nor estimated from the above statistical algorithms, values and uncertainties were specified as simple functions of V, based again on Table 6.5. The exceptions, of course, were the cloud parameters L and z_c which, after discarding pixels with obvious heavy cloudiness, were arbitrarily assigned the values 0.1 ± 0.1 kg m^{-2} and 1.0 ± 1.0 km, respectively. The viewing angle θ was obtained directly from the SSM/I data tapes, but the value given was assumed to be accurate only to $\pm 0.3°$.

The path leading to the final adjusted calibration coefficients was lengthy and convoluted and involved numerous iterations, as well as subjective decisions affecting the sequence in which the calibration data sets were processed and the manner in which the impact of uncertainties in relevant environmental variables was reduced. The following is therefore only a qualitative description of the way in which each of the three data sets described above were employed.

In general, only a subset of the calibration coefficients were subject to adjustment at any given time; the remainder were held fixed by temporarily specifying zero variance for those parameters in the sequential estimation scheme. Moreover, only small subsets of the available channels were used to compute adjustments to specific coefficients. These subsets were chosen on the basis of their relative insensitivity to the uncertainties in the remaining parameters. In this way, the number of model derivatives to be computed and the size of the matrices to be inverted at each step were kept to a minimum, and the rate of convergence (per iteration) remained reasonable.

First, the Antarctic Airmass Data Set was used to establish initial estimates of the constant emissivity biases δ_ε in each channel and the wind speed dependences of the effective surface slope variances g^2 for each frequency. To minimize potential ambiguities due to variations in V or the appearance of wind-driven foam, only those pixels were processed for which $T22V - T19V < 8$ K and for which U (as estimated from the GSW algorithm) was less than 7 m s^{-1} .

Table 8.2: Calibration Coefficients for Brightness Temperature Model

ν(GHz)	19.35		22.235	37.0		85.5	
Pol.	V	H	V	V	H	V	H
δ_ε	.004	.004	−.005	−.012	−.013	−.002	.054
δ_v	1.01		0.95	1.06		0.92	
C_g	3.49−3		3.60−3	4.85−3		6.22−3	

Next, the Raob Comparison Data Set was processed in order to adjust δ_v for 19 and 22 GHz. Since the uncertainty in L was rather large for this data set, the 37 and 85 GHz channels, which are most sensitive to L, could not be reliably adjusted with this data set. As before, only pixels with estimated $U < 7$ m s^{-1} were processed.

In the third stage, the Cloud-free Data Set was used to adjust δ_v for the 37 and 85 GHz channels, using the regression-based estimates of V and U as initial inputs. Because $L = 0$ for this data set, an important source of ambiguity is removed from the calibration of the model for these channels. On the other hand, new ambiguities are introduced by the atypical meteorological character of large cloud-free regions over the ocean. For example, it may be questioned whether the global statistical relationship between vapor scale height H and V (Table 6.5) holds for the Cloud-free Data Set, given the likelihood of stronger-than-average atmospheric subsidence and other special conditions. As the value of H has some bearing on the sensitivity of the SSM/I to V, the potential for minor model calibration biases cannot be completely excluded.

The steps described were repeated until no further reduction was noted in the rms difference between predicted and observed brightness temperatures. Table 8.2 gives the final values obtained for the calibration coefficients.

Values of δ_ε are remarkably similar for both polarizations at 19.35 and 37.0 GHz, although there was no known reason to expect such a result. Since a change of emissivity of $\sim$.003 equates to a change in T_B of approximate 1 K, the δ_ε values listed translate to apparent radiometer calibration errors of 1 K, -1 K, and -3 K for the 19, 22, and 37 GHz channels, and -1 K and $\sim$15 K for the 85V and 85H channels, respectively. Of particular interest is that the results here appear to confirm a negative bias of $\sim$3 K in the 37 GHz channels. This apparent bias is consistent both with the results of the independent calibration check described in section 8.1 and with the Calibration /Validation Report issued by Hollinger (1988). Also of interest is the strikingly large bias correction required for the 85H channel. It is not known whether this can be attributed to errors in the 85H brightness temperature data themselves, to an error in the seawater dielectric constant calculated for this frequency, or perhaps to the inadequacy of the geometric optics model for sea surface emissivity. Since the 85V channel does not exhibit such a large apparent bias, an error in the dry atmospheric optical depth does not seem likely to be the reason.

The correction factors δ_v to the water vapor optical depth differ almost insignificantly from unity for 19 and 37 GHz. For the most water vapor-sensitive channels, on the other hand, the corrections are larger than expected, and suggest that the theoretical water vapor absorption model of Liebe (1985) overestimates total atmospheric optical depth due to water vapor by 5% at 22.235 GHz and 8% at 85.5 GHz. The latter apparent error can be easily attributed to unresolved questions concerning the correct physical model for water vapor continuum absorption; the correction needed for 22 GHz, on the other hand, is somewhat more surprising, since the spectroscopic properties of the resonant absorption line at this

frequency have generally been assumed to be well established. It may be speculated that the laboratory spectroscopic measurements of absorption under typical near-surface conditions are reliable, while those few measurements made for lower pressures and temperatures are less so. In this case, the apparent overestimate of total atmospheric optical depth may also imply a corresponding overestimate of the theoretically predicted absorption scale height H_v and thus the values of the scaling factors γ appearing in Table 6.4 as well. However, no attempt has been made here to estimate modified values of γ based on this hypothesis.

Although no *a priori* assumptions were made concerning the relationship between g^2 and U at each frequency (other than that it is approximately linear), the magnitudes of the C_g determined empirically for the lower three frequencies are remarkably close to those obtained from the Wilheit (1979b) formula, which predicts that

$$C_g = \begin{cases} .0048(0.3 + 0.02\nu), & \nu < 35 \text{ GHz} \\ .0048, & \nu \geq 35 \text{ GHz} \end{cases} \tag{8.4}$$

(the constant in the original Wilheit version of this formula is absorbed in the δ_ϵ determined for the present model). Eq. (8.4) gives C_g equal to .0033, .0036, and .0048 s m^{-1} for 19.35, 22.235, and 37.0 GHz, respectively, or differences of only 6%, 0.5%, and 1% from the values in Table 8.2. On the other hand, we find that the empirically determined value of .00622 for C_g at 85.5 GHz contradicts Wilheit's assumption that the frequency dependence vanishes above 35 GHz. Since Wilheit adopted the Cox and Munk (1955) relationship between slope variance and wind speed (rescaled to reflect a 20 m reference height) as the limiting relationship at higher frequencies, our results imply an 85.5 GHz effective slope variance which is 30% *greater* than that determined via sun glitter measurements by Cox and Munk. No obvious physical explanation for this discrepancy immediately comes to mind.

In Fig. 8.1, calibrated model brightness temperatures for a cloud-free atmosphere are plotted as functions of V, with the dashed lines indicating the theoretical upper and lower bounds associated with realistic variability in all remaining

model input parameters. For comparison, observed SSM/I brightness temperatures from the Raob Comparison Data Set are also plotted. Because the latter are not necessarily associated with cloud-free skies, the plotted theoretical upper bound does not apply to these points, while the lower bound *should* apply. Those few radiosonde points which do fall at or below the theoretical minimum generally do so for all frequencies, suggesting the possibility that the radiosonde water vapor values in these cases are erroneously high.

Somewhat more disturbing is the occurence of a larger number of points above the theoretical maximum curve for 19 and 22 GHz than for 37 and 85 GHz — if these excess brightness temperatures had resulted from the presence of cloud water, one would expect the excess to be greater, on average, for the higher frequencies. The reason for this apparent discrepancy has not yet been determined. One possible explanation is that contamination by land may not have been completely eliminated by the screening procedure described earlier. Since the lower frequency channels have much poorer spatial resolution, they are susceptible to contamination at greater distances from land, and it is therefore very possible for all four of the original pixels from a given radiosonde-SSM/I matchup to experience significant land contamination. Fortunately, if land contamination is indeed the source of the discrepancy in Fig 8.1, it does not appear to have had a fatal effect on the overall fit of the model.

8.3 Empirical determination of the 'foam' contribution

Having calibrated the brightness temperature model for low wind speeds, we now must complete the specification of the model by considering the wind speed dependence of the surface foam fraction F. As noted earlier (section 7.2c), the meaning of the word 'foam' should not be taken too literally; rather, it may be regarded as a catch-all variable which accounts for wind-induced brightness

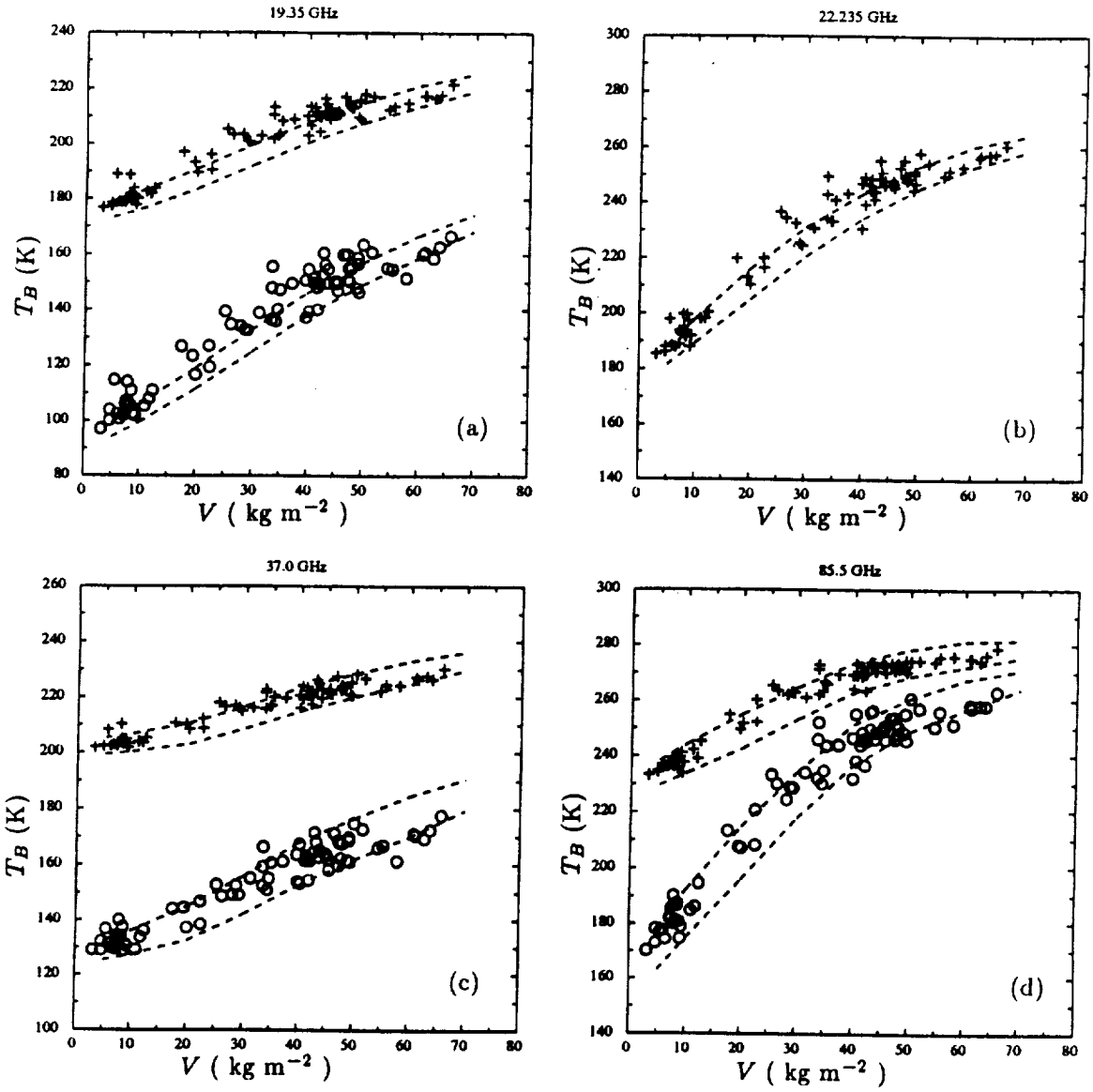

Fig. 8.1 Observed SSM/I brightness temperatures plotted vs radiosonde-derived values of integrated water vapor V and compared with approximate upper and lower bounds (dashed lines) predicted by the calibrated brightness temperature model in the absence of clouds. '+' symbols indicate vertical polarization; o indicates horizontal polarization. (a) 19.35 GHz (b) 22.235 GHz (c) 37.0 GHz (d) 85.5 GHz.

temperature variations not adequately described by the geometric optics model of section 7.2.

The Antarctic Airmass Data Set was processed again as before, but this time only two variables were considered unknown: the surface wind speed U and the effective foam coverage F. In contrast to earlier, the pixels processed were not limited to those with low wind speeds. For each pixel, both U and F were estimated three times, using the 19, 37, and 85 GHz channels, respectively. The use of dual polarization measurements to estimate two variables reduces the problem of retrieving U and F to solving a pair of nearly linear equations in two variables. Two or three iterations were sufficient to find a pair of U and F for which the predicted and observed brightness temperatures at the specified frequency were identical.

Errors in the specification of other model variables will, of course, introduce corresponding errors in estimates of U and F. As it turns out, most such errors — especially those arising from uncertainties in the true atmospheric opacity — affect primarily the retrieval of F. This is because F and all atmospheric variables share the property of driving brightness temperature changes in the direction of (or away from) an unpolarized value somewhere near ~280 K (i.e., the approximate temperature of the surface and lower atmosphere), whereas wind-induced surface roughness decreases the vertically polarized radiance at the same time that it increases the horizontally polarized radiance.

This procedure resulted in separate estimates U_{19}, U_{37}, and U_{85} for wind speed and F_{19}, F_{37}, and F_{85} for foam coverage. Since U and F are being treated as completely independent model variables here, the respective U estimates are in fact no more than physical retrievals of g^2/C_g, where g^2 is the large scale surface slope variance and C_g is the frequency dependant proportionality constant determined in the previous subsection. Fig. 8.2a shows a scatter plot of U_{37} *vs* the wind speed U_{GSW} retrieved using the GSW statistical algorithm. The relationship

between the two is very nearly linear, with an rms difference of less than 1.0 m s^{-1} ; there is considerably more scatter in the relationship between U_{GSW} and the other two single-frequency U estimates (not shown)*. Figs. 8.2b–d depict the relationships between U_{19}, U_{37}, and U_{85}. The slopes of the clouds of points are all near unity, thus confirming at least the *ratios* of the constants C_g determined earlier; however, there remains moderate scatter in the relationships between the U estimates for the different frequencies. For characterizing the F as a function of wind speed, therefore, we have arbitrarily chosen the arithmetic mean $\overline{U}$ of the three single-frequency U estimates to serve as the independent variable.

Fig. 8.3a depicts a scatter plot of $\overline{U}$ *vs* U_{GSW}, again exhibiting the general agreement between the physically-derived and statistically-derived estimates of surface wind speed from the SSM/I brightness temperatures. Figs. 8.3b–d show plots of effective foam coverage F *vs* wind speed for each of the three frequencies. At 19 GHz, F appears to be nearly independent of $\overline{U}$ below ~7 m s^{-1} and to begin increasing rather abruptly and steadily thereafter. Given past controversy surrounding the correct form of the $F(U)$ relationship, this result is in almost surprising agreement with the simple model of Wilheit (1979b). The results for 37 GHz (Fig. 8.3c) are more difficult to characterize in a plausible way, since the systematic variability in F associated with $\overline{U}$ is barely distinguishable against the scatter. Nevertheless, the most obvious 'upturn' still occurs near 7 m s^{-1} . On the other hand, at 85 GHz (Fig. 8.3d), the scatter is large enough to completely obscure any relationship between F and U.

It is not known whether the scatter in these cases is intrinsic to the relationship between F and U or whether it is in fact a consequence of contamination

* One intriguing inference that can be made from these results is that the GSW algorithm, which was obtained by way of linear statistical regression without recourse to physical models, has effectively singled out $g^2(37\ GHz)$ as the most reliable linear predictor of the surface buoy winds used in Goodberlet's et al. (1989) comparison data set.

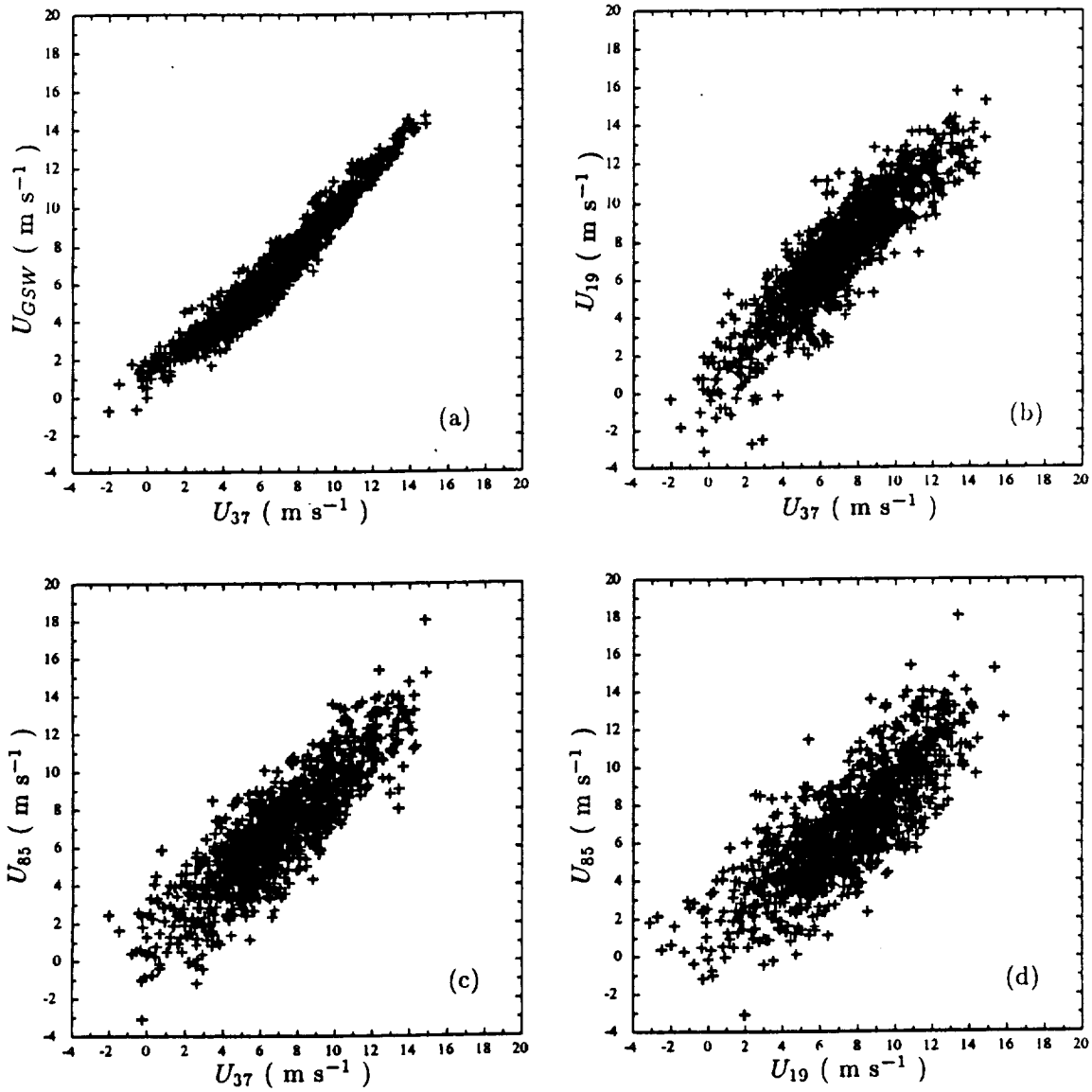

Fig. 8.2 Comparisons between U-estimates obtained by various algorithms from the *Antartic Air Mass* set of observed SSM/I brightness temperatures.(a) Physical retrieval of U using 37 GHz channels compared with the results of the Goodberlet et al. (1989) statistical wind speed algorithm. (b) physical retrievals of U using 37 GHz channels compared with physical retrievals from 19 GHz channels. (c) physical retrievals of U using 37 GHz channels compared with those from 85 GHz channels. (d) physical retrievals of U using 19 GHz channels compared with those using 85 GHz channels.

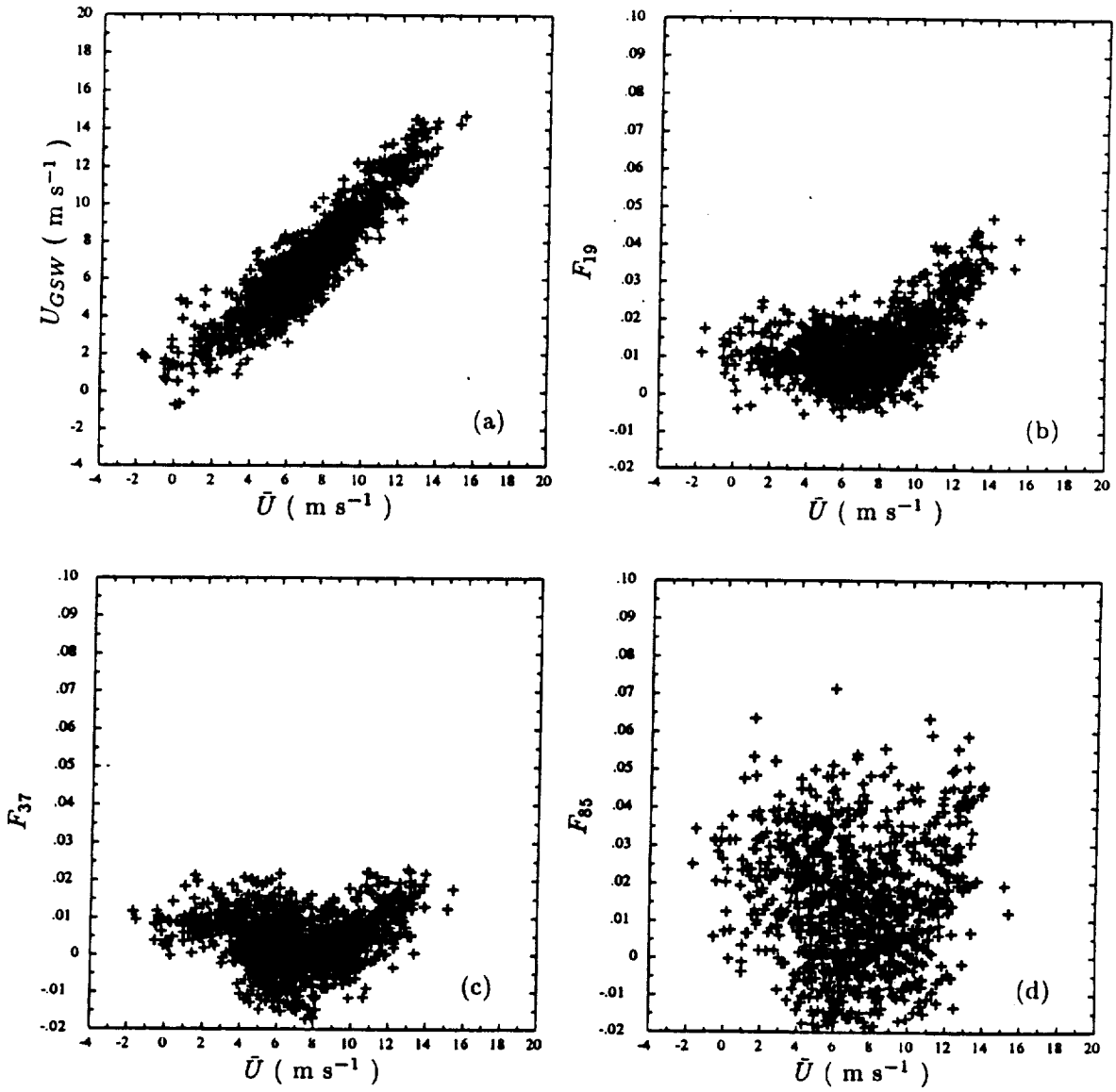

Fig. 8.3 Comparison of retrieved 'foam' fraction with retrieved wind speed for three SSM/I frequencies. The latter ($\overline{U}$) is taken to be the average of the wind speeds retrieved separately using the 19, 37, and 85 GHz channels. $\overline{U}$ is compared with the Goodberlet et al. (1989) estimate of U in (a). (b) $\overline{U}$ vs F_{19} (c) $\overline{U}$ vs F_{37} (d) $\overline{U}$ vs F_{85}

by small amounts of cloud water. For the time being, we shall tentatively regard the scatter as a manifestation of apparent 'geophysical noise.' Given that a fluctuation in F of 0.0036 corresponds to a brightness temperature fluctuation of approximately 1.0 K, this noise may be treated as an 'equivalent instrument noise' with a standard deviation of approximately 1.5 K for the 19V, 19H, and 22V channels, 2 K for the 37V and 37H channels, and 3 K for the 85V and 85H channels. These noise contributions will prove relevant to the theoretical maximum precision of the parameter retrievals discussed in Chapter 11.

Overall, the data examined here do not appear to justify a more complex model for $F(U)$ than that used by Wilheit (1979b), namely,

$$F(U) = \begin{cases} 0, & \text{for } U < 7 \text{ m s}^{-1} \\ C_F(U-7), & \text{for } U > 7 \text{ m s}^{-1} \end{cases}, \tag{8.5}$$

Unfortunately, the data displayed in Fig. 8.3 also do not permit confident determination of the C_F in (8.1) for each frequency. In an effort to obtain at least tentative estimates of C_F, pending a more comprehensive empirical study, a fourth set of SSM/I observations were brought into play. These were obtained in a region affected by an exceptionally intense — and widely reported — cyclone which ultimately overran the British Isles and inflicted considerable wind damage there during the early morning of 16 October 1987. 46 SSM/I pixels in this instance were taken from a 2.5×10^4 km^2 area centered on 45.2°N, 6.6°W during the pass occurring at 1920 UTC, 15 October 1987. Conventional surface pressure analyses suggested gale force winds in the region, and the GSW wind algorithm applied to the SSM/I data yielded a mean value of 20.4 m s^{-1} . Most importantly, conventional satellite imagery appeared to rule out heavier clouds in this region. Standard deviations of SSM/I brightness temperatures were small within this sample, exceeding 2.6 K only for those channels most sensitive to water vapor, namely the 22V and 85H channels. Thus it could be surmised that conditions within the region were reasonably uniform and free of serious liquid water contamination.

Following the usual procedure and making the usual assumptions about model input parameters, C_F was estimated within the high wind region to be approximately 8×10^{-3} m^{-1} s *irrespective of frequency.* The data analyzed in this subsection are too limited to permit a high level of confidence in these exact values; indeed, the 37 GHz data plotted in Fig. 8.3c would appear to contradict such a large value for C_F. In any event, the present data do not appear to support a C_F which *increases* by 8% over the frequency range of the SSM/I, as is assumed by Wilheit (1979b). Note also, however, that the maximum C_F assumed by Wilheit, (6×10^{-3} s m^{-1}), is somewhat lower than that found here.

In developing and tuning the brightness temperature model throughout this and the previous chapters, we deliberately avoided directly invoking specific assumptions about the quantitative relationship between either g^2 or F and U, or between SSM/I brightness temperatures and U, despite the availability of several independent studies relating one or more pairs of these variables*. It is therefore reassuring that the results we have obtained here are comparable to those obtained independently by others (e.g., Wilheit 1979b) for frequencies at and below 37 GHz. On the other hand, our results suggest that none of the previously available models correctly predict the sensitivity of 85.5 GHz brightness temperature to wind speed.

None of the results presented in this chapter should be regarded as final; much more work is needed, for example, to establish a more convincing model for the dependence of F on wind speed. However, the calibrated atmosphere/sea surface brightness temperature model is undoubtedly accurate enough to permit considerable insight into the capabilities and limitations of the SSM/I for observing the

---

* With few exceptions, direct incorporation of earlier empirical brightness temperature results would have been difficult anyway because of significant differences in incidence angle or because of a lack of information concerning the precise atmospheric conditions affecting the data recorded by the other authors.

marine environment. The ultimate test of the absolute accuracy of the model will be its eventual incorporation into physical algorithms for global SSM/I retrievals, since inaccuracies in the model should then manifest themselves via biases in one or more of the parameters retrieved. Analysis of such biases should permit further tuning of the physical model.

9. SENSITIVITY OF THE SSM/I TO MODEL PARAMETERS

In Chapters 6, 7, and 8, we derived and calibrated an analytic model which predicts SSM/I brightness temperatures as a function of a relatively small number of environmental parameters. We also described some aspects of the natural variability of the atmospheric parameters, as inferred from the global radiosonde profile set. In this chapter, the calibrated brightness temperature model is used to gain insight into the quantitative responses of the seven SSM/I channels to variations in each of the ten surface and atmospheric parameters on which the model depends.

First, typical cloud-free SSM/I brightness temperatures T_B are plotted in Fig. 9.1 for the entire natural range of atmospheric water vapor content. 'Base conditions' for H, T_A, Γ, p_0 were allowed to vary as functions of V in accordance with the statistics in Table 6.5. Viewing angle θ was taken as 53.0°, the surface wind speed U was set to 5 m s^{-1} , and T_S was set equal to T_A.

For a completely dry atmosphere ($V = 0$) atmospheric opacity is rather low, and differences in brightness temperatures for each channel mainly reflect differences in sea surface emissivity. In this case all of the horizontally polarized channels observe brightness temperatures below 160 K — as low as 90 K for the 19H channel, while the four vertical channels observe brightness temperatures ranging from 170 K to 230 K. In the absence of water vapor, the 19V and 22V channels respond to the environment in a very similar way and record T_B no more than ~3 K apart.

As V increases from zero, different channels respond at different rates, depending on both the background brightness temperature of the ocean surface for that channel and on the absorption coefficient of water vapor at the frequency in question. In general, the horizontal channels respond more strongly to a given change in atmospheric *opacity* because of the greater initial brightness temperature difference between the open ocean and a completely opaque atmosphere whose

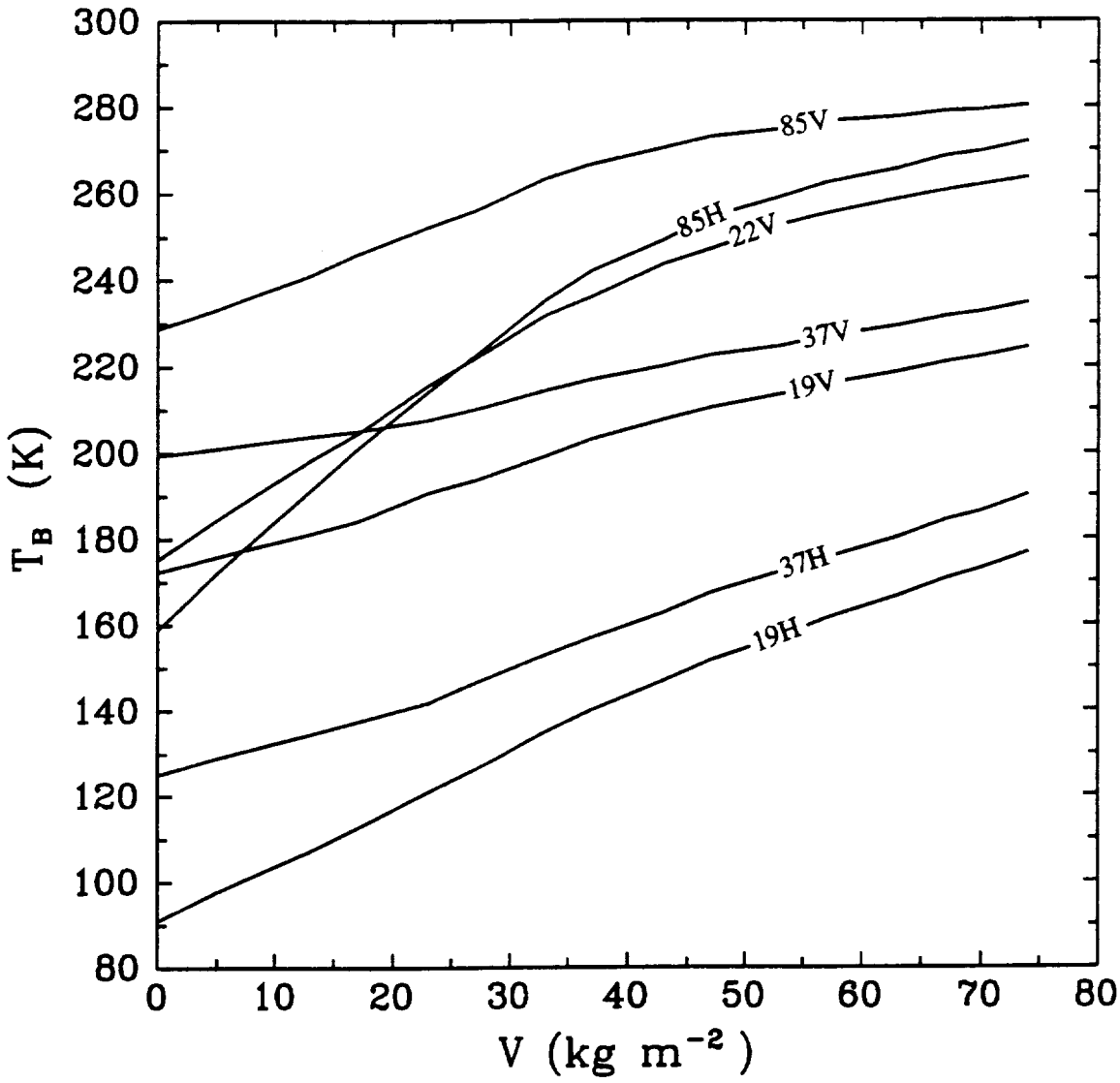

Fig. 9.1 Typical SSM/I brightness temperatures plotted as functions of total atmospheric water vapor V. Atmospheric temperature and other parameters are allowed to vary with V in accordance with Table 6.5. No cloud water is assumed

brightness temperature is equal to its effective radiating temperature (~290 K). The 22V, 85H, and 85V channels, however, change most rapidly in response to an initial increase in V, owing to a much higher water vapor absorption coefficient at these frequencies, but the response is approximately linear only as long as the slant path optical depth $[\sigma / \cos\theta] \ll 1$. Beyond about 30–40 kg m^{-2}, the response of all three of these channels begins to level off, while the four remaining channels remain more or less linear in V even beyond 70 kg m^{-2}.

Fig. 9.2 illustrates the brightness temperatures changes observed in response to the addition of cloud water at a height of 1.0 km, assuming fixed water vapor content V of 35 kg m^{-2}. Even with 1.0 kg m^{-2} of liquid water, corresponding to a very heavy cloud layer, the 19V, 19H, and 22V channel responses are almost perfectly linear, owing to the relatively low opacity of cloud water at these low frequencies. The 37V and 37H channels begin to show some mild non-linearity but brightness temperatures are still nowhere near the upper limit imposed by the thermodynamic temperature of the cloud. The 85 GHz channels, on the other hand, show moderately strong non-linearity and saturate relatively quickly with increasing L; this saturation is accelerated by the already substantial contribution of water vapor alone to the atmospheric optical depth.

Fig. 9.3 depicts SSM/I brightness temperatures for fixed $V = 35$ kg m^{-2} and no cloud, but with surface wind speed U varying from 0 to 40 m s^{-1}. Below 7 m s^{-1}, the vertically polarized channels show weak *decreases* in brightness temperature with increasing surface roughness, while the horizontal channels show moderate increases. Above 7 m s^{-1}, the model assumes an increasing fraction of high-emissivity foam on the the ocean surface, so that both vertical and horizontal channels register brightness temperature increases.

The plots described above are intended simply to orient the reader with regard to the characteristic absolute values of the brightness temperatures associated

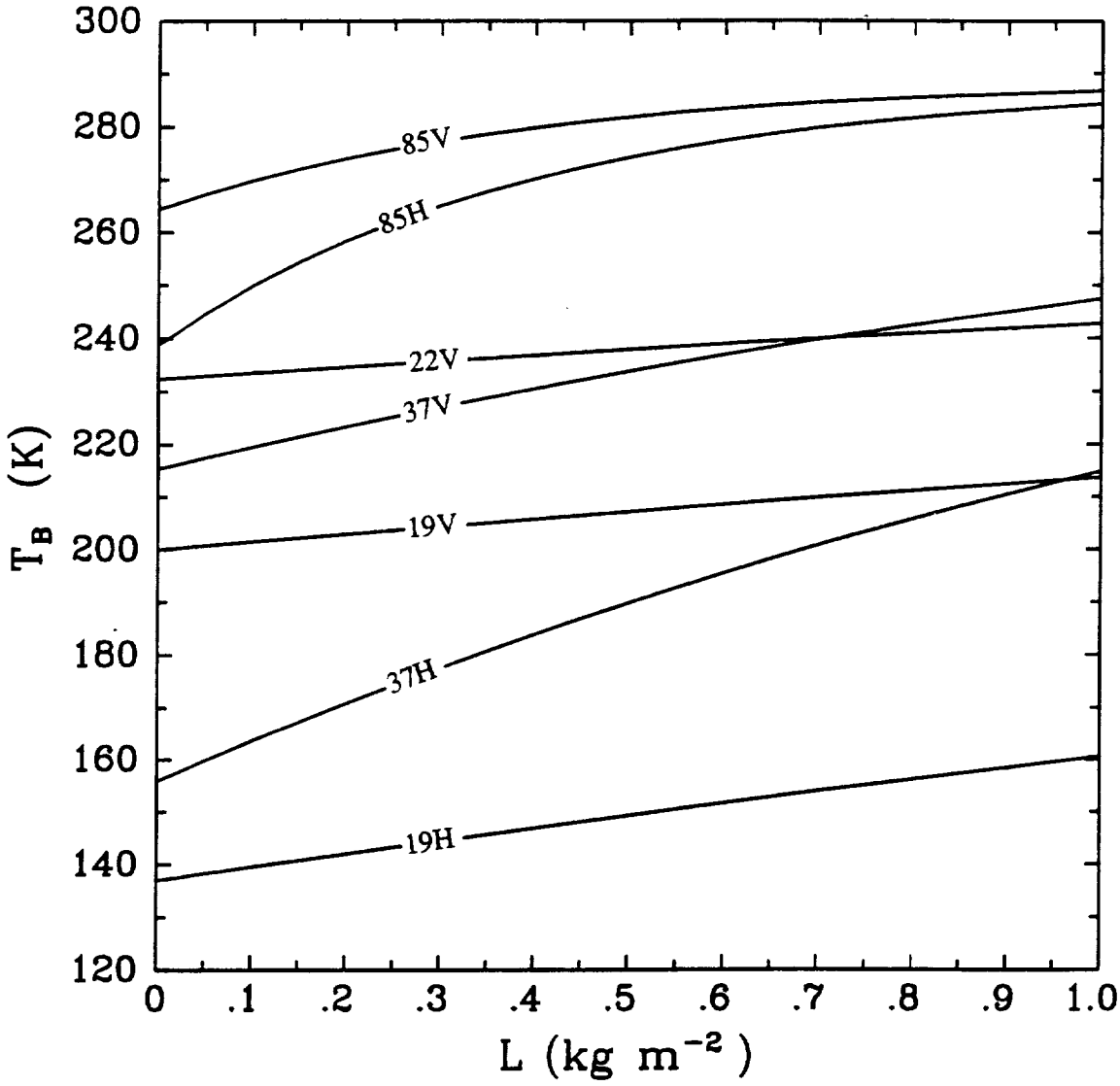

Fig. 9.2 SSM/I brightness temperatures plotted as functions of total cloud liquid water L, assuming all other parameters fixed at the 'baseline' values given in the text.

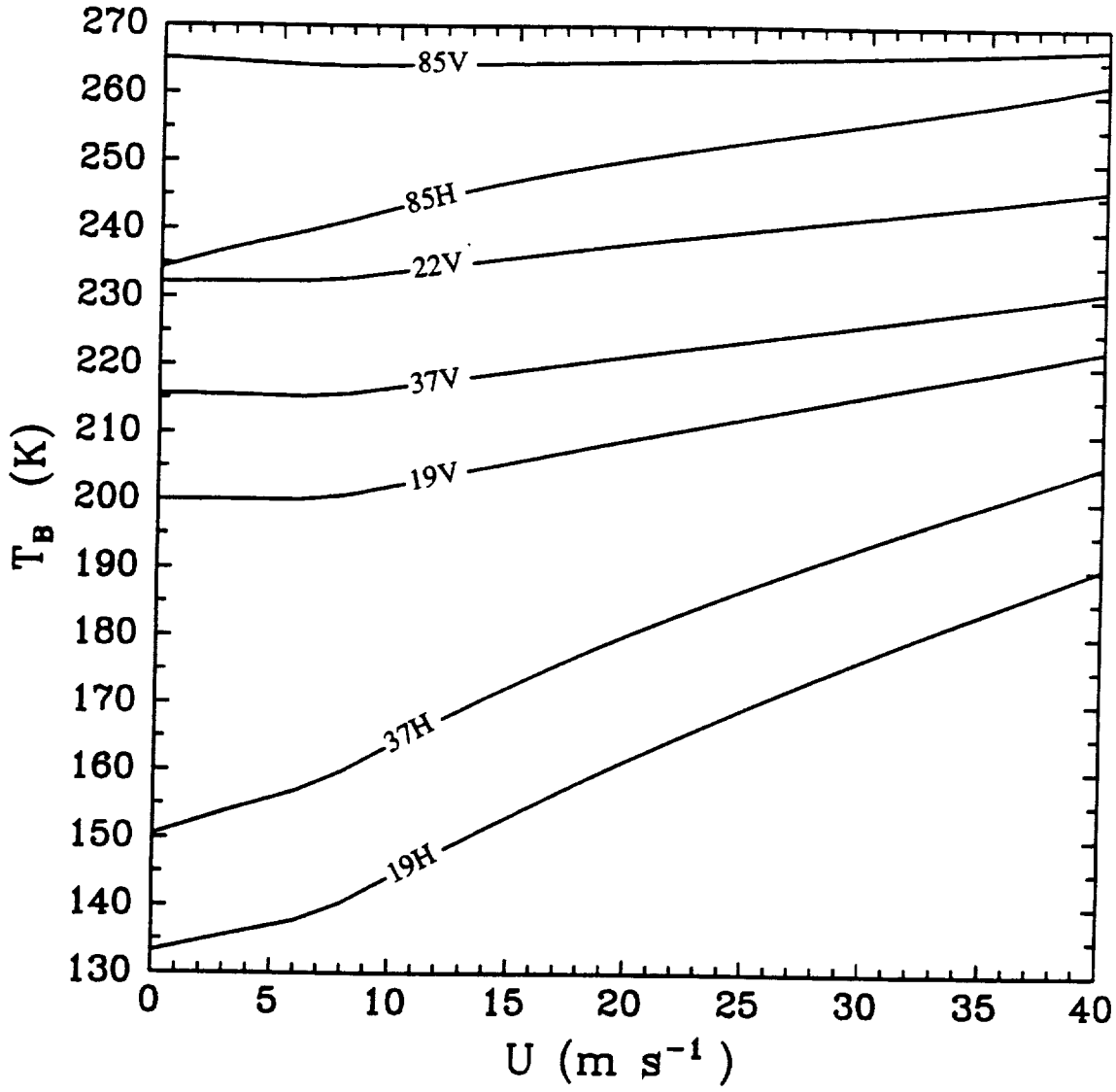

Fig. 9.3 SSM/I brightness temperatures plotted as functions of surface wind speed U, assuming all other parameters fixed at the 'baseline' values given in the text.

with each SSM/I channel. For geophysical retrievals, absolute brightness temperatures are less interesting than the magnitude of brightness temperature *changes* accompanying perturbations of each the model parameters. The sensitivity of a given channel to a parameter p_i is defined as $\partial T_B/\partial p_i$. Since the relationship between T_B and environmental parameters is generally non-linear, $\partial T_B/\partial p_i$ will normally be a non-constant function of p_i and/or the other model parameters. In the following, the brightness temperature model is used to evaluate the sensitivity of each SSM/I channel to each model parameter, including its functional dependence on selected other parameters.

When considering the results presented below, one should keep in mind that, in order for any variable to be retrievable from SSM/I data, the brightness temperature signal of that variable must not only exceed the instrument noise threshold ($\sim$0.5 K) of one or more SSM/I channels, but there must also exist a vector component of the signal (in channel space) which is significantly larger than the same component of the signals associated with all other variables. This and other aspects of the retrieval problem, as it relates to the SSM/I, will be discussed in some detail in Chapter 11.

The 'base state' chosen for the following examples is the same as that given above for Figs. 9.2 and 9.3, i.e., $V = 35$ kg m^{-2} , $H = 1.7$ km, $T_A = 297$ K, $\Gamma = 5.7$ K km^{-1}, $T_S = 297$ K, $U = 5$ m s^{-1} , $L = 0$, and $\theta = 53°$, unless otherwise noted. Under these conditions, satellite brightness temperatures are computed to be 201, 137, 233, 216, 156, 265, and 239 K for the 19V, 19H, 22V, 37V, 37H, 85V and 85H channels, respectively.

Fig. 9.4a depicts the SSM/I's sensitivity to integrated water vapor V ($\partial T_B/\partial V$) as a function of V. As already noted in the discussion of Fig. 9.1, the 22V channel does not exhibit the greatest sensitivity to V, despite its position on the center of the water vapor resonance line at 22.235 GHz. Indeed, for $V > 30$ kg m^{-2} , all three of the horizontally polarized channels (19H, 37H, 85H)

show markedly greater sensitivity. This is again a consequence of (i) the lower emissivity of the sea surface in horizontal polarization, so that the ocean provides a colder radiometric background against which to view changes in atmospheric emission, and (ii) the relatively rapid 'saturation' in brightness temperature which occurs as the atmosphere becomes increasingly opaque at 22 GHz. Only at much lower values of V does the sensitivity of 22V to V exceed that of almost all the other channels, the exception being 85H, for which non-resonant ('continuum') absorption by water vapor is comparable in magnitude to resonant absorption at 22 GHz and is rendered more visible by the lower sea surface emissivity.

Fig. 9.4b also depicts plots of $\partial T_B/\partial V$ for each channel, but this time as functions of cloud liquid water L (throughout the rest of the chapter z_c is set to 1.0 km unless otherwise noted). As expected, the ability of L to reduce the SSM/I's sensitivity to V is a strong function of frequency. For example, 0.4 kg m^{-2} of liquid water is sufficient to reduce the sensitivity of both the 85V and 85H channels to less than 0.5 K/(kg m^{-2}), i.e., less than that of all other channels, despite the fact that the 85H channel shows the greatest sensitivity under cloud free conditions for $V < 45$ kg m^{-2} .

Changes in the vapor scale height H affect both the mean pressure and the mean temperature experienced by the vapor column. Both factors influence the width of the resonant water vapor absorption line at 22 GHz and the strength of the continuum absorption in the spectral windows. In addition, the colder temperatures implied by a greater scale height act to reduce the downward and upward thermal emission for a given atmospheric opacity. Fig. 9.4c indicates the net effect of these factors on the SSM/I's sensitivity to V. Interestingly, the increasing sharpness of the absorption line at 22.235 GHz apparently offsets the reduction in emitting temperature, so that the net sensitivity of the 22V channel to V remains essentially unaltered by reasonable changes in H, at least for the base state considered here. For all other channels, increases in H give rise to decreases

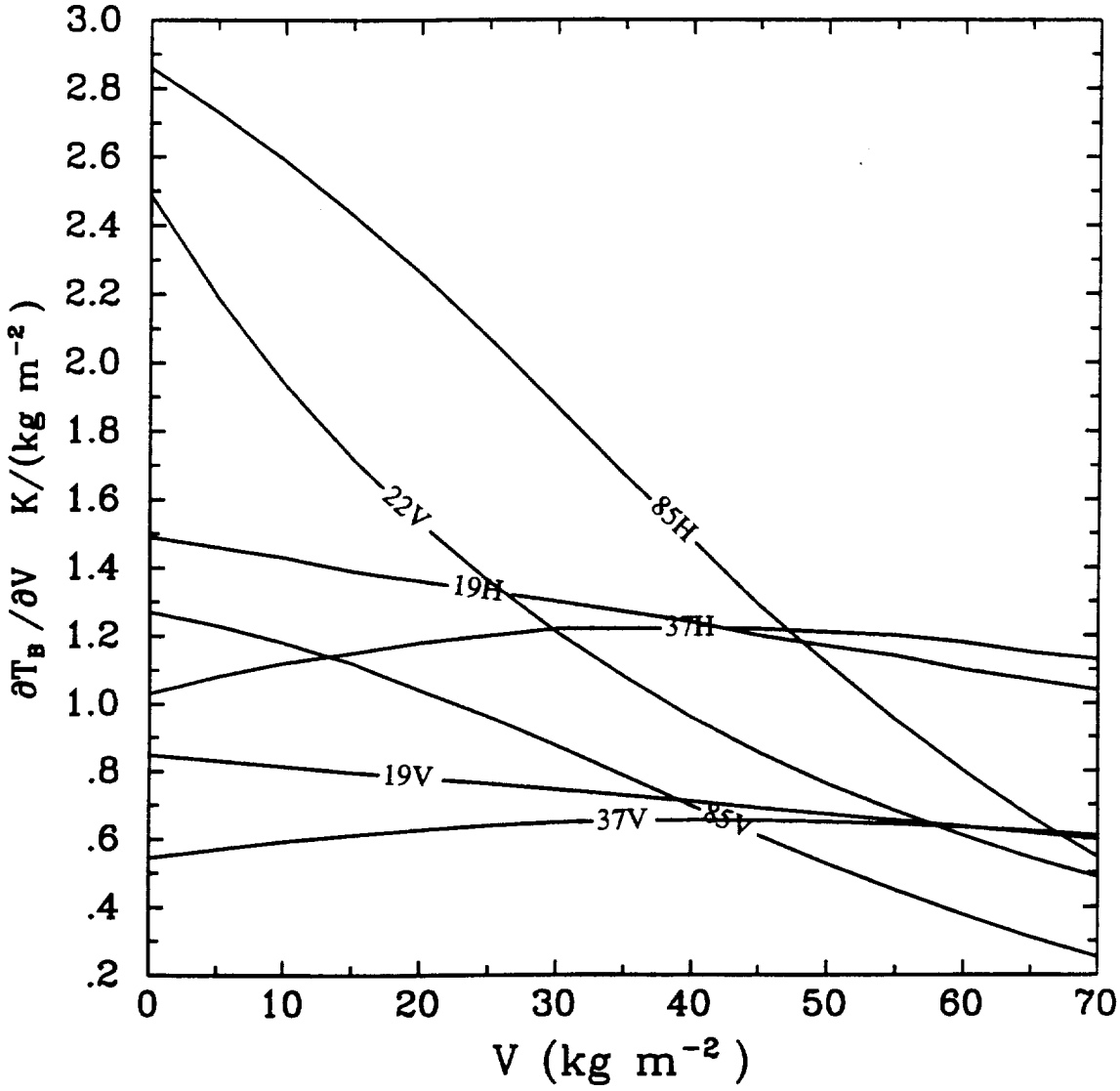

Fig. 9.4 (a) SSM/I brightness temperature sensitivities to integrated water vapor ($\partial T_B/\partial V$) as functions of V .

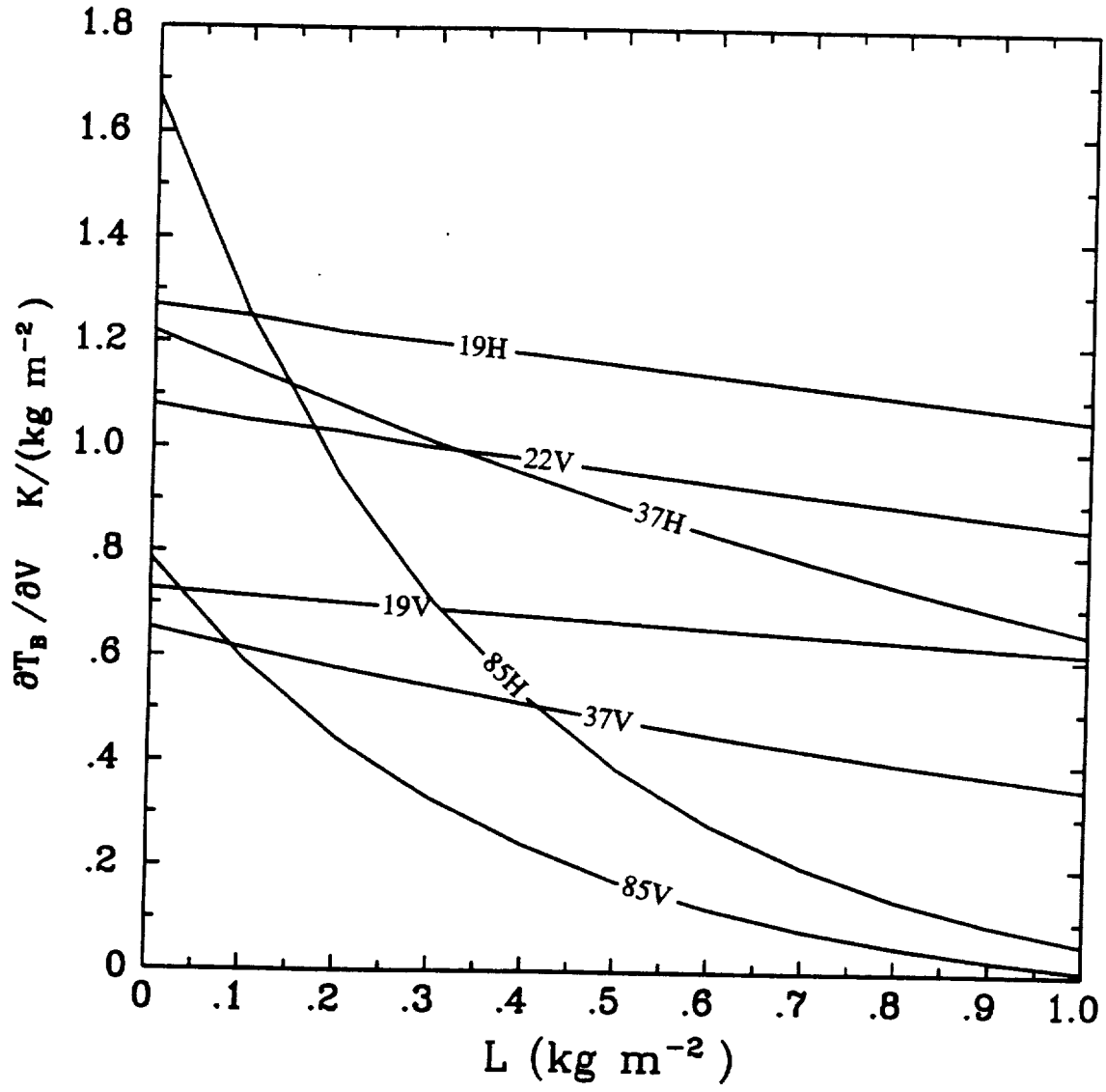

Fig. 9.4 (continued) (b) SSM/I brightness temperature sensitivities to integrated water vapor ($\partial T_B / \partial V$) as functions of L.

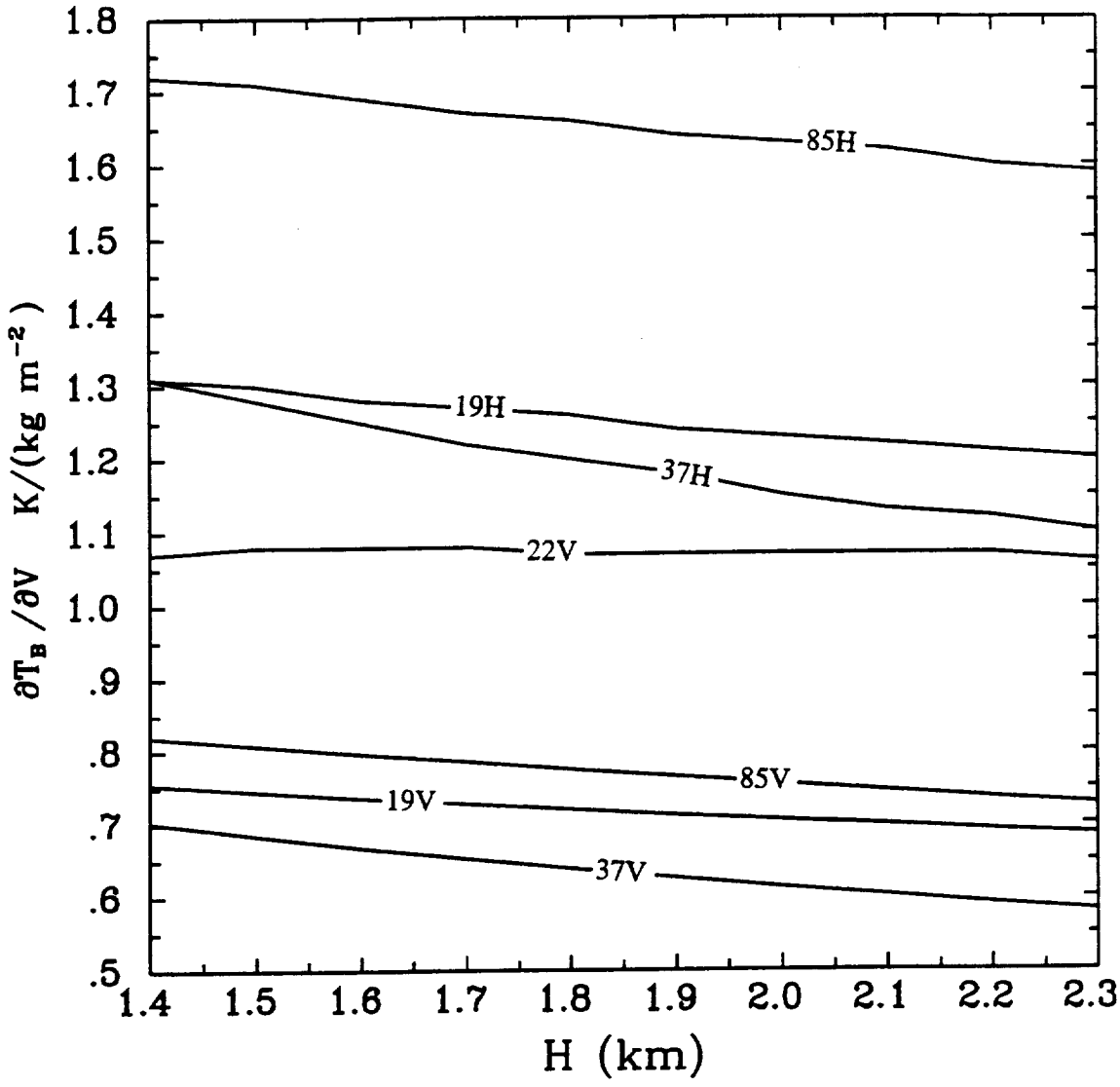

Fig. 9.4 (continued) (c) SSM/I brightness temperature sensitivities to integrated water vapor ($\partial T_B/\partial V$) as functions of H

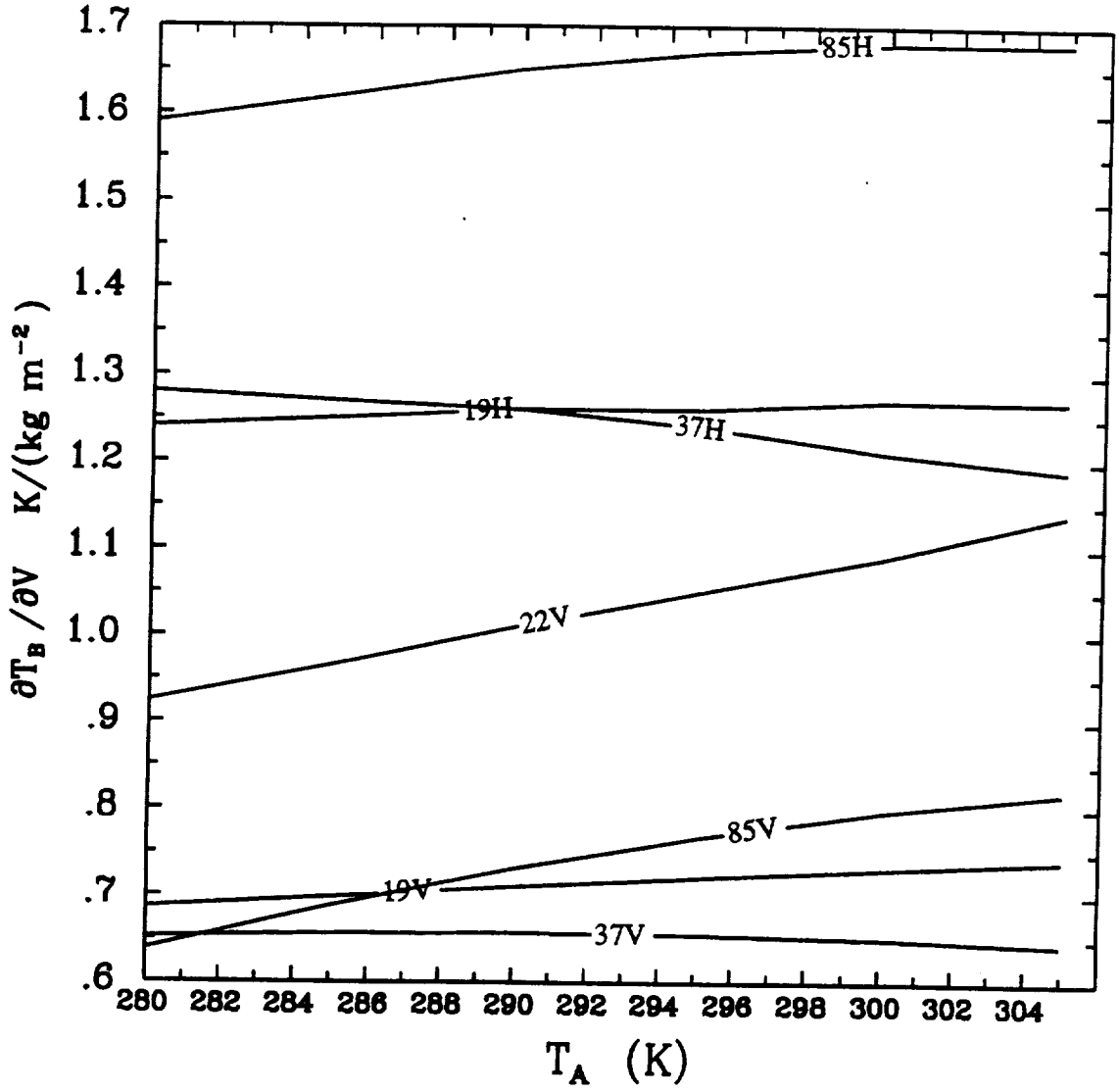

Fig. 9.4 (continued) (d) SSM/I brightness temperature sensitivities to integrated water vapor V ($\partial T_B/\partial V$) as functions of T_A .

both in mean water vapor column temperature and total opacity; consequently these channels experience a mild decrease in sensitivity to V.

Like H, the atmospheric temperature profile also affects both the absorption coefficient of water vapor and the effective radiating temperature of the atmosphere. Fig. 9.4d indicates the effect that the mean lower tropospheric temperature, varied here via the model variable T_A, has on the sensitivity of the SSM/I to V. The effect is seen to be greatest for those channels for which atmospheric opacity due to water vapor is relatively large, i.e., the 22V, 85V, and 85H channels.

The response of the SSM/I to cloud water L (Fig. 9.5) is subject to many of the same factors that influence its sensitivity to V: in general, the sensitivity of a given channel to L decreases as the atmospheric transmittance decreases. When the atmosphere is relatively transparent, i.e. for low V and low L, the 85H channel exhibits by far the greatest sensitivity to changes in L (Figs. 9.5a and 9.5b, the latter plotted for $L = 0.1$ kg m^{-2}), owing to the approximate proportionality between liquid water absorption and the square of the channel frequency.

The high sensitivity of the 85H channel to small amounts of cloud water (approximately 12 K change for the first 0.1 kg m^{-2} of water) make it an attractive candidate for use in cloud water retrievals when total atmospheric water content is relatively low, especially in view of the relatively high ($\sim$15 km) spatial resolution of the 85 GHz channels. Once either L or V becomes large, however, the 85 GHz channels rapidly saturate and lose their sensitivity to changes in L. Under such circumstances — say, in a tropical air mass, where V is almost always greater than 40 kg m^{-2} , the 37 GHz channels would appear to contain more information on changes in L. Furthermore, the non-linearity of the response of the 85 GHz channels to L implies that field-of-view (FOV) averaged L may not be estimated accurately with these channels when inhomogeneous cloud fields with locally large values of L occur within the satellite FOV.

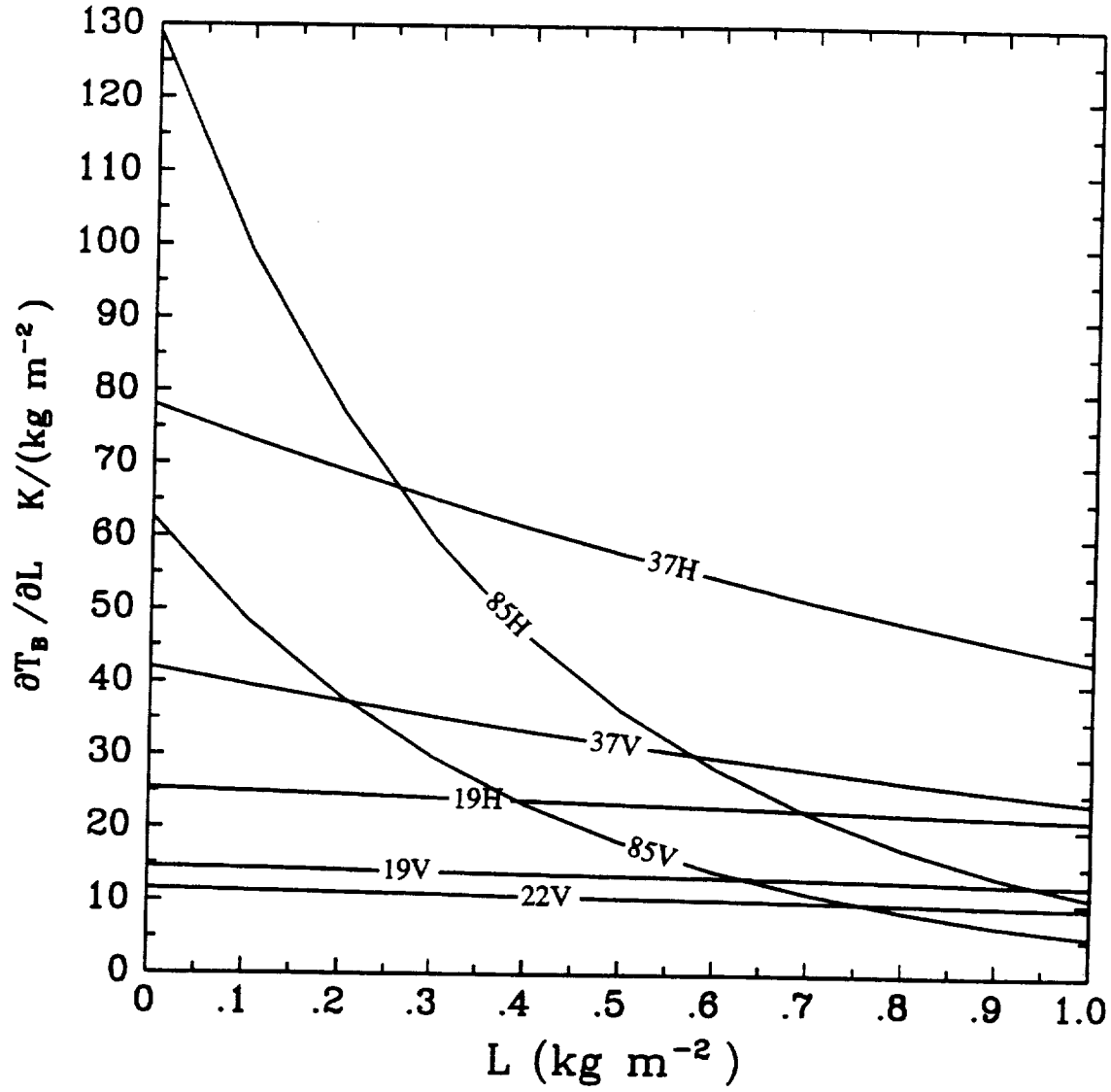

Fig. 9.5 (a) SSM/I brightness temperature sensitivities to integrated liquid water ($\partial T_B / \partial L$) as functions of L.

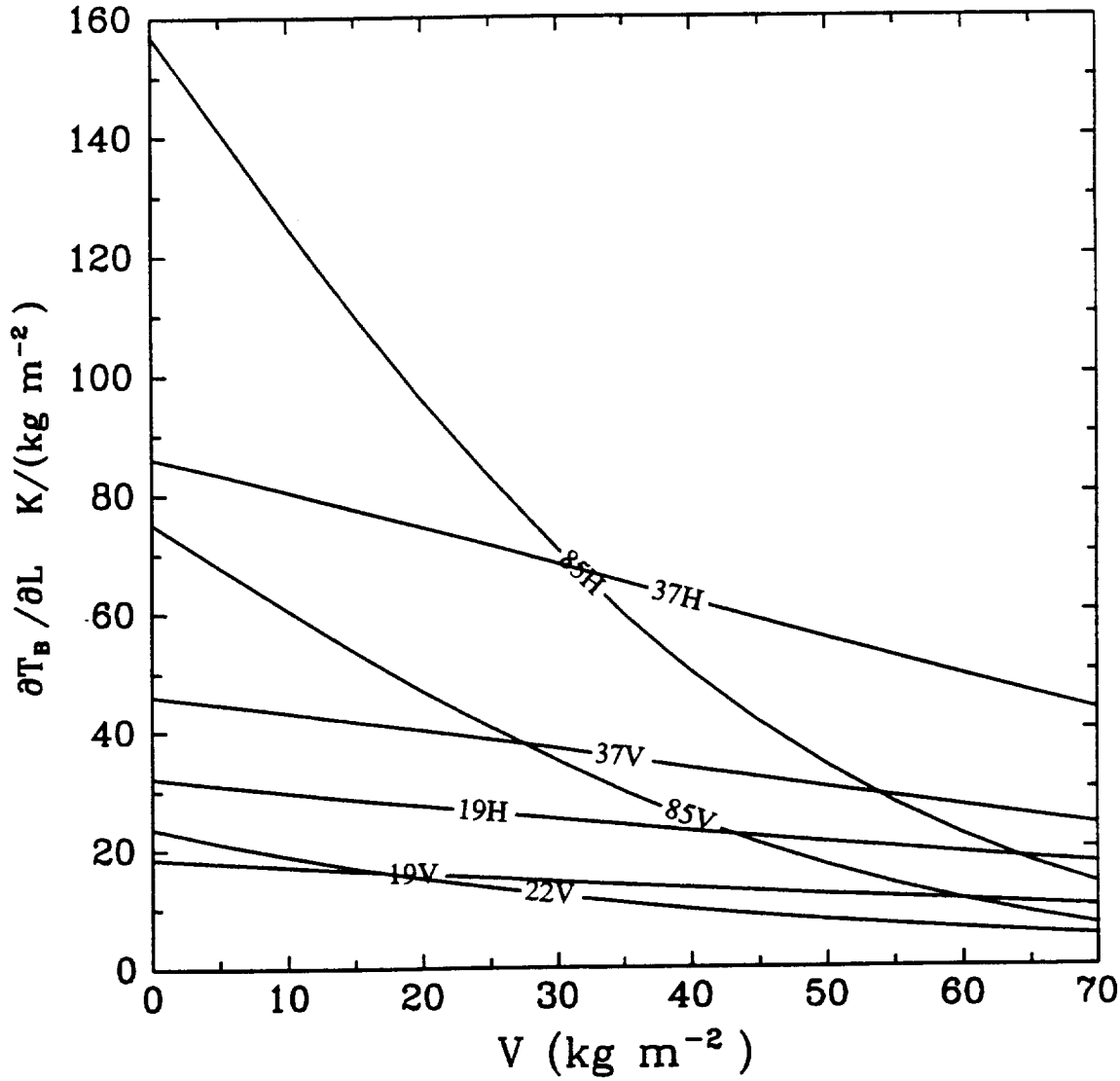

Fig. 9.5 (continued) (b) SSM/I brightness temperature sensitivities to integrated liquid water ($\partial T_B/\partial L$) as functions of V

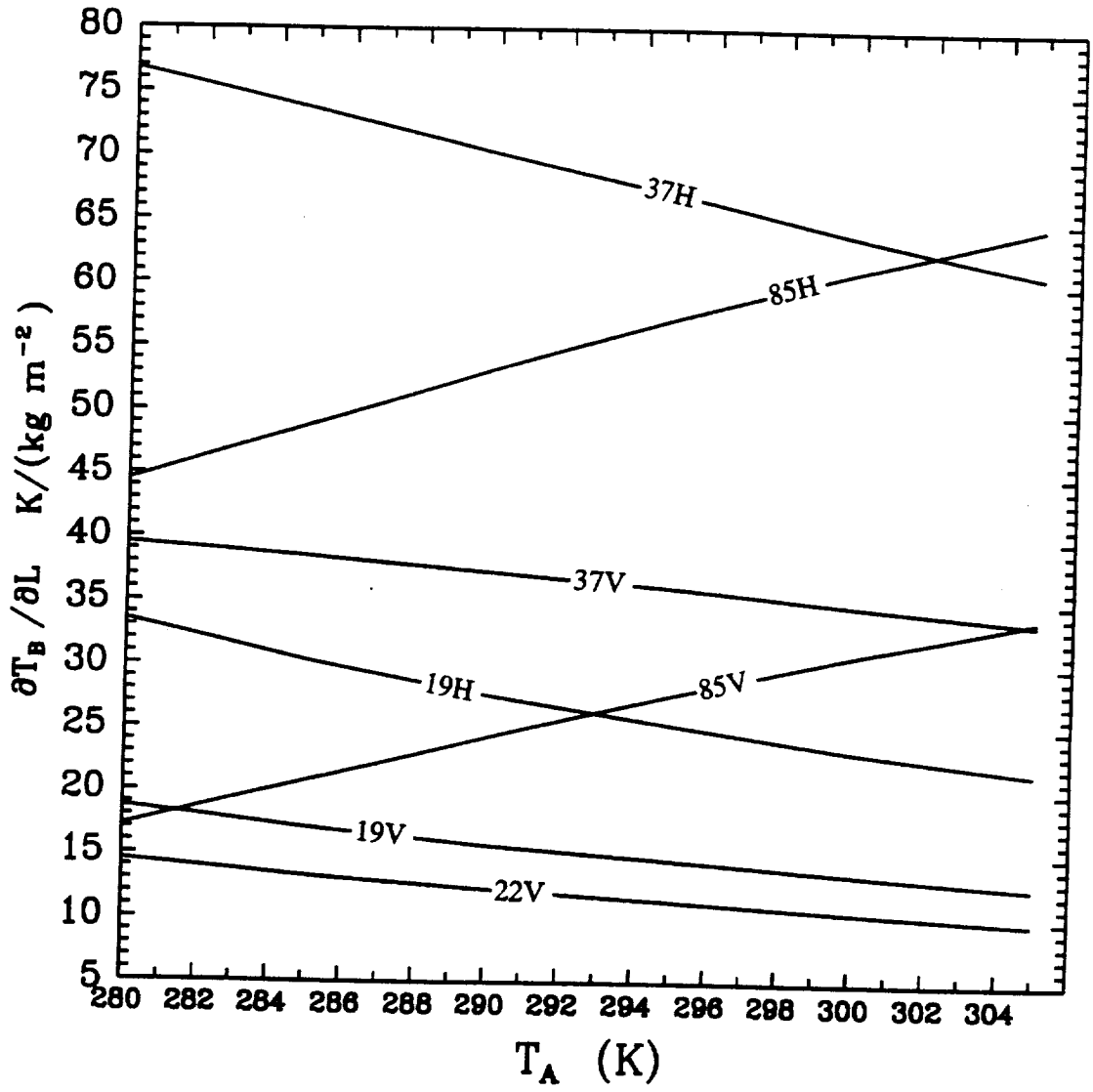

Fig. 9.5 (continued) (c) SSM/I brightness temperature sensitivities to integrated liquid water ($\partial T_B/\partial L$) as functions of T_A

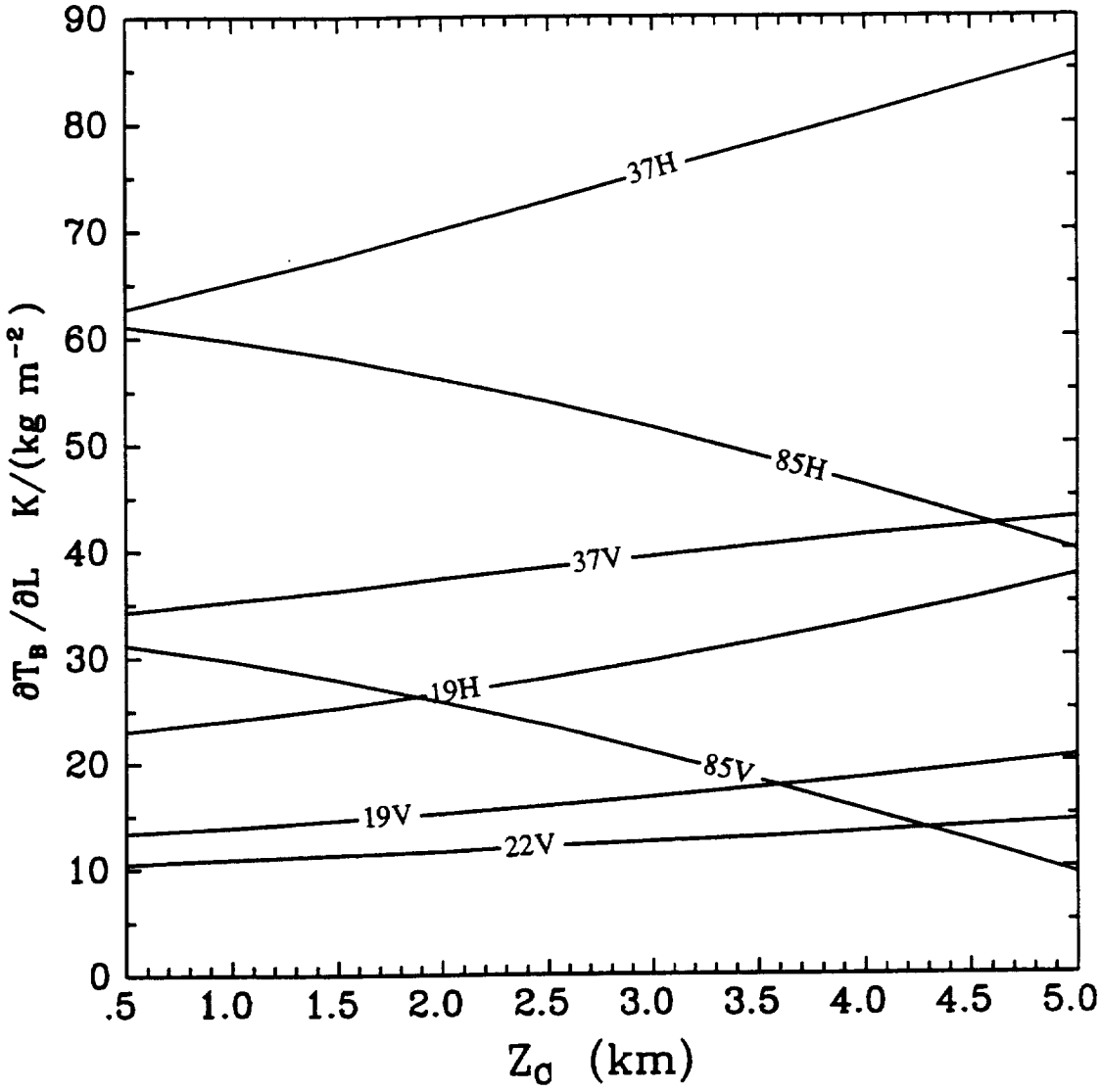

Fig. 9.5 (continued) (d) SSM/I brightness temperature sensitivities to integrated liquid water ($\partial T_B/\partial L$) as functions of z_c

As noted in section 6.2, the microwave absorption coefficient of liquid water varies significantly with cloud temperature. In the brightness temperature model, cloud temperature changes arise primarily from changes in the cloud height z_c or the surface temperature T_A (the natural variability of the lapse rate Γ is not normally large enough to be responsible for large changes in cloud temperature). Highest cloud temperatures are associated with high T_A and low z_c. For L = 0.1 kg m^{-2} , the sensitivities of each channel to L are plotted as functions of T_A and z_c in Figs. 9.5c and 9.5d, respectively. All but the 85 GHz channels show *decreasing* sensitivity to cloud water with increasing temperature, apparently because of a strong decrease in liquid water absorption which more than offsets the increase in cloud radiating temperature.

Brightness temperature changes associated with changes in U may be attributed both to large scale roughness (the effect of which is approximated by the geometric optics model of Chapter 7) and the appearance of surface foam. Large scale roughness, in turn, was seen to alter both the scene-averaged emissivity of the ocean surface and the effective zenith angle θ' of the atmospheric radiation reflected by the surface. Fig. 9.6a depicts the brightness temperature sensitivity to U as a function of U. As indicated earlier, sensitivity to large scale roughness is near zero or slightly negative for the vertical channels; it is substantially larger (~1.0 K per m s^{-1}) for the horizontal channels. The model assumption that foam increases linearly with U beginning at 7 m s^{-1} is responsible for the abrupt jump in T_B sensitivity at this wind speed (for clarity, a 3 m s^{-1} ΔU was used to compute $\partial T_B/\partial U$ for the purposes of the plot; in reality, the change in model sensitivity is discontinuous). Such an abrupt change in sensitivity is probably unphysical; the model for the dependence of foam coverage F on wind speed should eventually be refined to provide for a smoother transition from the foam-free to the foam regime, as has been done, for example, by Wentz (1983).

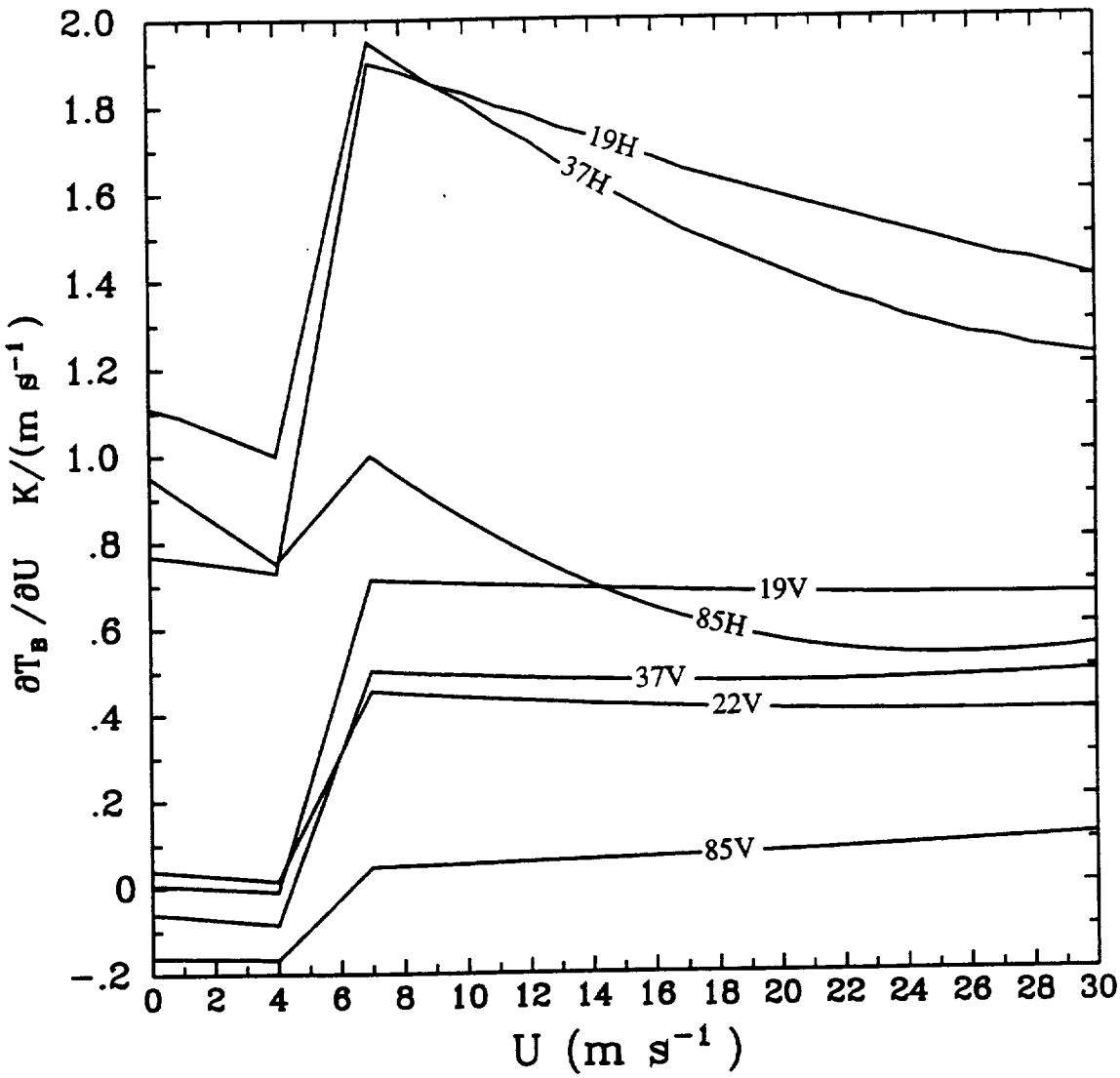

Fig. 9.6 (a) SSM/I brightness temperature sensitivities to surface wind speed ($\partial T_B / \partial U$) as functions of U .

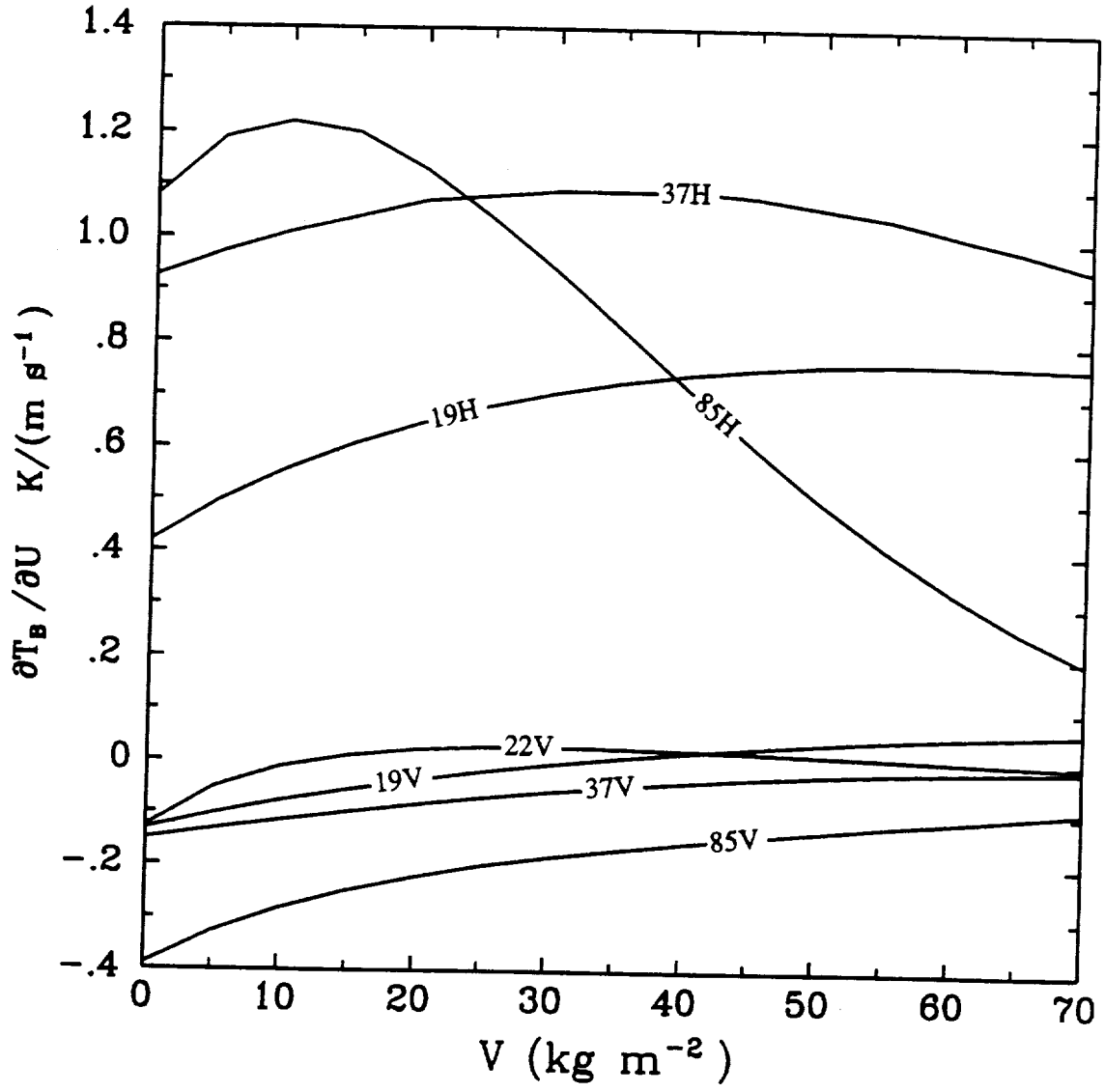

Fig. 9.6 (continued) (b) SSM/I brightness temperature sensitivities to surface wind speed ($\partial T_B/\partial U$) as functions of V .

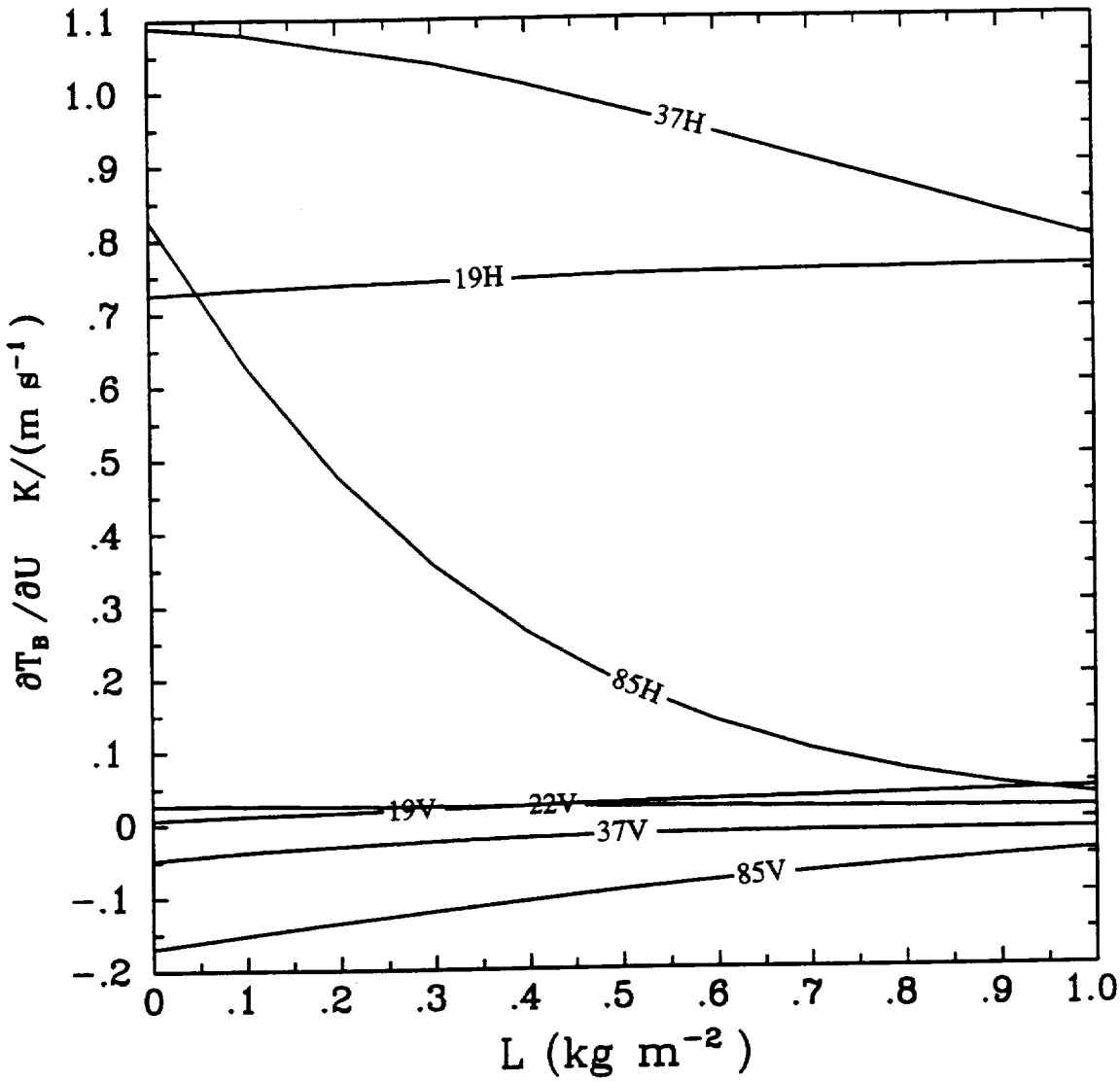

Fig. 9.6 (continued) (c) SSM/I brightness temperature sensitivities to surface wind speed ($\partial T_B/\partial U$) as functions of L .

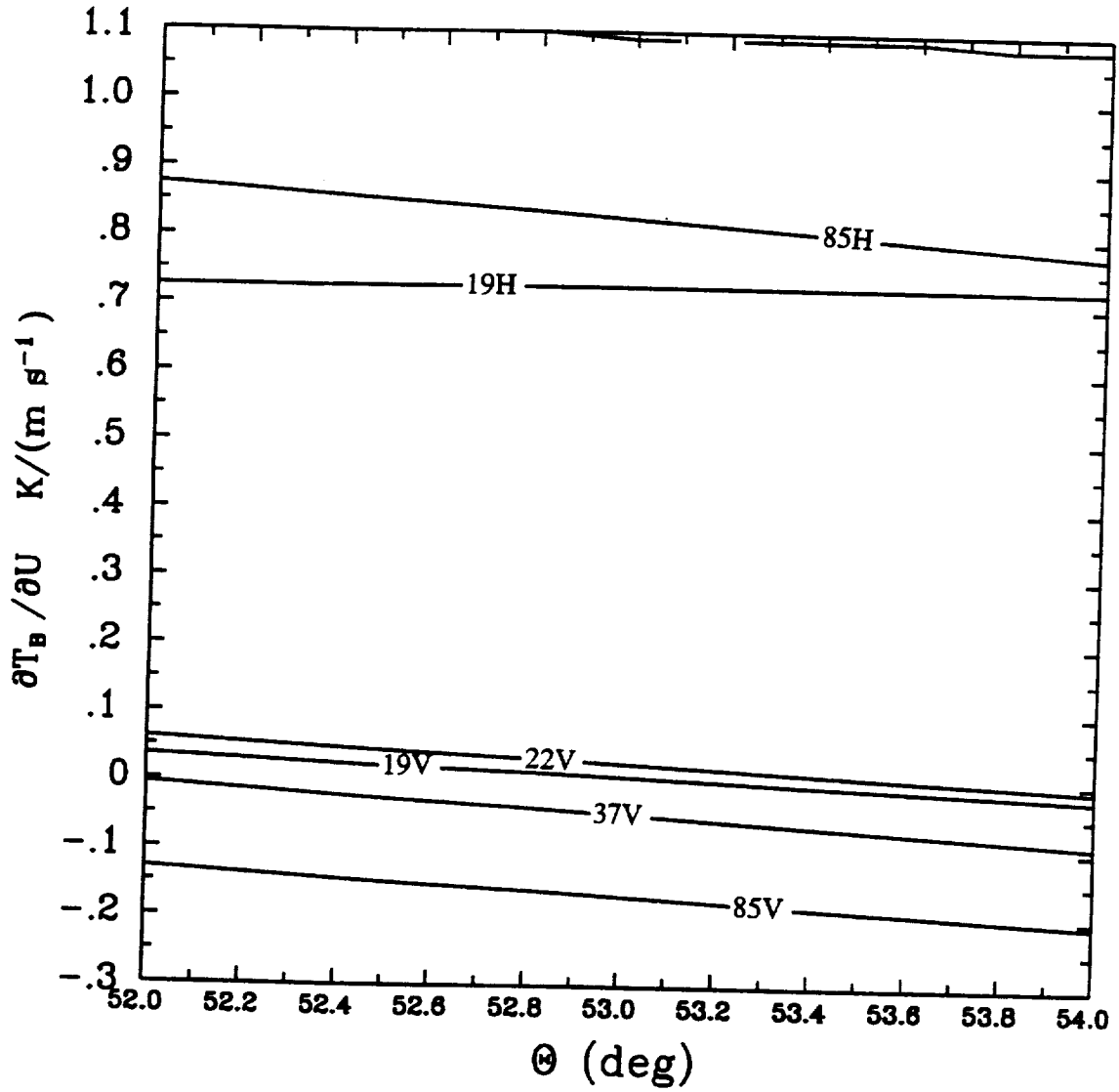

Fig. 9.6 (continued) (d) SSM/I brightness temperature sensitivities to surface wind speed ($\partial T_B/\partial U$) as functions of θ .

The fall-off in sensitivity to U at high wind speeds is mainly associated with decreases in the brightness temperature sensitivity to further roughness changes. In fact, if the foam component were absent, the sensitivity of all SSM/I channels to changes in U would fall to $\lesssim 0.2$ K per m s^{-1} for U near 30 m s^{-1} . The quantitative accuracy of this result depends on the model assumption that the effective surface slope variance g^2 at each frequency is linear in U. Of course, the validity of this assumption over such wide range of wind speeds cannot be easily tested without the help of coincident SSM/I and *in situ* measurements of wind speeds at the high end of the scale.

The relationship between V or L and the T_B sensitivity to wind speed, evaluated at $U = 5.0$ m s^{-1} , is shown in Figs. 9.6b and 9.6c. Not surprisingly, the effect of large atmospheric opacity is to reduce the sensitivity. However, given a relatively transparent atmosphere — e.g., for $V \lesssim 10$ kg m^{-2} and $L = 0$ (Fig. 9.6b), modest increases in opacity lead to significant *increases* in the sensitivity of the horizontal channels to changes in U. This increase in sensitivity can only be due to a rapid increase in the contribution of surface scattered radiation with increasing opacity; that is to say, $\partial^2 T_B^S / \partial\sigma\partial g^2$ is large and positive. Support for this interpretation may be found in Fig. 7.2b for $\sigma \lesssim 0.1$. For larger opacities, Fig. 7.2b suggests that the effect is greatly reduced, so that changes in diffusely scattered radiation play an ever smaller role in the brightness temperature sensitivity to U. To the author's knowledge, no previously published microwave brightness temperature model — analytic or numerical — correctly handles these aspects of the T_B dependence on U.

The dependence of $\partial T_B / \partial U$ is seen in Fig. 9.6d to depend only very weakly on reasonable changes in viewing angle θ. It is worth noting that three of the four vertically polarized channels — 19V, 22V, and 37V — each have null sensitivity to U at viewing angles within about 1° of the SSM/I's nominal viewing angle of 53.1°.

Fig 9.7 shows that the SSM/I response to sea surface temperature T_S is weak under almost all conditions, amounting to no more than a few tenths of a degree change in T_B per degree change in T_S for all channels. Moreover, the *sign* of the sensitivity may change with T_S, V or U. For both reasons, the SSM/I is not capable of retrieving useful estimates of T_S, in contrast to the earlier instrument, the SMMR, whose 6.6 GHz channels were both much more sensitive to T_S and relatively unaffected by atmospheric attenuation.

The remaining figures in this chapter (Figs. 9.8–9.13) illustrate the sensitivity of SSM/I brightness temperatures to vapor scale height H, air temperature T_A, lapse rate Γ, surface pressure p_0, cloud height z_c, and viewing angle θ. A detailed discussion will not be attempted here, except to note that the SSM/I sensitivity to each of these is relatively small compared to its sensitivity to V, L, and U. In viewing Figs. 9.8–9.13, it is worth keeping in mind the maximum probable uncertainties in the values of these secondary parameters (see Table 6.5) in order to estimate the magnitude of the associated brightness temperature perturbations. Later, it will be shown that uncertainties in the non-retrievable parameters may be regarded as a source of 'noise' in the retrieval of V, L, and U.

It should also be borne in mind that the sensitivities to geophysical parameters have been described above for a single set of base conditions, and these are given here for illustration purposes only. For a different set of base conditions, say for different V or U, plots of various sensitivities might differ considerably from those presented here. It is because of the relatively complex non-linear interactions between various environmental parameters that a comprehensive analytic model for SSM/I brightness temperatures is indispensable for understanding the information content of SSM/I multichannel imagery.

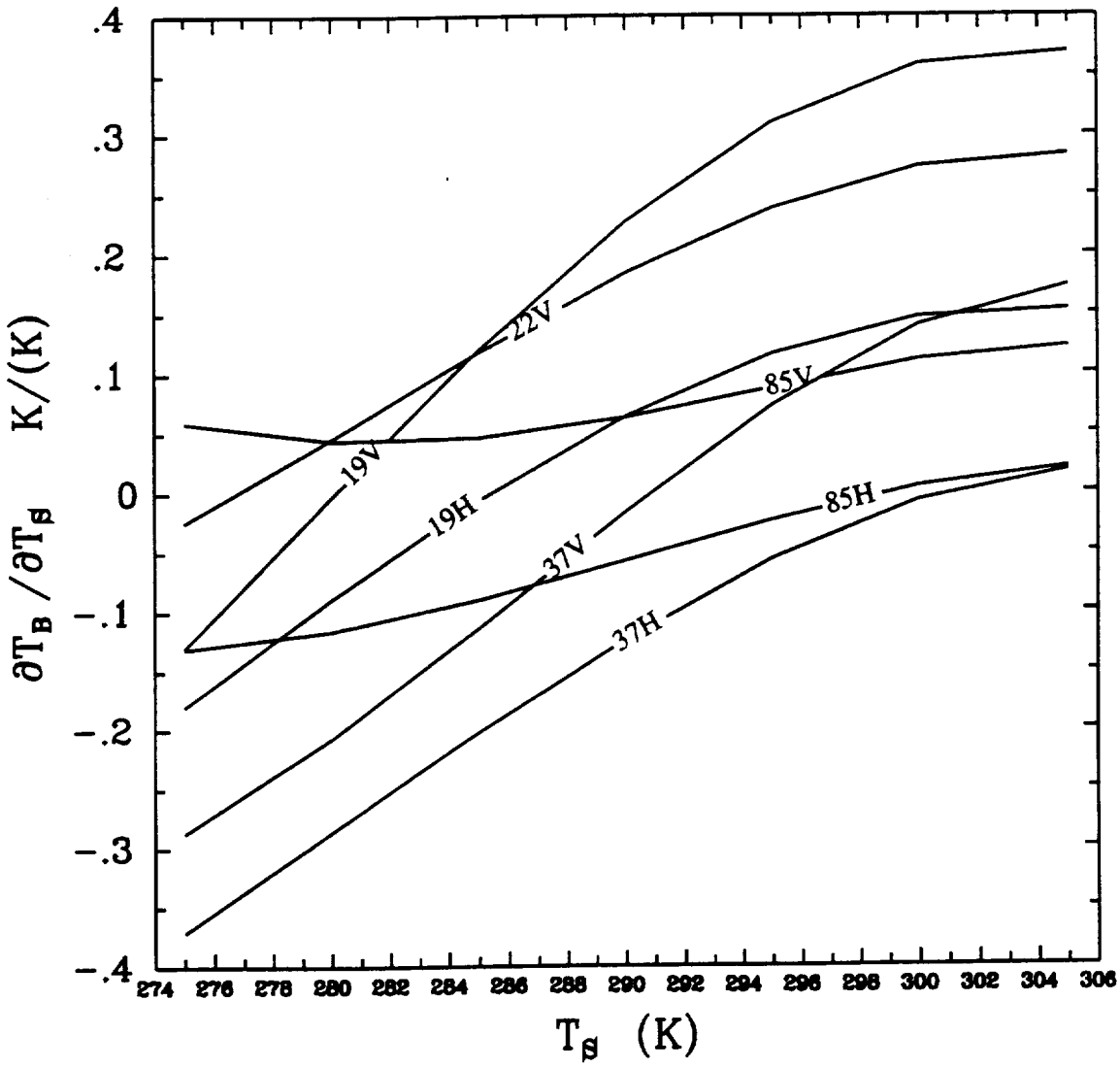

Fig. 9.7 (a) SSM/I brightness temperature sensitivities to sea surface temperature ($\partial T_B / \partial T_S$) as functions of T_S .

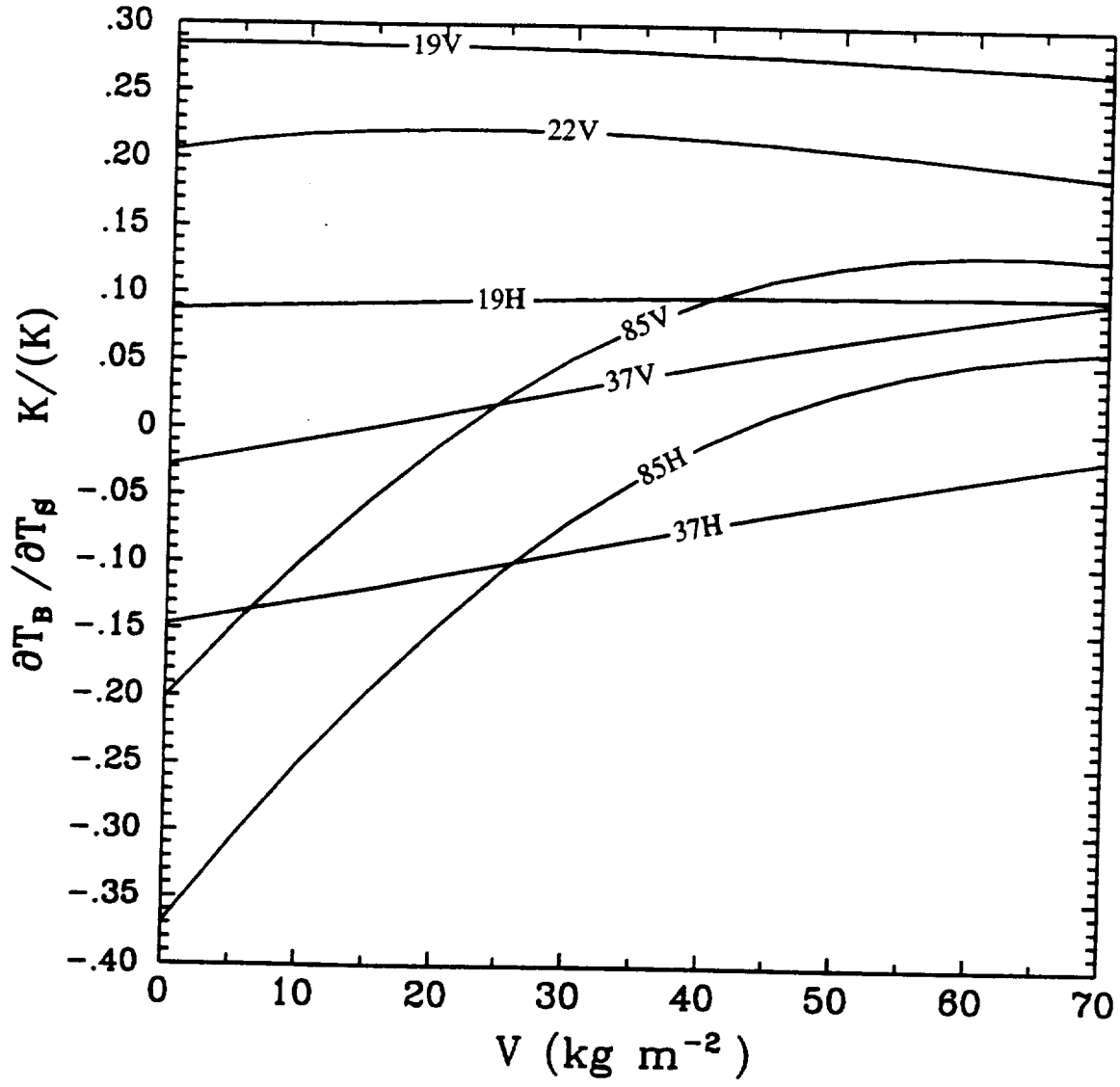

Fig. 9.7 (continued) (b) SSM/I brightness temperature sensitivities to sea surface temperature ($\partial T_B/\partial T_S$) as functions of V .

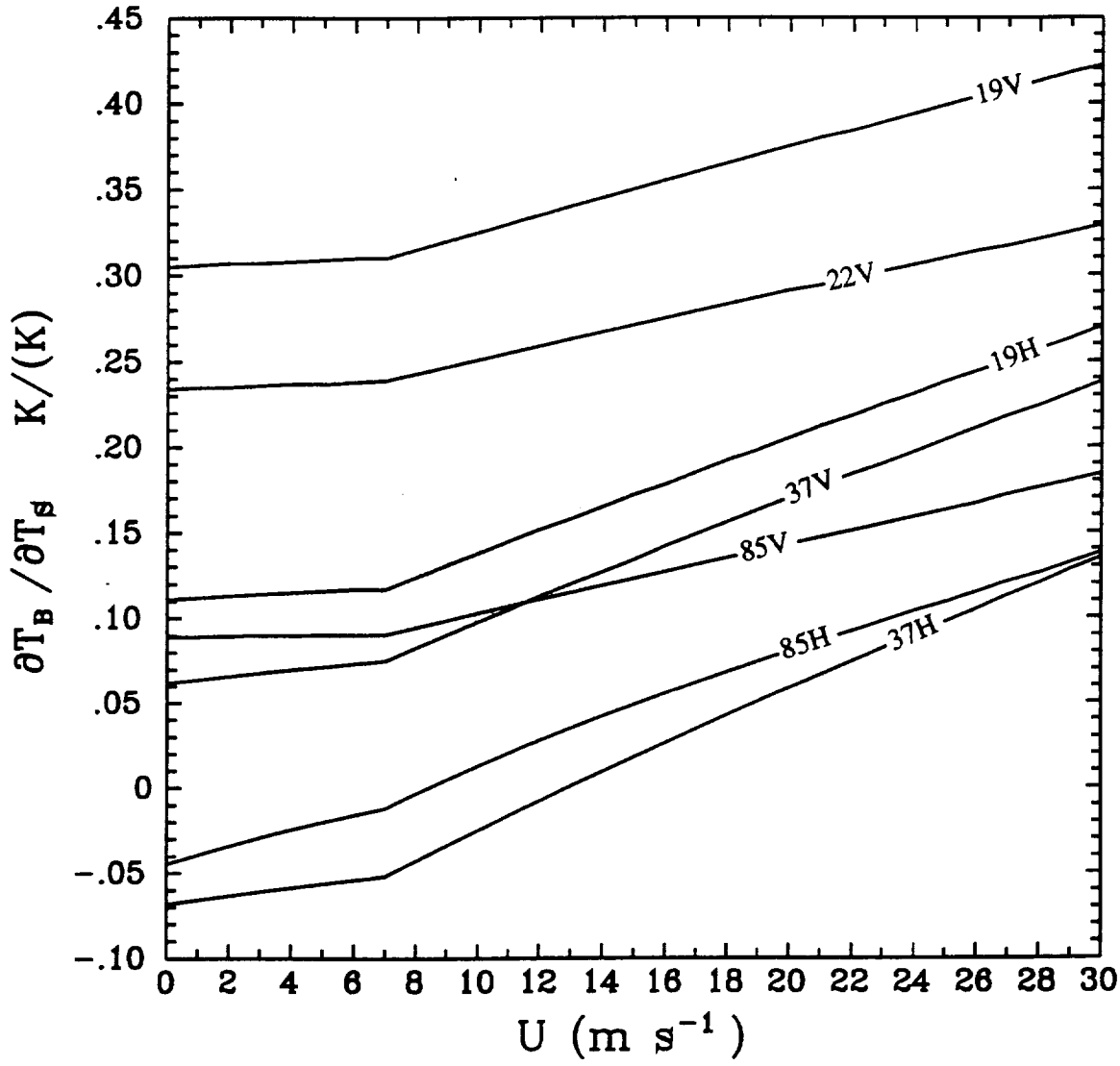

Fig. 9.7 (continued) (c) SSM/I brightness temperature sensitivities to sea surface temperature ($\partial T_B / \partial T_S$) as functions of U .

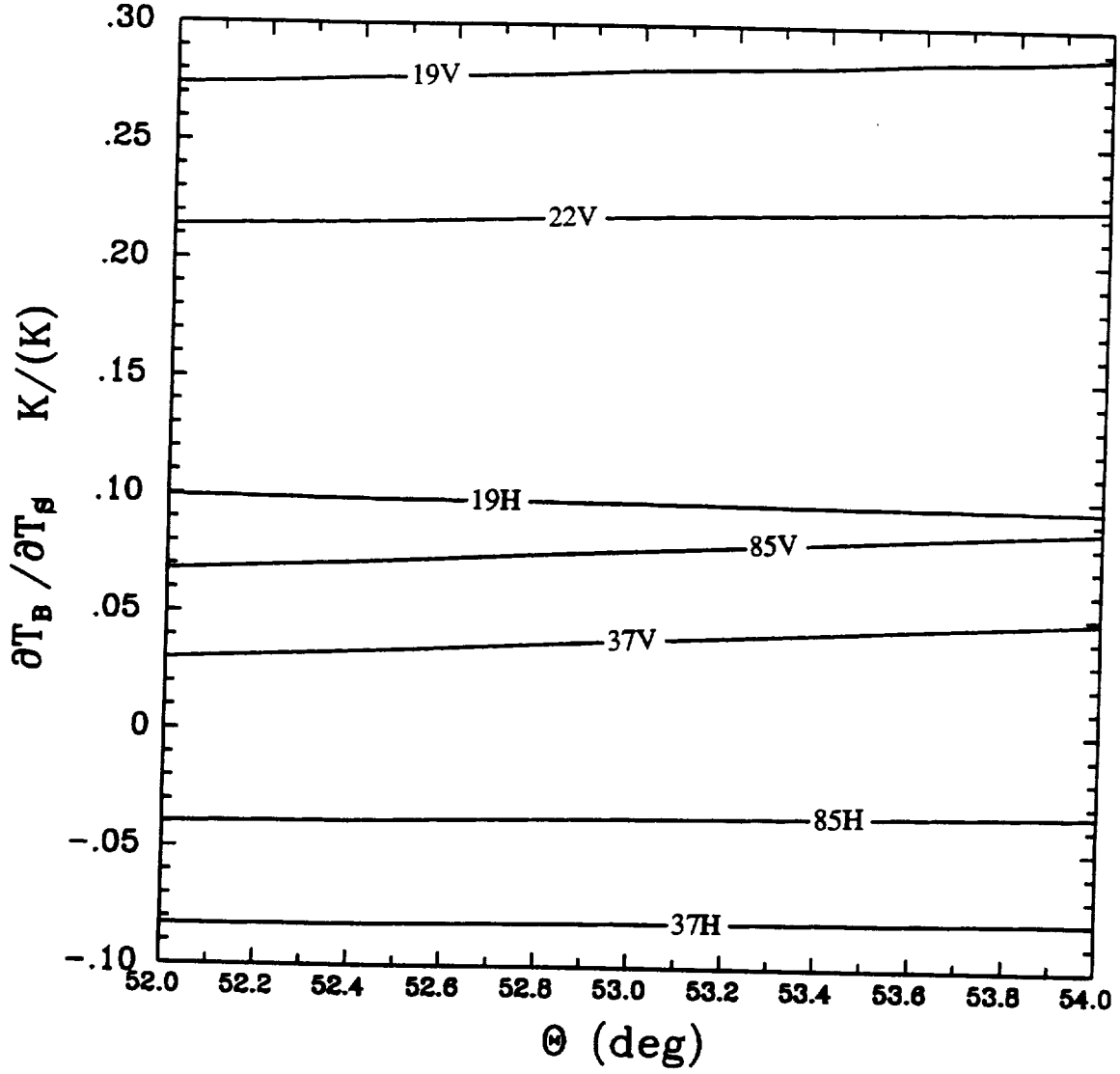

Fig. 9.7 (continued) (d) SSM/I brightness temperature sensitivities to sea surface temperature ($\partial T_B/\partial T_S$) as functions of θ .

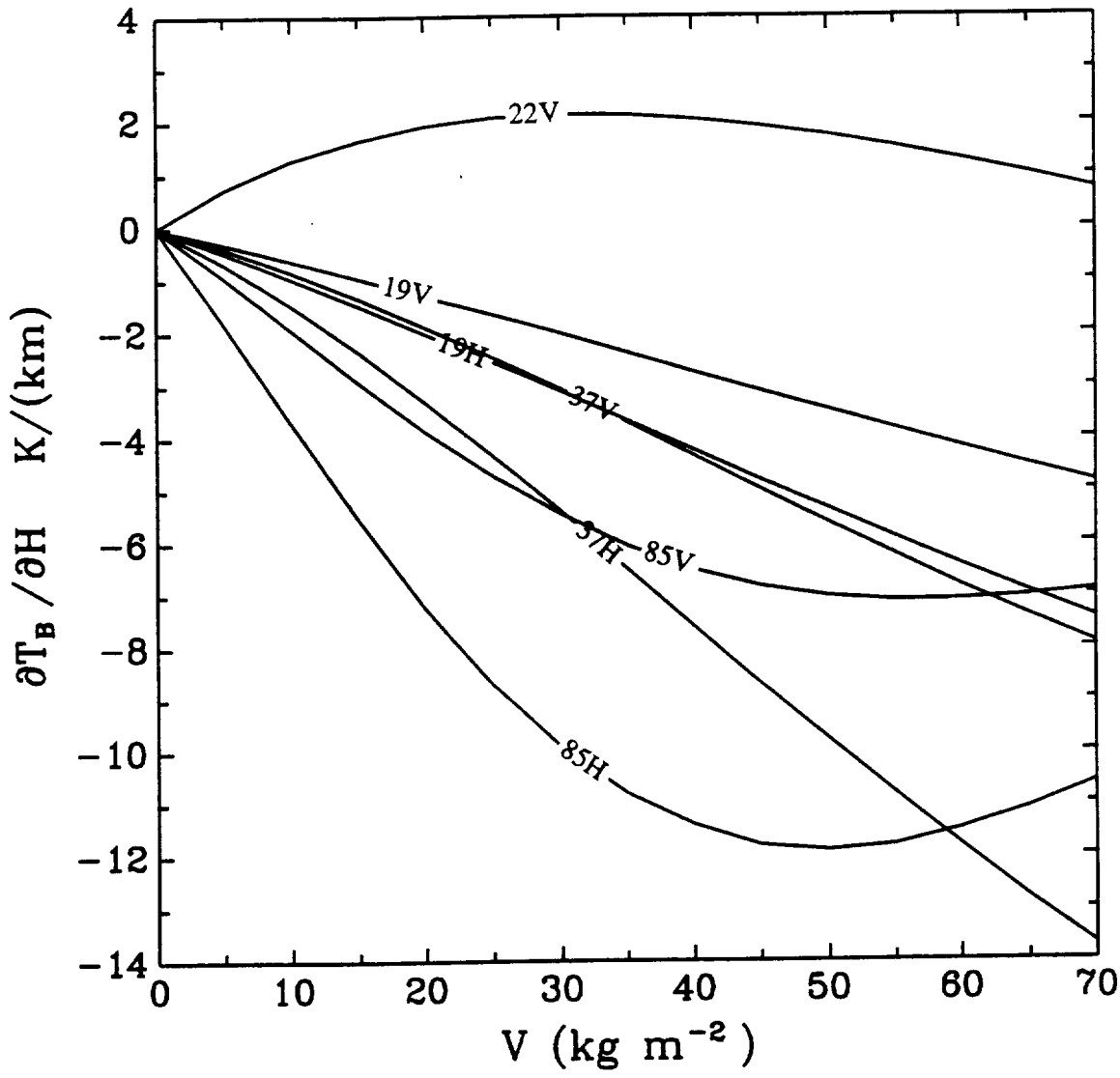

Fig. 9.8 SSM/I brightness temperature sensitivities to vapor scale height ($\partial T_B/\partial H$) as functions of V .

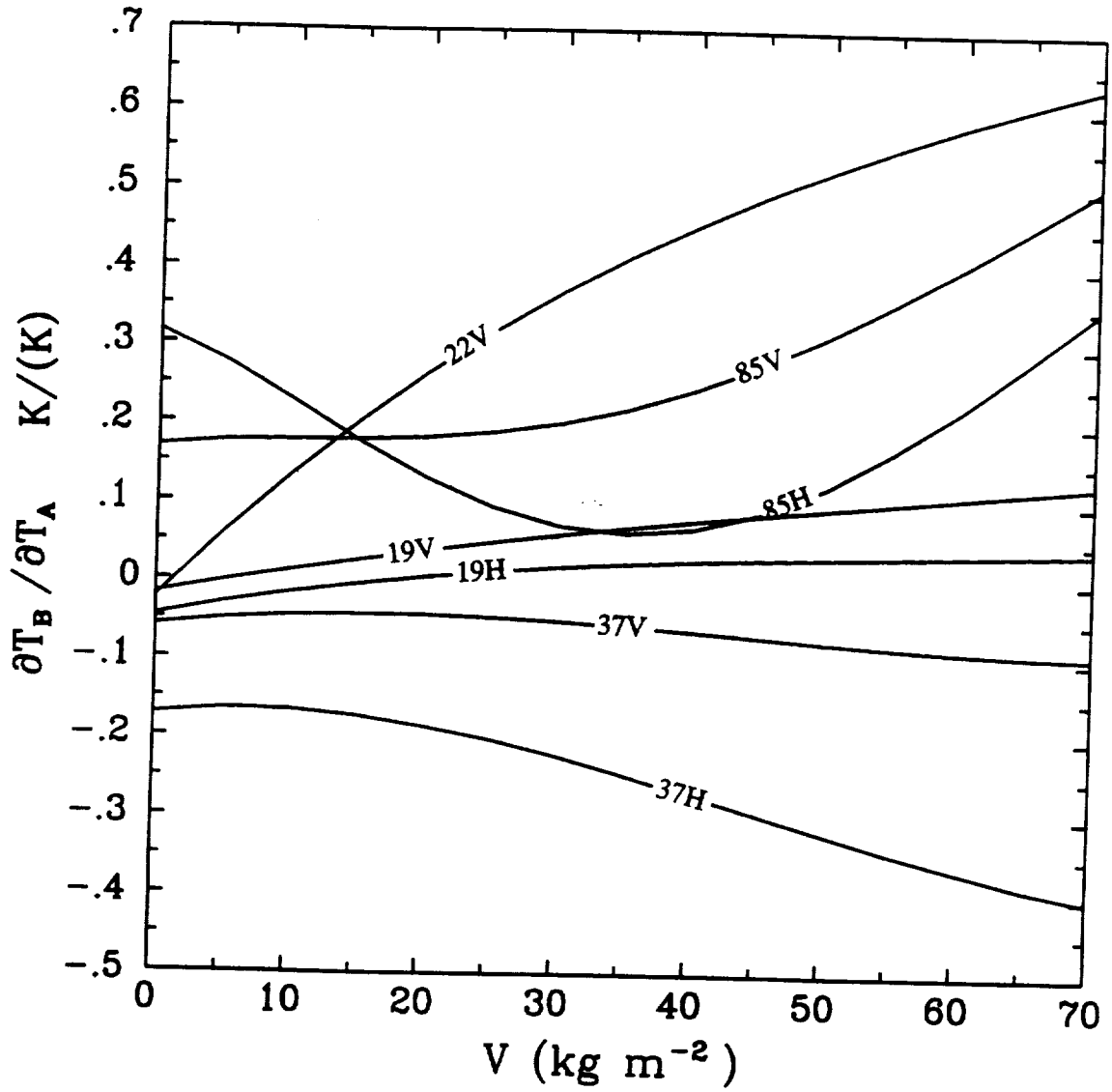

Fig. 9.9 (a) SSM/I brightness temperature sensitivities to effective surface atmospheric temperature ($\partial T_B/\partial T_A$) as functions of V .

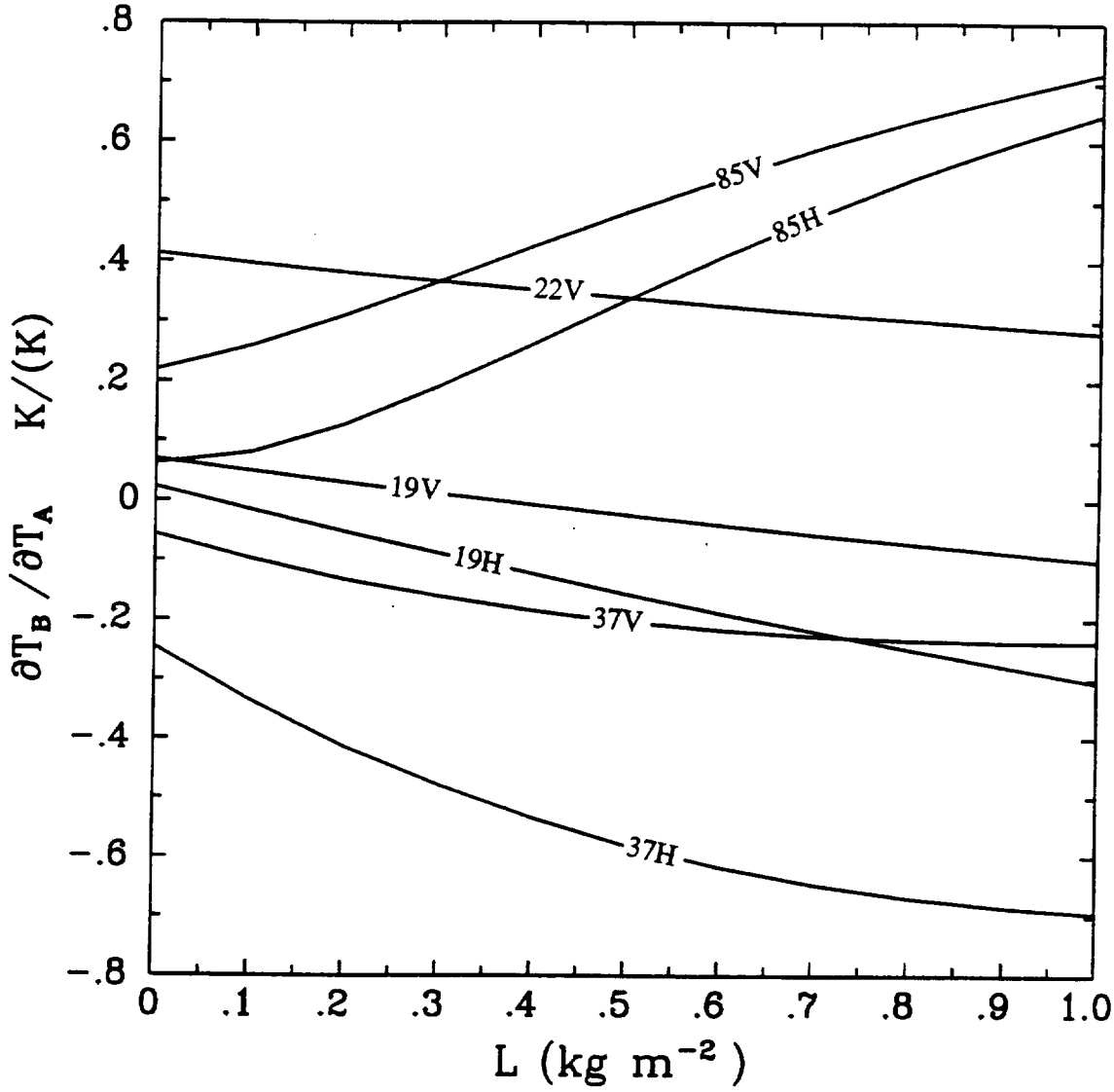

Fig. 9.9 (continued) (b) SSM/I brightness temperature sensitivities to effective surface atmospheric temperature ($\partial T_B / \partial T_A$) as functions of L .

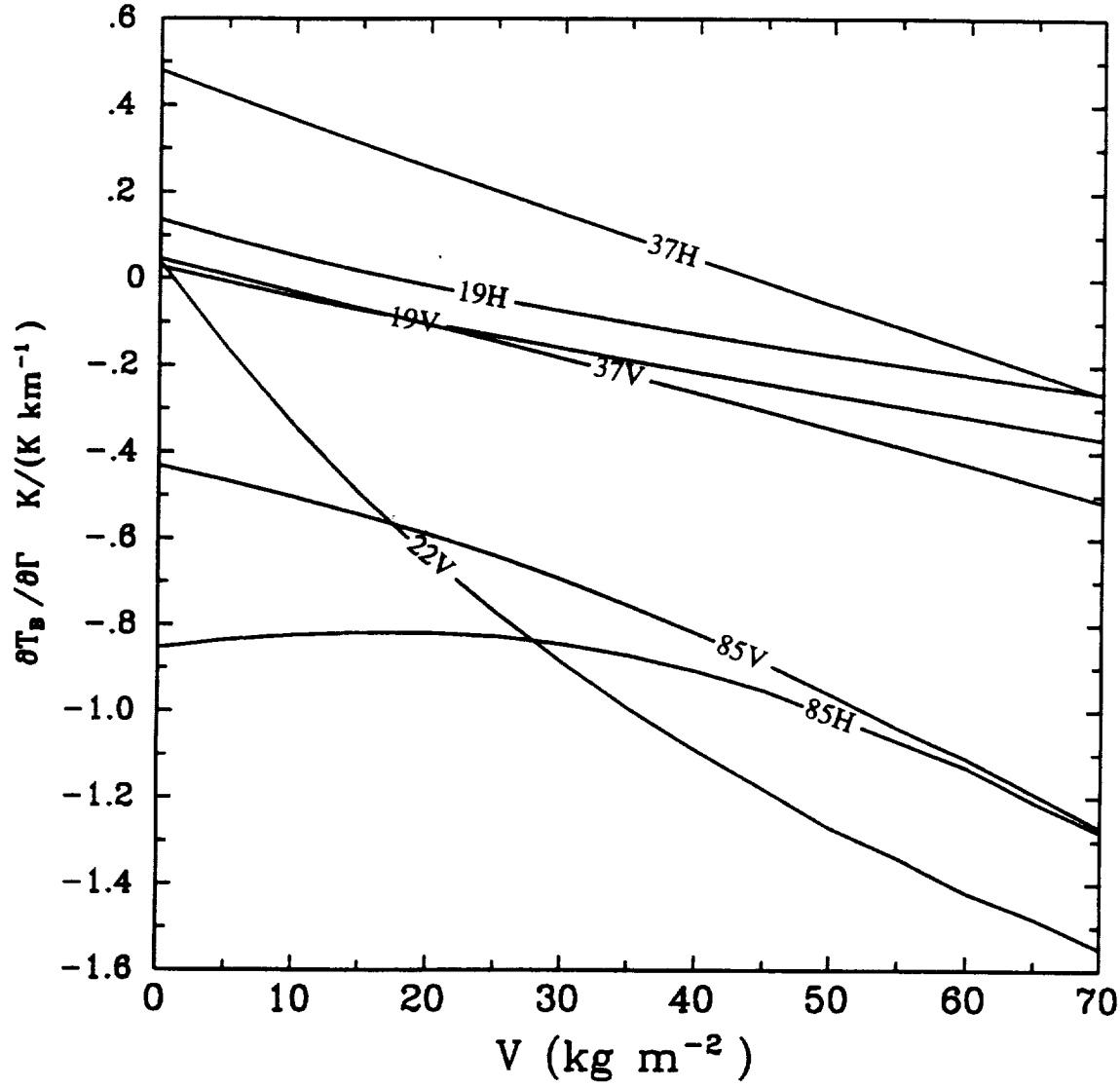

Fig. 9.10 SSM/I brightness temperature sensitivities to effective atmospheric lapse rate ($\partial T_B / \partial \Gamma$) as functions of V .

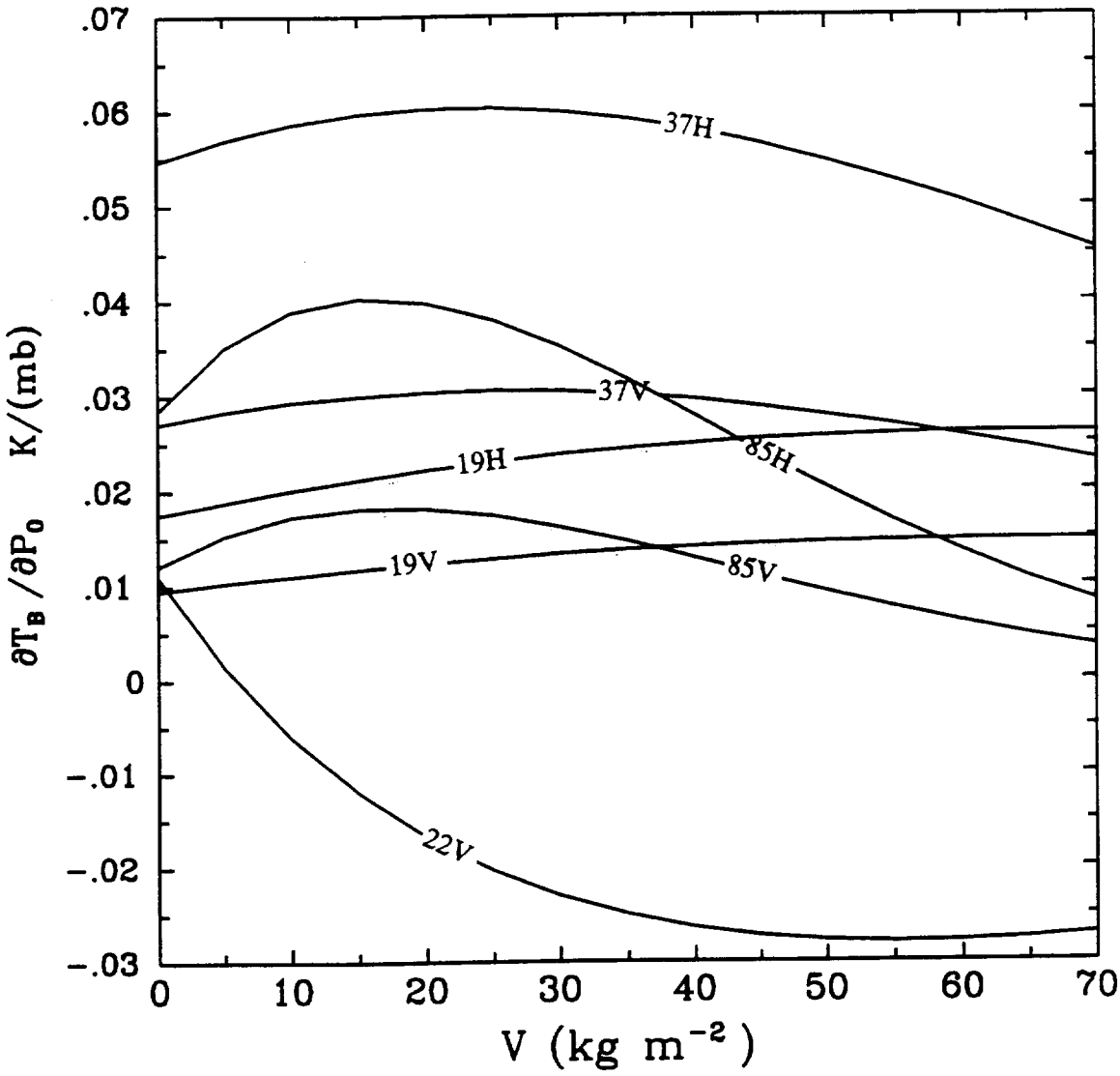

Fig. 9.11 SSM/I brightness temperature sensitivities to surface pressure ($\partial T_B / \partial p_0$) as functions of V .

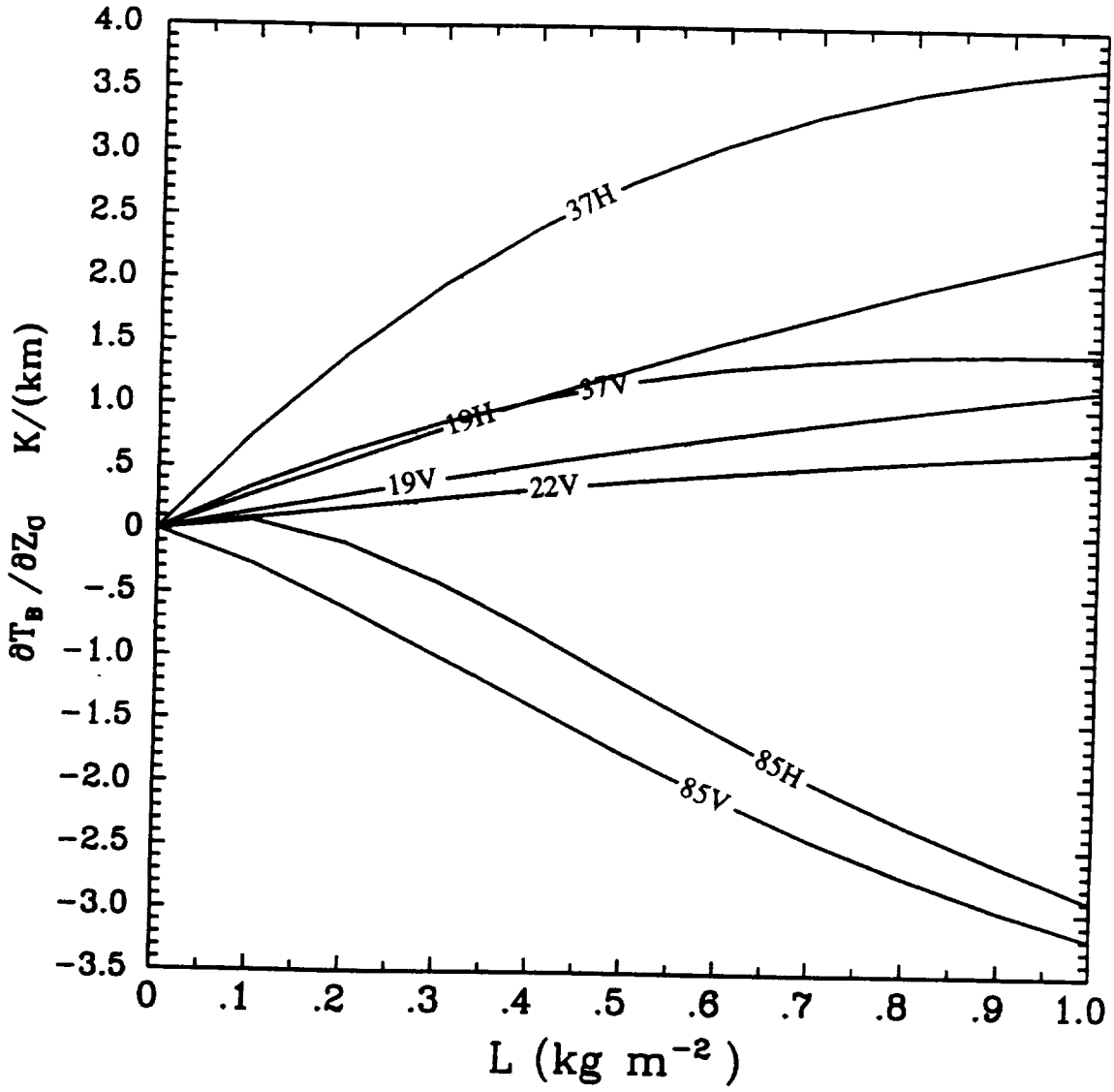

Fig. 9.12 SSM/I brightness temperature sensitivities to cloud height ($\partial T_B / \partial z_c$) as functions of L .

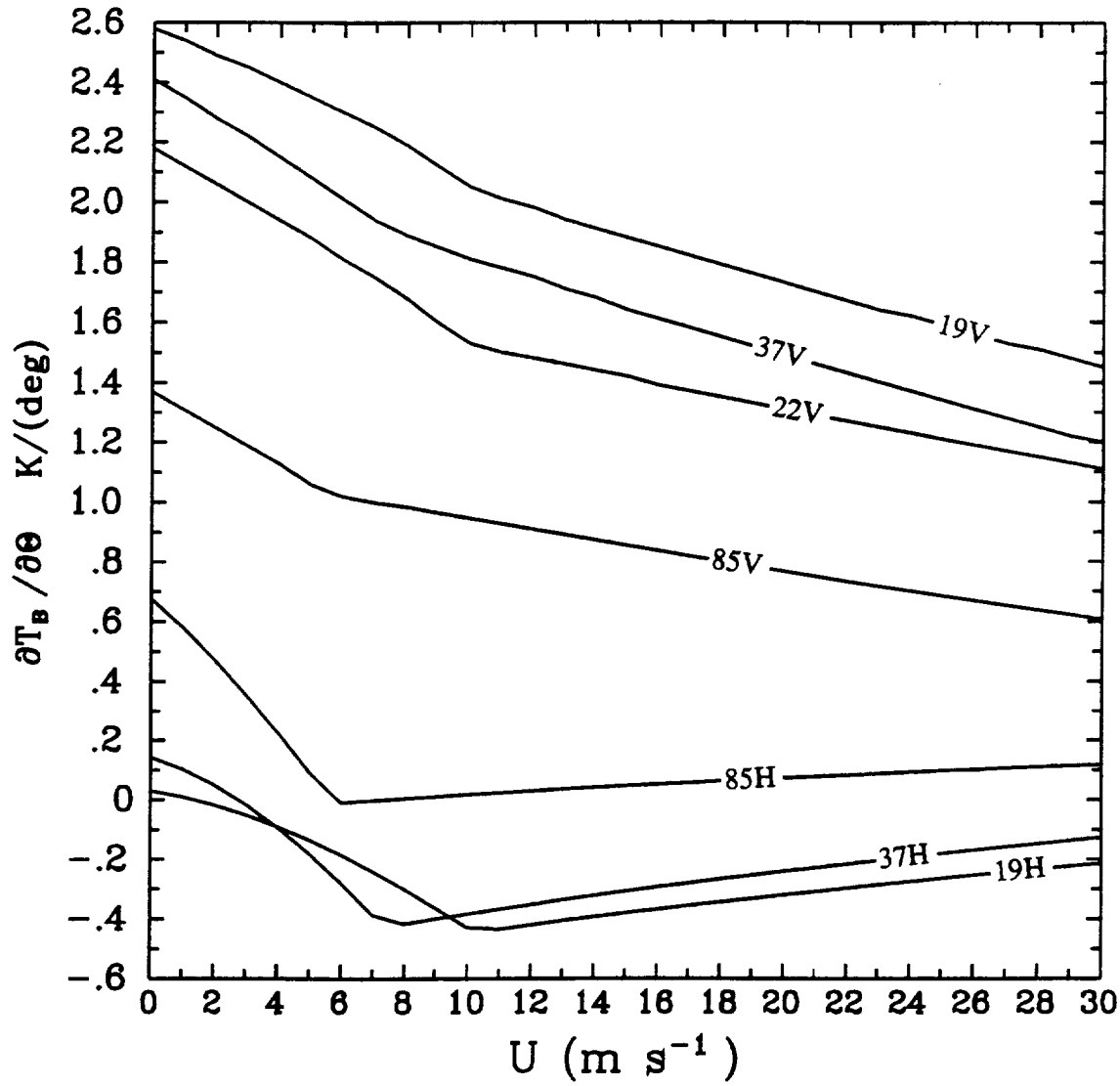

Fig. 9.13 (a) SSM/I brightness temperature sensitivities to viewing angle ($\partial T_B/\partial\theta$) as functions of U .

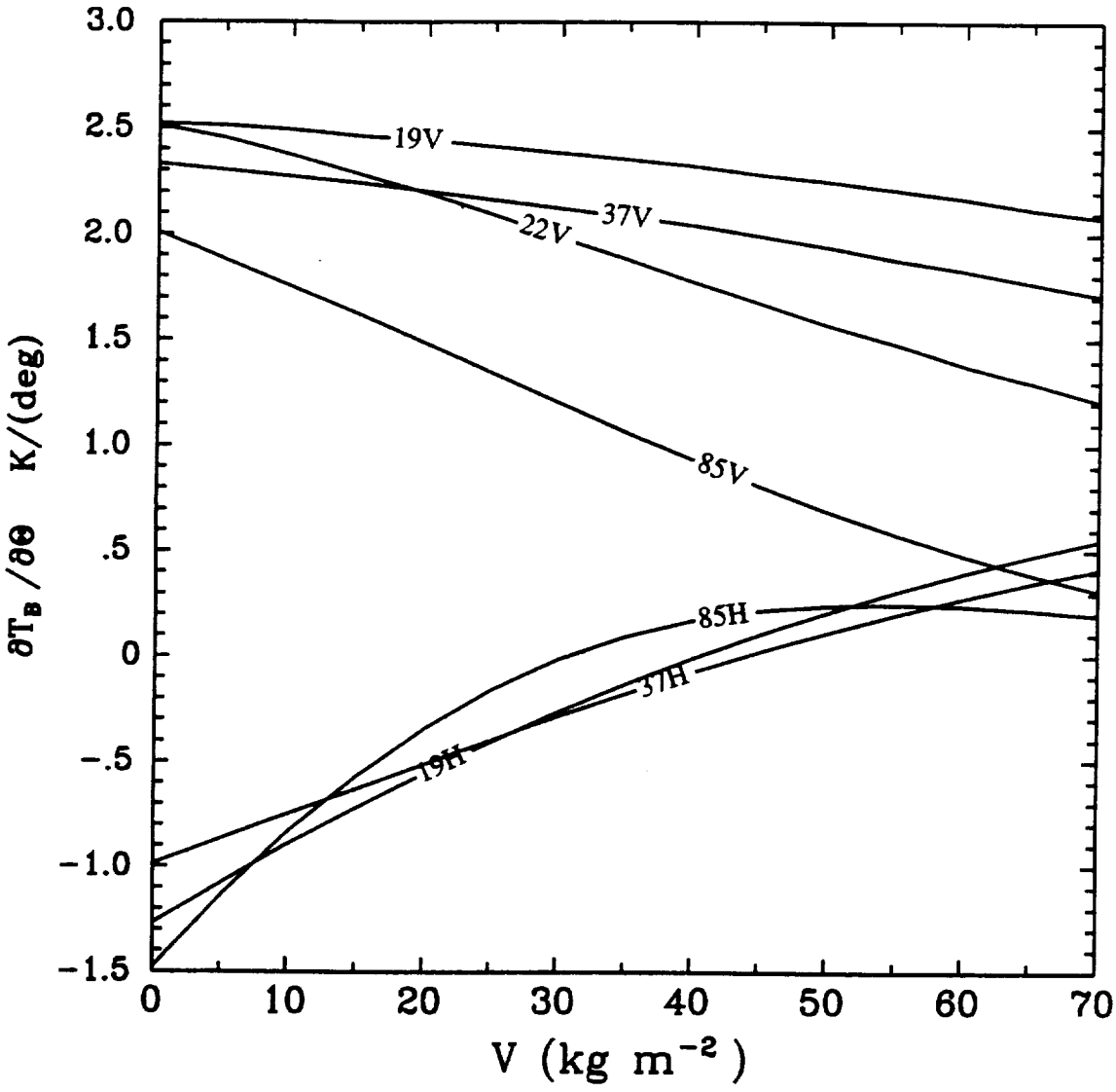

Fig. 9.13 (continued) (b) SSM/I brightness temperature sensitivities to viewing angle ($\partial T_B/\partial\theta$) as functions of V .

10. PRECIPITATION

In contrast to cloud droplets (cf. Chapter 6), the sizes of precipitation particles are generally too large compared with SSM/I wavelengths to permit the use of the small-sphere approximation (Eq. 6.2) for calculating microwave extinction. Furthermore, multiple scattering of microwave radiation by hydrometeors becomes important, and rain intensity and drop size distribution may vary dramatically over very short distances in both the vertical and horizontal. Aspherical precipitation particles, whose extinction and scattering properties may be both extremely difficult to model theoretically* and are likely to vary considerably from one storm to the next, may also play a decisive role in determining the satellite-observed microwave brightness temperature of a precipitating cloud system. For these reasons, calculations of microwave transfer through rain clouds are quite complex and must normally be based on rather extreme simplifications of both the spatial distributions (in three dimensions) and angular characteristics of scattering and absorption due to hydrometeors.

Because of the complexity of the problem, it is beyond the scope of this thesis to offer a comprehensive quantitative treatment of microwave radiative transfer in rain clouds or to discuss in detail the problem of retrieving rain rate from satellite microwave data. Both topics have received a great deal of attention in recent years,

---

* Theoretical calculation of the radiative properties of aspherical particles becomes more difficult, the more radically the particle shape deviates from sphericity. In the case of flattened rain drops, the shape may be reasonably well approximated by oblate spheroids or ellipsoids, for which generalizations of Mie theory may be employed, and a number of studies have succeeded in calculating radiative properties for idealized distributions of raindrop sizes, shapes, and orientations (e.g., Oguchi 1983). For most ice particles, an ellipsoidal approximation is somewhat less convincing, but the small complex index of refraction of ice at microwave frequencies, coupled with relatively small size parameters, allows one to resort to other approximate theories for computing scattering and absorption properties (e.g., Kummerow and Weinman 1988b).

particularly following the decision to include space-based microwave radiometers (possibly a copy of the SSM/I) as a key component of the Tropical Rainfall Measuring Mission (TRMM) scheduled for the mid-1990s (Simpson et al. 1988). Yet it is probably safe to say that enormous problems remain to be solved, not the least of which are those arising from the relatively coarse spatial resolution of satellite microwave sensors relative to the scale of variability of precipitation. For examples of recent empirical and theoretical studies of the microwave radiometric response to precipitation, the reader is referred to Petty and Katsaros (1990a, 1990b), Alishouse et al. (1990), Adler et al. (1990), Yeh et al. (1990), Hakkarinen and Adler (1988), Kummerow and Weinman (1988a), Wu and Weinman (1984), Spencer et al. (1983), and further papers cited in the above studies.

Nevertheless, since precipitation occurs over a significant fraction of the ocean's area at any given time and is closely associated with the most meteorologically interesting and operationally significant weather systems, it remains desirable to have at least a qualitative understanding of how precipitation may affect the retrieval of other atmospheric and surface parameters using SSM/I data. Moreover, although the reliable quantitative estimation of rain rate from satellite microwave data remains an open problem, even relatively simple techniques may permit one to *identify* and *characterize* regions of precipitation. Such qualitative information is still of considerable value for diagnosing cyclone structure and intensity, frontal location, etc. (e.g., Katsaros et al. 1988, 1989)

10.1 Radiative characteristics of precipitation viewed at SSM/I frequencies

At SSM/I frequencies, rain attenuates and emits radiation more effectively than any other atmospheric constituent, commonly producing optical depths of unity or greater. This is largely due to the relatively large total column water content associated with rain. For example, even a layer of only light rain, say

2.5 mm h^{-1} , extending from the surface to a freezing level of 2 km contains about 0.4 kg m^{-2} , comparable to the water content of the heaviest non-precipitating stratiform clouds; heavy tropical rain ($\sim$100 mm h^{-1}) in a 4.5 km deep column may contain $\sim$20 kg m^{-2} or more.

Added to the large atmospheric water content associated with rain is the enhanced mass extinction coefficient of raindrops whose radius is comparable to the wavelength of the radiation. Microwave extinction by rain may thus be substantially greater than that for a non-precipitating cloud containing the same total water mass. For a Marshall-Palmer distribution of rain drops at 10° C, theoretical calculations by Savage (1976) indicate that the volume extinction coefficient k_e (km^{-1}) of rain is approximately given by $.015R^{1.1}$, $.077R^{0.97}$, and $.31R^{0.76}$ at 19.35, 37.0, and 89.5 GHz, respectively. For a 2 km deep layer, these models yield optical depths of unity at rain rates of 24 mm h^{-1} , 7 mm h^{-1} , and 2 mm h^{-1} , respectively. Conveniently (and fortuitously), k_e is almost linear in rain rate R at 19 and 37 GHz.

Precipitation affects observed SSM/I brightness temperatures in at least two important ways: First, the emissivity of an optically thick rain cloud is much closer to unity than that of the ocean surface; consequently, rain may normally be observed against an ocean background as a dramatic increase in brightness temperature. Second, rain emits and attenuates radiation almost independently of polarization (barring modest polarizing effects by large, flattened raindrops; see below), thus the highly polarized emission from the ocean surface is increasingly replaced by nearly unpolarized atmospheric emission as a rain cloud becomes increasingly opaque.

In addition, there may be significant scattering of microwave radiation by raindrops and large, frozen precipitation particles, especially at higher microwave frequencies, such as the SSM/I's 37 and 85 GHz channels. The single scatter albedo ϖ of precipitation particles increases with increasing size parameter and

acts to depress satellite observed brightness temperatures below those which would occur in a layer of equal opacity but without scattering. Hence, as rain rate increases, the brightness temperature first increases rapidly and then reaches a maximum for some critical value of rain rate. This is generally followed by a steady reduction in brightness temperature with further increases in rain rate, as more large rain drops influence the radiative properties of the cloud and as the effective emitting level of the rain layer moves to higher, colder altitudes (Savage 1976). The depression of brightness temperatures by volume scattering is greatly enhanced by the presence of precipitation-size ice particles (e.g., graupel, hail, and snow aggregates) within the rain cloud (Wu and Weinman 1984, Spencer 1986, Spencer et al. 1989) since such ice particles possess rather large single scatter albedos. Particularly at 85 GHz, scattering by frozen precipitation in intense convective storms may be strong enough to depress brightness temperatures to well below the brightness temperature of the open ocean, and occasionally even below 100 K (Spencer et al. 1989).

The precise response of a microwave imager like the SSM/I to precipitation is likely to depend on a large number of variables, most of which cannot easily be determined *a priori*. The most important of these are probably the effective height of the rain column (frequently assumed to correspond to the melting level in stratiform rain), horizontal geometry and spatial statistics (e.g., autocorrelation length of rain intensity), and microphysical structure (including particle sizes, phases, and shapes at all levels).

However, certain general features of the microwave signature of precipitation, may be readily exploited to provide qualitative indications of precipitation activity, even if the precise quantitative interpretation remains ambiguous. These properties are best understood with the help of plots of theoretical brightness temperature 'trajectories' in vertical and horizontal polarization (for a single SSM/I

frequency), corresponding to changes in rain rate within a horizontally homogeneous region of precipitation.

Fig. 10.1 depicts an example of such a bipolarization plot at 37 GHz, adapted from Spencer (1986). The horizontal axis gives the brightness temperature polarization difference $\Delta T_B = (T_{B,V} - T_{B,H})$, while the vertical axis gives the average brightness temperature $\overline{T_B} = (T_{B,V} + T_{B,H})/2$. The ocean brightness temperature in the absence of heavy cloud and rain is characterized by large ΔT_B and low $\overline{T_B}$. When cloud and/or light rain first begins to obscure the open ocean, there is a trend toward higher $\overline{T_B}$ and lower ΔT_B. If the optical depth increases without bound in a hypothetical case without scattering, ΔT_B goes to zero, reflecting the decreasing visibility of the polarizing sea surface, while $\overline{T_B}$ approaches the effective radiating temperature of the atmosphere. The latter is in turn well-approximated by the effective thermodynamic temperature of the opaque cloud layer alone, owing to the relatively small radiative contribution by the atmosphere above the cloud layer. In the present example, this temperature is assumed to be 273 K, corresponding to the limiting brightness temperature indicated in Fig. 10.1 by the label 'Opaque Cloud.'

To a reasonably good approximation in most cases, the changes in brightness temperature resulting from changes in cloud opacity, without scattering, follow a linear trajectory (the 'emission only' line referred to by Spencer 1986) in polarization space from the open-ocean value to the opaque cloud value. Of course, the position along that trajectory for specific conditions is non-linearly dependent on optical depth.

As already noted, the effect of scattering is to reduce the bulk emissivity, and hence the brightness temperature, of a cloud layer of given optical depth and thermodynamic temperature. As long as the scattering particles are spherically

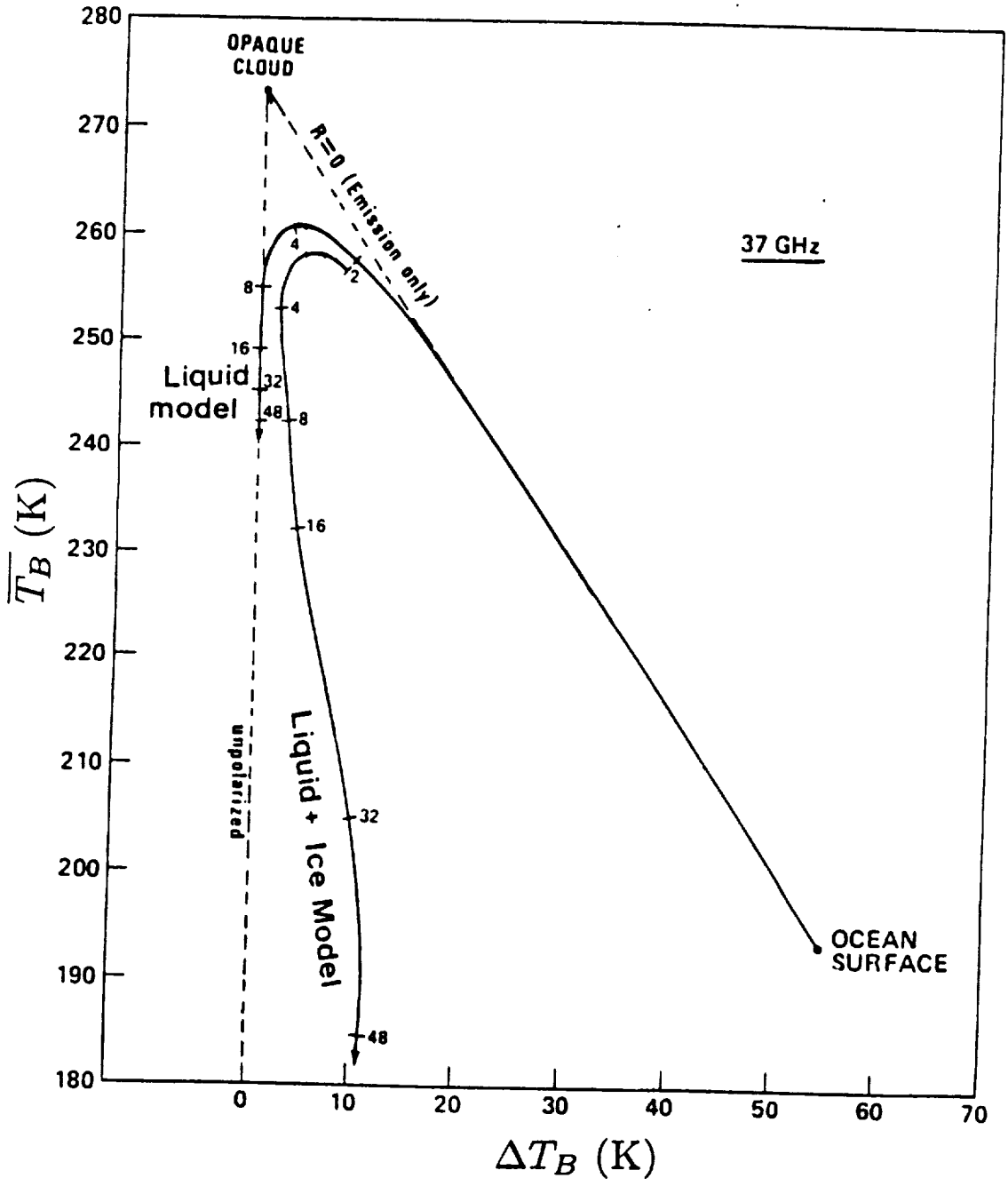

Fig. 10.1 Schematic depiction of how 37 GHz brightness temperatures change with increasing rain rate and/or cloud opacity. Horizontal axis is $\Delta T_B \equiv (T_{B,V} - T_{B,H})$; vertical axis is $\overline{T_B} \equiv (T_{B,V} + T_{B,H})/2$. See text for explanation of various curves. Adapted from Spencer (1986).

symmetrical and/or randomly oriented, the satellite observed polarization difference ΔT_B is not greatly affected by scattering, since it is, to first order, a function of the visibility of the sea surface only.

A theoretical trajectory corresponding to increasing rain rate, this time with consideration of scattering due to large rain drops alone, might therefore look like the one labeled 'Liquid Model' in Fig. 10.1. As before, the bipolarization brightness temperature starts out from the 'Ocean Surface' position and follows a more or less linear trajectory toward the 'Opaque Cloud' point, as long as scattering is weak. But as the rain rate increases (numeric labels '2', '4', '8', etc., representing mm hr^{-1}), so do the drop sizes and, consequently, the single scatter albedo as well. The trajectory continues to zero ΔT_B as before, but $\overline{T_B}$ is depressed increasingly below the brightness temperature corresponding to an opaque but non-scattering cloud.

For more realistic results, one must consider the effects of preferentially oriented, aspherical particles as well. In such cases, the scattering and extinction properties of the cloud are not entirely independent of polarization. Ensembles of particles which tend to have larger horizontal dimensions than vertical dimensions (the most common case) will scatter horizontally polarized radiation more effectively than vertically polarized radiation. This situation arises to a certain degree in heavy rain, owing to the aerodynamic forces exerted on the rain drops as they fall. According to Pruppacher and Klett (1978), rain drops with equivalent-volume radii $a \lesssim 140$ μm are nearly perfect spheres, but larger raindrops falling at terminal velocity become increasingly deformed with increasing radius, resembling oblate spheroids for $140 \lesssim a \lesssim 500$ μm , and acquiring strongly flattened bases for $a \gtrsim 500$ μm *.

---

* At very high rain rates ($\gtrsim 100$ mm hr^{-1}), some raindrop radii may be as large as 3 mm; at more moderate rain rates, maximum radii are generally no larger than $\sim$1.5 mm, since large drops tend to break up as a result of collision with other drops (Pruppacher and Klett 1978).

More importantly, when precipitation-size ice particles are present, especially vapor grown crystals (e.g., plates, needles, dendrites) and rimed crystals, these are often highly asymmetric and, in the absence of sufficiently strong turbulence, tend to fall with their minor axes oriented nearly vertically. To the extent that such flattened rain drops and/or oriented precipitation size ice particles are present in sufficient concentrations to affect the radiative properties of a rain cloud, observed polarization difference may tend to some non-zero value even for large rain cloud opacities. Theoretical radiative transfer calculations by Wu and Weinman (1984) (plotted as 'Liquid and Ice Model' trajectory) show this effect very clearly, with hydrometeor-induced polarization differences (vertical minus horizontal) exceeding 10 K at 37 GHz for rain rates >32 mm h^{-1} . Similar polarization differences have been observed by Adler et al. (1990) in aircraft observations of intense convection. As expected, the 'Liquid and Ice Model' data also show much stronger depressions of $\overline{T_B}$ for a given rain rate than do the 'Liquid Model' data. Qualitatively similar results are obtained for all SSM/I frequencies; the most important differences are in the rain rate needed to achieve a given degree of attenuation, as noted earlier, and the sizes and concentrations of ice particles needed to bring about a given brightness temperature depression.

To summarize, the effects of two distinct variables overwhelmingly dominate the microwave signature of a rain cloud seen by the SSM/I: its effective transmittance and the importance of radiative scattering. The former is controlled largely by the depth, intensity, and horizontal uniformity (on scales $\lesssim$ the sensor FOV) of the liquid precipitation layer and acts to simultaneously increase brightness temperature and decrease the polarization difference; the latter is mainly a function of the size and concentration of particles with high single scatter albedo — particularly large ice particles like hail, graupel and snow aggregates — and acts primarily to depress both vertical and horizontal polarizations by similar amounts. The simultaneous use of both vertical and horizontal polarizations to observe rain

allows each component — rain cloud attenuation and volume scattering — to be separated from one another, thus offering the possibility of two physically independent indices of precipitation activity.

10.2 Implications for SSM/I estimates of other geophysical parameters

There are two reasons why precipitation, of all the phenomena observable by the SSM/I, is the most likely of these to have a serious adverse effect on SSM/I retrievals of other geophysical parameters. The first, of course, is the high microwave opacity and consequent strong brightness temperature signature of rain, as compared with all other atmospheric constituents. The ability of the SSM/I to estimate surface and atmospheric parameters depend on the ability of the SSM/I to "see" through the atmosphere all the way to the surface, yet precipitation can easily obscure the surface and lower troposphere from view. Often, of course, rain does not completely fill the field-of-view (FOV). In principle at least, there would thus seem to be at least some hope of retrieving surface and atmospheric parameters in the presence of rain when the ocean remains partially visible between rain cells within the FOV.

Paradoxically, however, the spatial inhomogeneity of rain which would appear to offer at least a partial solution to the first problem is the basis for the second problem: not only the rain intensity and depth, but also the effective fractional coverage become additional unknowns in the retrieval of the other geophysical variables. Perhaps more seriously, the fractional coverage and other rain-related parameters and geometric factors are likely to be very different for each of the four SSM/I frequencies, owing to large differences in spatial resolution. Retrieval algorithms which employ multifrequency brightness temperature observations at each channel's intrinsic resolution therefore have to contend with a large additional 'noise' term which can easily mask the signature of the desired parameter, even when the surface and lower troposphere remain partially visible between rain

cells within each FOV. One partial solution would be to reduce the resolution of the high-frequency channels to match the poorer resolution of the low-frequency channels, as was done routinely for data from the earlier SMMR. To the author's knowledge, this procedure has not yet been employed operationally with SSM/I data, presumably because of the disproportionate complexity and computational cost which would be introduced into SSM/I processing software in order to achieve relatively modest gains in the usefulness of the data. Another possible solution, preferred by the author, is to avoid using SSM/I channels with widely disparate spatial resolutions to retrieve a given parameter at each pixel location. This is the approach which will be used in the atmospheric parameter retrieval algorithms presented later in this thesis.

Most often, the problem of contamination by rain is dealt with by simply flagging affected pixels, based on some empirically determined criterion, and discarding (or at least treating with suspicion) geophysical retrievals for those pixels. The principal challenge involved in this approach is to determine how much precipitation can be tolerated in the retrieval of a given parameter and how to reliably and objectively identify those pixels in which that amount is exceeded.

10.3 A Closer Look at Extinction by Liquid Precipitation

In a section 11.6, a simple attenuation-based method for retrieving cloud liquid water and estimating precipitation parameters from SSM/I data will be introduced. For this reason, we wish now to examine in somewhat greater detail the microwave extinction properties of an ensemble of hydrometeors. The results bear on the sensitivity of liquid water retrievals to drop sizes and on the potential for separately estimating precipitating and non-precipitating liquid water content from SSM/I observations.

As noted earlier, large rain drops associated with heavy rain may be significantly flattened along the vertical axis as the result of aerodynamic forces.

For simplicity, and because the asphericity of rain drops is normally a factor of only second-order importance in determining microwave extinction, the results described below will be based on Mie (1908) theory calculations which are strictly applicable only to spherical particles.

Given the assumption of sphericity, the bulk microwave properties of an ensemble of liquid hydrometeors are determined entirely by the dielectric constant of water (a function of temperature and frequency) and the detailed distribution of particle sizes. In previous studies, it has been customary to calculate microwave attenuation and emission as a function of rain rate for specified models of the drop size spectrum. Mention has already been made of the study by Savage (1976), who derived power laws for the dependence of microwave absorption, extinction, and scattering on rain rate for the Marshall and Palmer (1948) and Best (1950) drop size distributions.

In reality, observed drop size distributions may vary widely from time to time and place to place, depending on the dominant microphysical processes and the kinematics of a given precipitating cloud system. The most important factors determining the drop size distribution probably include the relative predominance of warm cloud processes (e.g., collision/coalescence) and cold cloud processes (e.g., vapor growth of ice crystals, riming, aggregation), updraft intensities within the cloud (strong updrafts tend to support the production of larger hydrometeors), the rate of evaporation below the cloud base, and, in some cases, the importance of drop size sorting due to differing fall speeds (Pruppacher 1981). In general, it has been found that stratiform rain consists of a higher proportion of small rain drops for a given rain rate than convective rainfall; this fact is reflected in the common use of different radar reflectivity–rain rate relations for stratiform and convective rainfall (e.g., Austin 1987). However, rain rates in excess of about 25 mm h^{-1} are always associated with convective clouds (Rogers and Yau 1989, p. 183).

Here, we temporarily postpone consideration of specific drop size distributions and examine the more general problem of microwave extinction and scattering as a function of radius for a monodisperse ensemble of droplets. Various radiative properties for real precipitation may be obtained simply by integrating the results, weighted by the appropriate drop size distribution. Mie calculations of extinction and scattering efficiencies for spherical water droplets were performed using the MIEV0 subroutine of Wiscombe (1980). As for cloud water, the complex index of refraction was obtained from Ray (1972).

Fig. 10.2 depicts the mass extinction coefficients $\kappa_{e,r}$ of spherical raindrops at 19.35, 37.0, and 85.5 GHz as functions of radius (results for 22.235 GHz are similar to those for 19.35 GHz). Droplet temperature is assumed to be 10° C. For small size parameters, $\kappa_{e,r}$ is seen to be nearly independent of drop size, consistent with the results of section 6.2. At larger drop sizes, the extinction spectrum is strongly dependent on drop size, with a rather sharp peak occurring for each SSM/I frequency at the radius for which the size parameter $x \approx 0.9$; i.e., at 2.2, 1.1, and 0.5 mm, for 19.35, 37.0, and 85.5 GHz, respectively. $\kappa_{e,r}$ at the peaks is found to be be approximately proportional to $\nu^{1.1}$, whereas in the small-drop limit, the dependence was shown earlier to be $\nu^{1.7}$. Interestingly, for drop sizes to the right of the peak, the mass extinction coefficient becomes nearly independent of frequency for all higher frequencies.

The same data are plotted in Fig. 10.3, only this time the mass extinction coefficients are expressed as a multiple of the value in the small drop limit. These values are 0.060, 0.209, and 0.878 m^2 kg^{-1} for 19.35, 37.0, and 85.5 GHz, respectively. This plot gives an indication of the potential of SSM/I attenuation measurements at each frequency for over-estimating total column liquid water when precipitation is present. As expected, the higher frequency channels are the first to be susceptible to errors when drop sizes increase beyond the usual size for cloud droplets. More surprisingly, however, *the theoretical maximum possible*

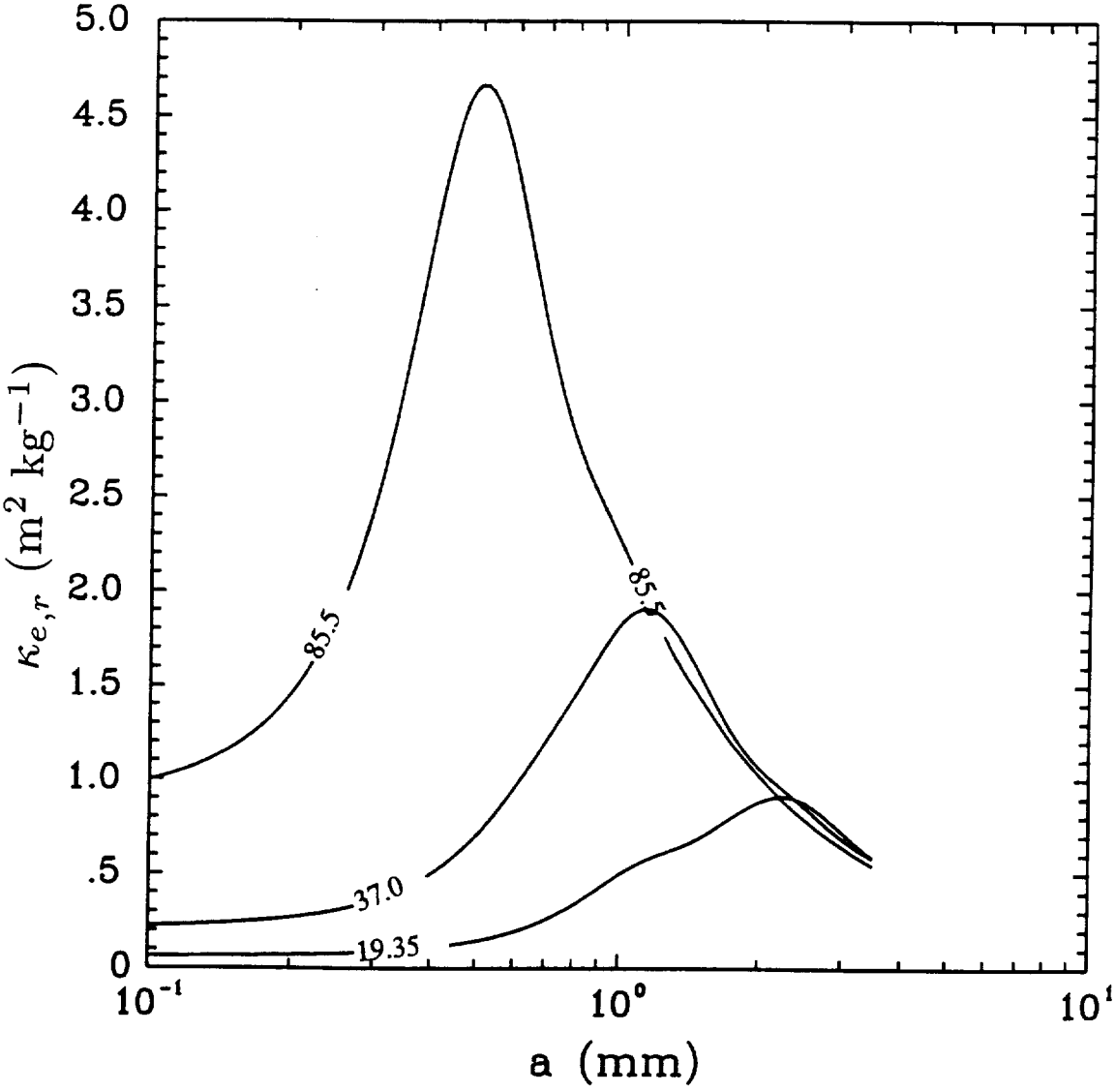

Fig. 10.2 Mass extinction coefficients $\kappa_{e,r}$ of spherical raindrops at 19.35, 37.0, and 85.5 GHz as functions of radius.

error is largest for the lowest frequencies, with drop sizes near 2 mm radius giving rise to a 15-fold increase in κ_e at 19.35 GHz, compared with a maximum factor 5 increase for 85.5 GHz near 0.5 mm radius.

The computed single-scatter albedo ϖ, defined by

$$\varpi \equiv 1 - \frac{\kappa_a}{\kappa_e}, \tag{10.1}$$

is shown in Fig. 10.4. As already discussed section 6.2, ϖ is seen to be negligible for very small drop sizes, so that $\kappa_a \approx \kappa_e$; thus, scattering may be neglected in radiative transfer calculations when only cloud size droplets are present. As size parameter x exceeds ~0.5, however, ϖ rapidly becomes significant, achieving values of up to ~0.6 for the largest raindrops.

It is instructive now to consider the *volume* extinction coefficients of a hypothetical *monodisperse* rain, as functions of radius a, *normalized to unit rain rate.* This is calculated as

$$k_{e,r}(a) = \frac{\kappa_{e,r}(a)\rho_w}{v_\infty(a)}, \tag{10.2}$$

where ρ_w is the density of pure water and v_∞ is the terminal fall velocity of raindrops in still air. Expressions used for $v_\infty(a)$ are those of Beard (1976), as given by Pruppacher and Klett (1978). Figure 10.5 depicts $k_{e,r}$ as functions of droplet radius a for 19.35, 37.0, and 85.5 GHz, plotted as extinction per km per mm hr^{-1} rain rate. Here we have assumed an air pressure of 1013 hPa and a temperature of 10° C for both water and air.

The physical interpretation of Fig. 10.5 is straightforward: if one assumes a hypothetical monodisperse rain with drop size a, then the total microwave extinction per km is given by the product of the rain rate R (in mm hr^{-1}) and the plotted value of $k_{e,r}$. It is immediately apparent that, at least theoretically, there could be a large ambiguity in the rain rate associated with a given observed microwave attenuation for a single SSM/I frequency. For example, at 85 GHz, the path extinction due to 1 mm hr^{-1} of drizzle size droplets ($a \approx 0.45$ mm) is seen to

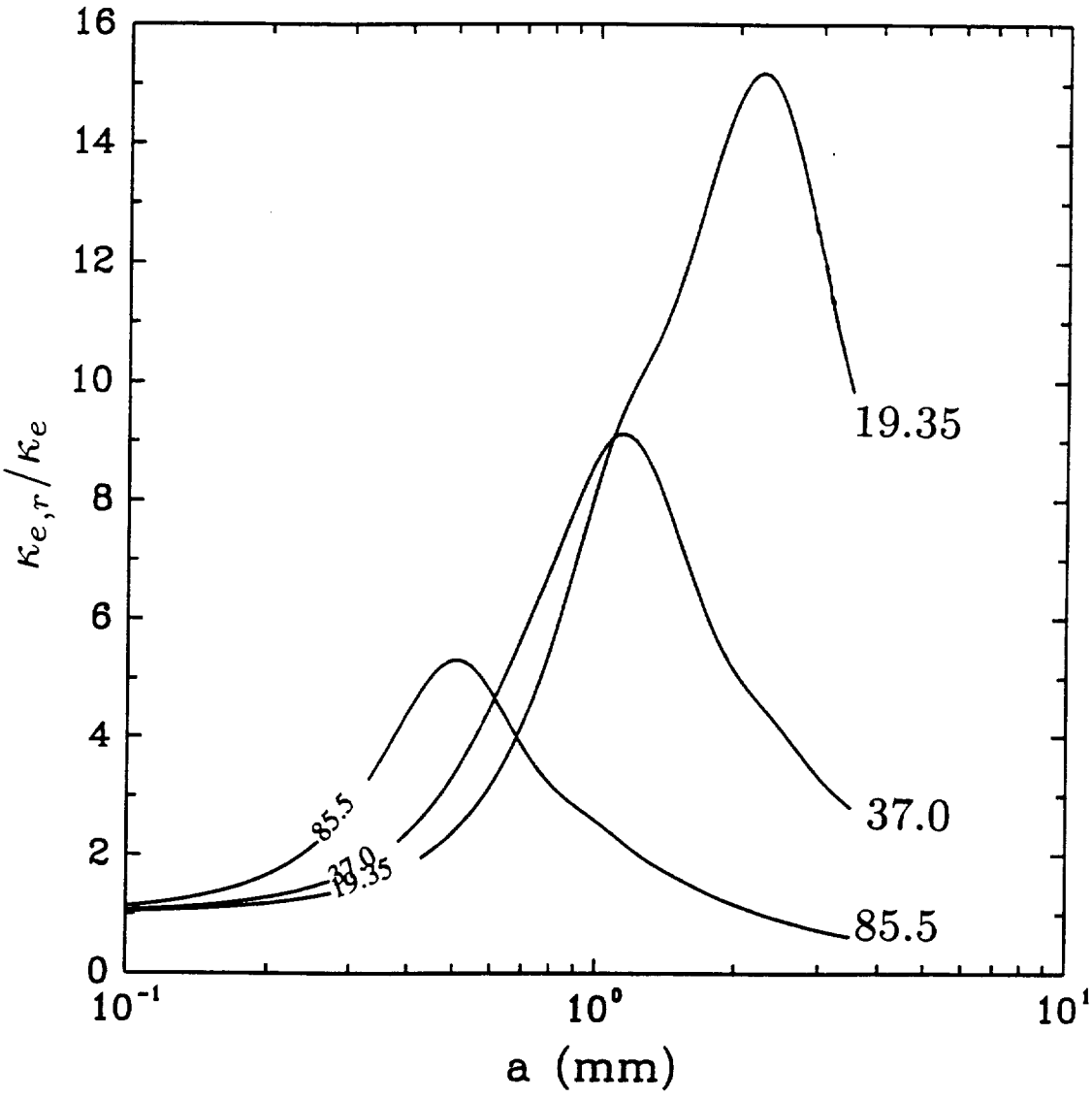

Fig. 10.3 Same as Fig. 10.2, but extinction coefficients $\kappa_{e,r}$ are expressed as a fraction of the extinction coefficient κ_e for cloud size droplets.

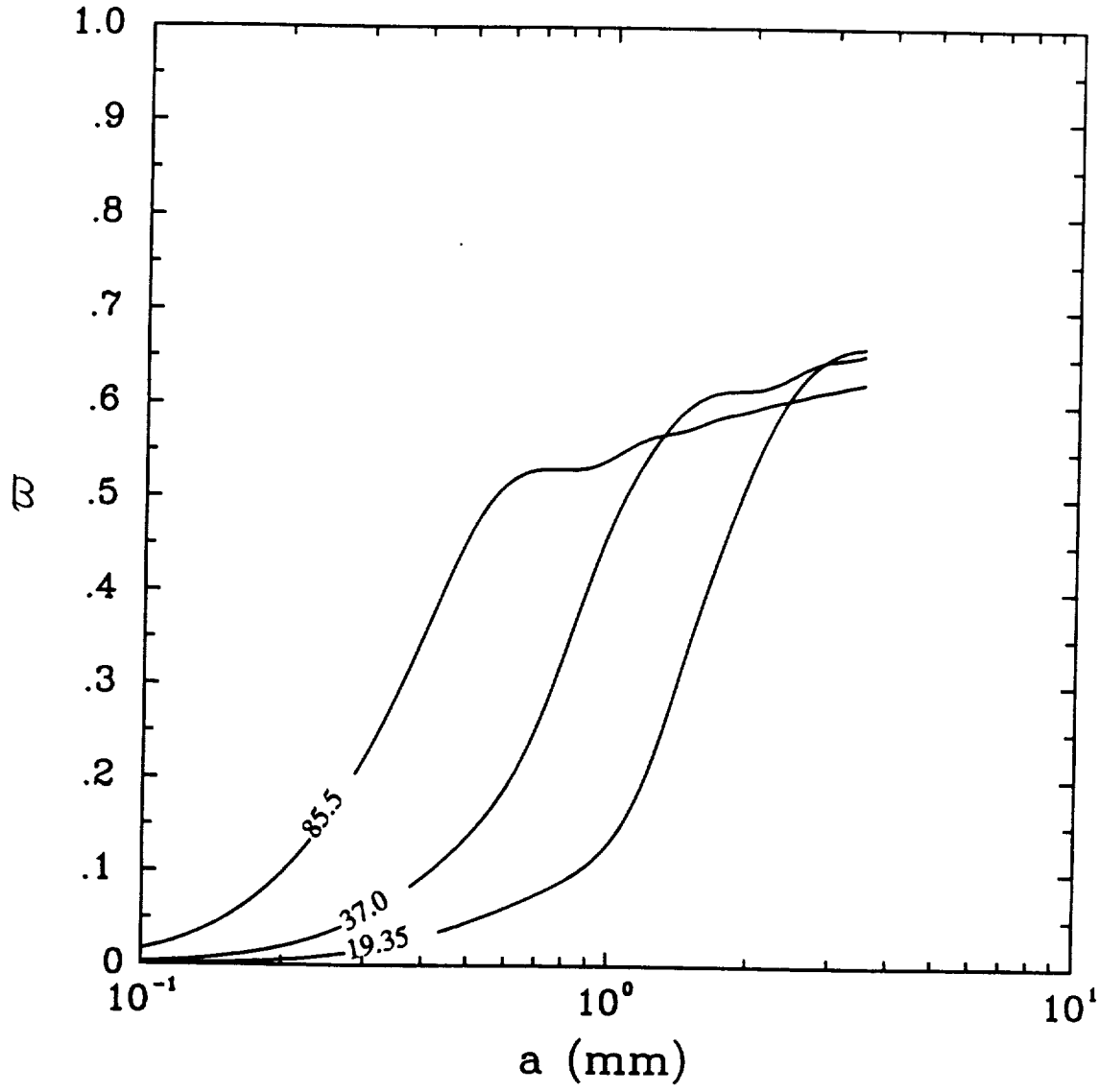

Fig. 10.4 Single scatter albedo ϖ of spherical raindrops as a function of radius a.

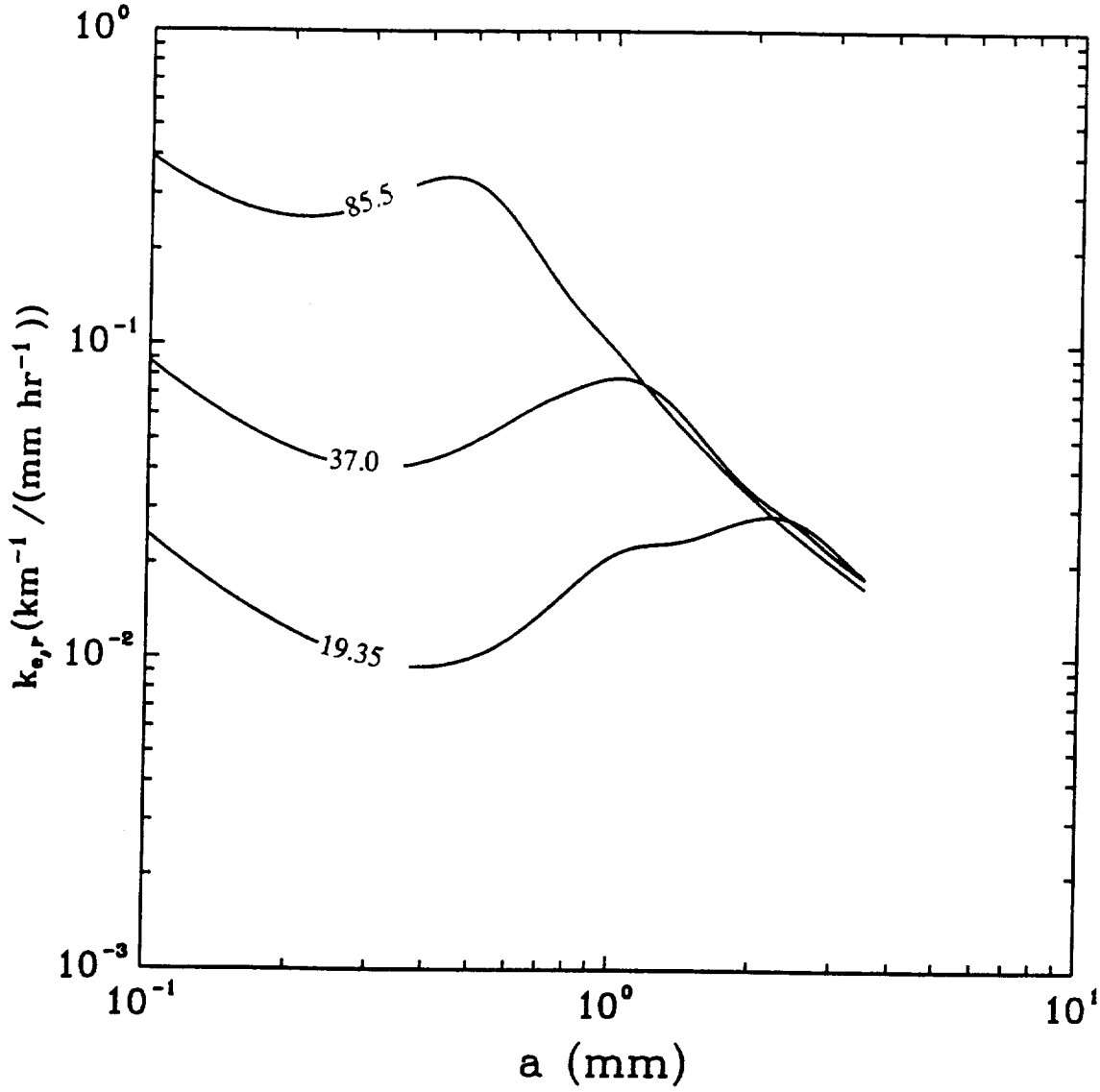

Fig. 10.5 Volume extinction coefficient $k_{e,r}$ per unit rain rate of monodisperse rain as function of radius a .

be approximately the same as that associated with 7 mm hr^{-1} of rain consisting of droplets larger than 1.5 mm radius.

Real rain, of course, is never monodisperse, but rather consists of a broad spectrum of drop sizes which may range from $\lesssim 0.1$ mm up to about 3.5 mm. Microwave extinction due to polydisperse rain is easily calculated by integrating $k_{e,r}$ over a, weighted by a function $P(a)$ which expresses *the contribution of each drop size to the total rain rate R*:

$$k_{e,R} = \int_0^\infty k_{e,r}(a)P(a)\ da, \tag{10.3}$$

where

$$P(a) = \frac{4\pi}{3}a^3 n(a)v_\infty(a). \tag{10.4}$$

The drop size distribution $n(a)$ gives the number of drops per unit interval a per unit volume air. Note also that the rain rate R is then simply given by

$$R = \int_0^\infty P(a)\ da. \tag{10.5}$$

The *shape* of $P(a)$ is normally a function of rain rate R as well, with a larger fraction of the total rainfall coming from large drops as R increases. One convenient and frequently used model for the raindrop size spectrum is that of Marshall and Palmer (1948):

$$n(a) = n_0 \exp(-\Lambda a), \tag{10.6}$$

where $n(a)$ expresses the number of drops per cubic meter of air per unit interval of radius a, $\Lambda = 8.2R^{-0.21}$ mm^{-1}, and $n_0 = 1.6 \times 10^2$ m^{-3} mm^{-1}.

Fig. 10.6 shows $P(a)$ (normalized to unit area and scaled by a for plotting vs a logarithmic a-axis) for Marshall-Palmer drop size distributions corresponding to nominal rain rates of 0.25, 2.5, and 25 mm hr^{-1}. The actual rain rates computed

from (10.5) are 0.29, 3.0, and 28.2 mm hr^{-1}, respectively. The first precipitation rate is a representative value for drizzle in marine stratocumulus clouds.

The main point of Fig. 10.5 is to illustrate how the microwave attenuation properties of rain, for fixed rain rate, can be significantly altered simply by introducing minor modifications to the shape and/or position of the corresponding constant-area curve in Fig. 10.6. In fact, despite the popularity and convenience of the Marshall-Palmer model with fixed coefficients, recent studies have shown that both n_0 and Λ may vary considerably from one rainfall to another, and cases have also been frequently observed for which the exponential form assumed by Marshall and Palmer must be replaced by a more complicated, even bimodal distribution (e.g., Strantz, 1971). For rain rate retrievals using microwave attenuation data, uncertainties in the drop size distribution are clearly an important potential source of error, much as they are for radar reflectivity-based rain rate estimates (e.g., Austin 1987).

For column liquid water retrievals, it is more interesting to consider the mass extinction contribution by various drop sizes in precipitation. Analogous to Eqs. (10.3)–(10.5), the total mass extinction coefficient $\kappa_{e,R}$ by rain may be written

$$\kappa_{e,R} = \int_0^\infty \kappa_{e,r}(a) P_M(a)\, da, \tag{10.7}$$

where $\kappa_{e,r}(a)$ appears in Fig. 10.2 and (in normalized form) in Fig. 10.3, while

$$P_M(a) = \frac{4\pi}{3} a^3 n(a) \rho_w. \tag{10.8}$$

The total mass M per unit volume of air is then given by

$$M = \int_0^\infty P_M(a)\, da. \tag{10.9}$$

Fig. 10.7 depicts normalized plots of $P_M(a)$ for the same Marshall-Palmer distributions appearing in Fig. 10.6. Total computed mass densities M for the three rain rates are 0.028, 0.192, and 1.33 g m^{-3}.

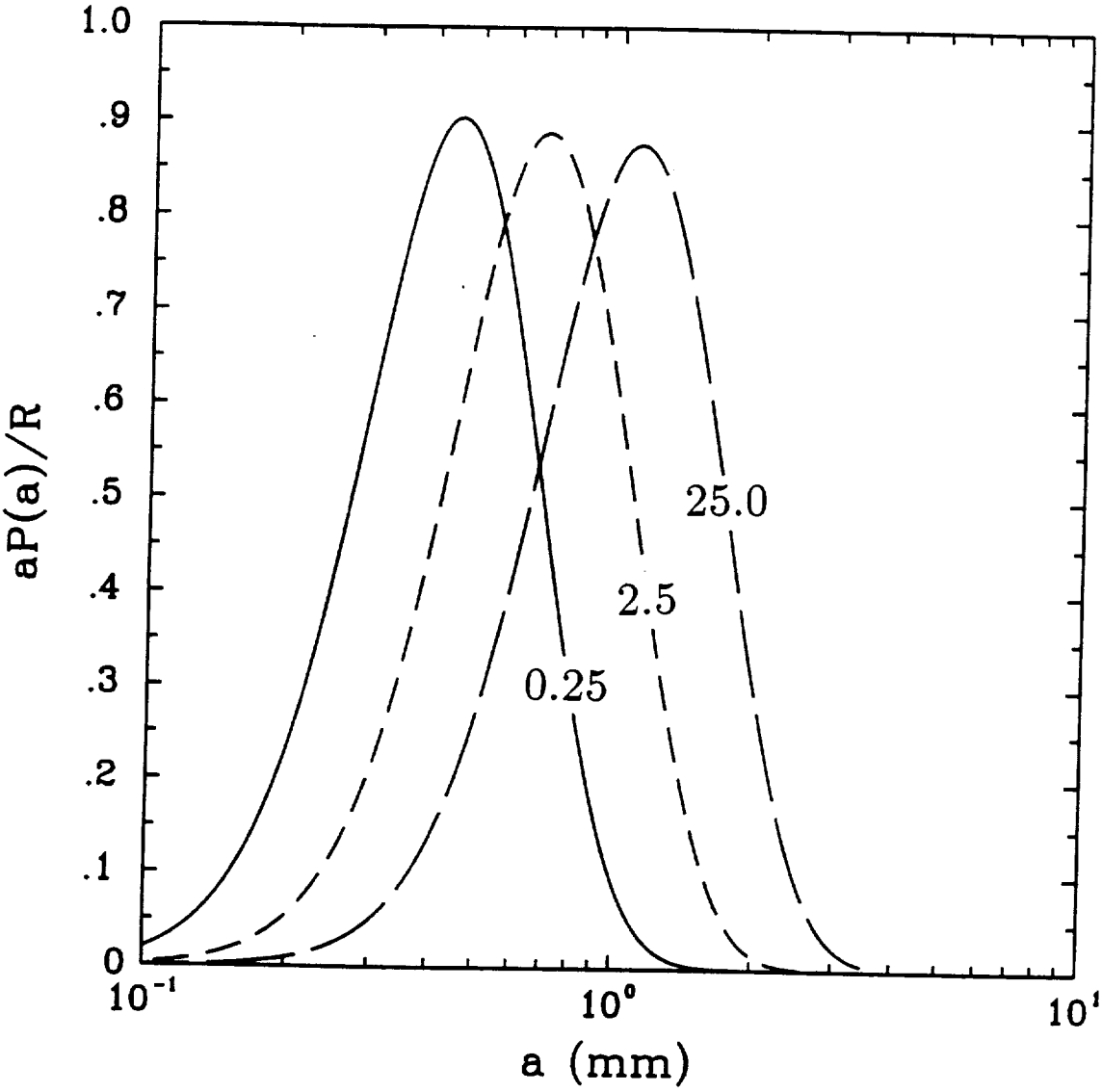

Fig. 10.6 Weighting functions $P(a)$ expressing the relative contribution of individual drop sizes to the total rain rate for a Marshall-Palmer drop size distribution. Curves are plotted for nominal rain rates of 0.25, 2.5, and 25.0 mm h^{-1} and are scaled to give unit area.

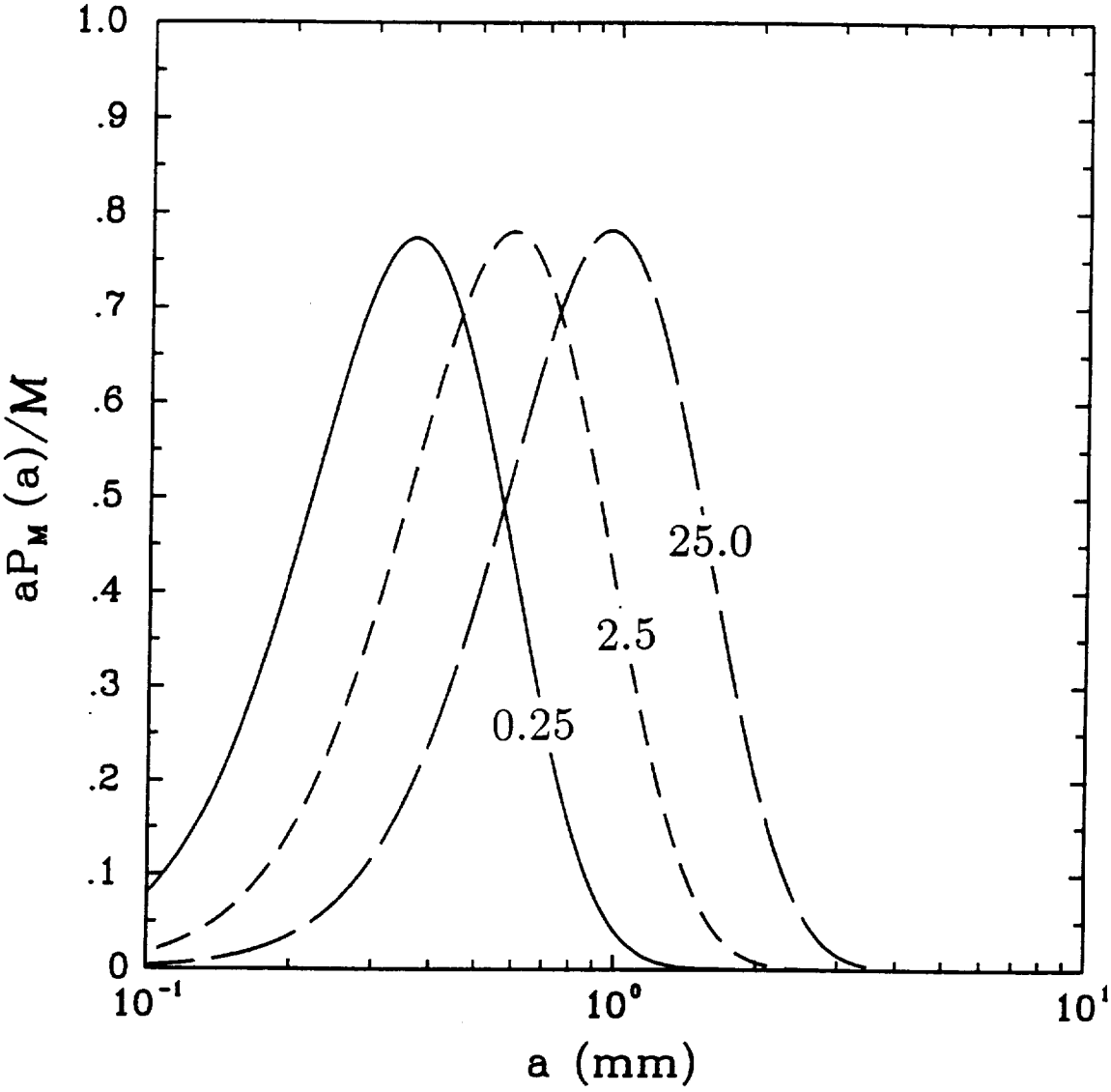

Fig. 10.7 Weighting functions $P_M(a)$ expressing the relative contribution of individual drop sizes to the total liquid water mass per unit volume for a Marshall-Palmer drop size distribution. Curves are plotted for nominal rain rates of 0.25, 2.5, and 25.0 mm h^{-1} and are scaled to give unit area.

The position of the peak in the in the 85 GHz extinction curve (Fig. 10.3) partially overlaps the peak in the drop size distribution for 0.25 mm hr^{-1}, so that mass extinction by drizzle is likely to be a factor of 2-3 higher than for cloud size droplets. If drizzle at this precipitation rate were to extend from the surface to an altitude of ~750 m, as might be expected in marine stratocumulus clouds near the west coast of the U.S., the corresponding total water mass due to drizzle alone would amount to ~0.02 kg m^{-2} , and would extinguish 85 GHz radiation to the same degree as ~0.05 kg m^{-2} of cloud water. However, the total cloud water mass in drizzling stratocumulus clouds is typically up to an order of magnitude larger than this. It thus appears unlikely that drizzle should give rise to more than errors of a few percent in cloud liquid water retrievals using the SSM/I's 85 GHz channels.

11. EXTRACTION OF GEOPHYSICAL INFORMATION FROM SSM/I OBSERVATIONS

Up to this point, we have been concerned with the quantitative response of the SSM/I to changes in the scene being observed. This is conventionally known as the *forward* or *direct* problem. Henceforth, we shall be concerned with the *inverse* problem; that is, the task of inferring something about the state of the scene being viewed based on remotely sensed SSM/I data.

At the most fundamental level, one may discern two distinct, but complementary modes of extracting meteorological information from SSM/I observations. The first is essentially qualitative, spatially oriented, and at least to some extent subjective, treating SSM/I data much in the same way as conventional visible and infrared satellite images. The second, and unquestionably the most widely represented in the literature to date, is decidedly quantitative, with the primary aim being to accurately estimate the values of specific atmospheric or surface parameters at each pixel location in the SSM/I's data swath. In conventional terminology, the distinction is that of "satellite meteorology" vs "remote sensing."

According to the first mode, spatial patterns in SSM/I multichannel radiances (or simple functions of the latter) may be viewed as snapshots of the earth-atmosphere system, which, with the help of a little knowledge of microwave radiative transfer or even just experience alone, potentially offer a wealth of information on the location, structure, intensity and stage of development of oceanic weather systems. Especially advantageous *vis-à-vis* conventional imagers is the microwave radiometer's unique "X-Ray view" through the cirrus and thinner liquid water clouds which often obscure the underlying horizontal structure of a storm at sea. Indeed, it can be argued on this basis that microwave imagery could supplement or even supercede infrared imagery from polar orbiters for many common diagnostic tasks, especially those for which spatial resolution is not a critical factor. It may therefore seem somewhat surprising that the "satellite meteorology" mode

of interpreting microwave imagery has yet to be explored in greater depth in the literature, despite the long-established value of similar techniques for interpreting visible and infrared imagery. This failure perhaps reflects only the relatively recent availability of SSM/I imagery, coupled with the severe sampling limitations of earlier microwave radiometers like the SMMRs. Nevertheless, progress is now being made in this area, as reported for example by McMurdie and Katsaros (1985), Katsaros et al. (1989), Negri et al. (1989), and others.

The systematic classification and meteorological interpretation of synoptic and mesoscale spatial patterns in SSM/I imagery will undoubtedly come with time and experience. In the following, we shall concentrate instead on further understanding the capabilities and limitations of the SSM/I for obtaining quantitative estimates of atmospheric and surface parameters over the ocean (i.e., the "remote sensing" mode).

11.1 Review of available quantitative methods

In principle, quantitative retrieval algorithms for microwave sensors like the SSM/I or SMMR can be grouped into two basic categories: statistical and physical. Statistical retrieval algorithms are those which are based primarily on empirical correlations or other statistical relationships between satellite brightness temperatures and the parameters to be retrieved. Physical algorithms, on the other hand, depend on an accurate theoretical (though not necessarily closed-form) solution of the forward problem, that is, the prediction of brightness temperatures from a known state of the environment, coupled with some means for inverting the functional relationship in order to estimate environmental parameters from the satellite observations. In practice, the distinction between the two categories may be blurred — many statistical retrieval methods are constructed based on at least partial knowledge of the physics involved, while a physically-based retrieval

method often requires the use of statistical constraints in order to find a unique solution which is also, hopefully, near-optimal in terms of its error statistics.

a. Statistical retrievals

Statistical algorithms for passive microwave retrievals are most frequently based on standard multiple linear regression of observed brightness temperatures (or functions thereof) against coincident "ground truth" observations of the parameter to be retrieved. The result is a set of channel coefficients which minimizes the rms difference between the sensor estimates and the values for the specific comparison data set used in the regression.

The principal advantage of a purely statistical approach is its simplicity and robustness: no knowledge of the physics of the problem nor even of the absolute calibration of the sensor is required. The contribution of instrument noise to retrieval errors is automatically accounted for in the process of empirically minimizing the rms error of the algorithm. Also, since the algorithm rarely entails more than a linear combination of brightness temperatures or simple functions of brightness temperatures, regression-type retrievals are generally very undemanding computationally. Examples of purely statistical algorithms developed for the SSM/I include the water vapor and liquid water algorithms of Alishouse et al. (1990a,b) and the wind speed algorithm of Goodberlet et al. (1989). An alternative statistical algorithm for water vapor is also presented later in this chapter.

A serious disadvantage of these methods is their dependence on a suitable set of coincident satellite and "ground truth" measurements in order to generate the retrieval coefficients. If the surface observations are biased toward a particular region or set of meteorological conditions, then there is no guarantee that a statistical retrieval algorithm will yield good results when applied to a new region or under a different set of conditions. For some variables such as integrated cloud liquid water content L, direct measurements over the open ocean are extremely

scarce in any form; the compilation of a coincident set of SSM/I data and *in situ* liquid water observations which is truly representative of the range of global maritime conditions would seem to be a logistical impossibility.

One way to circumvent the dependence of statistical methods on coincident surface measurements lies in the use of synthetic data. Wilheit and Chang (1980), for example, calculated theoretical SMMR brightness temperatures for a large ensemble of model atmospheres in which the relevant parameters were allowed to vary over the expected ranges encountered in nature. They then used statistical regression in the usual way to generate linear algorithms which predicted model parameters from the simulated brightness temperatures.

Although the use of synthetic data mitigates the need for coincident measurements (except for the purpose of validating the algorithm), two of the most important advantages of a statistical approach based on real data are lost: the success of the algorithm is now dependent both on the accuracy of the theoretical radiative transfer calculations and on precise knowledge of the absolute calibration of the instrument. As was shown in Chapter 8, neither is guaranteed. Furthermore, it is easy to neglect to include in the models secondary sources of brightness temperature variability which nevertheless affect the accuracy of the retrievals.

An example of where the synthetic data approach has failed may be found in the geophysical parameter retrieval algorithms (the so-called "Hughes Algorithms") developed for the SSM/I prior to its launch in June 1987. According to the Calibration/Validation study (Hollinger 1988) undertaken during the first year of the SSM/I's operation, almost all of the pre-launch algorithms failed to meet government specifications, some by rather large margins. Prior expectations of retrieval accuracies had been relatively optimistic, even for such unlikely candidates as fractional cloud amount over land (target accuracy ±20%!). It is this author's opinion that the discrepancy between predicted and actual performance was, in large part, a consequence of unrealistically simple atmospheric and surface models

used in the generation of the simulated brightness temperatures, in addition to the inevitable uncertainties in theoretical and/or measured absorption and emission coefficients at these frequencies.

The choice whether to use 'natural' or 'simulated' comparison data sets raises another issue as well: a regression algorithm based on real comparison data will exploit natural correlations between parameters in the data set in order to minimize the rms error. This is normally considered a drawback for satellite retrievals, since it leads to an algorithm which may perform poorly when conditions deviate markedly from those reflected in the regression data set. On the other hand, it can occasionally be an advantage when the parameter to be estimated has a less distinct radiometric signature than one with which it is highly correlated (see Section 11.3), especially if the net global rms error of the retrieval is of greater importance than its robustness in the face of atypical conditions. A synthetic data base will not normally reproduce natural correlations; indeed, correlations may be deliberately minimized (e.g., Wilheit and Chang 1980) in order to produce an algorithm which depends entirely on the *physical* information content of the brightness temperatures for its estimates.

Any linear method, including standard multiple regression, is optimal only when the relationship between observables (e.g., brightness temperatures) and retrievables (e.g., water vapor, wind speed, etc.) is approximately linear or can be recast in a quasi-linear form. It should already be apparent from the results of Chapters 6, 9, and 10 that there are in fact significant non-linearities both in the physical response of the SSM/I to the environment as well as in the statistical relationship between various environmental parameters. Their potential impact on retrieval accuracies must be considered, along with possible ways to reduce that impact where necessary.

Wilheit and Chang (1980), and other authors as well, have used functions such as $\log(280°\text{K} - T_B)$ as independent variables in linear algorithms. Such

transformations "straighten out" much of the non-linearity in the relationship between the untransformed microwave brightness temperatures and changes in atmospheric optical depth. Another approach, which has now been employed for SSM/I estimates of water vapor, has been to include both linear and quadratic brightness temperature terms among the independent variables used in the linear regression (Alishouse et al. 1990a).

The Hughes algorithms already mentioned attempted to circumvent the worst non-linearities in the SSM/I response to water vapor and other variables by using a piecewise scheme in which different linear coefficients were used in the retrievals depending on season and climate zone. One unpleasant consequence of this approach, documented by Alishouse et al. (1990a), was the appearance of obvious discontinuities in the retrieved water vapor field at the latitude line which separated two climate zones.

b. Physical retrievals

Physical algorithms, in contrast to the statistical algorithms described above, rely on theoretical models (such as the one presented in chapters 6–8 of this thesis) for the dependence of satellite observables on the relevant environmental variables and seek to invert that relationship mathematically. In the event that the model depends on more independent variables than there are sensor channels, direct inversion will lead to a non-unique solution. In such a case, additional constraints, including perhaps statistical information, must usually be employed.

To date, few published physical retrieval algorithms for microwave radiometers like the SMMR or SSM/I have used statistical constraints; instead, the constraint has consisted in most cases of simply limiting the number of independent variables in the brightness temperature model to be less than or equal to the number of available channels. For example, Wentz et al. (1982), using the physical brightness temperature model described by Wentz (1983), inverted all ten SMMR

channels to retrieve the four variables T_S, U, V, and L. Since the number of channels in this case exceeds the number of variables in the model, an iterative scheme was used to minimize the weighted least-squares difference between computed and observed brightness temperatures.

A nearly identical approach is described by Francis et al. (1983). The principal difference appears to be that they used direct numerical integration of the radiative transfer equation for a model atmosphere, instead of an analytic model function like that of Wentz (1983), to compute theoretical brightness temperatures at each step in the iteration. An advantage of such an algorithm over one which uses a closed form model is that the former may utilize arbitrary (and presumably more realistic) atmospheric absorption and temperature profiles in the forward calculations, rather than being restricted to those few mathematically simple profiles for which a closed-form approximation may be found for the integral in the radiative transfer equation. The obvious disadvantage, of course, is that such an algorithm places vastly greater demands on one's computational resources.

Later, Wentz et al. (1986) used a simplified, deterministic inversion method in which the number of channels used and the number of parameters to be estimated were the same. In effect, this method attempts to retrieve the values of the variables for which the brightness temperature model exactly predicts the observations. For the work described in that study, T_S was determined from climatology, and the remaining variables U, V, and L were determined from three of the ten SMMR channels. The specific subset of channels which produced the best retrievals was determined experimentally.

The Wentz et al. (1982) and the Wentz et al. (1986) methods appear to be capable of producing reasonable results, in some cases better than those based on the Wilheit and Chang (1980) statistical algorithm (e.g., Katsaros et al. 1981; Lipes 1982; Alishouse 1983), especially once the brightness temperature model of

Wentz (1983) had been tuned using independent surface and satellite data. However, neither of the Wentz methods (nor, for that matter, the Francis et al. 1983 algorithm) may be regarded as optimal: *minimizing the rms difference between predicted and observed brightness temperatures is not the same as minimizing the rms error in the retrieval,* even assuming a perfectly calibrated brightness temperature model.

To the author's knowledge, the only published method which explicitly attempts to optimize the physical retrieval of environmental parameters from microwave images is the spatial filter technique of Rosenkranz (1978, 1982a, 1982b). This method is unique and particularly intriguing in that it applies theoretically-derived optimal linear estimators, not to the multichannel brightness temperatures at each pixel location as is usually the case, but to each element of *two-dimensional spatial Fourier transforms* of the SMMR imagery. The results of this operation are then inverse Fourier-transformed to yield the spatial fields of each retrieved parameter.

Advantages of the Rosenkranz spatial filter approach include the simultaneous optimal inversion and spatial deconvolution of the microwave data, plus the convenient imposition of spatial constraints (i.e., *a priori* autocovariance lengths) on the retrievals of each parameter. One disadvantage of the method is the necessity of adequately expressing the sensor brightness temperatures in terms of linear combinations of environmental variables and pseudovariables, the latter being comprised of selected higher-order products of the former. Another disadvantage is contamination of the retrievals by edge effects ('ringing') which naturally arise from applying a Fourier Transform to an image whose periodic extension is not smoothly varying.

The published record gives no indication that the spatial filter approach was ever used other than for demonstration purposes. Nevertheless, the general principles (e.g., spatial constraints) incorporated in the Rosenkranz method are worthy

of careful consideration in the development of future algorithms for the SSM/I, especially if ways can be found to minimize the problems described.

At the time of this writing, the Wentz et al. (1986) algorithm, using the Wentz (1983) brightness temperature model with updated coefficients (unpublished), appears to be the only physical retrieval algorithm currently being used for geophysical retrievals from SSM/I data. To the author's knowledge, no systematic studies of its performance have yet been published in the open literature, though the "Ocean Product Tapes" produced with the algorithm and distributed by Remote Sensing Systems (RSS), Inc., are now in relatively wide circulation.

A question that may be raised at this point is *why* optimal physical retrieval algorithms have yet to be developed for the SSM/I and, in general, why optimal estimation theory has yet to leave a significant mark in the field of satellite microwave imaging. One contributing factor immediately comes to mind: prior to the present work, no brightness temperature model appears to have been available which was reasonably comprehensive in its description of the sensor response to the environment, including the brightness temperature dependence on non-retrievable as well as retrievable variables, and the non-linear interactions between these. With the development of such a model in Chapters 6–8, it is now worth exploring how traditional retrieval theory, which has long had a role in atmospheric profile retrievals, might plausibly be adapted to SSM/I retrievals.

11.2 Applicability of Traditional Retrieval Theory

In the atmospheric sciences, presentations of mathematical retrieval theory have almost invariably been biased toward the problem of atmospheric profile retrieval (e.g., Houghton et al 1984). The general theory is of course applicable to *all* problems involving the inversion of indirect measurements, but it is not necessarily obvious in all cases how specific features of the SSM/I retrieval problem

translate into the language of profile retrieval and *vice versa*. For example, atmospheric profile retrieval methods are often able to invoke assumptions of vertical coherence or 'smoothness' in soundings in order to improve the behavior of the solution (e.g., Twomey 1963; Tikhonov 1963) or to understand the nature of the 'noise vs vertical resolution' tradeoff (Conrath 1972). In contrast, SSM/I observations cannot be understood as representing discrete measurements of a continuous function of a single variable. Indeed, the various parameters to which the SSM/I is sensitive do not even all have the same units. One aim of this chapter, therefore, will be to attempt to recast certain aspects of 'traditional' remote sensing theory into a form taylored for the SSM/I.

The general retrieval problem may be viewed as having two levels of solution: (i) given a set of indirect measurements, find *a* state of the system being observed which is radiometrically consistent with those measurements, to within measurement and model uncertainty; and (ii) given that the retrieval problem is underconstrained and that an infinity of possible solutions exist which satisfy the criterion above, many of which may be completely unphysical, select a 'best' or 'most probable' single solution from the candidate solutions, using any of a number of possible criteria, and attempt to characterize the probable error of that solution.

The first level of solution may be sufficient when the spectral signature of a given variable is so strong and distinct compared to those of all other variables (and noise) that only a limited range of values for the variable to be retrieved can plausibly be consistent with the observations, even allowing for reasonable amounts of both instrument noise and geophysical noise . An example in the case of the SSM/I might be the retrieval of total water vapor V using the 19V and 22V channels*. These two channels are close enough in frequency that they respond

* The SMMR analog to this method, using channels at 18 and 21 GHz, was first proposed by Prabhakara et al. (1982).

to almost all environmental variables in a very similar way. The exceptions are those variables related to atmospheric water vapor — the 22V channel is centered on a resonant absorption line, while the 19V channel is on the wing of that line. As a result, the brightness temperature *difference* 22V - 19V is, except in heavy cloud or rain, a nearly direct (albeit non-linear) measure of the total optical depth due to water vapor. The optical depth in turn is nearly proportional to V. Other variables (e.g., vapor scale height H) can affect the relationship between (22V - 19V) and V, but not enough to introduce more than modest uncertainty in V retrieved this way. Thus, useful estimates of V may be had without recourse to anything resembling traditional retrieval theory.

Most other variables of interest, on the other hand, e.g., cloud water L and surface wind speed U, have somewhat less distinct spectral signatures. Thus, rms errors in their retrieval can be unnecessarily large if the contaminating effects of the other variables and the various sources of noise are not accounted for in the retrieval algorithm. In such cases it is desirable to find an approach to processing the observed microwave brightness temperatures which fulfills definition (ii), above.

It is already apparent that the direct mathematical inversion of SSM/I brightness temperatures represents an underconstrained problem, because there are at most 7 channels observing the ocean and atmosphere at a given location, while the brightness temperature model developed in Chapters 6–9 requires the specification of 10 input parameters (counting the viewing angle θ, which is uncertain to at least $\pm 0.5°$). More degrees of freedom enter the problem when one considers the frequency dependent spatial resolution of the SSM/I: *for those pixels centered on a given surface location, pixel-averaged cloud liquid water* (for example) *can be quite different for each of the four SSM/I frequencies.* Variability of other input parameters on scales of less than one footprint can also not be excluded; one may

therefore reckon with up to three *additional* unknowns each for many of the model input parameters.

In order to transform the problem of SSM/I retrievals from an ill-posed (underconstrained) one with an infinity of solutions to a well-posed problem with a unique solution, it is necessary to supply constraints. As pointed out by Houghton et al. (1984), constraints may be regarded as 'virtual measurements,' so that, with sufficient constraints, the total number of 'measurements' may be made to equal or exceed the number of unknowns*. Obvious constraints for the present problem would include independently measured values for one or more input parameters (e.g., sea surface temperature T_S, surface pressure p_0, etc.), and/or statistical variances and covariances of certain input parameters, such as those described in section 6.3.3. Other constraints could be based on assumptions concerning the horizontal smoothness (e.g., autocorrelation length) of each field to be retrieved.

---

* Microwave retrieval algorithms have often been developed which are based on the assumption that all significant variations in observed brightness temperatures may be expressed entirely in terms of a simple theoretical function of only the two or three parameters to be retrieved (e.g., liquid water content L, precipitable water V, surface wind speed U). In such cases, the ill-posedness of the retrieval problem disappears from view, since a unique solution for each variable is easily found provided only that the number of channels used in the retrieval equals the number of variables to be retrieved. Already implicit in these methods, however, are severe (and sometimes unrealistic) constraints on the remaining variables affecting the brightness temperatures, including vertical distributions of water vapor and/or liquid water, atmospheric temperature, etc. Although such assumptions may not have a catastrophic impact on the usefulness of the results, they nevertheless preempt both the development of an optimal, statistically unbiased retrieval algorithm and a rigorous determination of the expected retrieval error. A frequent consequence, in my opinion, has been the overly optimistic assessment of probable retrieval errors for certain simple retrieval methods, even when one neglects those additional errors associated with uncertainties in theoretical absorption and emission models, etc.

Two other issues further add to the complexity of the retrieval problem: (i) noise and (ii) non-linearity. 'Noise,' as used in this thesis, includes not only instrument noise, which, as indicated in Chapter 4, is thought to amount to less than 1 K for the SSM/I, but also geophysical noise arising from unmodeled physical contributions to brightness temperature variations, as well as those arising from residual uncertainties in the model input parameters. Examples of the former include the quasi-random differences in the apparent surface wind speeds observed independently by the 19, 37, and 85 GHz channels, as well as scatter in the relationship between apparent fractional foam coverage and surface wind speed. Based on the results of Chapter 8, it appears that these noise sources significantly exceed the nominal instrument measurement noise.

The effect of any kind of noise is to reduce the confidence with which a given variable can be estimated with the SSM/I. In the case of some variables, the noise-induced uncertainty may easily approach or exceed the natural range of that variable so that any SSM/I estimate is worthless. Thus, certain atmospheric or surface parameters, while having a significant influence on SSM/I brightness temperatures, may nevertheless be regarded as non-retrievable. Note also that anytime the value of the variable is not known with perfect precision (i.e, always), its uncertainty must be regarded as an additional potential source of 'noise' in the retrieval of other variables. These arguments will be placed on a firmer footing shortly.

The *non-linearity* of the relationship between SSM/I brightness temperatures and certain geophysical variables was clearly illustrated in Chapter 9. This non-linearity potentially complicates both the determination of the optimal solution to the inverse problem (regardless of how 'optimal' is defined) and the analysis of the solution error. Fortunately, the non-linearity is mild enough in the case of the SSM/I so that a local linearization of the response function may be reasonably

employed both in iterative techniques for finding a solution and in performing approximate error analyses for the final solution. Also, much of the non-linearity in the dependence of brightness temperature on atmospheric constituents is in fact a direct consequence of the logarithmic relationship between transmittance and optical depth. Hence, the use of certain non-linear functions of brightness temperature (like the $\log(280 - T_B)$ of Wilheit and Chang 1980) as independent variables, rather than the brightness temperatures themselves, can effectively transform the retrieval of atmospheric absorber amounts from a moderately non-linear problem to a nearly linear one.

It is conventional in the atmospheric sciences to evaluate the quality of a measurement (whether *in situ* or remote) on the basis of the statistical variance of the error in the measurement; i.e., the mean-squared difference between the measured value and the true value. The most desirable solution to the remote sensing problem is therefore often considered to be the one which minimizes this error variance. The following subsection examines the mathematical basis for such a method.

11.3 A Minimum-Variance Method

Houghton et al. (1984) present the minimum variance method for retrieving an atmospheric profile from a set of multi-wavelength radiance observations. For the linear case, a solution is sought of the form

$$\hat{\mathbf{x}} = \mathbf{D}\mathbf{y}, \tag{11.1}$$

where $\hat{\mathbf{x}}$ is the desired profile estimate (at discrete levels of the atmosphere), and $\mathbf{D}$ is a matrix of coefficients multiplying the observed radiances $\mathbf{y}$. The matrix $\mathbf{D}$ for which the error variance in $\hat{\mathbf{x}}$ is a minimum may be derived either empirically from a large set of coincident satellite and surface-based profile measurements, i.e., using standard multiple linear regression, or theoretically, from knowledge of

the statistical covariance $\mathbf{S}_X$ of temperatures at each level, sensor channel noise covariance $\mathbf{S}_\epsilon$, and the channel weighting function matrix $\mathbf{K}$. In the latter case, the optimal $\mathbf{D}$ is given by

$$\mathbf{D} = \mathbf{S}_X\mathbf{K}^T(\mathbf{K}\mathbf{S}_X\mathbf{K}^T + \mathbf{S}_\epsilon)^{-1}. \tag{11.2}$$

Both approaches are equally applicable to SSM/I retrievals as well, once one interprets $\hat{\mathbf{x}}$ as a vector of geophysical parameter estimates appropriate to the SSM/I, rather than as temperatures at discrete levels of the atmosphere. However, the conventional mathematical statement of the minimum variance method given by (11.1) and (11.2) reflects certain assumptions which are common in profile retrievals but are not necessarily valid for SSM/I retrievals.

First, it may not be necessary or even desirable to simultaneously retrieve all elements of the vector $\hat{\mathbf{x}}$ using the same subset of SSM/I channels, in contrast to the usual practice for profile retrievals. This minor distinction from the profile retrieval problem is easily made explicit in the mathematical formulation simply by replacing the vector $\hat{\mathbf{x}}$ in (11.1) with a single scalar variable and by replacing the matrix $\mathbf{D}$ with a vector of coefficients $\mathbf{d}$. This modified formulation is then invoked separately for each parameter to be retrieved, with coefficients $\mathbf{d}$ appropriate to the specific subset of channels represented by the measurement vector $\mathbf{y}$.

Furthermore, if one intends to derive the retrieval coefficients $\mathbf{d}$ theoretically rather than by way of statistical regression, it is also important to keep in mind that number of parameters potentially contributing to variations in the observed SSM/I radiances will generally exceed the number of parameters to be retrieved. For example, while it is often not even necessary to obtain an estimate of more than a single element of the vector $\hat{\mathbf{x}}$ (using the original notation of Eq. 11.1) — say, if one is interested only in integrated water vapor — all other variables will continue to contribute to the observed brightness temperatures and these contributions must be accounted for. An analogous retrieval problem for an atmospheric profiler

might be the estimation of the temperature at a single level. In such a case, the $\mathbf{S}_X\mathbf{K}^T$ appearing just to the right of the equal sign in (11.2) must be replaced by the product of the *scalar* variance of the parameter to be retrieved and a *vector* containing the value of the weighting functions for all channels evaluated at that single level. The other instances of $\mathbf{S}_X$ and $\mathbf{K}^T$ remain unchanged and continue to reflect the contributions of *all* levels of the atmosphere to the observed radiances.

To highlight the slightly different 'flavor' of SSM/I retrievals as compared with more traditional retrieval problems, we may consider the following alternative formulation of the minimum variance method. If the problem is linear, then brightness temperatures observed by M of the 7 channels of the SSM/I may be represented as a column vector $\mathbf{t}$ which depends in the following manner on the scalar parameter p to be retrieved:

$$\mathbf{t} = p\mathbf{a} + \mathbf{b}, \tag{11.3}$$

where $\mathbf{a}$ expresses the sensitivity of each channel to p, and $\mathbf{b}$ may be regarded as a total noise term which contains both the intrinsic measurement noise of the sensor and the contribution of all geophysical parameters other than p to the variability in $\mathbf{t}$. Thus, $\mathbf{b}$ may be written out as

$$\mathbf{b} = \mathbf{s} + \mathbf{A}\mathbf{q}, \tag{11.4}$$

where $\mathbf{s}$ is the instrument noise contribution, $\mathbf{q}$ represents the remaining N physical parameters to which the SSM/I is sensitive, and $\mathbf{A}$ is an $M \times N$ sensitivity matrix. For algebraic simplicity, we have assumed that statistical means (indicated by angle brackets) have been subtracted from all quantities, so that

$$\langle \mathbf{t} \rangle = \langle p \rangle = \langle \mathbf{b} \rangle = 0. \tag{11.5}$$

We now seek a set of M coefficients, expressed in the form of a vector $\mathbf{d}$, which may be multiplied with the observed brightness temperatures $\mathbf{t}$ to yield an estimate $\hat{p}$ of the value of p:

$$\hat{p} = \mathbf{d} \cdot \mathbf{t} = \mathbf{d} \cdot (p\mathbf{a} + \mathbf{b}). \tag{11.6}$$

The validity of $\hat{p}$ as an estimate of p may be characterized by the size of the mean squared difference between the two, which is found via the following steps:

$$\hat{p} - p = (\mathbf{d} \cdot \mathbf{a} - 1)p + \mathbf{d} \cdot \mathbf{b}; \tag{11.7}$$

$$(\hat{p} - p)^2 = (\mathbf{d} \cdot \mathbf{a} - 1)^2 p^2 + 2(\mathbf{d} \cdot \mathbf{a} - 1)p\mathbf{d} \cdot \mathbf{b} + (\mathbf{d} \cdot \mathbf{b})^2; \tag{11.8}$$

$$\langle (\hat{p} - p)^2 \rangle = (\mathbf{d} \cdot \mathbf{a} - 1)^2 \langle p^2 \rangle + 2(\mathbf{d} \cdot \mathbf{a} - 1)\mathbf{d} \cdot \langle p\mathbf{b} \rangle + \langle (\mathbf{d} \cdot \mathbf{b})^2 \rangle; \tag{11.9}$$

Substituting (11.4) into (11.9) and noting that

$$\langle p\mathbf{s} \rangle = 0, \tag{11.10}$$

$$\langle \mathbf{s}\mathbf{q}^T \rangle = 0, \tag{11.11}$$

one finds that the error variance of $\hat{p}$ may be written

$$\delta_p^2 \equiv \langle (\hat{p} - p)^2 \rangle = \underbrace{(\mathbf{d} \cdot \mathbf{a} - 1)^2 \sigma_p^2}_{\text{(A)}} + \underbrace{2(\mathbf{d} \cdot \mathbf{a} - 1)\mathbf{d} \cdot \mathbf{A}\langle p\mathbf{q} \rangle}_{\text{(B)}} + \underbrace{\mathbf{d} \cdot \left[\left(\mathbf{S}_\epsilon + \mathbf{A}\mathbf{S}_q\mathbf{A}^T \right) \mathbf{d} \right]}_{\text{(C)}}, \tag{11.12}$$

where

$$\sigma_p^2 \equiv \langle p^2 \rangle, \tag{11.13}$$

is the initial squared uncertainty in p,

$$\mathbf{S}_\epsilon \equiv \langle \mathbf{s}\mathbf{s}^T \rangle, \tag{11.14}$$

is the instrument error covariance matrix (usually assumed to be diagonal), and

$$\mathbf{S}_q \equiv \langle \mathbf{q}\mathbf{q}^T \rangle, \tag{11.15}$$

is the covariance of the remaining radiometrically important geophysical parameters $\mathbf{q}$.

Before proceeding to find the $\mathbf{d}$ which minimizes δ_p^2, it is instructive to examine the individual terms contributing to the total retrieval error. Term (A) simply represents the error arising from a $\mathbf{d}$ which does not accurately represent the scale relationship between changes in p and changes in the component of $\mathbf{t}$ projected on $\mathbf{d}$. In the absence of noise (i.e., for $\mathbf{b} = 0$), terms (B) and (C) vanish, in which case (11.12) is obviously at a minimum (zero) for any $\mathbf{d}$ satisfying $\mathbf{d} \cdot \mathbf{a} = 1$.

Term (B) describes the influence of statistical correlations between p and the other parameters $\mathbf{q}$ affecting the brightness temperatures. Minimization of (11.12) will tend to produce a $\mathbf{d}$ which attempts to exploit such correlations. Thus, the sign of term (B) may actually be negative and serve to *reduce* the retrieval error. In other words, a minimum variance solution which includes consideration of term (B) may be expected to interpret radiometrically detectable variations in another geophysical parameter as evidence for a variation in p, simply on the strength of their statistical correlation. The result will be improved overall retrievals (assuming that the covariances $\langle p\mathbf{q} \rangle$ are correctly specified), but at the cost of partially decoupling the solution from the direct radiometric signature of p. One undesirable consequence, of course, is that *atypical* combinations of p and $\mathbf{q}$ will be associated with poorer retrievals of p. Another difficulty arises in actually determining the required covariances; some may be computed directly from radiosonde data sets such as the one described in Chapter 6; other covariances, such as those involving cloud liquid water L or cloud height z_C, might not be so easily estimated.

On the other hand, assuming that the necessary covariances can be determined, there is nothing to prevent one from minimizing $\mathbf{d}$ even for the case that

$\mathbf{a} = 0$, in which case Term (B) ensures that *any* arbitrary geophysical parameter p can be estimated with an error variance δ_p^2 less than or (at worst) equal to p's climatological variance σ_p^2. The only condition needed for $\delta_p^2 < \sigma_p^2$ to hold is that $\mathbf{A}\langle p\mathbf{q}\rangle$ be large enough.

Consequently, certain useful meteorological variables like 1000-500 mb thickness or surface humidity, while not directly affecting observed microwave radiances, can probably be estimated from the SSM/I with useful accuracy for some purposes, simply because they are known to be highly correlated with precipitable water vapor V, which is easily retrieved from SSM/I data. Indeed, Liu (1984, 1986, 1988) has already demonstrated the use of satellite-derived V as a proxy for surface specific humidity q in surface latent heat flux calculations; the use of the minimum variance formalism described here would simply represent a more direct — and perhaps more optimal — path to q than that used by Liu.

Finally, term (C) expresses the retrieval error arising from all sources of radiometric variability not contributed by the parameter to be retrieved. It can be seen that the role of instrument noise is qualitatively no different than that of the statistical uncertainty in the values of the elements of $\mathbf{q}$ weighted by the strength of their respective radiometric signatures.

Mathematically, minimization of (11.12) is accomplished in the standard way, by taking the partial derivative with respect to $\mathbf{d}$, setting the resulting expression equal to zero and solving for $\mathbf{d}$. This procedure yields a set of M equations for the M elements of $\mathbf{d}$, expressible in matrix form as

$$\left[\sigma_p^2 \mathbf{a}\mathbf{a}^T + \mathbf{a}\langle p\mathbf{q}\rangle^T \mathbf{A}^T + \mathbf{A}\langle p\mathbf{q}\rangle \mathbf{a}^T + \mathbf{S}_\epsilon + \mathbf{A}\mathbf{S}_q\mathbf{A}^T\right] \mathbf{d} = \sigma_p^2 \mathbf{a} + \mathbf{A}\langle p\mathbf{q}\rangle, \quad (11.16).$$

It is common in remote sensing literature to conclude by giving an explicit formal solution for $\mathbf{d}$ as the right hand side of (11.16) pre-multiplied by the matrix inverse of the term in square brackets. However, the inverse matrix is not in itself of great interest, and a direct numerical solution of (11.16) using LU decomposition

is a factor of three more economical computationally than the standard techniques for inverting matrices (Press et al. 1986). If **d** can be computed once-and-for-all, as should be the case for a purely linear retrieval problem, this difference is of no consequence. But when the minimum variance method is used iteratively on a non-linear problem, almost every term in (11.16) must be recomputed at each step, in which case numerical efficiency may assume considerable importance. This point is emphasized here by leaving the solution for **d** implicit in (11.16) rather than making use of notation involving inverse matrices.

It is beyond the scope of this thesis to describe in detail a generalization of the linear minimum variance method to the non-linear retrieval of environmental variables from SSM/I data; this shall be left a topic for future work. Broadly speaking however, a non-linear, iterative algorithm based on the above linear formulation may be had simply by expanding the brightness temperature model as a Taylor series about the current best guess for each input parameter and discarding all but the linear terms (see Houghton et al. 1984). Changes Δp in each parameter p are then estimated in turn as for the linear case, possibly using an 'optimal' subset of the available channels, and the new estimates serve as the point about which the brightness temperature model is linearized in preparation for the next iteration. Those model parameters which cannot be confidently estimated directly from SSM/I data may be assigned expected values and uncertainties which are statistically consistent with what is known about the other variables. The most important new subtleties which must be considered in a non-linear iterative algorithm concern the criterion used to terminate iteration and the determination of the *a priori* variances and covariances appearing in (11.16).

11.4 Theoretical Accuracy Limits for SSM/I retrievals

Even if a non-linear iterative approach is probably required for optimal SSM/I retrievals of most parameters, the linear formulation developed above is well-suited

to the task of placing a lower bound on the estimation error associated with a given solution. All that is required is a linearization of the analytic brightness temperature model about the assumed solution, plus reasonable estimates of $\mathbf{S}_\epsilon$ and $\mathbf{S}_q$.

Here we ignore correlations among the environmental variables, except that we allow the mean values and uncertainties of p_0, H, T_A, and Γ to be constrained by the assumed atmospheric water vapor estimate V, in accordance with Table 6.5. In effect, this approach assumes *a priori* that V can always be estimated with sufficient accuracy — i.e., with standard error <3.0 kg m^{-2} — to choose the appropriate entry in this table). This assumption is in fact quite reasonable, both in view of the reported precision of simple empirical algorithms (e.g., Alishouse et al. 1990a) and based on the results to follow.

Eqs. (11.12) and (11.16) thus reduce to

$$\delta_p^2 = (\mathbf{d} \cdot \mathbf{a} - 1)^2 \sigma_p^2 + \mathbf{d} \cdot \left[\left(\mathbf{S}_\epsilon + \mathbf{A}\mathbf{S}_q\mathbf{A}^T \right) \mathbf{d} \right] \tag{11.17}$$

and

$$\left[\sigma_p^2 \mathbf{a}\mathbf{a}^T + \mathbf{S}_\epsilon + \mathbf{A}\mathbf{S}_q\mathbf{A}^T \right] \mathbf{d} = \sigma_p^2 \mathbf{a}, \tag{11.18}$$

where $\mathbf{S}_\epsilon$ and $\mathbf{S}_q$ are now diagonal matrices whose non-zero elements are, respectively, channel noise variances and the squared *a priori* uncertainties in $\mathbf{q}$. The sensitivity terms $\mathbf{a}$ and $\mathbf{A}$ are simply $\partial T_B/\partial p$ and $\partial T_B/\partial \mathbf{q}$ evaluated for the assumed values of p and $\mathbf{q}$.

The channel noise variances specified by $\mathbf{S}_\epsilon$ are taken to include not only instrument noise, which amounts to only ~0.5 K, but also noise arising from unmodeled geophysical contributions to brightness temperature variations. Based on results presented in Chapter 8, it would appear that the effective noise term may be significantly larger and that it increases with frequency. Here we assume noise standard deviations of 1.5 K for the 19V, 19H, and 22V channels, 2 K for

the 37V and 37H channels, and 3 K for the 85V and 85H channels. In fact, the actual values probably vary somewhat depending on the scene being viewed.

Although we have already implicitly assumed that it should be possible to estimate V accurately enough to set constraints on p_0, H, T_A, and Γ from Table 6.5, a correspondingly small variance in V should normally *not* be assumed when estimating retrieval errors from (11.17). This is because σ_p^2 and $\mathbf{S}_q$ are supposed to represent *a priori* uncertainties which do not depend on knowledge of the satellite brightness temperatures used in the retrievals. For the purposes of (11.17) and (11.18), therefore, the uncertainty in V is assigned the more conservative value of 10 kg m^{-2} .

For liquid water content L we arbitrarily assumed a value of 0.1 kg m^{-2} with a standard deviation of 0.06 kg m^{-2} . Mean cloud height z_c was taken as $0.5(T_A - 273)/\Gamma$, with a standard deviation equal to 60% of this value. The mean surface wind speed U was assumed to be 7.0 m s^{-1} with a uncertainty of 4.0 m s^{-1} . The sea surface temperature T_S was assumed to be known to ± 5 K from independent data sources in middle and high latitudes (i.e., for $V < 40$ kg m^{-2}), ± 3 K in the subtropics and tropics ($V > 40$ kg m^{-2}). Finally, the viewing angle θ was specified to be 53.0° with an uncertainty of 0.3°, corresponding to the sensor "pointing problem" described in Chapter 4.

Eq. (11.18) was solved to find the optimal **d** for the retrieval of each parameter (not shown), and these **d** were substituted into (11.17) in order to estimate the retrieval error variances δ_p^2. Theoretical standard retrieval errors are given for wind speed U, total water vapor V, and liquid water L in Tables 11.1–11.3. *For all other parameters* (i.e., H, T_A, Γ, T_S, z_c, p_0), *minimum retrieval error estimates ranged between 80% and 100% of the a priori uncertainties, implying that the*

Table 11.1: Minimum theoretical rms retrieval uncertainty for wind speed U (m s^{-1}). (A) Seven channels used, standard assumptions (including uncertainty in θ). (B) Same as A, but θ assumed known with zero uncertainty. (C) Same as A, but heavy cloud assumed (L = 1.0 kg m^{-2} with uncertainty of 0.6 kg m^{-2}). (D) Same as A, but no 85 GHz channels.

V (kg m^{-2})	A	B	C	D
0–10	2.1	1.9	2.2	2.3
10–20	2.0	1.8	2.3	2.1
20–30	2.1	1.9	2.4	2.2
30–40	2.1	2.0	2.5	2.2
40–50	2.2	2.1	2.6	2.3
50–60	2.2	2.1	2.6	2.3
60–70	2.2	2.1	2.5	2.2

SSM/I is incapable of providing significant additional information concerning these parameters, at least for the conditions assumed in this analysis.

Each column in Tables 11.1–11.3 represents a slightly different set of conditions for the determination of δ_p^2. In column A, the base set of conditions described above were used, and all seven SSM/I channels were assumed to be included in the retrieval. Column B is the same, but the uncertainty in θ was neglected in the computations. In column C, a significantly heavier cloud layer was assumed, amounting to 1.0 kg m^{-2} instead of 0.1 kg m^{-2} and with an *a priori* uncertainty of 0.6 kg m^{-2} . Finally, the column D gives retrieval errors computed for the case that the 85V and 85H channels are excluded from the retrievals.

The results in Table 11.1 suggest that *even an algorithm using all seven SSM/I channels, without any uncertainties in θ, might still have some difficulty meeting*

Table 11.2: Minimum theoretical rms retrieval uncertainty for integrated water vapor V (kg m^{-2}). (A) Seven channels used, standard assumptions (including uncertainty in θ). (B) Same as A, but θ assumed known with zero uncertainty. (C) Same as A, but heavy cloud assumed (L = 1.0 kg m^{-2} with uncertainty of 0.6 kg m^{-2}). (D) Same as A, but no 85 GHz channels.

V (kg m^{-2})	A	B	C	D
0–10	1.5	1.5	2.0	1.5
10–20	0.9	0.9	1.4	1.1
20–30	1.5	1.4	1.9	1.5
30–40	1.8	1.7	2.1	1.8
40–50	2.0	2.0	2.4	2.0
50–60	2.1	2.1	2.6	2.1
60–70	2.2	2.2	2.8	2.3

the ± 2.0 m s^{-1} precision standard for SSM/I retrievals of U which was specified by the Department of Defense. The accuracy computed here also does not account for additional errors arising from directional effects (neglected in the geometric optics model of Chapter 7) and from variations in surface layer stability and other factors affecting the relationship between U and surface roughness.

The inclusion of $\pm 0.3°$ uncertainty in θ contributes an additional 0.1–0.2 m s^{-1} error to the retrievals. An optimal algorithm which excludes the 85 GHz channels might be expected to achieve a mean precision of 2.2 m s^{-1} . The addition of very thick water cloud reduces the maximum precision to between 2.2 and 2.6 m s^{-1} . Recall that the situation under consideration here assumes that cloud is uniformly distributed throughout the fields-of-view of all SSM/I channels; *when integrated cloud water varies on horizontal scales shorter than the resolution of the 19 GHz*

Table 11.3: Minimum theoretical rms retrieval uncertainty for integrated liquid water L (kg m^{-2}). (A) Seven channels used, standard assumptions (including uncertainty in θ). (B) Same as A, but θ assumed known with zero uncertainty. (C) Same as A, but heavy cloud assumed (L = 1.0 kg m^{-2} with uncertainty of 0.6 kg m^{-2}). (D) Same as A, but no 85 GHz channels.

V (kg m^{-2})	A	B	C	D
0–10	0.014	0.014	0.044	0.028
10–20	0.016	0.016	0.042	0.028
20–30	0.022	0.022	0.048	0.030
30–40	0.026	0.026	0.053	0.031
40–50	0.030	0.030	0.059	0.033
50–60	0.033	0.033	0.063	0.034
60–70	0.036	0.036	0.069	0.036

channels (~50 km), as is usually the case, retrieval noise may be significantly worse.

Table 11.2 indicates that water vapor should theoretically be retrievable with an accuracy of $\lesssim$ 2 kg m^{-2} under most circumstances, or as accurately as ~1 kg m^{-2} in regions for which 10 kg m^{-2} $\lesssim V \lesssim$ 20 kg m^{-2} . Sensitivity to errors in θ appears to be minimal, while uniform heavy cloud can degrade retrieval accuracy by ~0.5 kg m^{-2} . Elimination of the 85 GHz channels from the retrievals has little to no effect on accuracy, suggesting that these channels normally do not provide much additional information on V, despite their high sensitivity to water vapor.

Finally, Table 11.3 shows that cloud liquid water is theoretically retrievable with a precision of between 0.014 and 0.036 kg m^{-2} , depending on whether the air

mass in question is dry or moist. While the 85 GHz channels contribute markedly to reducing retrieval errors in the driest cases ($V \lesssim 40$ kg m^{-2}), their contribution is greatly weakened in tropical air masses on account of the relatively high opacity of water vapor at this frequency. For a thick cloud with 1.0 kg m^{-2} of liquid water, maximum precision of L retrievals degrades to between 0.04 and 0.07 kg m^{-2} . Much of this error can be attributed to the uncertainty in the cloud height z_c and, hence, in the liquid water absorption coefficient which depends on temperature.

11.5 Estimation of precipitation parameters with the SSM/I

A number of workers continue to experiment with ways to use multifrequency microwave information to retrieve surface rain rate, occasionally resorting to fairly elaborate physical model-based retrieval methods (e.g., Kummerow et al. 1989, Olson 1989). In assessing the potential success of such algorithms, it should be borne in mind that the number of radiatively significant degrees of freedom per $\sim$600 km^2 affected by rain is likely to easily exceed the maximum of 13 independent pieces of information (5 channels sampled once each, 2 channels sampled four times each) available from the SSM/I for the same physical area. Consequently, an optimal rain rate retrieval algorithm for the SSM/I will probably of necessity rely on statistical constraints in addition to physics. Unfortunately, a suitable body of statistical information on the spatial structure and microphysics of global oceanic precipitation does not yet exist, though the increasingly common use of numerical cloud model results as input to microwave radiative transfer calculations (e.g., Szejwach et al. 1986; Mugnai et al. 1990) may help fill part of the gap in the future.

Several more modest, single frequency rain rate algorithms have seen considerable experimental use with SSM/I's predecessors, the two SMMR's and the ESMR. For example, Wilheit et al. (1977) exploited the brightness temperature increase associated with precipitation to estimate rain rate from ESMR 19 GHz

data (horizontal polarization only), using a theoretical relationship derived from a very simple, plane-parallel radiative transfer model. At that point it was becoming apparent that such single-frequency "emission-based" algorithms suffered from significant ambiguities introduced by uncertainties in the effective rain layer depth, which, together with the rain rate, determined the layer optical depth, and the effective fractional coverage of the sensor footprint by rain. The latter issue arose from the non-linear, even non-monotonic dependence of brightness temperature on rain rate — rain rates retrieved based on the assumption of a uniformly filled field-of-view (FOV) could thus seriously underestimate the true FOV-averaged rain rate when rain was concentrated in heavier showers only partially filling the FOV (Lovejoy and Austin 1980, Wilheit 1986).

More recently, Spencer (1986) demonstrated a single-frequency, dual-polarization technique which relates the observed scattering properties of deep convective clouds at 37 GHz to rain intensity. The basis for the method is the observation that, for a given polarization difference $\Delta T_B = T_{B,V} - T_{B,H}$, pixels affected by scattering have a lower mean brightness temperature $\overline{T_B} = 0.5(T_{B,V} + T_{B,H})$ than those affected by non-scattering constituents of the atmosphere*. The so-called *volume scattering signal* is thus calculated as the Euclidean distance of an observed bipolarization brightness temperature pair from the 'pure emission line' connecting the 'open ocean' brightness temperature pair and an unpolarized 'opaque cloud' brightness temperature (see Fig. 10.1).

One of the most important advantages of this technique is that it largely removes the land-sea contrast from the microwave imagery, so that the scattering signal is equally distinguishable over both land and ocean. This is possible

* Credit for what is commonly referred to as the Spencer (1986) scattering-based algorithm should in fact be shared with Weinman and Guetter (1977), whose use of a linear combination of the 37.0 GHz channels of the earlier ESMR instrument to detect precipitation over both land and water is conceptually almost indistinguishable from the Spencer (1986) method

because the radiative characteristics of land are not much different from those of the hypothetical opaque cloud which defines one end of the 'emission only' line in Fig. 10.1, both exhibiting low polarization and high emissivity, with mean brightness temperatures near ~270 K.

Another advantage claimed for this technique is that the so-called scattering signal may be more linearly related to rain rate than the emission signal, thus mitigating the problem of incomplete FOV-filling. Using 37 GHz data, the method shows the greatest promise for retrieval of large rain rates associated with strong convective clouds containing significant numbers of large frozen precipitation particles (i.e., graupel, hail) above the melting level, and may thus prove to be a useful complement to emission-based algorithms which "saturate" at higher rain rates. The signal-to-noise ratio of this method, however, appears to be rather unfavorable at lighter rain rates (e.g., Petty and Katsaros 1990a); as a result, there some question as to whether the Spencer method can reliably discern FOV-averaged rain rates of less than ~10 mm h^{-1} from 37 GHz data.

The Spencer algorithm was also calibrated from observations of intense storms over the North American continent, where the relationship between concentrations of ice particles aloft and surface rain rate may not be representative of convection elsewhere. For example, LeMone and Zipser (1980) and Zipser and LeMone (1980) found considerably lower maximum updraft velocities in tropical oceanic convection than are typical in thunderstorms over North America. This result suggests that there may also be proportionally fewer of the largest ice particles to which the scattering-based method is most sensitive. Moreover, rain originating in stratiform clouds or warm clouds containing none, or very few, large frozen precipitation particles will not be detected using the Spencer method.

Following the launch of the SSM/I, Spencer et al. (1989) adapted the scattering based approach to 85.5 GHz data. Because of the factor of two reduction in the size of the frozen precipitation particles required to produce an equivalent

scattering signal, 85 GHz scattering measurements have been found to offer a much improved signal-to-noise ratio over the earlier 37 GHz results. The spatial resolution of the SSM/I's 85 GHz channels (~15 km) is also much more commensurate with the horizontal structure of precipitation.

In addition to the 'emission-based' and 'scattering-based' classes of single frequency rain algorithms described above, an 'attenuation-based' approach has been proposed by Petty and Katsaros (1990a, 1990b). This method exploits the effect of attenuation by rain on the polarization of the observed microwave brightness temperatures. As discussed in earlier chapters, there is generally a large polarization difference ΔT_B for obliquely viewed microwave radiation over the unobscured ocean. But the atmosphere, including rain, both attenuates and emits nearly independently of polarization, so that ΔT_B decreases with increasing atmospheric opacity due to water vapor, cloud, and rain. The usefulness of ΔT_B as an index of atmospheric opacity had already been noted by Beer (1980), Spencer et al. (1983), and many others. However, Petty and Katsaros (1990a) offered a refinement to this interpretation by expressing the polarization difference as a non-dimensional fraction of the value expected in the absence of rain and cloudiness. That is, they defined a normalized polarization difference P such that

$$P \equiv \frac{\Delta T_B}{\Delta T_{B\,clr}}, \tag{11.19}$$

where the hypothetical clear-sky polarization difference $\Delta T_{B\,clr}$ may be determined either using a histogram technique applied to microwave imagery or based on independent information concerning other parameters affecting polarization, principally U and V.

The advantage claimed for this approach is that P can be interpreted in a relatively straightforward way in terms of an effective microwave transmittance associated with cloud and rain only, with much of the influence of unrelated geophysical parameters having been factored out via the denominator in (11.19). A

single threshold value of P might therefore be found which consistently distinguishes most rain areas from non-raining areas, irrespective of background variations in the polarization difference due to surface wind roughening and atmospheric attenuation due to water vapor.

Furthermore, it may be readily shown using the atmospheric brightness temperature model of the previous chapters that $\log(P)$ is approximately proportional to the optical depth of a horizontally homogeneous liquid water layer in the atmosphere. Thus, in cases where the optical depth due to liquid water is $\lesssim$ unity throughout the FOV, reasonable estimates of the column liquid water content and/or rain rate might be had simply by multiplying $\log(P)$ by a single coefficient appropriate to the frequency used and any necessary assumptions about rain layer depth or liquid water temperature. For the opposite extreme case of an intermittent field of optically thick rain separated by completely cloud-free areas within the satellite FOV, P is simply equal to one minus the fractional coverage F of that rain.

A disadvantage of polarization as an index of precipitation activity is that it provides little direct physical evidence of rain intensity when the optical depth within the raining portion of the satellite FOV greatly exceeds unity. Furthermore, physical interpretation of the polarization signal may be complicated by the presence of preferentially oriented scatters, as discussed earlier in this chapter. Nevertheless, the SMMR-radar comparisons conducted by Petty and Katsaros (1990b) suggest that statistically unbiased rain estimates may be possible using 37 GHz P observations, even if rain rate uncertainties on a pixel-by-pixel basis are likely to remain large.

Abstracts of the Petty and Katsaros (1990a) and Petty and Katsaros (1990b) papers are provided in Appendix A. For the purposes of the remainder of this thesis, it is sufficient to note that radar comparisons with the Nimbus 7 SMMR 37 GHz channels appear to support a P threshold of $\sim$0.8–0.9 for distinguishing

rain from no-rain in the tropics and subtropics. No detailed comparisons have yet been performed for the midlatitudes.

12. A UNIFIED ALGORITHM PACKAGE FOR SSM/I ESTIMATES OF ATMOSPHERIC PARAMETERS

Although three years have now passed since the launch of the first Special Sensor Microwave Imager (SSM/I), relatively few well-tested, well-documented, globally applicable algorithms have appeared for the estimation of atmospheric parameters over the ocean. Given the considerable interest at the University of Washington and elsewhere in applying SSM/I data to case studies of weather systems over the ocean, we therefore undertook to assemble a unified set of algorithms which will permit us to obtain meaningful estimates of all of the parameters which the SSM/I is capable of sensing. First, of course, we considered those oceanic parameter algorithms for the SSM/I which have already been developed and documented by other investigators. Where we felt that an existing algorithm for a given parameter could be improved upon (according to our own theoretical and/or practical criteria) we sought to refine it or to replace it outright with one of our own design.

New statistical algorithms for water vapor V, wind speed U, and column liquid water L were derived as part of the SSM/I Calibration/Validation effort in order to partially replace the failed Hughes algorithm set developed prior to launch. All of these new algorithms are based on multiple linear regression of SSM/I brightness temperatures against *in situ* observations of the desired parameter, as described in section 11.1. Because these new algorithms were primarily intended as direct substitutes for the Hughes algorithms within the framework of existing operational retrieval software of the Naval Oceanography Command and the Air Force Weather Service, they were required to meet the same severe computational constraints as were the Hughes algorithms; namely, that each algorithm should entail only linear combinations of at most four SSM/I channels.

Despite these constraints, and despite the fundamental limitations of a purely statistical approach, the GSW wind speed algorithm (Goodberlet et al. 1989) has

been reported to have an accuracy of ± 2 m s^{-1} except in precipitation. This stated accuracy, using a linear combination of four channels, is remarkably similar to the theoretical maximum accuracy predicted in section 11.4 for wind speed estimates derived from all seven channels, presumably using a non-linear, iterative generalization of the the minimum variance method presented in section 11.3. If it were not for the fact that the error analysis in section 11.3 used what may have been rather conservative estimates of geophysical noise contributions and ignored possible correlations between U and other parameters, it might be difficult to understand how the GSW algorithm could appear to come so close to achieving optimal results. In any event, practical experience with the GSW wind speed algorithm has reassured this author that it gives at least reasonable results under most conditions, the exceptions being in the vicinity of precipitation and possibly at wind speeds in excess of $\sim$20 m s^{-1} .*

For integrated water vapor V, Alishouse et al. (1990a) used statistical regression of SSM/I brightness temperatures vs. coincident radiosonde measurements of humidity to obtain a global algorithm which met Department of Defense performance specifications, albeit only after departing from a purely linear algorithm formulation (the squared 22V brightness temperature was used as an additional independent variable in the regression). Although the performance of their algorithm appears to be very good under most conditions, their Fig. 3 suggests that it has difficulty reproducing very high and very low observed water vapor values, i.e., above 60 kg m^{-2} and below 5 kg m^{-2} .

---

* The author and other workers (e.g., Dr. Eric Barrett, personal communication, 1990) have noted an apparent tendency for the GSW algorithm to underestimate high wind speeds; such a tendency, if confirmed, would not be surprising in view of the various non-linearities in the relationship between U and T_B described in Chapter 9.

To the best of our knowledge, no completely satisfactory algorithm for SSM/I retrievals of integrated cloud liquid water over the ocean has yet been demonstrated. As part of the SSM/I Calibration/Validation ("Cal/Val") effort, attempts have been made to generate new cloud water algorithms using the same statistical procedure as for integrated water vapor. In contrast to water vapor, however, coincident "surface truth" measurements of integrated cloud liquid water are extremely scarce, especially over the ocean. Cal/Val team members were thus able to obtain only a small set of surface-based observations of cloud liquid water that could reasonably be compared with SSM/I data. These were made by upward-looking microwave radiometer at two locations: San Nicolas Island off the southern coast of California and Kwajalein Island in the tropics.

We tested the resulting preliminary* four-channel and six-channel algorithms (Dr. John Alishouse, 1989; personal communication) by applying them to a large ensemble of SSM/I brightness temperatures which were determined from GOES visible imagery to represent essentially cloud-free conditions (the *Cloud-free Data Set* of Chapter 8), so that the true liquid water content was known to be near zero. Unfortunately, we found that retrieved values were distributed over a range of over 0.30 kg m^{-2} — i.e., close to the natural range of non-precipitating clouds — and were highly correlated with retrieved integrated water vapor. Our conclusion is that the surface-based observations used to derive those algorithms represented too small a subset of possible meteorological conditions, and that a strong natural correlation between cloud water and integrated water vapor apparently led to regression relations which tend to equate high water vapor with high cloud water, even when no cloud water is in fact present.

---

* Revised coefficients for cloud water retrievals have recently been reported by Alishouse et al. (1990b). At the time of this writing, the author has not yet had the opportunity to independently evaluate the performance of the revised algorithm.

Based on our experience with the above algorithms, we chose to adopt only the Goodberlet et al. (GSW) wind speed algorithm in unchanged form as part of our algorithm package. Only minor modifications pertaining to the flagging of potential contamination by precipitation were made; these are described shortly. While the Alishouse et al. (1990a) algorithm for water vapor is accurate enough for most purposes, we felt that it should be possible to eliminate the minor problems that that algorithm has on the extreme ends of the water vapor range. None of the algorithms for cloud liquid water which we have tested appear to be entirely without problems; moreover, no existing cloud water algorithm known to us has taken full advantage of both the high spatial resolution and high sensitivity to liquid water offered by the 85 GHz channels of the SSM/I.

In addition to U, V, and L estimates from SSM/I imagery, we were interested in producing at least qualitatively useful images of precipitation location and character. Two precipitation indices are described here: one is based on the 37 GHz normalized polarization method of Petty and Katsaros (1990a, 1990b); the other is essentially a modification of the 85 GHz scattering based method described by Spencer et al. (1989). The former method is useful for identifying all regions of rain, including stratiform and warm-cloud rain, at 25 km resolution, though it may provide only limited information on the presence of heavier convective rain, owing to the problem of saturation. The 85 GHz scattering-based method provides high-resolution (15 km) images of the locations and relative intensity of cold-cloud precipitation, especially convection and strong frontal rainbands, but it is unable to detect warm-cloud rain or weak stratiform rain in most cases. Also, the latter method is less direct with regard to surface precipitation intensity, since it in fact responds to the concentration and size of frozen precipitation particles above the freezing level.

12.1 Surface Wind Speed

For near surface wind speed U, the Global D-Matrix algorithm of Goodberlet et al. (1989) is attractive for its simplicity and apparent reliability under most conditions, provided care is taken to exclude pixels contaminated by precipitation. The algorithm is given by

$$\begin{aligned} U(\text{m s}^{-1}) = & 1.0969T_{19V} - .4555T_{22V} \\ & -1.760T_{37V} + .7860T_{37H} - 147.90 \end{aligned} , \tag{12.1}$$

where the subscripts for each SSM/I brightness temperature T indicate frequency and polarization.

In a minor departure from GSW, we flag U as indeterminate in pixels for which $T_{19V} > 215$ K or $T_{37V} > 221$ K. In terms of atmospheric opacity due to rain, these thresholds are essentially identical, under typical conditions, to the Rain Flag "0" criteria specified by GSW; we have substituted vertically-polarized 19 and 37 GHz brightness temperature thresholds simply in order to reduce the sensitivity of the rain test to wind induced surface roughness. In a further modification to the original GSW algorithm, our experience to date has indicated that *it is highly advisable to discard not only those pixels flagged as described above, but adjacent pixels as well.* We surmise that this is because of the tendency for the low resolution 19 GHz channels to be significantly affected by precipitation in neighboring pixels, even when the higher resolution channels are not.

After rejecting all pixels suspected of contamination, we use a (3×3)-pixel moving average to smooth the retrieved U field. This operation significantly reduces pixel-scale noise, while having little effect on the desired synoptic scale wind field. Following smoothing, remaining areas of missing values are "patched" by interpolating values inward from the valid pixels bordering the missing regions. The latter step is taken partly for cosmetic reasons (e.g., for contouring purposes) and, more importantly, in order to provide at least qualitatively reasonable estimates of U for use in the computation of the various precipitation indices.

12.2 Integrated Water Vapor

In deriving our own statistical algorithm for integrated water vapor, we used the same radiosonde/SSM/I data set employed by Alishouse et al. (1990a), but with slightly modified criteria for selecting pixels to be included in the regression. This is the *Raob Comparison Date Set* already described in Chapter 8. Since we used essentially the same data set as Alishouse et al. (1990a), our algorithm is distinguished primarily by our choice of channels (19V, 19H, and 22V) and our use of $\log(280 - T_B)$ as the independent variable for each channel, this function being much more nearly linear with respect to atmospheric opacity than the untransformed brightness temperatures (e.g., Wilheit and Chang 1980).

The choice to use only the three lowest frequency channels of the SSM/I rested on two considerations: first, these channels are least affected by moderate amounts of cloud or rain water (see Chapter 9); secondly, they have very similar spatial resolutions so that very little additional 'noise' is introduced by differing amounts of cloud or precipitation within each channel's field of view. As noted earlier, the 19V and 22V channels alone already contain the bulk of the water vapor information available from SSM/I data; the addition of a third channel (19H) simply permits the water vapor algorithm to achieve somewhat greater orthogonality with respect to the two other major parameters affecting SSM/I brightness temperatures, namely liquid water and surface wind speed.

The resulting regression equation, based on 515 nearly coincident soundings, exhibits overall error statistics (outside of precipitation) virtually identical to the Alishouse et al. (1990a) algorithm applied to the same dataset, but with significantly reduced biases at very low and very high water vapor values (Fig. 12.1). The RMS difference between our algorithm and the radiosonde values is the greater of 2.0 kg m^{-2} or $0.13V$. Of course, an unknown fraction of this difference arises

from errors in the soundings themselves, as well as from spatial and temporal mismatches.

Our water vapor algorithm is given by the following:

$$\begin{aligned} V(\text{kg m}^{-2}) =& 11.98 \log_e(280 - T_{19V}) \\ &+ 42.06 \log_e(280 - T_{19H}) \\ &- 54.36 \log_e(280 - T_{22V}) - 20.5. \end{aligned} \tag{12.2}$$

In practice, we have found that contamination of V estimates by rain, as evidenced by anomalous depressions in V near the centers of tropical cloud clusters, becomes noticeable when $(T_{19V} - T_{19H}) < 24$ K. Using this test as a criterion to flag rain-contaminated V, we smooth and 'patch' the retrieved V field as described above for U.

As discussed in Chapter 8, we must admit the possibility that the island stations used in the data set may have introduced significant land contamination into some of the SSM/I 19 and 22 GHz brightness temperatures. It has not yet been determined whether and how much this might affect the accuracy of this algorithm under uncontaminated conditions. It has been observed that our V algorithm gives systematically lower retrievals ($\sim$5 kg m^{-2}) than the Alishouse et al. (1990a) algorithm in certain midlatitude cases over the open ocean (Dr. William S. Olson, personal communication, September 1990), but it is not known which of the two algorithms is more likely to be responsible for this discrepancy. Preliminary tests using synthetic brightness temperatures from the analytic model derived in earlier chapters indicate that each algorithm is capable of giving results deviating by up to 5 kg m^{-2} from the model input value, depending on the values of other parameters such as wind speed U and cloud liquid water content L. More systematic tests are still needed of the regression algorithms and of the brightness temperature model as well, since the latter was calibrated in part using the same Raob Comparison Data Set.

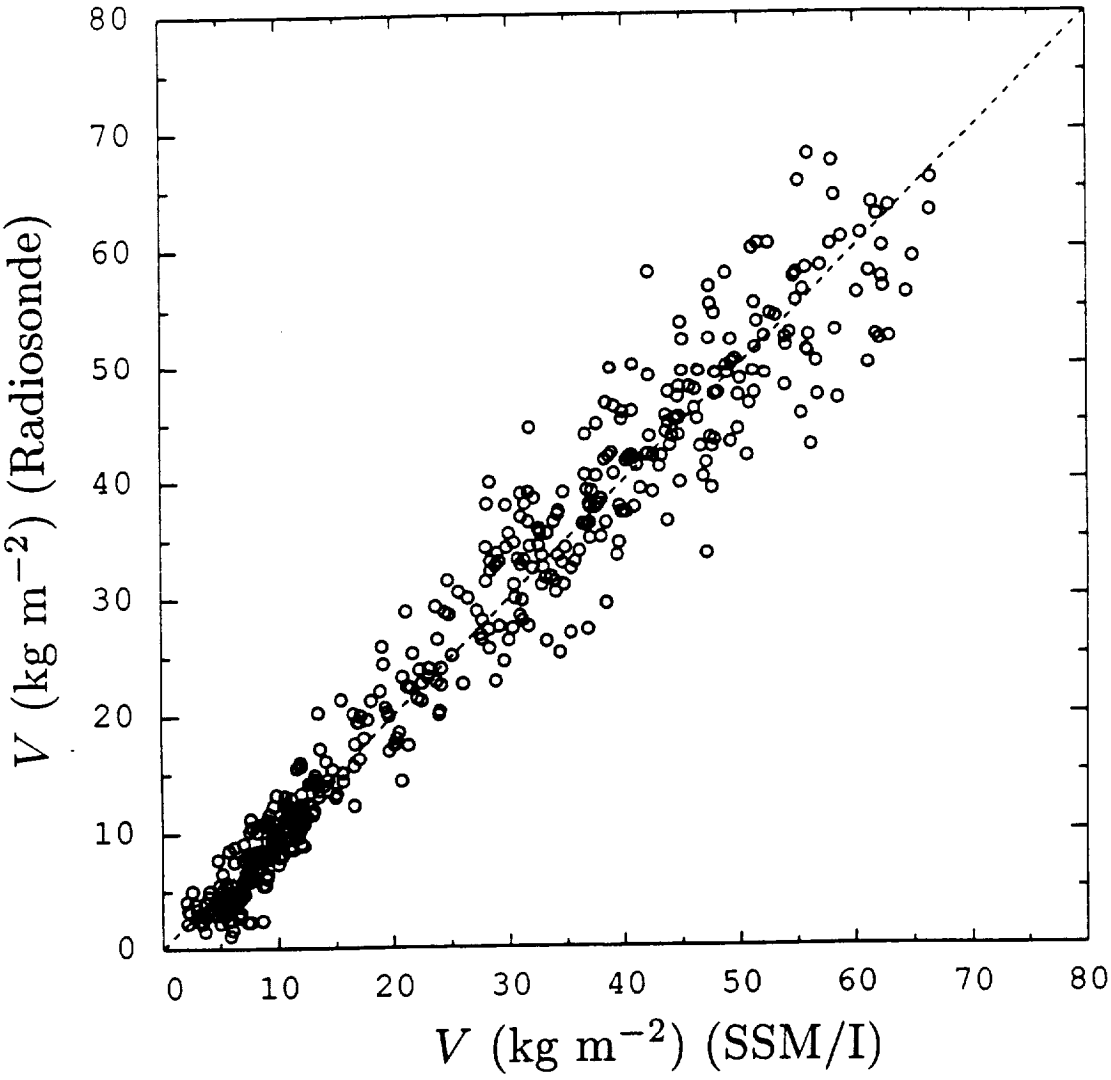

Fig. 12.1 Integrated water vapor V, derived from Eq. (12.2) applied to SSM/I data, compared to near-coincident radiosonde estimates of V.

12.3 85 GHz precipitation estimates (scattering based)

The Spencer et al. (1989) scattering based precipitation index uses a "polarization corrected" 85 GHz brightness temperature PCT which responds to volume scattering by ice particles. This variable appears to be strongly correlated with surface precipitation intensity, particularly in convection and frontal rain bands. However, as formulated by Spencer et al., who used the constant linear coefficients 1.818 and −0.818 for the 85V and 85H channels, respectively, significant large-scale variations in background PCT arise due to changes in atmospheric and surface temperature and surface wind roughening. These changes are quite obvious when one uses the fixed coefficients to plot PCT for a complete SSM/I swath segment extending from the tropics to high latitudes; the brightness temperature model of this thesis can also be used to demonstrate that such background PCT changes may be expected as a result of differences in surface wind speed, atmospheric water vapor content and temperature. In short, the fixed coefficients proposed by Spencer et al. (1989) do not account for significant variations in the position of the 'open ocean' bipolarization brightness temperature, and hence in the definition the 'emission only' line (see Fig. 10.1) which serves as the baseline for detecting scattering due to atmospheric ice.

Here we propose an alternative formulation of the volume scattering signal which, while otherwise conceptually identical to that of Spencer et al. (1989), may be interpreted as allowing the slope of the assumed 'emission only' line to vary in such a way that the latter always passes through (or near) the true 'open ocean' brightness temperature pair and through a fixed, unpolarized reference brightness temperature corresponding to an opaque, non-scattering cloud at the freezing level.

We thus calculate the 85.5 GHz *polarization corrected brightness temperature depression* S_{85} as

$$S_{85}(\mathrm{K}) = P_{85}T_{85V,O} + (1 - P_{85})T_C - T_{85V}, \tag{12.3}$$

where the normalized 85 GHz polarization P_{85} is the ratio of the observed polarization difference Δ_{85} to the polarization difference $\Delta_{85,O}$ expected in the absence of clouds under otherwise similar conditions; similarly, $T_{85V,O}$ is the value of T_{85V} expected under cloud-free conditions. $T_C\,(= S + PCT)$ is the limiting brightness temperature of an increasingly opaque, non-scattering cloud layer, which we take to be a constant 273 K.

Expressions for $\Delta_{85,O}$ and $T_{85V,O}$ were found by regressing observed Δ_{85} and T_{85V} against retrieved U and V for 1.2×10^4 SSM/I pixels obtained from known cloud-free regions of the ocean (the *Cloud-free Data Set* of Section 8.2). This led to the following expressions:

$$P_{85} = (T_{85V} - T_{85H}) \exp(.0241U + .0271V - 4.44), \tag{12.4}$$

$$T_{85V,O} = 280.0 - \exp(4.20 - .00567U - .0406V). \tag{12.5}$$

In practice, we have found that S_{85} consistently remains within 10 K of zero except in localized regions of precipitation. Experience with this index, which in fact contains about the same physical information as the Spencer PCT except for the removal here of background variations, suggests that larger values of S_{85} are an excellent indication of the relative strength of cold-cloud precipitation*. Direct calibration of S_{85} and/or PCT in terms of surface rain rate under various conditions is still lacking.

---

* While $S_{85} > 10$ appears to provide reliable evidence for the presence of precipitation, $S_{85} < 10$ is *not* sufficient to rule out light stratiform or warm-cloud precipitation.

12.4 Cloud Liquid Water

In the absence of anisotropic extinction by precipitation particles, it can be shown using the brightness temperature model of this thesis that the normalized polarization P at any SSM/I frequency is well approximated by the effective microwave transmittance τ_C associated with liquid water alone, raised to a power $\alpha\,(\approx 2)$ which depends only weakly on other variables. That is,

$$P \approx \tau_C^{\alpha} \approx \exp\left[-\frac{\alpha\kappa_e L}{\cos\theta}\right], \tag{12.6}$$

where κ_e is the effective mass extinction coefficient of the liquid water in the cloud, L is the vertically integrated liquid water mass, and $\theta\,(\approx 53°)$ is the SSM/I viewing angle.

Of all the SSM/I channels, those at 85 GHz have the best spatial resolution and sampling density and correspond to the highest κ_e for liquid water. We used the brightness temperature model of previous chapters to determine $\alpha\kappa$ at this frequency, assuming conditions typical for regions of marine stratus near the California coast. We then inverted (12.6) to obtain

$$L_{85}(\mathrm{kg\,m^{-2}}) = -0.339\log_e(P_{85}), \tag{12.7}$$

where P_{85} is given by (12.4).

When significant radiative scattering by preferentially oriented, precipitation-size ice particles occurs, the 85 GHz polarization difference is no longer a useful measure of cloud opacity. Consequently, we flag L_{85} as indeterminate whenever S_{85} (as given by Eq. 12.3) exceeds 10 K.

The scaling coefficient shown in (12.7) is strictly correct only for a cloud temperature near 285 K; for colder or warmer clouds there will be systematic relative errors ($\sim$10%) in retrievals of L using this formula, owing to the strong dependence of κ_e on temperature. For marine stratus, where liquid water estimates are

currently of great practical interest, the temperature of the cloud is normally confined to a fairly narrow and well-determined range because of the strong coupling between cloud temperature and ocean surface temperature.

For most other weather regimes, cloud temperature may be extremely difficult to specify *a priori*, and a variety of other problems (e.g., precipitation, strong horizontal inhomogeneity, strong water vapor emission in the tropics) may also adversely affect the absolute accuracy of cloud water estimates (see Chapters 9 and 10). Note that if there are inhomogeneities of order 0.3 kg m^{-2} or greater within the 85 GHz footprint (as might be the case with cold airmass cellular convection), the non-linear relationship between P_{85} and L may lead to significant *underestimates* of L from (12.7). Consequently, there is probably little to be gained by using a more complex expression for L_{85} which would explicitly include cloud temperature.

A relation analogous to (12.7) holds between integrated cloud water L and P_{37}. Again using the theoretical brightness temperature model to determine $\kappa_e \alpha$, we have the following alternate algorithm for L:

$$L_{37}(\mathrm{kg\,m^{-2}}) = -1.42 \log_e(P_{37}). \tag{12.8}$$

where the same approach as before was used to derive an expression for P_{37}:

$$P_{37} = (T_{37V} - T_{37H}) \exp(.0151U + .00607V - 4.40), \tag{12.9}$$

Advantages of L_{37} over L_{85} include reduced sensitivity to the effects of variations in V and to precipitation size particles, as well as greater linearity in the response of 37 GHz channels to liquid water (hence reduced errors due to inhomogeneity within the satellite footprint). Disadvantages include significantly poorer spatial resolution (30 km vs. 15 km) and, in middle and high latitudes (i.e., for low V), somewhat poorer signal-to-noise ratio.

We applied the above algorithms for L_{37} and L_{85} to the Cloud Free Data Set and verified that the mean retrieved value of L was zero — this is of course the expected result since the same data set was used to derive the regression coefficients in (12.4) and (12.9). Standard deviations were 0.025 kg m^{-2} and 0.021 kg m^{-2}, respectively, and these may be interpreted as approximate *lower bounds* on the rms error of cloud liquid water estimates using these specific algorithms. These results are remarkably close to, or even slightly better than, the theoretical minimum retrieval errors for cloud liquid water presented in Table 11.3 for five channel retrievals (no 85 GHz) and seven channel retrievals, respectively. However, those theoretical results were derived for global conditions rather than for the more restricted range of conditions encountered in regions of marine stratocumulus.

We also applied both algorithms to a region of marine stratocumulus sampled on three successive passes near the coast of Southern California, and we compared the retrieved values of L (Fig. 12.2). The slope of the best fit line for these data is 0.99; this confirms that at least the *ratio* of the theoretically derived coefficients appearing in (12.7) and (12.8) has been accurately predicted by the analytic brightness temperature for marine stratocumulus conditions.

12.5 37 GHz precipitation estimates (attenuation based)

As noted in section 11.5, Petty and Katsaros (1990a, 1990b) found that the normalized 37 GHz polarization difference P_{37} (see above) is a useful index of precipitation intensity and/or fractional coverage by precipitation. The results of those studies, which employed data from the Scanning Multichannel Microwave Radiometer (SMMR) on Nimbus 7, suggest that $P_{37} < 0.8$ ordinarily occurs only in the presence of precipitation, while $P_{37} > 0.9$ generally implies precipitation-free pixels. Values between 0.8 and 0.9 appear to imply at most light precipitation, if any. Experience to date suggests that only in heavy marine stratocumulus clouds are values of P_{37} likely to fall much below $\sim$0.8 due to cloud liquid water alone,

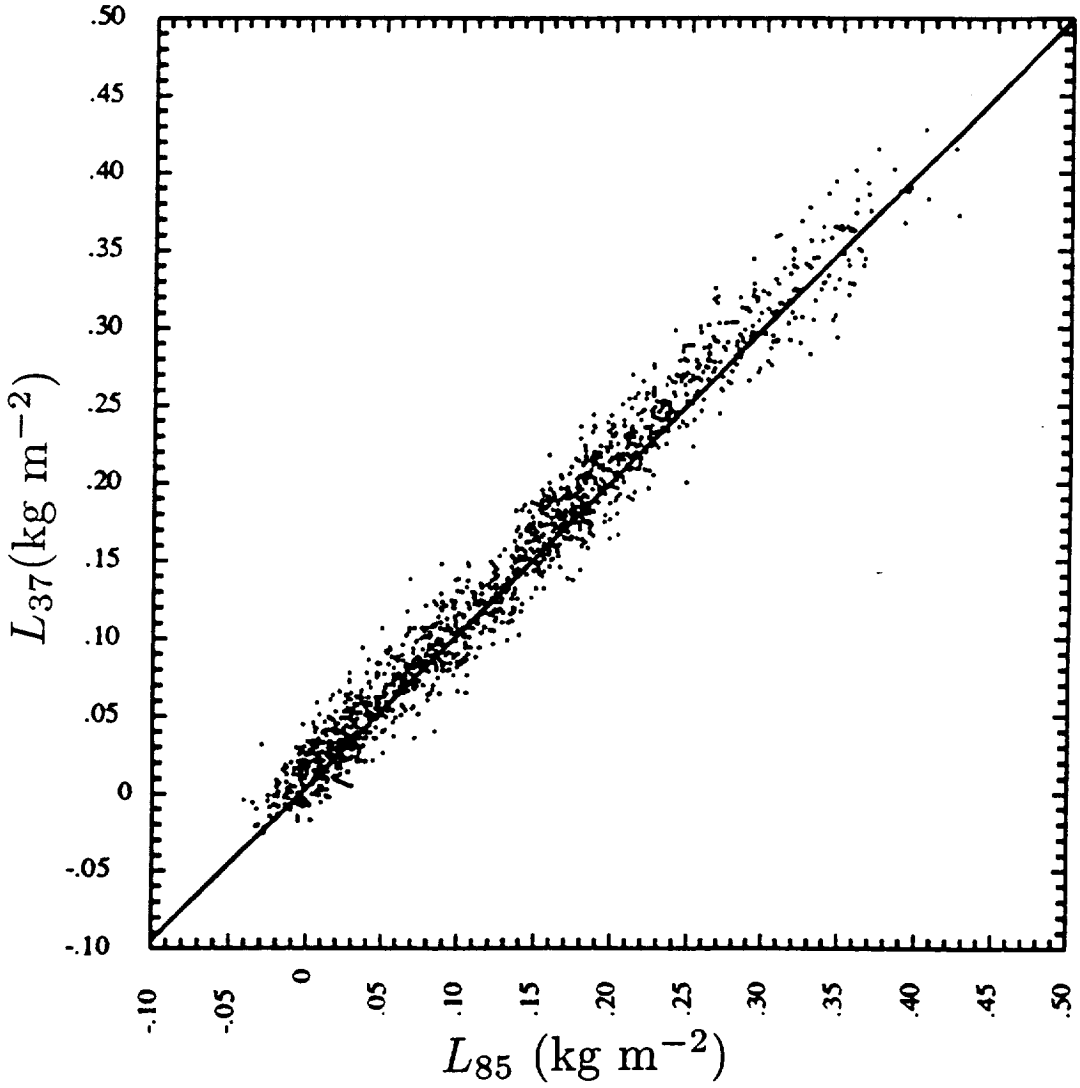

Fig. 12.2 Comparison of 37 GHz-derived and 85 GHz-derived estimates of integrated cloud liquid water (from Eqs. 12.7, 12.8) for a region of marine stratocumulus observed near the coast of California during three successive SSM/I passes.

and even these clouds are very likely associated with at least some precipitation in the form of drizzle.

Pending the results of comparisons between surface radar data and P_{37} obtained from the SSM/I, we tentatively assume that the SMMR thresholds described above are also valid for the SSM/I, both in the tropics and midlatitudes. See Petty and Katsaros (1990b) for a discussion of the interpretation of P_{37} in terms of actual footprint averaged rain rate.

12.6 An Example

To illustrate the characteristics of the geophysical fields estimated from SSM/I data using the algorithm package described above, an occluded midlatitude cyclone affecting the British Isles on 18 October 1987 was selected as an example. Fig. 12.3 depicts the 0600 UTC surface analysis, which was taken from the *Fronts '87* field experiment Meteorological Atlas. At this time, the cold front extended from the Irish Sea southwestward, with a wave-like feature analyzed some 400 km northwest of the Iberian peninsula. The exact position and amplitude of this 'wave' was uncertain, owing to the sparsity of surface reports in the vicinity.

Fig. 12.4 shows the NOAA-10 infrared image of the same storm at 0420 UTC. The circulation around the low pressure center is evident west of Ireland, as is an extensive cirrus shield accompanying most of the occluded front and the upper portion of the cold front. Behind the cold front, considerable open-cell convection is visible, including a region of stronger, more organized convection near 47°N, 20°W which is apparently associated with the secondary low seen in the surface analysis.

Fig. 12.5 depicts composite SSM/I views of the cyclone from 0445 UTC (eastern swath) and 0620 UTC (overlapping western swath), using the algorithm package described above. The cirrus shield seen in the infrared image (Fig. 12.4) is transparent to microwaves and is therefore invisible in the SSM/I images.

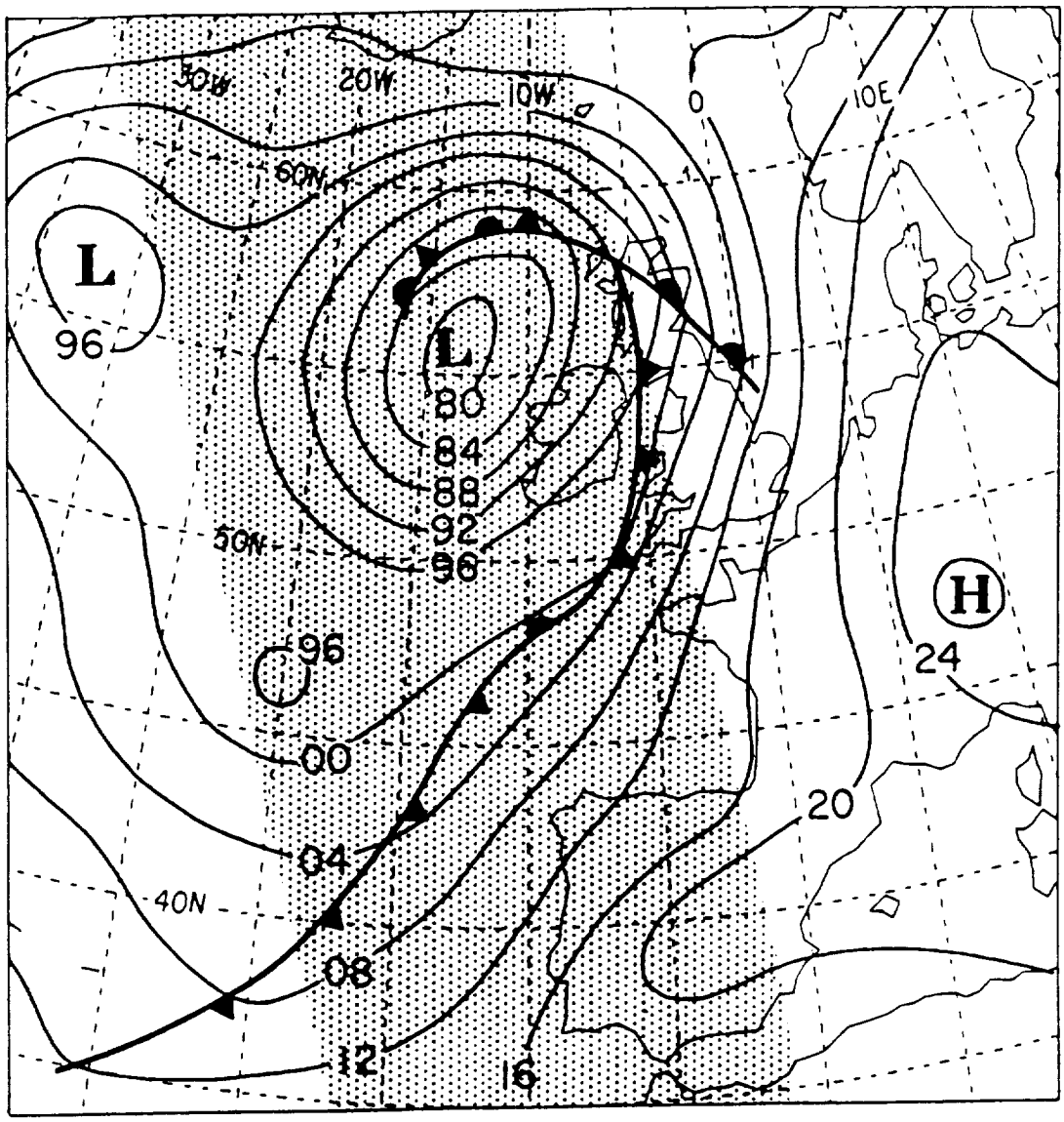

Fig. 12.3 Surface analysis of an occluded cyclone overrunning the British Isles. Valid time is 06 UTC, 18 October 1987. Shaded swath indicates geographic swath covered by SSM/I at 0620 UTC.

Fig. 12.4 NOAA-10 infrared image for 0420 UTC, 18 October 1987.

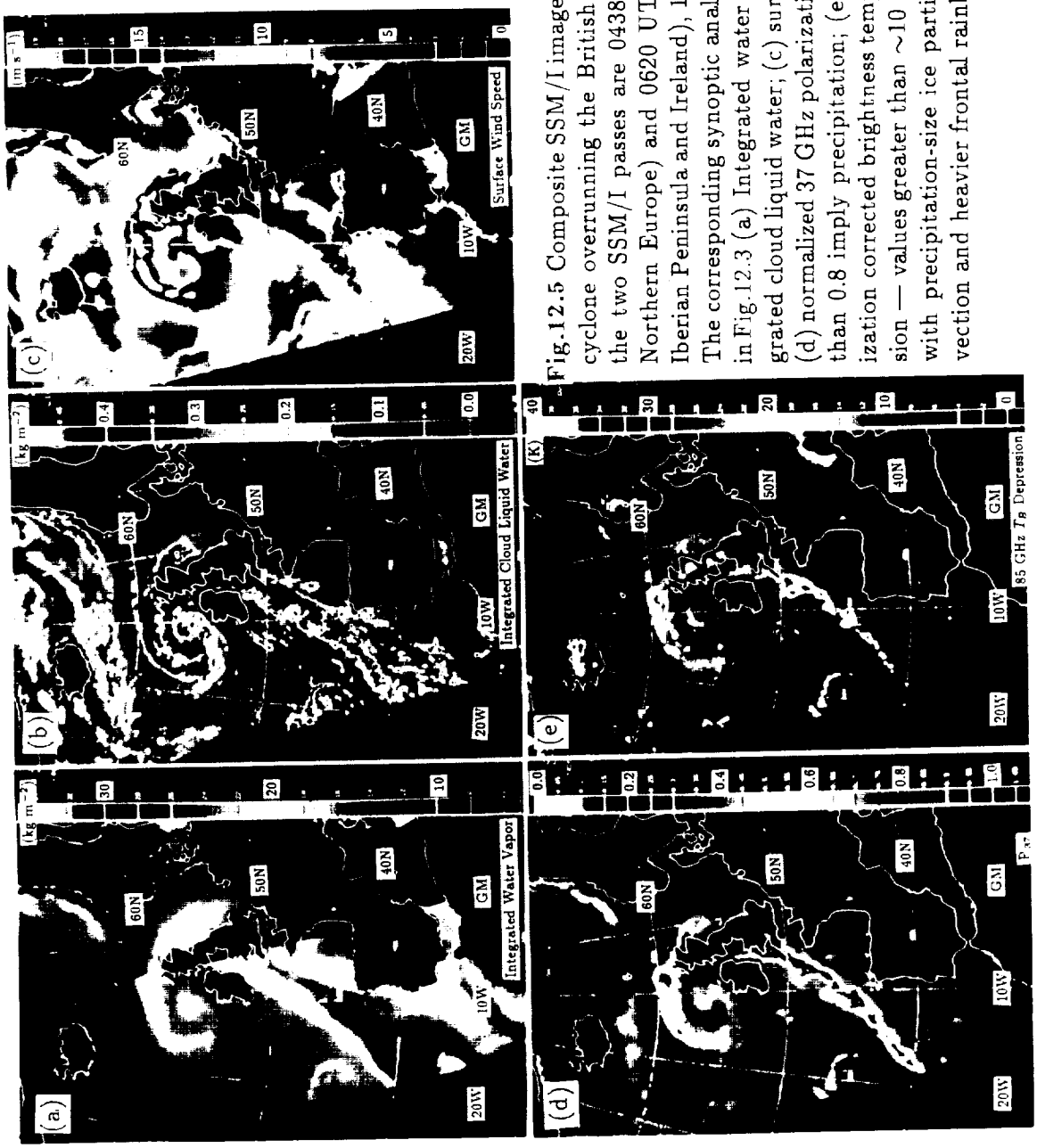

Fig.12.5 Composite SSM/I images of an occluded cyclone overrunning the British Isles. Times of the two SSM/I passes are 0438 UTC (crossing Northern Europe) and 0620 UTC (crossing the Iberian Peninsula and Ireland), 18 October 1987. The corresponding synoptic analysis is presented in Fig.12.3 (a) Integrated water vapor; (b) integrated cloud liquid water; (c) surface wind speed; (d) normalized 37 GHz polarization — values less than 0.8 imply precipitation; (e) 85 GHz polarization corrected brightness temperature depression — values greater than ~10 K are associated with precipitation-size ice particles within convection and heavier frontal rainbands.

The SSM/I integrated water vapor image (Fig. 12.5a) exhibits the characteristic water vapor maximum in the warm air sector ahead of the cold front, accompanied by a sharp decrease across the front in the direction of the cold air mass, as documented by McMurdie and Katsaros (1985) in SMMR data. In a recent study (Katsaros et al. 1989), it was found that the location of SSM/I water vapor gradients exceeding 0.1 (kg m^{-2})/km provides and excellent objective indication of the location of many surface cold fronts, irrespective of latitude and season. Note that there is no obvious sign in the water vapor field of the weak frontal wave that appears in the surface analysis.

The liquid water image (Fig. 12.5b) shows a detailed map of the vertically integrated liquid water content of the atmosphere (L_{85}), many features of which bear little apparent relation to the infrared brightness temperatures seen in Fig. 12.4 (because of the time elapsed between the SSM/I swaths and the infrared image, only general comparisons are meaningful). For example, the extensive layer of stratus northeast of Iceland appears very uniform in the infrared image, yet the SSM/I reveals significant variations in the total liquid water content of these clouds, with maxima near 0.4 kg m^{-2} . The strong SSM/I liquid water signal just south of Iceland appears to be associated with low clouds which are barely discernible in the infrared image because of the intervening cirrus layer. Blacked out pixels are those for which precipitation has been flagged, based on $S_{85} > 10$ K. Numerous cold air mass convective cells are evident behind the cold front; most of these appear to have pixel-averaged liquid water contents of less than 0.2 kg m^{-2} .

The SSM/I derived surface wind speed field is depicted in Fig. 12.5c. In general, the wind speed field is in good agreement with the pressure gradient field in the conventional surface analysis. For example, the distinct wind speed minimum just west of the low center is close to the location of a pressure col analyzed in Fig. 12.3. An exception to the general agreement occurs near the south coast of Iceland, where the relatively high wind speeds retrieved by the

SSM/I would seem to support a tighter packing of the isobars toward Iceland and a weaker gradient midway between Iceland and the occluded front. Note that some of the relatively high wind speeds indicated in the immediate vicinity of the frontal cloud band may be due to unflagged contamination of the wind signal by precipitation.

Fig. 12.5d depicts the normalized 37 GHz polarization difference P_{37} which, as explained earlier, may be interpreted as a measure of the visibility of the polarized sea surface through clouds and precipitation. A narrow, well-defined band of $P_{37} < 0.8$ (assumed to be rain) is seen along the entire length of the front, including the occluded portion wrapping around the low center near 55°N, 13°W. Some mesoscale structure in the form of kinks and local enhancements in the rainband is evident, particularly west of France. However, if one assumes that the shape and location of the precipitation band should be correlated with the location of the surface cold front, then there would again appear to be little evidence of the wave analyzed in Fig. 12.3. It may be speculated that an analyst having access to the SSM/I data for this case might not have included this feature, as it appears to have been inferred primarily from the shape of the cirrus shield seen in Fig. 12.4.

Fig. 12.5e depicts the polarization-corrected depression S_{85} of the 85.5 GHz brightness temperature. Values departing greatly from zero are associated with strong radiative scattering due to precipitation-size ice particles within convective clouds and frontal rainbands. Despite the use of the same channels for both S_{85} and the liquid water field (Fig. 12.5b), the two fields are seen to be quite different. For example, the significant liquid water features observed north of 60°N latitude in Fig. 12.5b have little or no associated scattering signal. This is consistent with our identification of that region of liquid water with low stratiform clouds in which vertical motions are weak and the formation of large ice particles is unlikely. Certain portions of the spiral cloud band near 55°N also show relatively high liquid water content but little or no scattering by ice. Apart from the frontal band itself,

the strongest scattering features are associated with a few isolate clusters of well-developed cumulonimbus clouds in the unstable cold air mass behind the front.

Of greatest interest, of course, are the well-defined regions of precipitation-size ice appearing within the frontal cloud band. Although they appear exclusively within those regions also identified as precipitating by the $P_{37} < 0.8$ criterion (Fig. 12.5d), the ice scattering signal S_{85} provides considerable additional meso-α scale information concerning the locations and relative intensities of apparent convective activity along the front. For example, individual precipitation 'cores' with diameters of less than 30 km appear to be easily resolvable within the southern end of the frontal rain band. Although further 'ground truth' studies are needed to confirm the relationship between S_{85} and precipitation, preliminary studies by the author (Petty and Katsaros 1989) and by others (e.g., Barrett and Kidd 1990) indicate that the structure and relative strength of features in the SSM/I ice-scattering images closely match the structure and intensity of coincident surface radar echoes.

13. SUMMARY AND CONCLUSIONS

The overall objective of this dissertation has been to offer a reasonably rigorous yet practical quantitative basis for understanding the meteorological information content of SSM/I observations of the marine environment. That such a basis had been lacking in the past is suggested in part by the current predominance of linear regression-type retrieval algorithms in the published SSM/I literature, as opposed to physical retrieval algorithms based on accurate knowledge of the sensitivity of the SSM/I to changes in the atmosphere and the ocean surface. To achieve the stated objective, several distinct problems relating to remote sensing with the SSM/I were addressed in turn.

First, a comprehensive algebraic parameterization of the response of the SSM/I to each of ten relevant variables was developed. These include seven atmospheric variables (integrated water vapor amount and scale height, surface atmospheric temperature and lapse rate, integrated cloud liquid water and effective cloud height, and surface pressure) and two surface variables (wind-induced roughening and sea surface temperature), plus the SSM/I viewing angle. FORTRAN subroutines implementing the SSM/I brightness temperature model are provided in Appendix B.

While the model was derived theoretically, modest 'tuning' of certain channel-dependent coefficients was found necessary in order to remove detectable inconsistencies between model-predicted brightness temperatures and observed brightness temperatures. Of course, the eventual availability of improved 'surface truth' data will undoubtedly enable the detection and correction of further errors which escaped the calibration procedure described in Chapter 8. Since even relatively small errors in a radiative transfer parameterization can seriously undermine its usefulness for physical retrievals from satellite data, the acquisition of quality comparison data sets over the ocean for the SSM/I should have a high priority for future work. An example of where a significant improvement can probably be

made with reasonable effort is in the careful screening of land contamination from radiosonde-SSM/I comparison data sets involving island stations. Indeed, the possibility of island contamination of the Raob Comparison Data Set employed in this thesis represents perhaps the largest single source of uncertainty regarding the validity of the atmospheric portion of the brightness temperature model, as well as that of the statistical water vapor retrieval algorithm presented in section 12.2.

Not all aspects of the SSM/I response to the atmosphere can be easily validated or calibrated using *in situ* comparison data alone. Examples include the microwave brightness temperature sensitivity to water vapor scale height, cloud water temperature, and other 'lesser' variables. For this reason, further experimental and theoretical work is needed to confirm or improve the accuracy of microwave absorption models for water vapor, dry air, and liquid water, especially at the lower temperatures and pressures that are characteristic of higher altitudes. The results of section 8.2, for example, suggest that there may still be significant uncertainties (~5–10%) in models for the mass absorption coefficient of water vapor near 22 and 85 GHz.

A novel aspect of the brightness temperature model presented in this thesis is the parameterization not only of sea surface emissivity changes with increasing surface roughness but also of changes in the *effective zenith angle* of sky radiation reflected by the wind-roughened sea surface, including its dependence on atmospheric opacity. It was shown that significant errors (up to ~10 K) in computed brightness temperature could result in some cases from the common assumption that the effective zenith angle of reflected sky radiation is equal to the viewing angle of the satellite.

Numerical calculations of the surface emission and scattering effects described by the above parameterization were based on a geometric optics model which assumes a non-directional, Gaussian slope distribution whose effective variance

depends on frequency. Ratios of the effective slope variances at each SSM/I frequency were determined empirically from SSM/I data over the open ocean, and the absolute magnitudes of the latter were then expressed as linear functions of a nominal wind speed which was scaled to match the wind speed retrieved using the statistical algorithm of Goodberlet et al. (1989). Previous empirical data on the effective slope variance as a function of wind speed and frequency (published by Wilheit 1979b) were found to be in surprisingly good agreement with the results obtained here for 19–37 GHz, especially considering the rather indirect nature of the wind speed calibration used in this thesis. On the other hand, the Wilheit (1979b) model was found to extrapolate poorly to 85.5 GHz, which lies well above the frequency range for which satellite data had been available before the SSM/I.

Further work on the problem of emission and reflection from the sea surface at SSM/I frequencies is clearly needed. The most important unanswered questions concern the limits to the usefulness of the modified geometric optics approximation (e.g., is a two-scale model or some other higher order approximation worth the extra computational complexity?), the errors arising from ignoring the directionality of the wind wave spectrum and/or variations in the relationship between effective slope spectrum and wind speed due to air-sea temperature difference, fetch, or other factors, and finally, a realistic model for the dependence of 'foam' coverage (as seen in the microwave spectrum) on wind speed.

Notwithstanding any residual uncertainties in the quantitative accuracy of the brightness temperature model, the second problem addressed by this thesis was that of examining the practical consequences of the relationship between SSM/I brightness temperatures and the scene being observed. Several aspects of this relationship are particularly worth noting: (i) the SSM/I has non-negligible sensitivity to a number of environmental variables in addition to the three which are routinely retrieved (i.e., integrated water vapor V, integrated liquid water L, and wind speed U); (ii) there are significant non-linearities in the SSM/I response to

almost all parameters, including cross-parameter dependences — that is, changes in one parameter will generally affect the sensitivity of the SSM/I to changes in other parameters; (iii) uncertainties in the values of non-retrievable parameters will therefore inevitably introduce uncertainties into SSM/I retrievals of V, L, and U.

In order to quantify such uncertainties, the well-known minimum-variance retrieval formalism, which has been extensively documented in the context of atmospheric temperature profile retrievals, was recast in a form appropriate to a linearized version of the SSM/I retrieval problem. An extensive set of of radiosonde profiles from all latitudes and seasons provided global statistics of many of the variables on which SSM/I brightness temperatures depend; together with these observed statistics and *ad hoc* assumptions about the statistics of the remaining variables, the minimum-variance algorithm permitted estimates to be made of the theoretical minimum retrieval uncertainty of each parameter to which the SSM/I is sensitive. The results of these calculations for U, L, and V were presented in Tables 11.1–11.3.

In some respects, the computed minimum retrieval uncertainties presented are conservative, in that only global parameter variances were considered, and parameter correlations which might have been exploited in some cases to reduce overall retrieval errors were ignored. It is likely that greatly improved error statistics could be achieved in restricted climate regimes — e.g. coastal marine stratocumulus — for which *a priori* uncertainties in total water vapor, vapor scale height, cloud temperature, etc., are much smaller.

On the other hand, a number of factors were ignored which, if considered, could have led to larger error estimates. These include, among other things, the effects of disparate channel resolution and sampling, deviations of the cloud liquid water field from the plane-parallel assumption of the brightness temperature

model, and the non-unique relationship between true wind speed and the sea surface roughness field to which the SSM/I directly responds. The possibility of contamination by precipitation was also neglected, although much of chapter 10 was devoted to describing the potential complications introduced when precipitation is present. Finally, it must be borne in mind that the above-cited estimates of maximum retrieval accuracy can only be realized in practice if the brightness temperature model which is used in the inversion algorithm (presumably a non-linear, iterative generalization of the minimum-variance method) is a completely accurate expression of the true response of the instrument to the environment, including possible sensor calibration errors.

The most convincing practical proof of the validity of the results presented in this thesis would be the demonstration of a physical inversion algorithm which retrieves all parameters of interest without detectable biases and with rms errors approaching the theoretical minimum errors calculated according to the method described. At the time of this writing, a general physical retrieval scheme incorporating the full model has not yet been completed. However, continued investigation of various possible approaches to near-optimal, non-linear physical retrievals clearly represents the next logical step beyond the work presented here.

Although a successful physical retrieval methodology must remain a topic for future work, we presented a unified set of simpler statistical and semi-physical algorithms for obtaining fields of surface wind speed, integrated water vapor, cloud liquid water, and precipitation from SSM/I brightness temperature data over the ocean. Unique features of these algorithms include: (i) a semi-physical method for retrieving integrated cloud liquid water at the resolution of the 85 GHz channels, with no appreciable absolute bias and with rms absolute errors (as measured in cloud-free conditions) of only $\sim$0.02 kg m^{-2}; (ii) apparently unbiased estimates of integrated water vapor over the entire natural range of this parameter, using a three-channel statistical algorithm which was constructed so as to have reduced

sensitivity to precipitation; and (ii) two complementary indices of precipitation activity (based on 37 GHz attenuation and 85 GHz scattering, respectively), each of which are constructed so as to be relatively insensitive to variations in other environmental parameters.

A graphic display and analysis software package which implements these algorithms has already seen extensive use at the University of Washington for the study of the structure of synoptic scale oceanic weather systems; indeed, many of the specific applications of passive microwave data outlined in Chapter 3 are now being further expanded and refined using the new SSM/I data.

Particularly the 85 GHz retrieval algorithm for integrated cloud liquid water opens new possibilities for documenting the horizontal structure and temporal statistics of liquid water in oceanic cloud fields. The method appears to be especially well suited to coastal stratocumulus, whose physical characteristics are currently of considerable interest owing to their role in the planetary radiation budget.

It is recognized that those SSM/I algorithms which depend on the 85 GHz vertically polarized channel cannot be used for data obtained from the F-8 SSM/I after mid-1988; however, nearly a complete year's worth of SSM/I data is available prior to that time, and a series of new SSM/Is, presumably with all seven channels functioning, are scheduled to begin replacing the F-8 sensor in the immediate future.

REFERENCES

Adler, R.F., R.A. Mack, N. Prasad, H.-Y.M. Yeh, and I.M. Hakkarinen 1990: Aircraft microwave observations and simulations of deep convection from 18 to 183 GHz. Part I: Observations. *J. Atmos. Ocean. Tech.*, **7**, 377–391

Alishouse, J.C., S. Snyder, J. Vongsathorn, and R.R. Ferraro 1990a: Determination of oceanic total precipitable water from the SSM/I. *IEEE Trans. Geosci. Remote Sensing*, in press.

Alishouse, J.C., J.B Snider, E.R. Westwater, C. Swift, C. Ruf, S. Snyder, J. Vongsathorn, and R.R. Ferraro 1990b: Determination of cloud liquid water using the SSM/I. *IEEE Trans. Geosci. Remote Sensing*, in press.

Alishouse, J.C. 1983: Total precipitable water and rainfall determination from the Seasat Scanning Multichannel Microwave Radiometer (SMMR). *J. Geophys. Res.*, **88**, 1929–1935

Austin, P.M. 1987: Relation between measured radar reflectivity and surface rainfall. *Mon. Wea. Rev.*, **115**, 1053–1070

Barrett, A.H., and V.K. Chung 1962: A method for the determination of high-altitude water vapor abundance from ground-based microwave observations. *J. Geophys. Res.*, **67**, 4259–4266

Barrett, A.H., and A.E. Lilley 1963: Mariner-2 microwave observations of Venus. *Sky and Telescope*, 192–195

Barrett, E.C. and C. Kidd 1990: Rainfall monitoring by the SSM/I in the middle latitudes. Preprints Volume, Fifth Conf. on Satellite Meteorology and Oceanograpy, London, September 3–7, pp. 210–214

Basharinov, A.E., A.S. Gurvich, S.T. Yegorov, A.A. Kurskaya, D.T. Matvyev, and A.M. Shutko 1971: The results of microwave sounding of the earth's surface according to experimental data from the satellite Cosmos 243. *Space Research,11*, Akademie-Verlag, Berlin.

Beard, K.V. 1976: Terminal velocity and shape of cloud and precipitation drops aloft. *J. Atmos. Sci.*, **33**, 851–864

Beer, T. 1980: Microwave sensing from satellites. *Remote Sensing of the Environment*, **9**, 65–85

Best, A.C. 1950: The size distribution of raindrops. *Quart. J. Roy. Met. Soc.*, **76**. 16–36

Bierman, G.J., R.G. Lipes, and F.J. Wentz 1978: Modern estimation techniques applied to microwave sensing of the marine boundary layer, *Proc. Twelve Asilomar Conference on Circuits, Systems and Computers*, IEEE Society, 101–106

Bohren, C.F., and D.R. Huffman 1983: *Absorption and Scattering of Light by Small Particles.* Wiley-Interscience, 530 pp.

Buettner, K.J.K. 1963: Regenortung vom Wettersatelliten mit Hilfe von Zentimeterwellen (Rain localization from a weather satellite using centimeter waves). *Naturwiss.*, **50**, 591

Cardone, V., T. Chester, and R. Lipes 1983: Evaluation of SEASAT SMMR wind speed measurements. *J. Geophys. Res.*, **88**, 1709–1726

Chang, A.T.C, and T.T. Wilheit 1979: Remote sensing of atmospheric water vapor, liquid water, and wind speed at the ocean surface by passive microwave techniques from the Nimbus 5 satellite. *Radio Science*, **14**, 793–802

Chang, H.D., P.H. Hwang, T.T. Wilheit, A.T.C. Chang, D.H. Staelin, and P.W. Rosenkranz 1984: Monthly distributions of precipitable water from the Nimbus 7 SMMR data. *J. Geophys. Res.*, **89**, 5328–5334

Clough, S.A., F.X. Kneizys, G.P. Anderson, E.P. Shettle, J.H. Chetwynd, L.W. Abreu, L.A. Hall, and R.D. Worsham 1989: FASCOD3: Spectral Simulation. In *IRS '88: Current Problems in Atmospheric Radiation.* J. Lenoble and J.F. Geleyn (Eds.), A. Deepak Publishing 372–375

Conrath, B.J. 1972: Vertical resolution of temperature profiles obtained from remote radiation measurements. *J. Atmos. Sci.*, **29**, 1262–1271

Cox, C.S., and W.H. Munk 1954: Measurement of the roughness of the sea surface from photographs of the sun's glitter. *J. Opt. Soc. Amer.*, **44**, 838–850

Cox, C.S., and W.H. Munk 1955: Some problems in optical oceanography. *J. Marine Res.*, **4**, 63–78

Dicke, R.H., R. Beringer, R.L. Kyhl, and A.B. Vane 1946: Atmospheric absorption measurements with a microwave radiometer. *Phys. Rev.*, **70**, 340

Droppleman, J.D. 1970: Apparent microwave emissivity of sea foam. *J. Geophys. Res.*, **75**, 696–698

Eymard, L., C. Klapisz, and R. Bernard 1989: Comparison between Nimbus-7 SMMR and ECMWF model analyses: the problem of the surface latent heat flux. *J. Atmos. Ocean. Tech.*, **6**, 866–881

Francis, C.R., D.P. Thomas, and E.P.L. Windsor 1983: The evaluation of SMMR retrieval algorithms in satellite microwave remote sensing. In: *Satellite Microwave Remote Sensing*, Allan, T.D. (ed.), Chichester, Ellis Horwood, 481–498

Francis, E.A. 1987: *Calibration of the Nimbus-7 Scanning Multichannel Microwave Radiometer (SMMR), 1979–1984.* Master of Science Thesis, Dept. of Oceanography, Oregon State University, 248 pp.

Gloersen, P., and F.T. Barath 1977: A scanning multichannel microwave radiometer for Nimbus-G and Seasat-A. *IEEE J. of Ocean. Eng.*, **OE-2**, 172–178

Goodberlet, M.A., C.T. Swift, and J.C. Wilkerson 1989: Remote sensing of ocean surface winds with the Special Sensor Microwave/Imager. *J. Geophys. Res.*, **94**, 14,547–14,555

Goyette, J.A., W.D. Klein, and A.L. Adams 1990: The Defense Meteorological Satellite Program review. *Preprints Vol., Fifth Conference on Satellite Meteorology and Oceanography*, London, September 3–7, 1990

Grody, N.C. 1976: Remote sensing of atmospheric water content from satellites using microwave radiometry. *IEEE Trans. on Antennas and Propagation*, **AP-24**, 155–161

Grody, N.C., A. Gruber, and W.C. Shen 1980: Atmospheric water content over the tropical Pacific derived from the Nimbus 6 Scanning Microwave Spectrometer. *J. Appl. Meteor.*, **19**, 986–996

Guissard, A. and P. Sobieski 1987: An approximate model for the microwave brightness temperature of the sea. *Int. J. Remote Sensing*, **8**, 1607–1627

Hakkarinen, I.M., and R.F. Adler 1988: Observations of precipitating convective systems at 92 and 183 GHz: Aircraft results. *Meteor. Atmos. Phys.*, **38**, 164–182

Hollinger, J.P. 1971: Passive microwave measurements of sea surface roughness. *IEEE Trans. Geosci. Elect.*, **GE-9**, 165–169

Hollinger, J.P., 1988: *DMSP Special Sensor Microwave/Imager Calibration/Validation Final Report.* Space Sensing Branch, Naval Research Laboratory, Washington, DC 20375-5000

Houghton, J.T., F.W. Taylor, and C.D. Rodgers 1984: *Remote Sounding of Atmospheres.* Cambridge University Press, 343 pp.

Huang, N.E., L.F. Bliven, S.R. Long, and C.-C. Tung 1986: An analytic model for oceanic whitecap coverage. *J. Phys. Ocean.*, **16**, 1597–1604

Katsaros, K.B., I.A. Bhatti, L.A. McMurdie, and G.W. Petty 1989: Passive microwave measurements of water vapor fields and rain for locating fronts in cyclonic storms. *Weather Forecasting*, 4, 449–460

Katsaros, K.B., G.W. Petty, and U. Hammarstrand 1988: Liquid water and water vapor in mid-latitude cyclones observed by microwave radiometry and compared to model calculations. *Proceedings of Palmen Memorial Symposium*, Aug. 29 – Sept. 2, 1988, Helsinki, Finland

Katsaros, K.B., and R.M. Lewis 1986: Mesoscale and synoptic scale features of North Pacific weather systems observed with the Scanning Multichannel Microwave Radiometer on Nimbus 7. *J. Geophys. Res.*, **91**, 2321–2330

Katsaros, K.B., P.K. Taylor, J.C. Alishouse, and R.J. Lipes 1981: Quality of Seasat SMMR (Scanning Multichannel Microwave Radiometer) atmospheric water determinations, in *Oceanography from Space*, Gower (ed.), 691–706, Plenum Publishing Corp., New York

Klein, L.A., and C.T. Swift 1977: An improved model for the dielectric constant of sea water at microwave frequencies, *IEEE Trans. Antennas Propagat.*, **AP-25**, 104–111

Kreiss, W.T. 1969: The influence of clouds on microwave brightness temperatures viewing downward over open seas *Proc. IEEE*, **57**, 440–445

Kummerow, C.D., R.A. Mack, and I.M. Hakkarinen 1989: A self-consistency approach to improve microwave rainfall estimates from space. *J. Appl. Meteor.*, **28**, 869–884

Kummerow, C.D., and J.A. Weinman 1988a: Determining microwave brightness temperatures from precipitating horizontally fine and vertically structured clouds. *J. Geophys. Res.*, **93**, 3720–3728

Kummerow, C.D., and J.A. Weinman 1988b: Radiative properties of deformed hydrometeors for commonly used passive microwave frequencies. *IEEE Trans. Geosci. Remote Sens.*, **26**, 629–638

LeMone, M.A., and E.J. Zipser 1980: Cumulonimbus vertical velocity events in GATE. Part I: Diameter, intensity and mass flux. *J. Atmos. Sci.*, **37**, 2444–2457

Liebe, H.J. 1985: An updated model for millimeter wave propagation in moist air. *Radio Sci.*, **20**, 1069–1089

Lipes, R.G. 1982: Description of Seasat radiometer status and results. *J. Geophys. Res.*, **87**, 3385–3395

Lipes, R.G., R.L. Bernstein, V.J. Cardone, K.B. Katsaros, E.J. Njoku, A.L. Riley, D.B. Ross, C.T. Swift, and F.J. Wentz 1979: Seasat scanning multichannel microwave radiometer: Results of the Gulf of Alaska workshop, *Science*, **204**, 1415–1417

Liu, W.T. 1984: Estimation of latent heat flux with SEASAT-SMMR, a case study in N. Atlantic. In *Large-Scale Oceanographic Experiments with Satellites*, C. Gautier and M. Fieux, eds, D. Reidel

Liu, W.T. 1986: Statistical relation between monthly mean precipitable water and surface-level humidity over global oceans. *Mon. Wea. Rev.*, **114**, 1591–1602

Liu, W.T. 1988: Moisture and latent heat flux variabilities in the Tropical Pacific derived from satellite data. *J. Geophys. Res.*, **93**, 6749–6760

Lovejoy, S., and G.L. Austin 1980: The estimation of rain from satellite-borne microwave radiometers, *Quart. J. R. Met. Soc.*, **106**, 255–276

Marshall, J.S., and W.H. Palmer 1948: The distribution of raindrops with size. *J. Meteor.*, **5**, 165–166

McMurdie, L.A. 1989: *Interpretation of Integrated Water Vapor Patterns in Oceanic Midlatitude Cyclones Derived from the Scanning Multichannel Microwave Radiometer.* Ph.D. Thesis, Dept. of Atmospheric Sciences, University of Washington, 224 pp.

McMurdie, L.A., and K.B. Katsaros 1985: Atmospheric water distribution in a midlatitude cyclone observed by the Seasat Scanning Multichannel Microwave Radiometer. *Mon. Wea. Rev.*, **113**, 584–598

McMurdie, L.A., G. Levy, and K.B. Katsaros 1987: On the relationship between scatterometer-derived convergences and atmospheric moisture. *Mon. Wea. Rev.*, **115**, 1281–1294

Meeks, M.L., and A.E. Lilley 1963: The microwave spectrum of oxygen in the earth's atmosphere. *J. Geophys. Res.*, **68**, 1683–1703

Mie, G. 1908: Beiträge zur Optik trüber Medien, speziell kolloidaler Metallösungen. *Ann. Phys.*, **26**, 597–614

Milman, A. 1987: How wind affects passive microwave measurements of sea surface temperature. *IEEE Trans. Geosci. Remote Sensing*, **GE-25**, 22–27

Monahan, E.C. 1969: Fresh water whitecaps. *J. Atmos. Sci.*, **26**, 1026–1029

Monahan, E.C. and I. O'Muircheartaigh 1980: Optimal power law description of oceanic whitecap coverage dependence on wind speed. *J. Phys. Oceanogr.*, **10**, 2094–2099

Mugnai, A., H.J. Cooper, E.A. Smith, and G.J. Tripoli 1990: Simulation of microwave brightness temperatures of an evolving hailstorm at SSM/I frequencies. *Bull. Amer. Meteor. Soc.*, 71, 2–13

Negri, A.J., R.F. Adler, and C.D. Kummerow 1989: False-color display of Special Sensor Microwave/Imager (SSM/I) data. *Bull. Amer. Meteor. Soc.*, 70, 146–151

Njoku, E.G. 1982: Passive microwave remote sensing from space – a review. *Proc. of the IEEE*, **70**, 728–750

Njoku, E.G., and L. Swanson 1983: Global measurements of sea surface temperature, wind speed, and atmospheric water content from satellite microwave radiometry. *Mon. Wea. Rev.*, **111**, 1977–1987

Nordberg, W., J. Conaway, D.B. Ross, and T. Wilheit 1971: Measurements of microwave emission from a foam-covered wind-driven sea. *J. Atmos. Sci.*, **28**, 429–435

Oguchi, T. 1983: Electromagnetic wave propagation and scattering in rain and other hydrometeors, *Proc. IEEE*, **71**, 1029–1078

Olson, W.S. 1989: Physical retrieval of rainfall rates over the ocean by multispectral radiometry — Application to tropical cyclones. *J. Geophys. Res.*, **94**, 2262–2280

Pandey, P.C., and R.K. Kakar 1982: An empirical microwave emissivity model for a foam-covered sea. *IEEE J. Ocean. Eng.*, **OE-7**, 135–140

Pedigo, C.B., and D.G. Vincent 1990: Tropical precipitation rates during SOP-1, FGGE, estimated from heat and moisture budgets. *Mon. Wea. Rev.*, **118**, 542–557

Petty, G.W., and K.B. Katsaros 1989: Empirical studies of the microwave radiometric response to rainfall in the tropics and midlatitudes. Preprints Volume, Fourth Conf. on Satellite Meteorology and Oceanograpy, San Diego, May 16–19, pp. 9–12

Petty, G.W., and K.B. Katsaros 1990a: Precipitation observed over the South China Sea by the Nimbus 7 Scanning Multichannel Microwave Radiometer during Winter MONEX. *J. Appl. Meteor.*, **29**, 273–287

Petty, G.W., and K.B. Katsaros 1990b: Nimbus 7 SMMR precipitation observations calibrated against surface radar during TAMEX. Conditionally accepted by *J. Appl. Meteor.*

Prabhakara, C., H.D. Chang, and A.T.C. Chang 1982: Remote sensing of precipitable water over the oceans from Nimbus 7 microwave measurements. *J. Appl. Meteorology*, **21**, 59–68

Prabhakara, C., D.A. Short, and B.E. Vollmer 1985: El Nino and atmospheric water vapor: observations from Nimbus 7 SMMR. *J. Climate Appl. Meteor.*, **24**, 1311–1324

Prabhakara, C., D.A. Short, W. Wiscombe, R.S. Fraser, and B.E. Vollmer 1986: Rainfall over oceans inferred from Nimbus 7 SMMR: application to 1982-83 El Nino. *J. Climate Appl. Meteor.*, **25**, 1464–1474

Press, W.H., B.P. Flannery, S.A. Teukolsky, and W.T. Vetterling 1986: *Numerical Recipes: the Art of Scientific Computing.* Cambridge University Press, New York, 818 pp.

Pruppacher, H.R. 1981: The microstructure of atmospheric clouds and precipitation. In *Clouds: Their Formation, Optical Properties, and Effects.* P.V. Hobbs and A. Deepak (Eds.), 93–186

Pruppacher, H.R., and J.D. Klett 1978: *Microphysics of Clouds and Precipitation.* Reidel, Dordrecht, Holland, 714 pp.

Rao, M.S.V., W.V. Abbott III, and J.S. Theon 1976: *Satellite-Derived Global Oceanic Rainfall Atlas*, NASA X-911-76-116, Goddard Space Flight Center, Greenbelt, MD

Ray, P.S. 1972: Broadband complex refractive indices of ice and water. *Appl. Optics*, **11**, 1836–1843

Rogers, R.R., and M.K. Yau 1989: *A Short Course in Cloud Physics (3d Edition).* Pergamom Press, New York. 293 pp.

Rosenkranz, P.W. 1975: Shape of the 5 mm oxygen band in the atmosphere. *IEEE Trans. Antennas Propag.*, **AP-23**, 498–506

Rosenkranz, P.W. 1978: Inversion of diffraction-limited multiwavelength remote sensors, 1. Linear case. *Radio Sci.*, **13**, 1003–1010

Rosenkranz, P.W. 1982a: Inversion of data from diffraction limited multiwavelength remote sensors, 2. Nonlinear dependence of observables on the geophysical parameters. *Radio Sci.*, **17**, 245–256

Rosenkranz, P.W. 1982b: Inversion of data from diffraction-limited multiwavelength remote sensors, 3. scanning multichannel microwave data. *Radio Sci.*, **17**, 257–267

Rosenkranz, P.W., F.T. Barath, J.C. Blinn III, and E.J. Johnston 1972: Microwave radiometric measurements of atmospheric temperature and water from an aircraft. *J. Geophys. Res.*, **77**, 5833–5844

Rosenkranz, P.W., and D.H. Staelin 1972: Microwave emissivity of ocean foam and its effect on nadiral radiometric measurements. *J. Geophys. Res.*, **77**, 6528–6538

Ross, D.B., and V.J. Cardone 1974: Observations of oceanic white caps and their relation to remote measurements of surface wind speed. *J. Geophys. Res.*, **79**, 444–452

Sasaki, Y., I. Asanuma, K. Muneyama, G. Naito, and T. Suzuki 1987: The dependence of sea-surface microwave emission on wind speed, frequency, incidence angle, and polarization over the frequency range from 1 to 40 GHz. *IEEE Trans. Geosci. Remote Sens.*, **GE-25**, 138–146

Savage, R.C. 1976: *The Transfer of Thermal Microwaves Through Hydrometeors*, Ph.D. Dissertation, University of Wisconsin, Madison, 147 pp.

Simpson, J., R.F. Adler, and G.R. North 1988: A proposed Tropical Rainfall Measuring Mission (TRMM) satellite. *Bull. Amer. Meteor. Soc.*, **69**, 278–295

Spencer, R.W. 1986: A satellite passive 37 GHz scattering-based method for measuring oceanic rain rates. *J. Climate Appl. Meteor.*, **25**, 754–766

Spencer, R.W., H.M. Goodman, and R.E. Hood 1989: Precipitation retrieval over land and ocean with the SSM/I: Identification and characteristics of the scattering signal. *J. Atmos. Ocean. Tech.*, **6**, 254–273

Spencer, R.W., B.B. Hinton, and W.S. Olson 1983: Nimbus-7 37 GHz radiances correlated with radar rain rates over the Gulf of Mexico. *J. Climate Appl. Meteor.*, **22**, 2095–2099

Staelin, D.H. 1966: Measurements and interpretation of the microwave spectrum of the terrestrial atmosphere near the 1 cm. wavelength, *J. Geophys. Res.*, **71**, 2875–2881

Staelin, D.H. 1969: Passive remote sensing at microwave wavelengths. *Proc. IEEE*, **57**, 427–439

Staelin, D.H., A.L. Cassel, K.F. Kunzi, R.L. Pettyjohn, R.K.L. Poon, and P.W. Rosenkranz 1975: Microwave atmospheric temperature sounding effects of clouds on Nimbus 5 satellite data. *J. Atmos. Sci.*, **32**, 1970–1976

Staelin, D.H., K.F. Kunzi, R.L. Pettyjohn, R.K.L. Poon, and R.W. Wilcox 1976: Remote sensing of atmospheric water vapor and liquid water with the Nimbus 5 Microwave Spectrometer. *J. Appl. Meteor.*, **15**, 1204–1214

Stogryn, A. 1967: The apparent temperature of the sea at microwave frequencies. *IEEE Trans. Antennas Propagat.*, **AP-15**, 278–286

Stogryn, A. 1972: The emissivity of sea foam at microwave frequencies. *J. Geophys. Res.*, **77**, 1650–1666

Strantz, R. 1971: *Meteor. Rundschau*, **24**, 23

Szejwach, G., R.F. Adler, I. Jobard, and R.A. Mack 1986: A cloud model-radiative model combination for determining microwave TB-rain rate relations. *Second Conf. on Satellite Meteorology/Remote Sensing and Applications.* Amer. Meteor. Soc., Williamsburg, 444–449

Taylor, P.K., K.B. Katsaros, and R.G. Lipes 1981: Determination by Seasat of atmospheric water and synoptic fronts. *Nature*, **294**, 737–739

Tikhonov, A.N. 1963: On the solution of incorrectly stated problems and a method of regularization. *Dokl. Acad. Nauk. USSR*, **151**, 501

Twomey, S. 1963: On the numerical solution of Fredholm integral equations of the first kind by the inversion of the linear system produced by quadrature. *J. Ass. Comput. Mach.*, **10**, 97

Ulaby, F.T., R.K. Moore, and A.K. Fung 1981: *Microwave Remote Sensing Active and Passive. Vol. I: Microwave Remote Sensing Fundamentals and Radiometry*, Addison-Wesley, 456 pp.

Warren, S.G. 1984: Optical constants of ice from the ultraviolet to the microwave. *Appl. Optics*, **23**, 1206–1225

Waters, J.W. 1976: Absorption and emission by atmospheric gases. *Methods of Experimental Physics*, Vol. 12, Part B, Academic Press, 142–176

Webster, W.J., Jr., T.T. Wilheit, D.B. Ross, and P. Gloersen 1976: Spectral characteristics of the microwave emission from a wind-driven foam-covered sea. *J. Geophys. Res.*, **81**, 3095–3099

Weinman, J.A., and P.J. Guetter 1977: Determinations of rainfall distributions from microwave radiation; measured by the Nimbus 6 ESMR. *J. Appl. Meteor.*, **16**, 437–442

Wentz, F.J. 1983: A model function for ocean microwave brightness temperatures. *J. Geophys. Res.*, **88**, 1892–1908

Wentz, F.J. 1988: *User's Manual, SSM/I Antenna Temperature Tapes.* RSS Tech. Rept. 032588, Remote Sensing Systems, Santa Rosa, California

Wentz, F.J., V.J. Cardone, and L.S. Fedor 1982: Intercomparison of wind speeds inferred by the SASS, altimeter, and SMMR. *J. Geophysical Res.*, **87**, 3378–3384

Wentz, F.J., L.A. Mattox, and S. Peteherych 1986: New algorithms for microwave measurements of ocean winds: applications to SEASAT and the Special Sensor Microwave Imager. *J. Geophys. Res.*, **91**, 2289–2307

Wilheit, T.T. 1978: A review of application of microwave radiometry to oceanography. *Boundary Layer Meteorology*, **13**, 277–293

Wilheit, T.T. 1979a: The effect of wind on the microwave emission from the ocean's surface at 37 GHz. *J. Geophys. Res.*, **84**, 4921–4926

Wilheit, T.T. 1979b: A model for the microwave emissivity of the ocean's surface as a function of wind speed. *IEEE Trans. Geosci. Electron.*, **GE-17**, 244–249

Wilheit, T.T. 1986: Some comments on passive microwave measurement of rain. *Bull. Amer. Meteor. Soc.*, **67**, 1226–1232

Wilheit, T.T., A.T.C. Chang, M.S.V. Rao, E.B. Rodgers, and J.S. Theon 1977: A satellite technique for quantitatively mapping rainfall rates over the ocean. *J. Appl. Meteor.*, **16**, 551–560

Wilheit, T.T., and A.T.C. Chang 1980: An algorithm for retrieval of ocean surface and atmospheric parameters from the observations of the Scanning Multichannel Microwave Radiometer (SMMR). *Radio Science*, **15**, 525–544

Wilheit, T.T., and M.G. Fowler 1977: Microwave radiometric determination of the wind speed at the ocean surface during BESEX. *IEEE Trans. Antenna Propagat.*, **25**, 111–120

Williams, G. 1969: Microwave radiometry of the ocean and the possibility of marine wind velocity determination from satellite observations. *J. Geophys. Res.*, **74**, 4591–4594

Williams, G. 1971: Microwave measurements of bubbles and foam. *IEEE Trans. Geosci. Electron.*, **GE-9**, 221–224

Wiscombe, W.J. 1980: Improved Mie scattering algorithms. *Appl. Optics*, **19**, 1505–1509

Wu, J. 1979: Oceanic whitecaps and sea state. *J. Phys. Oceanography*, **9**, 1064–1068

Wu, R., and J.A. Weinman 1984: Microwave radiances from precipitating clouds containing aspherical ice, combined phase, and liquid hydrometeors. *J. Geophys. Res.*, **89**, 7170–7178

Wu, S.T., and A.K. Fung 1972: A noncoherent model for microwave emissions and backscattering from the sea surface. *J. Geophys. Res.*, **77**, 5917–5929

Yeh, H.-Y.M, N. Prasad, R.A. Mack, and R.F. Adler 1990: Aircraft microwave observations and simulations of deep convection from 18 to 183 GHz. Part II: Model results. *J. Atmos. Ocean. Tech.*, **7**, 392–410

Zipser, E.J., and M.A. LeMone 1980: Cumulonimbus vertical velocity events in GATE. Part II: Synthesis and model core structure. *J. Atmos. Sci.*, **37**, 2458–2469

APPENDIX A: Comparisons between Satellite 37 GHz and Surface Digital Radar Observations of Precipitation (Abstracts)

G.W. Petty and K.B. Katsaros 1990a: Precipitation Observed over the South China Sea by the Nimbus 7 Scanning Multichannel Microwave Radiometer during Winter MONEX. *Journal of Applied Meteorology*, **29**, 273–287

ABSTRACT

Mesoscale cloud clusters near the northwestern coast of Borneo were observed by the Scanning Multichannel Microwave Radiometer (SMMR) on three occasions during the Winter Monsoon Experiment (WMONEX) in December 1978. A non-dimensional form of the SMMR 37 GHz polarization difference is introduced and used to identify regions of precipitation, and these are compared with visible and infrared imagery from the GMS-1 geostationary satellite. For two of the three cloud cluster cases, quantitative comparisons are made between nearly simultaneous SMMR observations and reflectivity observations made by the MIT WR-73 digital weather radar at Bintulu. Though limited in scope, these represent the first known direct comparisons between digital radar-derived rain parameters and satellite passive microwave observations of near-equatorial precipitation. SMMR 37 GHz observations are found to be much better indicators of fractional coverage of each SMMR footprint by rain than of average rain rate within the footprint. Total area coverage by precipitation is estimated for all three clusters using this result.

G.W. Petty and K.B. Katsaros 1990b: Nimbus-7 SMMR Observations of Precipitation Calibrated Against Surface Radar During TAMEX. Conditionally accepted by *Journal of Applied Meteorology*

ABSTRACT

Nimbus-7 Scanning Multichannel Microwave Radiometer (SMMR) normalized 37 GHz polarization differences were compared with surface digital radar observations of oceanic precipitation made during the Taiwan Area Mesoscale Experiment. Four cases were found for which SMMR and radar coverage of significant precipitation features was nearly simultaneous. These yielded 518 SMMR-radar data pairs, of which over half included precipitation. A statistical approach was used to correct the radar data for range-dependent errors, and empirical relationships were then found between the corrected pixel-averaged radar rain rate and fractional rain coverage and the SMMR-observed microwave polarization. In addition to the direct comparisons, simulations of SMMR observations from non-coincident TAMEX radar scans were performed in order to examine the statistical impact of footprint-filling.

APPENDIX B: FORTRAN Implementation of Brightness Temperature Model

```
* ================================================================
*
*  SUBROUTINE TB(IFREQ,THETA,P0,TA,GAMMA,SST,WV,HWV,U,ALW,ZCLD,
*        TBV,TBH)
*
*  This routine calculates miowave brightness temperatures
*  observed by the SSM/I over the ocean.
*
*  Input :
*    IFREQ = (1,2,3, or 4 ) for (19.35, 22.235, 37, or 85.5 GHz)
*    THETA = incidence angle (deg.)
*    P0    = surface pressure (mb)
*    WV    = precipitable water (kg/m**2)
*    HWV   = water vapor scale height (km)
*    TA, GAMMA = "effective" surface air temperature
*             and lapse rate (K ; km)
*           T(z) = Ta - gamma*z
*    SST   = sea surface temperature (K)
*    U     = surface wind speed (m/s)
*
*    ALW, ZCLD  = total cloud liquid water content (kg/m**2)
*              and height (km)
*
*  Output :
*    TBV, TBH = brightness temperature (K)
*            for Vertical, Horizontal polarization
*
*  Subroutines called : TBATMOS, EFFHT, SIGMA_V
*----------------------------------------------------------------
     subroutine tb(ifreq,theta,p0,ta,gamma,sst,wv,hwv,u,alw,
    &  zcld,tbv,tbh)
     integer ifreq
     real theta,p0,wv,hwv,alw,zcld,rho,ta,gamma,tbup,tbdn,tauatm
     real tc,freq(4),ebiasv(4),ebiash(4),cf(4),cg(4)
     data freq/19.35,22.235,37.0,85.5/
     data cf/0.008,0.008,0.008,0.008/
     data cg/3.49e-3, 3.60e-3, 4.85e-3, 6.22e-3 /
```

```
* empirical bias corrections for surface emissivity
    data ebiasv/0.00400,-0.00451,-0.0124,-0.00189/
    data ebiash/0.00354,    0.0,-0.0125, 0.05415/
* 'foam' emissivity
    data fem /1.0/
*
    f = freq(ifreq)
    costhet = cos(theta*0.017453)
* effective surface slope variance
    gx2 = cg(ifreq)*u
* upwelling atmospheric brightness temperature
    call tbatmos(ifreq,theta,p0,wv,hwv,ta,gamma,alw,zcld,
   &                    tbup,tbdn,tauatm)
* convert transmittance to optical depth
    sigma = -alog(tauatm)*costhet
* rough surface emissivity
    call roughem(ifreq,gx2,sst,theta,remv,remh)
* effective zenith angles for scattered radiation at surface
    call effang(ifreq,theta,gx2,sigma,effangv,effangh)
* effective sky brightness temperatures for scattered radiation
    call tbatmos(ifreq,effangv,p0,wv,hwv,ta,gamma,alw,zcld,
   & dum,tbdnv,dum)
    call tbatmos(ifreq,effangh,p0,wv,hwv,ta,gamma,alw,zcld,
   & dum,tbdnh,dum)
* compute 'foam' coverage
    if (u .gt. 7.0) then
     foam = cf(ifreq)*(u-7.0)
    else
     foam = 0.0
    endif
* compute surface emissivities and reflectivity
    emissv = foam*fem + (1.0 - foam)*(remv + ebiasv(ifreq))
    emissh = foam*fem + (1.0 - foam)*(remh + ebiash(ifreq))
    refv = 1.0 - emissv
    refh = 1.0 - emissh
* compute surface emission term
    semv = sst*emissv
    semh = sst*emissh
* compute surface scattering term
    scatv = refv*tbdnv
    scath = refh*tbdnh
* combine to get space-observed brightness temperature
```

```
      tbv = tbup + tauatm*(semv + scatv)
      tbh = tbup + tauatm*(semh + scath)
      return
      end
*
```

```
*=================================================================
*
* SUBROUTINE TBCLEAR(IFREQ,THETA,PO,WV,HWV,TA,GAMMA,
*       TBUP,TBDN,TAUATM)
*
* This routine calculates upwelling and downwelling microwave
* atmospheric brightness temperatures and transmittance at SSM/I
* frequencies under cloud-free conditions (the routine "TBATMOS"
* is generalized to include a cloud layer of known height and
* total liquid water content).
*-----------------------------------
* Input :
*   IFREQ = (1,2,3, or 4 ) for (19.35, 22.235, 37, or 85.5 GHz)
*   THETA = incidence angle (deg.)
*   PO    = surface pressure (mb)
*   WV    = precipitable water (kg/m**2)
*   HWV   = water vapor density scale height (km)
*   TA, GAMMA = "effective" surface air temperature
*                and lapse rate (K ; km)
*        T(z) = Ta - gamma*z
*
* Output :
*   TBUP, TBDN = atmospheric upwelling and downwelling
*              brightness temperature (K)
*   TAUATM   = total atmospheric transmittance at
*              specified incidence angle.
*
* Subroutines called : EFFHT, SIGMA_V
*-----------------------------------
    subroutine tbclear(ifreq,theta,p0,wv,hwv,ta,gamma,
   &   tbup,tbdn,tauatm)
    integer ifreq
    real theta,p0,wv,hwv,ta,gamma,tbup,tbdn,tauatm
*
    real mu,zcld,hdn,hup,hdninf,hupinf
    real h0(4),const(4),par(10),a(10,4),b1(4),b2(4),b3(4)
    real c(4),d1(4),d2(4),d3(4),zeta(4)
    real tau
    real sigv,sigo,em
*
    data b1/-.46847e-1,-.57752e-1,-.18885,.10990/
    data b2/.26640e-4,.31662e-4,.9832e-4,.60531e-4/
```

```
      data b3/.87560e+1,.10961e+2,.36678e+2,-.37578e+2/
      data c/ .9207,  1.208,    .8253,    .8203/
      data zeta/4.2,4.2,4.2,2.9/
      data d1/-.35908e+1,-.38921e+1,-.43072e+1,-.17020e+0/
      data d2/ .29797e-1, .31054e-1, .32801e-1, .13610e-1/
      data d3/-.23174e-1,-.23543e-1,-.24101e-1,-.15776e+0/
C * mu = secant(theta)
      mu = 1.0/cos(theta*0.0174533)
C * get water vapor optical depth
      sigv = sigma_v(ifreq,p0,wv,hwv,ta,gamma)
C * otbar = one over "mean" temperature
      otbar = 1.0/(ta - gamma*zeta(ifreq))
C * sigo = oxygen optical depth
      sigo = b1(ifreq) + b2(ifreq)*p0  + b3(ifreq)*otbar
C * hv, ho = effective absorber scale heights for vapor, oxygen
      hv = c(ifreq)*hwv
      ho = d1(ifreq) + d2(ifreq)*ta + d3(ifreq)*gamma
C * zcld has a dummy value (no effect on results in clear-sky case)
      zcld = 2.0
      call effht(ho,hv,sigo,sigv,mu,zcld,hdn,hup,
     &  hdninf,hupinf)
C * atmospheric transmittance along viewing angle
      tauatm  = exp(-mu*(sigo+sigv))
C * atmospheric "emissivity"
      em  = 1.0 - tauatm
C * downwelling, upwelling brightness temperature from atmosphere
      tbdn = em*(ta - gamma*hdninf)
      tbup = em*(ta - gamma*hupinf)
C
C * the following lines apply an ad hoc correction to improve fit
C * at large angles and/or high gaseous opacities
C *  (downwelling brightness temperatures only)
      alph = (0.636619*atan(mu*(sigo+sigv)))**2
      tbdn = (1.0-alph)*tbdn + em*alph*ta
C
      return
      end
```

```
* ================================================================
*
* SUBROUTINE TBATMOS(IFREQ,THETA,PO,WV,HWV,TA,GAMMA,LW,ZCLD,
*             TBUP,TBDN,TAUATM)
*
* This routine calculates the upwelling and downwelling
* microwave atmospheric brightness temperatures and
* transmittance at an SSM/I frequency.  It is a
* generalization of "TBCLEAR" and includes a cloud layer
* of known height and total liquid water content.
*
* Input :
*   IFREQ = (1,2,3, or 4 ) for (19.35, 22.235, 37, or 85.5 GHz)
*   THETA = incidence angle (deg.)
*   PO    = surface pressure (mb)
*   WV    = precipitable water (kg/m**2)
*   HWV   = water vapor density scale height (km)
*   TA, GAMMA = "effective" surface air temperature
*                and lapse rate (K ; km)
*         T(z) = Ta - gamma*z
*   LW, ZCLD  = total cloud liquid water content (kg/m**2)
*            and height (km)
*
* Output :
*   TBUP, TBDN = atmospheric component of upwelling and
*            downwelling brightness temperature (K)
*   TAUATM   = total atmospheric transmittance at
*               specified incidence angle.
*
* Subroutines called : EFFHT, SIGMA_V
*----------------------------------------------------------------
      subroutine tbatmos(ifreq,theta,p0,wv,hwv,ta,gamma,lw,zcld,
     &   tbup,tbdn,tauatm)
      integer ifreq
      real theta,p0,wv,hwv,ta,gamma,lw,zcld,tbup,tbdn,tauatm
      real mu,hdn,hup,hdninf,hupinf
*
      real h0(4),const(4),par(10),a(10,4),b1(4),b2(4),b3(4)
      real c(4),d1(4),d2(4),d3(4),zeta(4)
      real kw0(4),kw1(4),kw2(4),kw3(4)
      real tau,tau1,tau2,taucld
      real tcld,tc,em,em1
```

```
      real sigv,sigo,sig,sig1,sigcld
      real teff1dn,teff1up,teffdn,teffup
      real tbcld,tbclrdn,tbclrup,tb1dn,tb1up,tb2dn,tb2up
*
      data b1/-.46847e-1,-.57752e-1,-.18885,.10990/
      data b2/.26640e-4,.31662e-4,.9832e-4,.60531e-4/
      data b3/.87560e+1,.10961e+2,.36678e+2,-.37578e+2/
      data c/ .9207,  1.208,    .8253,    .8203/
      data zeta/4.2,4.2,4.2,2.9/
      data d1/-.35908e+1,-.38921e+1,-.43072e+1,-.17020e+0/
      data d2/ .29797e-1, .31054e-1, .32801e-1, .13610e-1/
      data d3/-.23174e-1,-.23543e-1,-.24101e-1,-.15776e+0/
      data kw0/ .786e-1, .103,   .267,   .988/
      data kw1/-.230e-2,-.296e-2,-.673e-2,-.107e-1/
      data kw2/ .448e-4, .557e-4, .975e-4,-.535e-4/
      data kw3/-.464e-6,-.558e-6,-.724e-6, .115e-5/
* mu = secant(theta)
      mu = 1.0/cos(theta*0.0174533)
* get water vapor optical depth
      sigv = sigma_v(ifreq,p0,wv,hwv,ta,gamma)
* otbar = one over "mean" temperature
      otbar = 1.0/(ta - gamma*zeta(ifreq))
* sigo = dry air optical depth
      sigo = b1(ifreq) + b2(ifreq)*p0  + b3(ifreq)*otbar
* cloud parameters
      tcld  = ta - gamma*zcld
      tc = tcld - 273.15
      tc2 = tc*tc
      tc3 = tc2*tc
      sigcld = (kw0(ifreq) + tc*kw1(ifreq) + tc2*kw2(ifreq) +
     &    tc3*kw3(ifreq))*lw
      taucld = exp(-mu*sigcld)
      tbcld = (1.0 - taucld)*tcld
* hv, ho = effective absorber scale heights for vapor, dry air
      hv = c(ifreq)*hwv
      ho = d1(ifreq) + d2(ifreq)*ta + d3(ifreq)*gamma
* effective emission heights for layer 1 and total atmosphere
      call effht(ho,hv,sigo,sigv,mu,zcld,hdn,hup,
     &  hdninf,hupinf)
* atmospheric transmittances in layer one and two, and combined
      sig = sigo + sigv
      sig1 = sigo*(1.0-exp(-zcld/ho)) + sigv*(1.0-exp(-zcld/hv))
```

```
      tau  = exp(-mu*sig)
      tau1 = exp(-mu*sig1)
      tau2 = tau/tau1
*  atmospheric "emissivity"
      em1  = 1.0 - tau1
      em   = 1.0 - tau
*  downwelling, upwelling brightness temperature for each layer
      teff1dn = ta - gamma*hdn
      teff1up = ta - gamma*hup
      teffdn = ta - gamma*hdninf
      teffup = ta - gamma*hupinf
      tbclrdn = teffdn*em
      tbclrup = teffup*em
*
      tb1dn = em1*teff1dn
      tb1up = em1*teff1up
      tb2dn = (tbclrdn - tb1dn)/tau1
      tb2up =  tbclrup - tau2*tb1up
*  downwelling, upwelling brightness temperature, transmittance
      tbdn  = tb1dn + tau1*(tbcld + taucld*tb2dn)
      tbup  = tb2up + tau2*(tbcld + taucld*tb1up)
      tauatm = tau*taucld
*
*  the following lines apply an ad hoc correction to improve fit
*  at large angles and/or high gaseous opacities
*   (downwelling brightness temperatures only)
      alph = (0.636619*atan(mu*sig))**2
      tbdn = (1.0-alph)*tbdn + em*alph*ta
*
      return
      end
```

```
*=============================================================
*
* FUNCTION SIGMA_V(IFREQ,PO,WV,HWV,TA,GAMMA)
*
* This function returns the contribution of water vapor to total
* atmospheric optical depth at SSM/I frequencies.
* ------------------------------------------
* Input :
*  IFREQ = (1,2,3, or 4 ) for (19.35, 22.235, 37, or 85.5 GHz)
*  PO   = surface pressure (mb)
*  WV   = precipitable water (kg/m**2)
*  HWV  = water vapor density scale height (km)
*  TA, GAMMA = "effective" surface air temperature
*              and lapse rate (K ; km)
*       T(z) = Ta - gamma*z
*
* Return value:  SIGMA_V = total water vapor optical depth
*
* Note:  The following code has been written so as to minimize
* redundant multiplications and divisions during successive calls.
* A time savings of 50% or more is achieved when several input
* parameters are unchanged from one call to the next, as is
* often the case in retrieval applications.  Without this
* optimization, less than about 30 lines of code would be
* required to perform the same calculation.
*
*-------------------------------------------
    function sigma_v(ifreq,p0,wv,hwv,ta,gamma)
    integer ifreq
    real sigma_v,p0,wv,hwv,ta,gamma
*
    real wvc, wvcor(4)
*
    real told1,pold1,hold1,vold1,gold1
    real voh1,otbar1,pbar1
    real term21,term31,term41,term51,term61
    real a11,a21,a31,a41,a51,a61
*
    real told2,pold2,hold2,vold2,gold2
    real voh2,otbar2,pbar2
    real term22,term32,term42,term52,term62
    real a12,a22,a32,a42,a52,a62
```

```
*
      real told3,pold3,hold3,vold3,gold3
      real voh3,otbar3,pbar3
      real term23,term33,term43,term53,term63
      real a13,a23,a33,a43,a53,a63
*
      real told4,pold4,hold4,vold4,gold4
      real voh4,otbar4,pbar4
      real term24,term34,term44,term54,term64
      real a14,a24,a34,a44,a54,a64
*
      real const1,const2,const3,const4
      real h1,h2,h3,h4
*
      save told1,pold1,hold1,vold1,gold1
      save voh1,otbar1,pbar1
      save term21,term31,term41,term51,term61
      save told2,pold2,hold2,vold2,gold2
      save voh2,otbar2,pbar2
      save term22,term32,term42,term52,term62
      save told3,pold3,hold3,vold3,gold3
      save voh3,otbar3,pbar3
      save term23,term33,term43,term53,term63
      save told4,pold4,hold4,vold4,gold4
      save voh4,otbar4,pbar4
      save term24,term34,term44,term54,term64
*
      logical ttest,ptest,htest,vtest,gtest
      logical pbartest,vohtest,tbartest
      logical term2test,term3test,term4test,term5test,term6test
*
      data told1,pold1,hold1,vold1,gold1/5*-999.9/
      data told2,pold2,hold2,vold2,gold2/5*-999.9/
      data told3,pold3,hold3,vold3,gold3/5*-999.9/
      data told4,pold4,hold4,vold4,gold4/5*-999.9/
*
      data const1,const2,const3,const4/0.6,2.8,0.2,0.2/
      data h1,h2,h3,h4/5.0,4.9,6.8,6.4/
*
      data a11,a21,a31,a41,a51,a61/-.13747e-2,-.43061e-4,
     &  .14618e+1, .25101e-3, .14635e-1,-.18588e+3/
      data a12,a22,a32,a42,a52,a62/ .22176e-1,-.32367e-4,
```

```
     & -.10840e-4, -.63578e-1, .16988e-7,-.29824e+2/
      data a13,a23,a33,a43,a53,a63/-.10566e-2,-.12906e-3,
     &  .56975e+0, .10828e-8,-.17551e-7, .48601e-1/
      data a14,a24,a34,a44,a54,a64/-.60808e-2,-.70936e-3,
     &  .28721e+1, .42636e-8,-.82910e-7, .26166e+0/
*
      data wvcor/1.01,0.95,1.06,0.92/
*
      wvc = wv*wvcor(ifreq)
*
      if (ifreq.eq.1) then
       ptest = p0.ne.pold1
       if (ptest) pold1 = p0
       ttest = ta.ne.told1
       if (ttest) told1 = ta
       htest = hwv.ne.hold1
       if (htest) hold1 = hwv
       vtest = wv.ne.vold1
       if (vtest) vold1 = wv
       gtest = gamma.ne.gold1
       if (gtest) gold1 = gamma
       pbartest = ptest.or.htest
       tbartest = ttest.or.gtest.or.htest
       vohtest  = vtest.or.htest
       term4test = pbartest.or.tbartest
       term5test = vohtest.or.tbartest
       if (pbartest) then
        pbar1 = p0/(1.0 + hwv/h1)
       endif
       if (vohtest) then
        voh1  = wv/hwv
        term21 = a21*voh1
       endif
       if (tbartest) then
        otbar1 = 1.0/(ta - const1*gamma*hwv)
        term31 = a31*otbar1
        term61 = a61*otbar1*otbar1
       endif
       if (term4test) then
        term41 = a41*pbar1*otbar1
       endif
       if (term5test) then
```

```
   term51 = a51*voh1*otbar1
  endif
  sigv = a11 + term21 + term31 + term41 + term51 + term61
 else if (ifreq.eq.2) then
  ptest = p0.ne.pold2
  if (ptest) pold2 = p0
  ttest = ta.ne.told2
  if (ttest) told2 = ta
  htest = hwv.ne.hold2
  if (htest) hold2 = hwv
  vtest = wv.ne.vold2
  if (vtest) vold2 = wv
  gtest = gamma.ne.gold2
  if (gtest) gold2 = gamma
  pbartest = ptest.or.htest
  tbartest = ttest.or.gtest.or.htest
  vohtest  = vtest.or.htest
  if (pbartest) then
   pbar2 = p0/(1.0 + hwv/h2)
   term22 = a22*pbar2
   term52 = a52*pbar2*pbar2
  endif
  if (vohtest) then
   voh2  = wv/hwv
   term32 = a32*voh2
  endif
  if (tbartest) then
   otbar2 = 1.0/(ta - const2*gamma*hwv)
   term42 = a42*otbar2
   term62 = a62*otbar2*otbar2
  endif
  sigv = a12 + term22 + term32 + term42 + term52 + term62
 else if (ifreq.eq.3) then
  ptest = p0.ne.pold3
  if (ptest) pold3 = p0
  ttest = ta.ne.told3
  if (ttest) told3 = ta
  htest = hwv.ne.hold3
  if (htest) hold3 = hwv
  vtest = wv.ne.vold3
  if (vtest) vold3 = wv
  gtest = gamma.ne.gold3
```

```
   if (gtest) gold3 = gamma
   pbartest = ptest.or.htest
   tbartest = ttest.or.gtest.or.htest
   vohtest  = vtest.or.htest
   term5test = vohtest.or.pbartest
   term6test = vohtest.or.tbartest
   if (pbartest) then
    pbar3 = p0/(1.0 + hwv/h3)
    term43 = a43*pbar3*pbar3
   endif
   if (vohtest) then
    voh3  = wv/hwv
    term23 = a23*voh3
   endif
   if (tbartest) then
    otbar3 = 1.0/(ta - const3*gamma*hwv)
    term33 = a33*otbar3
   endif
   if (term5test) then
    term53 = a53*pbar3*voh3
   endif
   if (term6test) then
    term63 = a63*otbar3*voh3
   endif
   sigv = a13 + term23 + term33 + term43 + term53 + term63
 else if (ifreq.eq.4) then
  ptest = p0.ne.pold4
  if (ptest) pold4 = p0
  ttest = ta.ne.told4
  if (ttest) told4 = ta
  htest = hwv.ne.hold4
  if (htest) hold4 = hwv
  vtest = wv.ne.vold4
  if (vtest) vold4 = wv
  gtest = gamma.ne.gold4
  if (gtest) gold4 = gamma
  pbartest = ptest.or.htest
  tbartest = ttest.or.gtest.or.htest
  vohtest  = vtest.or.htest
  term5test = vohtest.or.pbartest
  term6test = vohtest.or.tbartest
  if (pbartest) then
```

```
      pbar4 = p0/(1.0 + hwv/h4)
      term44 = a44*pbar4*pbar4
     endif
     if (vohtest) then
      voh4  = wv/hwv
      term24 = a24*voh4
     endif
     if (tbartest) then
      otbar4 = 1.0/(ta - const4*gamma*hwv)
      term34 = a34*otbar4
     endif
     if (term5test) then
      term54 = a54*pbar4*voh4
     endif
     if (term6test) then
      term64 = a64*otbar4*voh4
     endif
     sigv = a14 + term24 + term34 + term44 + term54 + term64
    else
     sigv = 0.0
    endif
    sigma_v = sigv*wvc
    return
    end
*
```

```
*****************************************
*
* SUBROUTINE EFFHT(HO,HV,SIGO,SIGV,MU,ZCLD,HDN,HUP,HDNINF,HUPINF)
*
* This subroutine returns "effective emitting heights" for an
* atmosphere with gaseous absorption approximated by two
* exponentially-decaying profiles with distinct scale heights.
* For applications at SSM/I frequencies
* (i.e., 19, 22, 37, 86 GHz), these absorption profiles
* correspond to water vapor and dry air absorption,
* respectively.
*
* Input parameters:
*  HO,HV -- scale heights of absorption corresponding to
*                  dry air and water vapor (km):
*  SIGO, SIGV -- total optical depth due to each constituent
*  MU   -- secant(theta), where theta is the path angle from
*        vertical
*  ZCLD -- upper limit (km) of the atmospheric layer for
*        which hdn, hup are to be calculated. Layer
*        extends down to the surface. These parameters
*        permit the separate calculation brightness
*        temperature contributions from a lower and
*        upper atmospheric layer, separated by a
*        cloud layer at height zcld.
*
* Output parameters:
*
*  HDN, HUP -- "effective emitting height" of an atmospheric
*          layer bounded below by the surface and above
*          at height zcld. "Effective emitting temperature"
*          for upward and downward microwave radiation
*          emitted by that layer is then given by
*          (Ta - gamma*hup) and (Ta - gamma*hdn),
*          respectively, where Ta and gamma are effective
*          surface temperature (deg K) and lapse rate
*          (K / km), respectively. Brightness temperatures
*          due to emission from this layer are then
*          (1 - tau)(Ta - gamma*hup) and
*          (1 - tau)(Ta - gamma*hdn), respectively, where
*          tau is the slant path transmittance of the layer
*          at angle theta NF  -- same as hdn and hup, but
```

```
*           for the entire atmosphere
*           (i.e., zcld set to infinity)
*
*-----------------------------------------------
      subroutine effht(ho,hv,sigo,sigv,mu,zcld,hdn,hup,
     & hdninf,hupinf)
*
      real ho,hv,sigo,sigv,mu,zcld,gint,zgint,hint,zhint,
     &    ginf,zginf,hinf,zhinf,hdn,hup,hdninf,hupinf
      real hoold,hvold,sigoold,sigvold,muold,zcldold
      save hoold,hvold,sigoold,sigvold,muold,zcldold
      logical hotest,hvtest,sigotest,sigvtest,mutest,zcldtest
*
      real hoinv,hvinv,chio,chiv,ezho,ezhv,alpha,alph2,alph3
      real beta,beta2,beta3,mu2,mualph,cplus,cmin,dplus,dmin
      real chiov,chivv,chioo,chioov,chiovv,chiooo,chivvv
      real h11,h21,h12
      real sigoo,sigov,sigvv,sigooo,sigoov,sigovv,sigvvv
      real ezhoo,ezhov,ezhvv,ezhooo,ezhoov,ezhovv,ezhvvv
      real s,sprim,t,tprim,u,uprim,term1,term2,term3
      real halfmu,halfmu2,sixthmu2,etnthmu2,quartmu
*
      save hoinv,hvinv,chio,chiv,ezho,ezhv,
     &    alpha,alph2,alph3,beta,beta2,beta3
      save mu2,halfmu,sixthmu2,etnthmu2,quartmu,
     & halfmu2,mualph,cplus,cmin,dplus,dmin,dplus,dmin
      save h11,h21,h12,h11,chiov,chioo,chivv,chioov,
     & chiovv,chiooo,chivvv,chio,chiv,sigov,sigoo,sigvv,
     & sigooo,sigoov,sigovv,sigvvv,ezhoo,ezhov,ezhvv,ezhovv,
     & ezhoov,ezhooo,ezhvvv,s,sprim,t,tprim,u,uprim
*
      data hoold,hvold,sigoold,sigvold,muold,zcldold/
     &  -1.0,-1.0,-1.0,-1.0,-1.0,-1.0/
*
* check which input variables have changed since last call
      hotest = (ho.eq.hoold)
      hvtest = (hv.eq.hvold)
      zcldtest = (zcld.eq.zcldold)
      sigotest = (sigo.eq.sigoold)
      sigvtest = (sigv.eq.sigvold)
      mutest = (mu.eq.muold)
*
```

```
      if (.not.(hotest .and. hvtest .and. zcldtest
     &   .and. sigotest .and. sigvtest)) then
        hoinv = 1.0/ho
        hvinv = 1.0/hv
        chio = zcld*hoinv
        chiv = zcld*hvinv
        ezho = sigo*exp(-chio)
        ezhv = sigv*exp(-chiv)
        alpha = sigo + sigv
        alph2 = alpha*alpha
        alph3 = alpha*alph2
        beta =  ezho + ezhv
        beta2 = beta*beta
        beta3 = beta*beta2
*
        hoold = ho
        hvold = hv
        sigoold = sigo
        sigvold = sigv
        zcldold = zcld
      endif
*
      if (.not. mutest) then
        mu2 = mu*mu
        halfmu = 0.5*mu
        sixthmu2 = mu2/6.0
        etnthmu2 = mu2/18.0
        quartmu = 0.25*mu
        halfmu2 = 0.5*mu2
        mualph = mu*alpha
        cplus = 1.0 + mualph
        cmin  = 1.0 - mualph
        dplus = halfmu2*alph2
        dmin  = dplus
        dplus = cplus + dplus
        dmin  = cmin  + dmin
*
        muold = mu
      endif
*
      if (.not.(hotest .and. hvtest .and. zcldtest
     &   .and. sigotest .and. sigvtest)) then
```

```
      h11 = hoinv + hvinv
      h21 = 1.0/(h11 + hvinv)
      h12 = 1.0/(h11 + hoinv)
      h11 = 1.0/h11
      chiov = 1.0 + chio + chiv
      chioo = 1.0 + chio + chio
      chivv = 1.0 + chiv + chiv
      chioov = chioo + chiv
      chiovv = chio + chivv
      chiooo = chioo + chio
      chivvv = chivv + chiv
      chio = 1.0 + chio
      chiv = 1.0 + chiv
      sigov = sigo*sigv
      sigoo = sigo*sigo
      sigvv = sigv*sigv
      sigooo = sigoo*sigo
      sigoov = sigoo*sigv
      sigovv = sigo*sigvv
      sigvvv = sigvv*sigv
      ezhoo = ezho*ezho
      ezhov = ezho*ezhv
      ezhvv = ezhv*ezhv
      ezhovv = ezho*ezhvv
      ezhoov = ezhoo*ezhv
      ezhooo = ezhoo*ezho
      ezhvvv = ezhvv*ezhv
      s    = sigo*ho  +   sigv*hv
      sprim = ezho*ho*chio + ezhv*hv*chiv
      t    = sigoo*ho   +   4.0*sigov*h11    +  sigvv*hv
      tprim = ezhoo*ho*chioo + 4.0*ezhov*h11*chiov +
     &    ezhvv*hv*chivv
      u    = sigooo*ho+9.0*(sigovv*h21+sigoov*h12)+sigvvv*hv
      uprim = ezhvvv*hv*chivvv +
     &    9.0*(ezhovv*h21*chiovv + ezhoov*h12*chioov) +
     &      ezhooo*ho*chiooo
      endif
*
      term1 = s - sprim
      term2 = quartmu*(t - tprim)
      term3 = etnthmu2*(u - uprim)
      zgint = dmin*term1 +  cmin*term2 + term3
```

```
zhint = -dplus*term1 + cplus*term2 - term3
term2 = quartmu*t
term3 = etnthmu2*u
zginf = dmin*s +  cmin*term2 + term3
zhinf = -dplus*s + cplus*term2 - term3
term1 = alpha - beta
term2 = halfmu*(alph2 - beta2)
term3 = sixthmu2*(alph3 - beta3)
gint  = dmin*term1 +  cmin*term2 + term3
hint  = -dplus*term1 + cplus*term2 - term3
term2 = halfmu*alph2
term3 = sixthmu2*alph3
ginf  = dmin*alpha +  cmin*term2 + term3
hinf  = -dplus*alpha + cplus*term2 - term3
hdn   = zgint/gint
hup   = zhint/hint
hdninf = zginf/ginf
hupinf = zhinf/hinf
return
end
```

VITA

Grant William Petty was born in [redacted], [redacted], on [redacted]. [redacted]. He attended El Camino Real High School in Woodland Hills, California, graduating with honors in 1975. His university studies began at the University of California at San Diego, but he spent his junior year abroad at the Georg-August University in Göttingen, West Germany, and subsequently completed his undergraduate studies at the Davis campus of the University of California. There he received a Bachelor of Science degree in Applied Physics, with an emphasis in Atmospheric Physics (1984).